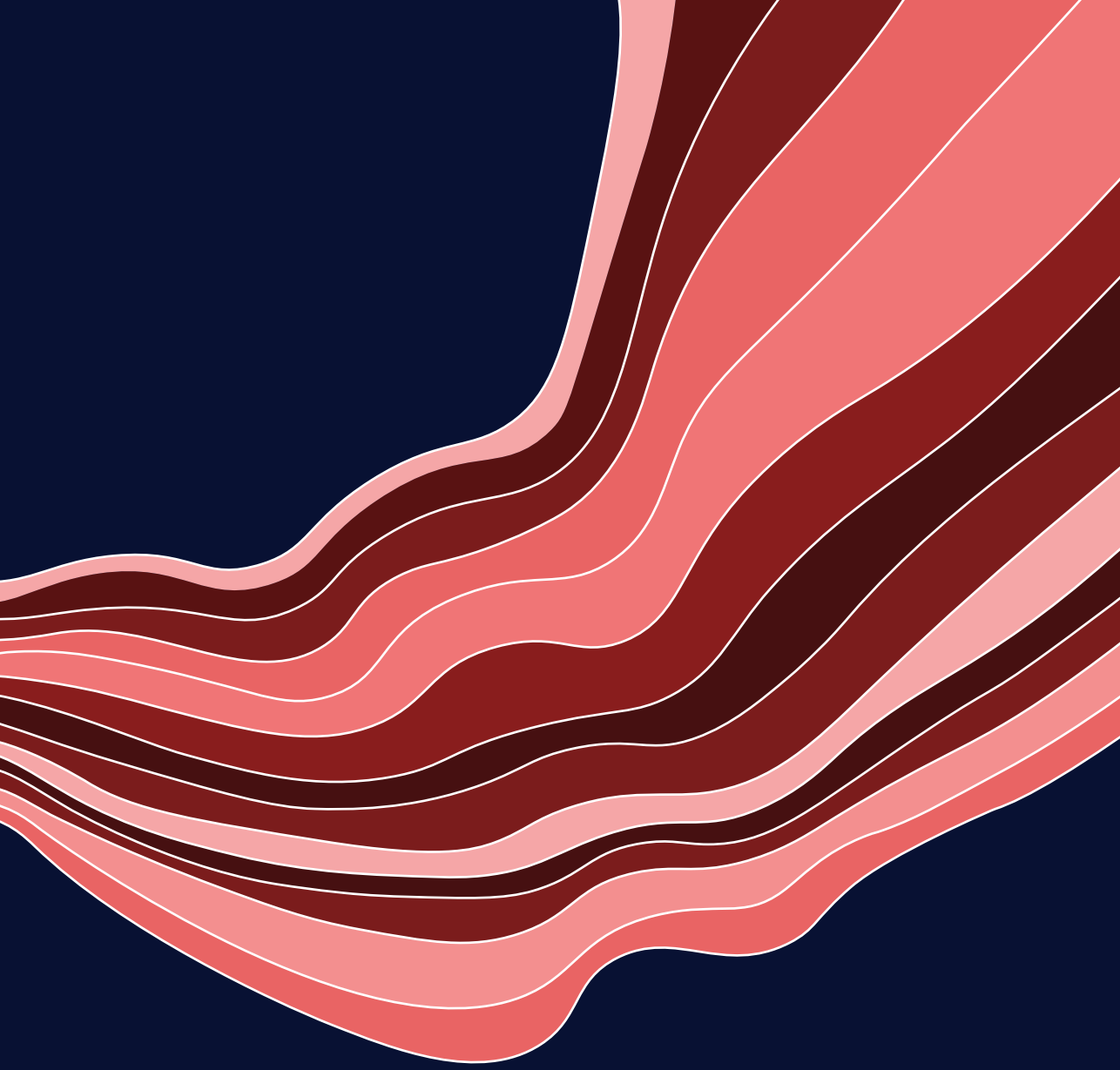

Amplifying Plasmonic Metasurfaces

Optical gain for response control, metasurface lasing and symmetry breaking

Nelson de Gaay Fortman

Amplifying Plasmonic Metasurfaces

Optical gain for response control, metasurface lasing and symmetry breaking

Ph.D. Thesis, University of Amsterdam, June 2025
Amplifying Plasmonic Metasurfaces - Optical gain for response control, metasurface lasing and symmetry breaking
Pieter Nelson Gaius de Gaay Fortman

ISBN: 978-94-92323-77-4

The work described in this thesis was performed at
AMOLF, Science Park 104, 1098 XG Amsterdam, The Netherlands.

This work is part of the Netherlands Organisation for Scientific Research (NWO).

A digital version of this thesis can be downloaded from
http://www.amolf.nl

Amplifying Plasmonic Metasurfaces

Optical gain for response control, metasurface lasing and symmetry breaking

ACADEMISCH PROEFSCHRIFT

ter verkrijging van de graad van doctor
aan de Universiteit van Amsterdam
op gezag van de Rector Magnificus
prof. dr. ir. P.P.C.C. Verbeek
ten overstaan van een door het College voor Promoties ingestelde commissie,
in het openbaar te verdedigen in de Agnietenkapel
op donderdag 5 juni 2025, te 10.00 uur

door

Pieter Nelson Gaius de Gaay Fortman

geboren te Blaricum

Promotiecommissie

Promotores:	prof. dr. A. F. Koenderink	Universiteit van Amsterdam
	prof. dr. P. Schall	Universiteit van Amsterdam
Overige leden:	prof. dr. M. S. Golden	Universiteit van Amsterdam
	prof. dr. A. Polman	Universiteit van Amsterdam
	dr. S. A. Mann	Universiteit van Amsterdam
	dr. H. Caglayan	TU Eindhoven
	prof. dr. J. J. Greffet	Institut d'Optique Graduate School

Faculteit der Natuurwetenschappen, Wiskunde en Informatica

Contents

Chapter 1

Introduction

1.1 A profound fascination with light

The interaction of light with matter is a source for life on Earth, and forms the complete human visual experience. It is therefore not surprising that humans are captivated by light in a spiritual way, viewing light as a symbol for enlightenment, creation and hope across cultures and religions, and also in an artistic way, as expressed in some of the most iconic paintings in history (e.g., Caravaggio's Calling of St. Matthew, Rembrandt's Night Watch, Van Gogh's Potato Eaters). Our awe with the phenomenon of light sparks our scientific interest. For ages we have asked ourselves the questions: What is light? How does it behave, and how can we control it? Already in ancient civilizations people studied refraction, the bending of light by a medium with higher refractive index n. Snellius formalized the law of refraction in the 17th century, which led to the technological advancement of microscopes to study the world of small things and telescopes to look at the universe. In the same period, Huygens conceptualized the wave nature of light. This realization, followed by discoveries related to electric and magnetic fields, laid foundations for a milestone scientific achievement by Maxwell in 1865: The formulation of the Maxwell equations [1], from which he deduced that light waves travel at constant speed c. Besides the huge implications for relativity physics and quantum mechanics, the increased scientific understanding of light subsequently led to ever increasing technological advancements that define our modern day societies. In the 20th century, people invented ever more ingenious light sources, such as the laser and light-emitting diodes (LEDs) [2], as well as exquisitely sensitive light sensors, such as pixel-array based CCD [3] and CMOS [4] cameras. Hand in hand, these innovations revolutionized scientific research across disciplines, while also becoming a part of every day

life through, for instance, current smartphone technology. What is more, optical fibers were invented [5] for transmission of information-encoded light beams, and the worldwide fiber network currently enables modern internet communication across continents. In the present day, scientists experience a resurgence in interest in optical processors that perform logical operations on information-encoded light waves, deemed particularly promising as running artificial intelligence algorithms with low energy cost [6, 7].

Reflecting on the magnificent progress in the science of light as assessed above, it is clear that many advances in history have been pushed by our desire to understand and control light. As we aim to understand and control behavior of light in ever smaller devices – the ambition of the field called nanophotonics – it has proved challenging to obtain sufficiently strong light-matter interactions [8] to effectively control the scattering and propagation of light. Nonetheless, it has recently become clear that it is possible to generate light-matter interactions that are strong enough to manipulate optical wavefronts at will, even in optical devices which in one dimension are much thinner than a wavelength. Such devices are called metasurfaces [9].

1.2 Metasurfaces

Metasurfaces emerged from the field of metamaterials [11, 12] as optically thin, two-dimensional (2D) planar systems composed of nanoparticles whose resonances offer extraordinary capabilities to control amplitude, phase and polarization of interacting light beams [9, 13, 14]. The surfaces constitute dense arrays of subwavelength resonant scatterers (also called optical antennas) with subwavelength interparticle spacing, generating a spatially varying

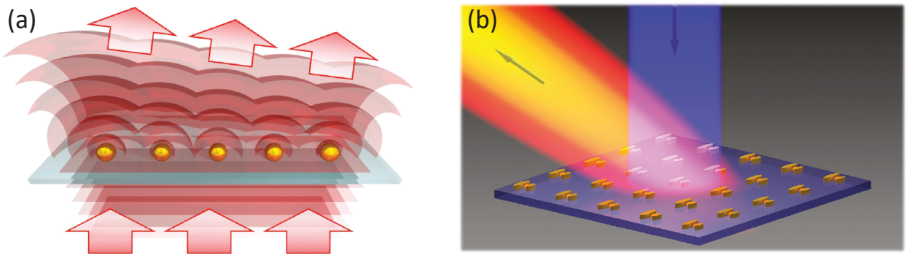

Figure 1.1: Illustration of scattering and light-emitting metasurfaces. (a) Scattering metasurfaces are 2D ensembles of nanoparticles that are both subwavelength in size and in interparticle distance. The strong antenna resonances can be tuned to locally vary metasurface phase response, for instance to redirect the incidint wavefront into an arbitrary direction in the far-field. (b) Light-emitting metasurface: Pump light in blue excites emitters embedded in the metasurface, whose carefully designed nanoparticle array exerts control over subsequent emission to the far-field (yellow-red). Images reused from Ref. [10], courtesy of R. Kolkowksi.

response to transmitted or reflected waves, see Figure 1.1(a). These arrays generalize the classical (19th century) notion of a diffraction grating in several ways. First, in a diffraction grating, objects are arrayed at pitches well above a wavelength, causing grating diffraction orders to appear. Instead, in metasurfaces the scatterers are subdiffractively spaced. Second, in classical diffraction gratings the unit cells are identical, whereas in a metasurface they are individually tailored to locally shape amplitude and phase response [13]. Third, to shape amplitude and phase response effectively, the scatterers, or *meta-atoms*, are often taken to have internal scattering resonances that derive from the constituent material and shape. Research on such *scattering metasurfaces* form a rich body of literature, for instance exhibiting anomalous refraction [15], lenses [16], geometrical phase change [17], and polarization state conversion [18]. We wish to distinguish scattering metasurfaces that are designed to transform incident waves as described above, from *light-emitting metasurfaces*: Metasurfaces that have emitters (quantum dots, quantum wells, dye molecules) embedded in their design so that the whole forms a flat nanostructured source of tailored light fields [10], see Fig 1.1. In contrast to scattering metasurfaces, light-emitting metasurfaces often do operate on basis of diffraction, while still possessing strongly collective near field modes. This connects them to recently emerged interest in nonlocal metasurfaces [19–23]. Although dipolar emitters in light-emitting metasurfaces radiate incoherently and isotropically, multiple scattering leads to directional emission, i.e., partial spatial coherence that can be tailored by engineering the diffractive collective modes [24, 25]. Resonant unit cells distinguish light-emitting metasurfaces from similar light-emitting photonic crystal research [26]. Light-emitting metasurfaces have been studied in the context of directionality of thermal emission [27], for light-emitting-diodes [28] and 2D lattice lasing [29–31]. In general, metasurface research comes with an advanced toolbox for functionality design by means of both meta-atoms themselves (structure, resonances, orientation) and their placement in the surface (interparticle spacing, lattice symmetries).

1.2.1 Plasmonic nanoparticles

Two types of metasurface building blocks are prevalent, namely metallic nanoparticles machined out of noble metals like gold and silver on one hand, and dielectric nanoparticles of high refractive index on the other hand. Metallic nanoparticles host resonances coined localized surface plasmon resonances (LSPR): A plasma of free electrons in the metal nanoparticle resonantly oscillates with an incoming radiation field [32, 33]. These oscillations generate strongly localized near field hotspots near the surface of the nanoparticle, where high local density of optical states lead to Purcell enhancement of radiation channels for emitters that are coupled to the nanoparticle [34]. Plasmonic nanoparticles are extremely strong scatterers for

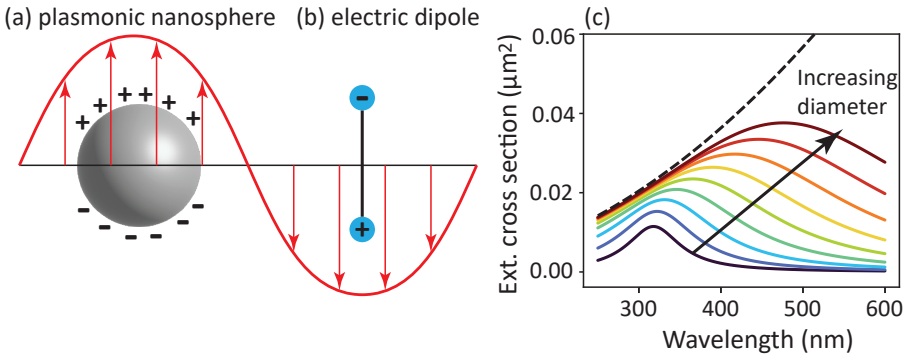

Figure 1.2: Metallic nanoparticle with localized surface plasmon resonance. (a) Sketch of the LSPR: When the metallic nanoparticle is placed in the oscillating electromagnetic fields of a passing light wave (in red), free electrons in the metal sphere make high density clouds near the surface, leading to separation of charges. (b) The charge separation creates an effective electric dipole moment, that can oscillate resonantly with the light field. (c) Calculated extinction spectra for metal nanoparticles in glass ($\epsilon_{\text{host}} = 1.45^2$). The blue to red curves indicate sizes of 40-120 nm, in steps of 10 nm. Ohmic parameters in the Drude model are $\omega_p = 1.5 \cdot 10^{16}$ rad/s and $\gamma_p = 0.05\omega_p$. The unitary limit of maximal possible extinction is plotted in dashed black. Note how both redshift and broadening become increasingly important for larger diameters, as a result of radiation damping.

their size: Their extinction cross-sections can be more than ten times the actual cross-sectional area of the particle [33]. However, the large Ohmic resistance that the oscillating electron cloud experiences can lead to strong absorption losses.

We shortly review a canonical framework for scattering by plasmonic nanoparticles [35]. The model starts with a Drude model for the dielectric response function of a metal at frequency ω, which is due to the electron plasma

$$\epsilon(\omega) = \epsilon_\infty - \frac{\omega_p}{\omega^2 + i\gamma\omega}. \tag{1.1}$$

Here, ϵ_∞ accounts for the permittivity contributed by bound charges of the constituent atoms of the metal, while ω_p represents the electron plasma frequency and γ quantifies the Ohmic damping rate. The plasma frequency directly depends on the electron density and effective mass, and for Ag and Au is in the blue/UV part of the optical spectrum [36]. For frequencies in this range, the dielectric constant is negative, yet in magnitude it is of order unity.

When driven by light, a small nanoparticle acts as a dipole scatterer, with the magnitude and phase of the dipole moment that is induced by the incident field $\mathbf{E}$ set by the complex-valued polarizability. In a convention where polarizabilities α have units of volume, this statement reads

$$\mathbf{p} = 4\pi\epsilon_{\text{host}}\epsilon_0\alpha\mathbf{E}, \tag{1.2}$$

with $\mathbf{p}$ the dipole moment induced by electric field $\mathbf{E}$, see Figure 1.2(a,b). For a particle in host medium with permittivity ϵ_{host}, we find the polarizability within the Rayleigh approximation for small spheres of radius r as[35]

$$\alpha_0(\omega) = r^3 \frac{\epsilon(\omega) - \epsilon_{\text{host}}}{\epsilon(\omega) + 2\epsilon_{\text{host}}}. \tag{1.3}$$

This *static polarizability* function generally displays a Lorentzian lineshape (when $\epsilon_\infty = \epsilon_{\text{host}}$) for the localized surface plasmon resonance that peaks at the condition $Re\{\epsilon(\omega)\} = -2\epsilon_{\text{host}}$. The LSPR resonance frequency is at $\omega_0 = \omega_p/\sqrt{3\epsilon_{\text{host}}}$. Appealing for metasurfaces is the combination of large scattering cross-sections, and the fact that the polarizability varies in phase when tuning across the resonance. Scattering towards the far-field presents a loss channel for the dipole resonance that comes on top of the intrinsic Ohmic loss. This *radiation damping* is especially significant for larger-sized particles, and it is expressed by the need to include a radiation damping factor $i2/3k^3$ in the dipole polarizability as

$$\alpha_{\text{dyn}}(\omega) = \frac{1}{1/\alpha_0 - i2/3k^3}, \tag{1.4}$$

where $k = n\omega/c$ is the wave number in medium $n = \sqrt{\epsilon_{\text{host}}}$ surrounding the scatterer [37, 38]. For the resulting *dynamic polarizability*, scattering and extinction cross-sections

$$\sigma_{\text{ext}} = 4\pi k \text{Im}\alpha_{\text{dyn}} \qquad \sigma_{\text{scatt}} = 8\pi/3k^4|\alpha_{\text{dyn}}|^2 \tag{1.5}$$

satisfy the optical theorem: extinction equals scattering in absence of Ohmic loss (real-valued α_0), and else extinction minus scattering equals absorption.

Figure 1.2(c) shows calculated extinction cross-sections for plasmon spheres of varying diameters. For small spheres, the extinction cross-section is up to 10-fold the geometrical cross-section πr^2, and the peak cross-section grows with particle diameter. As the particle gets larger in diameter, radiation damping becomes more important, leading to a significant broadening of the LSPR and a significant redshift. Moreover in the limit of $|\alpha_0| \to \infty$, dynamic polarizability does not reach infinite values: α_{dyn} is subject to a fundamental *unitary limit* set by the radiation damping term (i.e. $i2/3k^3$), and as a consequence the dipole cross-section is limited to $3\lambda^2/(2\pi n^2)$. This limit is overplotted in Fig. 1.2(c) as a dashed black line. It represents the strongest scattering that can be achieved with any dipolar scattering object, be it a plasmon particle or, e.g., an atomic scatterer probed on resonance.

The above analysis covered a simple isotropic nanoparticle that exhibits equal polarizability in the x, y, and z directions. As metasurface building blocks, plasmonic nanoparticles in fact offer much more design freedom, as they can be made anisotropic and obtain different polarizability resonances along three principal axes. Even more design freedom is offered by including

anisotropic magnetic dipolar terms for instance with split-ring antennas [39, 40], or by making shapes and coupled systems with multipolar (e.g. electric quadrupolar) resonances [41].

1.2.2 Mie-resonant particles

Owing to the strong optical absorption of metal nanoparticles, all-dielectric metasurfaces receive much attention [42–44]. Since resonances in dielectric structures typically require to fit a standing wave in the structure, it is a challenge to obtain resonant responses in a subwavelength object, unless the refractive index is high. In dielectric metasurfaces, the meta-atoms are often semiconductor particles made of materials like silicon, titanium dioxide, or III-V semiconductor, which present significantly higher index than their surroundings, typically air or glass. At high index contrast, even subwavelength particles can host electric and magnetic dipolar Mie resonances [45]. Instead of the actual current represented by oscillating free charges, the origin of these resonances can be viewed as local displacement current oscillations that form electric and magnetic multipolar resonant modes. The benefits of Mie-resonant particles over plasmonic nanoparticles is that they come with essentially zero absorption losses, while they still offer versatile engineering of scattering resonances. For instance, by tuning dielectric contrast and shape, one can find frequency regions in which multiple Mie modes contribute to resonant scattering. Silicon nanospheres can for instance exhibit complex interference signatures in the far-field, such as Kerker conditions when electric and magnetic dipoles overlap, anapole modes, and toroidal dipoles [43]. However, only for sufficiently high refractive index contrast with the background medium, Mie-resonant

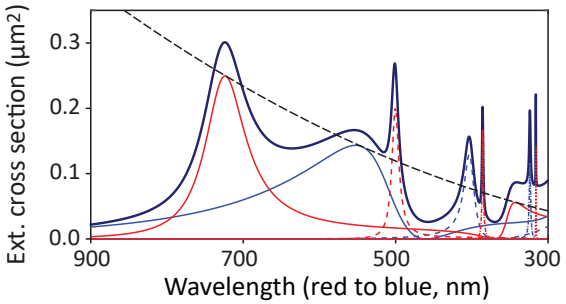

Figure 1.3: Mie calculations of extinction by a Silicon sphere. The sphere has diameter 200 nm and $\epsilon = 12$, and resides in air backround. The thick, darkblue line represents total extinction, while the red and blue colors indicate magnetic and electric multipolar contributions. Solid lines are the first dipolar contributions, while dashed lines represent the higher multipolar modes. The black dashed line is the unitary limit for dipole extinction.

particles can obtain extinction cross-sections comparable to those of plasmonic nanoparticles.

In Figure 1.3 we show a Mie calculation of extinction by a 200 nm silicon sphere in air (lossless, taking $\epsilon = 12$). We distinguish between magnetic and electric contributions with red and blue colored lines respectively, and dotted lines mean higher order multipolar modes. Also here, as in Fig 1.2, we plot the unitary limit for dipolar radiation as a black dotted line, which the magnetic and electric dipolar modes touch. All-dielectric Mie-resonant metasurfaces attain interest not only for linear, but also for nonlinear wavefront control, benefiting from the nonlinear susceptibility of semiconductors [46–48].

1.2.3 Periodic metasurfaces

Light-emitting metasurfaces are often structured in a periodic fashion. Therefore, standard concepts in solid-state physics for electrons in crystals also apply to photons in many light-emitting metasurfaces. For instance, the response of a periodic metasurface is often studied in terms of its photonic band structure, a method developed in photonic crystal research [49]. A commonly employed geometry for light emitting metasurfaces is to embed emitters in a 2D slab waveguide, together with a periodic lattice of optical nano-antennas. The benefit of the 2D waveguide is that even at modest index contrast it will present the main emission channel into which the emitters radiate [50]. The waveguide mode essentially determines the magnitude of the in-plane momentum of the emitted light, imparting a degree of spatial coherence to the emission, which can be utilized in the far field by diffraction. This method of directing light emitted from metasurfaces was pioneered by J.-J. Greffet for thermal emission [24, 25, 27], and was extensively researched for LED applications [26, 28].

Photons traveling through a waveguide with a periodic perturbation defined by a lattice with vectors $\mathbf{R}$, behave like Bloch waves: They are solutions of the electromagnetic wave equation that obey Bloch's Theorem [8, 36, 49]. Bloch's Theorem can be written as

$$\psi_{\mathbf{k}}^{n}(\mathbf{r}+\mathbf{R}) = e^{i\mathbf{k}\cdot\mathbf{R}}\psi_{\mathbf{k}}^{n}(\mathbf{r}). \tag{1.6}$$

This statement from solid state physics deals with modal solutions (Bloch modes) that are written as a wave function $\psi_{\mathbf{k}}^{n}$ (in solid state physics pertaining to electron wavefunctions, here to classical electromagnetic fields), and that are eigenfunctions of the wave equation (without driving term) in a periodic medium. According to Bloch's theorem, such solutions have the property that their values at position $\mathbf{r}$ or at a position $\mathbf{r}+\mathbf{R}$ shifted by any lattice vector $\mathbf{R}$, are identical up to a phase factor written as $e^{i\mathbf{k}\cdot\mathbf{R}}$. An equivalent way to write this, is to demand that the solutions have the form

$$\psi_{\mathbf{k}}^{n}(\mathbf{r}) = e^{i\mathbf{k}\cdot\mathbf{r}}\mathbf{u}_{\mathbf{k}}^{n}(\mathbf{r}) \tag{1.7}$$

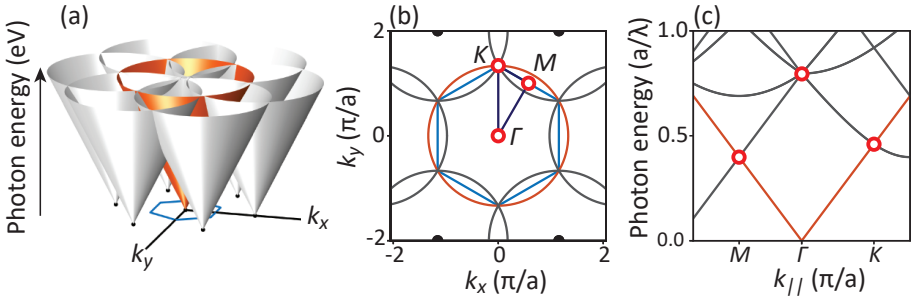

Figure 1.4: Folded zone scheme in the free-photon approximation for a hexagonal lattice. (a) The linear energy-momentum dispersion of light leads to conical dispersion in (ω, k_x, k_y) space in orange, which is repeated at the reciprocal lattice points. (b) Energy crosscut through the cones in (a), forming a (k_x, k_y) Fourier image. The Brillouin zone is displayed in light blue, and the irreducible BZ in dark blue, together with high symmetry points Γ, M and K. The pitch is chosen such that the folded circles intersect at the K-point, highlighted as a white-red dot. (c) Photon $(\omega, k_{||})$ dispersion image, obtained by crosscutting the cones in the energy plane. The band intersection at the K-point is again indicated as a white-red dot.

where the function $\mathbf{u}_{\mathbf{k}}^n(\mathbf{r}) = \mathbf{u}_{\mathbf{k}}^n(\mathbf{r} + \mathbf{R})$ has exactly the same periodicity as the dielectric function at hand. The wave vector $\mathbf{k}$ that enters the phase factor and that labels the solution is also known as 'Bloch wave vector', 'crystal momentum', or 'quasi momentum'. For a specific $\mathbf{k}$, the wave equation comes with a countable infinite set of Bloch eigenstates $\psi_{\mathbf{k}}^n$ (optical fields) that possess discretely spaced energy eigenvalues $\mathcal{E}_{\mathbf{k}}^n$ (optical frequency), and for each solution we assign an index n that enumerates the energy bands. The mapping of energy eigenvalues versus wave vectors forms the band structure of allowed energies for photons.

A useful starting point to understand the effect of the lattice symmetry on the photonic band structure is the free-photon dispersion approximation. As example we take a 2D lattice of hexagonal symmetry with lattice constant a, for which the set of lattice vectors $\mathbf{R}$ are spanned by two basis vectors $\boldsymbol{a_{1,2}}$

$$\mathbf{R} = i\boldsymbol{a_1} + j\boldsymbol{a_2}, \qquad \boldsymbol{a_1} = (a\sqrt{3}/2, a/2), \qquad \boldsymbol{a_2} = (0, a), \tag{1.8}$$

where i and j are integers. On basis of the real space lattice, the reciprocal lattice is the set of vectors $\mathbf{G}$ that satisfy the property $e^{i\mathbf{G}\cdot\mathbf{R}} = 1$ for all real space lattice vectors $\mathbf{R}$. The reciprocal lattices comprises the integer linear combinations of basis vectors $\mathbf{G}_1$ and $\boldsymbol{G_2}$

$$\mathbf{G} = m\boldsymbol{G_1} + n\mathbf{G}_2, \qquad \mathbf{G}_1 = \begin{pmatrix} \frac{2\pi}{2\sqrt{3}a} \\ \frac{2\pi}{2a} \end{pmatrix}, \qquad \mathbf{G}_2 = \begin{pmatrix} \frac{4\pi}{2\sqrt{3}a} \\ 0 \end{pmatrix}, \tag{1.9}$$

with m and n integers. In the reciprocal lattice, the first Brillouin Zone (BZ) can be composed as a Wigner-Seitz cell unit cell constructed from $\mathbf{G}_1$ and $\mathbf{G}_2$. The

first BZ of the hexagonal lattice also has hexagonal symmetry and is indicated in blue in Figure 1.4(a).

For 2D periodic lattices in a 3D space, discrete translation invariance in the xy-plane mandates that in-plane momentum $\mathbf{k}_{||} = (k_x, k_y)$ is a conserved quantity, up to reciprocal lattice vectors. This law is also known as the grating diffraction law, and is identical in form to the law stipulating the allowed angles for Von Laue diffraction by crystals: For a photon impinging on the lattice with parallel momentum $\mathbf{k}'_{||}$, constructive interference into a photon with momentum $\mathbf{k}_{||}$ will occur, provided their difference is exactly a reciprocal lattice vector,

$$\mathbf{k}'_{||} = \mathbf{k}_{||} + \mathbf{G}. \tag{1.10}$$

This relation is also contained in the first formulation of Bloch's Theorem in Eq.(1.7): Solutions with quasi momentum $\mathbf{k}_{||}$ and $\mathbf{k}_{||} + \mathbf{G}$ clearly result in the *same* net phase pickup $\exp[i\mathbf{k}_{||} \cdot \mathbf{R}]$ when shifting by a lattice vector $\mathbf{R}$, since $e^{i\mathbf{G}\cdot\mathbf{R}} = 1$ [36]. The implication is that all bands can be uniquely enumerated by constraining wavevectors to the first Brillouin Zone, since any $\mathbf{k}'_{||}$ outside of the the BZ is indistinguishable from wavevector $\mathbf{k}_{||}$ inside the BZ, by virtue of Eq. (1.10). This 'folded' band scheme is useful to summarize band diagrams. Sometimes it is useful for physical insight to instead examine 'repeated zone scheme' band diagrams, plotting also the band structure replicas based at nonzero $\mathbf{G}$.

Figure 1.4(a) presents a repeated zone scheme dispersion relation in the (nearly) free photon approximation. The starting point is that the photon dispersion for a homogeneous 2D system of refractive index n is a cone in (ω, k_x, k_y)-space, given by $\omega = c/n|\mathbf{k}|$ where c is the speed of light. This cone, displayed in orange, is replicated in momentum space at each reciprocal lattice vector $\mathbf{G}$. Common spaces to study a photonic band structure in optical experiments are the (k_x, k_y) space (Fourier space, imaged at a single frequency ω in Fourier microscopy), shown in panel (b), and the $(\omega, k_{||})$ space (dispersion diagram, typically fixing a line such as $k_x = 0$ in momentum space) in panel (c). The Fourier space image in panel (b) highlights the BZ in blue, and the repeating circles result from taking a fixed frequency crosscut through panel (a). Special points within the BZ are the center (Γ-point), the corners (K-points) and the points in between the corners (M-points). For specific lattice spacings, multiple repeated Bloch modes can intersect at these so-called high-symmetry points. For the band diagram (c), the wave vector axis to the left of the Γ-point follows a linear trajectory from Γ through M, while to the right of Γ the wave vector is swept over a linear trajectory from and through K. While a textbook band structure would strictly follow the trajectory $M - \Gamma - K - M$ (contour of the irreducible part of the Brillouin zone), here, for illustrative purposes, the dispersion relation is extended on linear trajectories also beyond the special points K and M, bringing out the geometry of the bands as lines and cones, and the occurrence of intersections. Bloch mode

intersections occurring at the M, Γ and K-point are indicated with white-red dots.

The free-photon approximation does not take into account the actual strength of scattering interactions, and describes photonic interactions in the limit of zero contrast in the dielectric function between the host medium and meta-atoms. For dielectric photonic crystals, such interactions are commonly taken into account by means of plane wave expansion methods [49]. At high symmetry points, the band crossings in the repeated free photon dispersion relation generically turn into anticrossings: The periodic dielectric contrast couples the bands, and the coupling of degenerate bands (crossings) usually turns into energy splittings, known in literature as stop gaps. In exceptional cases, even in presence of dielectric contrast, such band degeneracies can occur. A famous case in point are the K-point Dirac cones in hexagonal lattices, which also occur in photonic systems [51–54]. Based on group-theoretical arguments, each band can be assigned a modal symmetry, or an irreducible representation even without having to solve the wave equation in real space [49, 55]. Already in 1992, Robertson et al. [56] showed that photonic crystals can exhibit modes that are symmetry-mismatched with the polarization symmetry of far-field radiation and hence are not allowed to couple [49, 57, 58]. These modes are dark modes within the radiation continuum and they possess infinite quality factor (in absence of absorption losses). Later, in the 2010s, these modes were labeled *symmetry-protected BICs*, and it was realized that quasi-BICs exhibit polarization singularities carrying topological charge [20, 59–61]. This field has given rise to a body of literature on symmetry-protected bound modes as well as studies of slightly symmetry perturbed geometries in which symmetry-protected bound modes become slightly leaky. Such so-called *quasi-BIC*s often result in Fano lineshapes in optical reflection and transmission that emerge as a consequence of interference between the narrow quasi-BIC resonance and non-resonant background reflection/transmission contributions. Quasi-BICs receive interest for their high quality factors, which typically follow a square-root dependence with the geometrical symmetry breaking parameter as one approaches the true BIC condition [19].

Plasmonic metasurfaces are distinct from photonic crystals due to the dispersive metal permittivity, the plasmon resonance of the scatterers in the unit cell, and the fact that plasmons exhibit loss. These systems even fundamentally challenge the notion of 'modes' and 'band structures': Strictly, eigensolutions with real valued wave vectors and frequencies do not exist. Instead, observables like reflection, transmission and absorption show resonant features reminiscent of band structures, that are somewhat imprecisely discussed in the language of Bloch modes and band structures. In this language, hybridization between the plasmon resonance and Rayleigh diffraction anomalies (these essentially are the folded free-photon dispersion cones), lead to collective modes called *surface lattice resonances* [10, 38, 62, 63]. An

interesting feature of 2D plasmonic metasurfaces is that the surface lattice resonances carry strong near fields, while symmetries and tuning of the localized resonances relative to the Rayleigh anomalies give access to a variety of band structures. However, these systems are notoriously hard to model with plane wave-based Maxwell-equation-solvers, as plane wave expansions struggle with the huge discontinuities in permittivity and concomitantly in electric field that dispersive plasmonic permittivity functions in the unit cell entail. Recently, the T-matrix code *treams* developed by D. Beutel et al. [64] was shown to be a suitable tool for this problem (see e.g. the supplement of Chapter 6, where a calculation approach with reciprocity arguments to model emission is implemented by D. Pal from AMOLF in *treams*).

While surface lattice resonances exist for plasmonic lattices without any embedding layer, many designs for light-emitting metasurfaces include a slab waveguide. A slab waveguide is a 2D finite thickness slab with higher refractive index than its surroundings, for which total internal reflections leads to confined propagation in the 2D slab: $\mathbf{k}_{||} > \mathbf{k}_0$, with $\mathbf{k}_0$ the free space wavenumber. Slab waveguides by themselves are translationally invariant structures in the plane, and therefore have solutions of conserved in-plane momentum $\mathbf{k}_{||}$. Waveguide modes of 2D slabs are either transverse-electric (TE) or transverse magnetic (TM) polarized: Either the E-field or H-field oscillates fully in the plane of the slab and perpendicular to the in-plane momentum. In general, slab thicknesses are chosen such that it allows for just a single TE mode, or a single TE and a single TM mode. To first order, the bandfolding picture applies for both polarizations separately, starting with a dispersion such as the orange cone in Fig 1.4(a), which is then repeated by the periodicity of the metasurface. For plasmonic metasurfaces, the waveguide mode hybridizes with the plasmon lattice resonance to form waveguide plasmon polaritons. These modes have been studied extensively in the context of LEDs [28] and plasmon DFB lasers [30].

1.3 Amplifying metasurfaces

1.3.1 Optical gain

This thesis studies metasurface systems where energy is added to propagating waves by means of optical gain. Gain requires an active medium - in form of atoms, ions, molecules, quantum dots or quantum wells - with an optical transition that can offer stimulated emission. A canonical, simplified picture of light-matter interaction is the two-level energy transition scheme [65] visualized in Fig 1.5(a). The scheme considers an atom, molecule or quantum dot (here called *emitter*) that possesses an electronic level separation or bandgap of magnitude ΔE. Without external stimulus, the emitter is in the ground state $|g\rangle$ with the electron populating the lower energy level. If a photon with

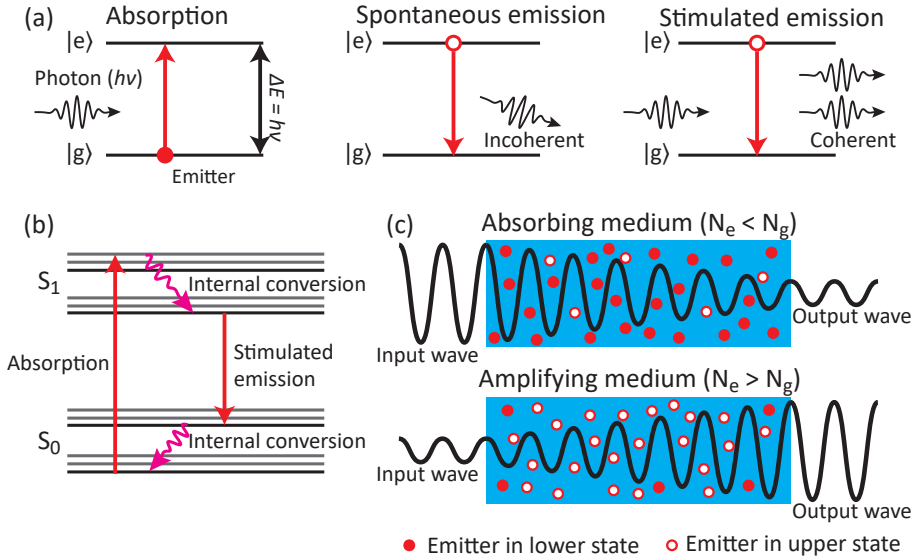

Figure 1.5: Basic physics of optical gain. (a) Three possible energy transitions of electrons in a simplified two-level emitter. After photon absorption bringing the electron to excited state, it can either relax spontaneously and emit incoherent radiation, or it can be stimulated to the ground state leading to coherent radiation. (b) Jablonski energy diagram for a four-level gain emitter, such as a fluorescent dye. Absorption and emission are decoupled through internal conversion of electrons over excited states/or vibrational sublevels. (c) Traveling through a medium with a large number of emitters, a light wave experiences de-amplification when most emitters are in the ground state, and amplification when most are in excited state.

energy $\hbar\omega = \Delta E$ passes, the emitter may absorb it, causing the electron to be promoted to the higher energy level $|e\rangle$. The emitter is now in the excited state. Two downward transitions can take place from this starting point: (1) Spontaneous emission of a photon wherein the electron spontaneously relaxes to the ground state upon emitting a photon of random phase and momentum, and (2) stimulated emission enabled by a second external photon that passes by. In stimulated emission, the electron energy is transferred to generate a photon with equal energy, phase, polarization and direction as the stimulating photon. Stimulated emission is therefore a process of coherent light amplification.

Most gain media are not based on two-level systems. In this work, we will use emitters as gain medium which can be understood in a four-level picture. A Jablonski diagram of energy levels as predicted by molecular physics is presented in Fig 1.5 [66]. In this picture, the electronic ground and excited states S_0 and S_1 are actually multiplets of closely spaced states, corresponding to vibrational excitations of the molecule at hand. While electronic levels in

fluorescent molecules are typically spaced by 1.5 to 2.5 eV in energy, vibrational energy quanta are typically much smaller, of order 50-100 meV [66]. Absorption of pump light typically excites a molecule from the electronic and vibrational ground state S_0 to some vibrationally excited sublevel of the first electronic excited states. Internal conversion processes ensure that, in picoseconds, the excited electron reaches the vibrational ground state of the electronic excited manifold. From this lowest level in the S_1 manifold, spontaneous and stimulated emission transitions can occur, bringing the electron down to one of the vibrationally excited sublevels of the electronic ground state, after which internal conversion moves the electron further down to the lowest state S_0, again at picosecond internal conversion rates. In such schemes, pump absorption is decoupled from stimulated emission, and population inversion can be reached by incoherent pumping at wavelengths blue shifted from the wavelength of emission. While the time dynamics of spontaneous emission are in the nanosecond domain for organic dyes, for optical gain the dynamics occur typically in the range of a few picoseconds, determined by the internal conversions rates, because absorption and stimulated emission are instantaneous processes. This thesis only considers fluorescent dyes as gain medium, and these have many radiative and rotational sub bands, which leads to broad absorption and emission spectra.

One can now consider a medium composed of many (four-level) emitters, through which a light beam passes. Disregarding any other loss channels, a beam resonant with the emitters can experience net absorption or amplification depending on the overall population of energy states within the ensemble of emitters. When the number of emitters in the excited state, N_e, is lower than the number of emitters in the ground state N_g, Fig 1.5(c), a light beam will lose intensity upon passing as more photons are being absorbed by the emitters than are amplified. In case of *population inversion* ($N_e > N_g$), see Fig 1.5(c)), a light beam experiences net amplification through stimulated emission. In a classical description of light absorption and amplification, this effect can be captured in a complex valued refractive index. The intensity I of a light wave propagating along z with wavelength λ experiences exponential (de-)amplification as described by the Lambert-Beer law

$$I(z) = I(0)e^{g_0 z}, \quad \text{with} \quad g_0 = -\frac{4\pi\kappa}{\lambda} \quad \text{and} \quad n = n_r + i\kappa,$$

where g_0 is the loss, respectively gain coefficient, which depends on wavelength λ and on the imaginary part of refractive index κ.

When an optical mode forms a cavity with standing wave mode profile, and the mode matches in space and wavelength with a gain medium, a system can transition to self-sustained oscillations called *lasing* [65, 67]. This transition starts from spontaneous emission noise, and as such requires only a supply of energy to pump the emitters, but no seeding beam. Typical lasing behavior is characterized by a nonlinear input-output curve: The laser output power

versus the input power of the (optical or electrical) pump [68, 69]. Below threshold, the power of fluorescent emission increases linearly with pump power. At the lasing threshold, stimulated emission takes over: Instead of incoherent, polychromatic and isotropic emission from fluorescence, the lasing output is coherent, monochromatic and directional. Crossing the lasing threshold leads to a kink in the input-output curve, beyond which laser output increases also linearly but with a steeper slope. In 2017, the journal Nature Photonics listed these characteristics of lasing in a checklist, in order to critically examine premature claims that are apparently prevalent in laser research [70]. At very high pump fluences, lasers typically become subject to nonlinear phenomena due to the strongly increased intensity of the laser field. One important nonlinear effect is *gain saturation*, where the population N_e cannot be replenished sufficiently fast by pumping, prohibiting further gain. Other nonlinear phenomena are spatial hole burning or intensity dependent refractive index changes due to self-phase modulation or two-photon absorption. In a system with multiple optical modes in the frequency window of the gain medium, complex nonlinear dynamic behavior typically arises, as different modes compete in space and time for the same gain.

1.3.2 Amplifying scattering metasurfaces

In scattering experiments, passive, linear scattering metasurfaces impart only a single hard-coded functionality on the interacting light beam. At the same time, scattering off the metasurface is constrained by passivity. It is immediately evident that passivity limits function through energy conservation: Output powers in all reflected and transmission channels together must at most be equal to the input power. More subtle is the fact that passivity limits its function even within energy conserving scenarios. For instance, if you calculate required phase maps to achieve certain metasurface functions like

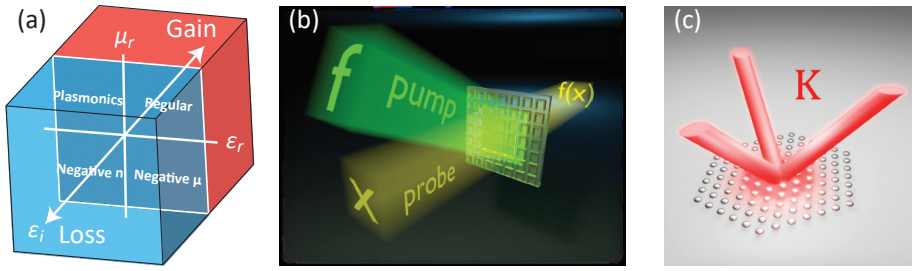

Figure 1.6: Amplifying metasurfaces. (a) Optical loss and gain extends the dimension of nanophotonics design toolbox. (b) In a pump-probe experiment, amplifying scattering metasurfaces can be altered in functionality on transmitted light by means of controlling the local gain with an optical pump. (c) Plasmon metasurface lasing from the K-points. (b,c) Image courtesy of R. Kolkowski.

anomalous refraction, you find that designs must have areas with both gain and loss to achieve unit efficiency [71]. Thus, both the characteristics of being hard-coded at fabrication time, and that of being locally and globally energy conserving limit applications and fundamental physics studies.

Although *reprogrammable metasurfaces* have emerged to overcome the first limit of hard-coded functionality, amplifying metasurfaces also sidestep the second limit of energy conservation. Reprogrammable metasurfaces are based on e.g. phase change materials, liquid crystals, graphene or other nonlinear materials, and change the refractive index of some component in the metasurface by an external energy source, often electrically, mechanically, optically, chemically, or otherwise [72–74]. In this way, the metasurface function can be dynamically controlled, usually on time scales much slower than the optical frequency. Nonlinear susceptibilities, such as $\chi^{(3)}$ nonlinearities, can be used for ultrafast optical modulation of refractive index, thereby switching metasurface scattering on (sub-)picosecond time scales [47, 75]. In this spirit, one can also envision amplifying metasurfaces: By optically pumping a gain medium integrated with a metasurface, dynamic response tuning with fast, ps timescales can be achieved. Moreover, such systems can disobey the optical theorem, possibly expanding the metasurface function set. Many experimental works examined amplification of waveguided light in optical gain-based (photonic crystal) waveguides [76–80] or waveguide fibers coupled through gain-microdisks [81, 82]. On the other hand, in the field of scattering metasurfaces, amplification of incident wavefronts [83–85], received attention mostly for plasmonic loss compensation [86–90]. However, interest in amplifying scattering metasurfaces seems to have dwindled since, and is largely confined to theoretical works such as Refs. [91, 92], despite the opportunities offered by the recognition that metasurface design space extends by including control over the imaginary part κ of the refractive index (see Figure 1.6(a)). This notion has been mainly recognized in the fields of parity-time (PT) symmetry breaking photonics [93, 94] and metasurface coherent perfect absorption and amplification [95].

In *PT-symmetry breaking photonics*, local material variations in loss and gain are carefully designed such that they form a potential invariant under the combined application of parity (spatial symmetry) and time symmetry operators – often this is achieved by equating losses in one resonator with gain in another. PT-symmetry physics in such resonant systems is studied for adaptive mode control by gain and loss, which arise from so-called exceptional points [93, 94]. Scattering metasurfaces and 2D diffractive photonic crystals have been theoretically shown to be a great arena for PT-symmetry studies [92, 96–102], and are for instance predicted to realize topological phenomena. This viewpoint on metasurfaces sees amplifying 2D photonic lattices as photonic simulators for seminal problems in condensed matter physics. Indeed, lattice particle plasmons have been investigated as special versions of tight-binding Hamiltonians [53, 103–110]. The advantage of optical systems is that

one can create 2D lattices of various symmetries with ease using standard nanofabrication techniques, while engineering particle placement, size, shape and resonance at will. At the same time, optical excitation and microscopy provide control over the distribution of optical gain and/or loss, and insight in the resulting physics. As such, this emulator platform stands out for the possibility to access (nonlinear) photon behavior beyond what nature offers us in crystals for electron behavior. So far, actual experiments of PT-symmetry physics in such 2D lattices have largely been shown in passive systems with loss-loss potentials [111, 112], which only map on loss-gain models modulo an overall shared loss rate.

Another viewpoint on amplifying scattering metasurfaces comes from the field of *scattering anomalies*: The description and engineering of scattering objects by means of tailoring zeros and poles in the complex frequency plane of their scattering-matrix (S-matrix) [69, 95, 113–115]. In the domain of radio frequency engineering, it has long been known that intrinsically weakly absorbing sheets of material can be turned into perfect absorbers by placing them at judicious distances of a reflector, in geometries known as Salisbury and Dallenbach screens [116–121]. It has been shown that this corresponds mathematically to bringing a zero in the scattering matrix of the absorber-reflector systems from the complex frequency plane onto the real axis. This *coherent perfect absorption* has been viewed as the time-inverse of lasing [113]. The understanding that zeros and poles in the complex plane of the scattering matrix correspond to conditions for minimal and maximal interaction, and by careful engineering can generate conditions for perfect absorption or amplification, has lead to a wealth of theoretical works [95, 118, 120]. It is surprising, however, that works on singular response in metamaterials with gain have mainly focused on low-frequency ranges [91, 122] and have not led to realizations at optical frequencies.

Finally, recent interest has sparked in metasurfaces performing all-optical analog processing operations on information-encoded light beams, such as taking spatial derivatives of datasets, solving integral equations, and performing inference tasks [6, 7, 123–125]. Amplifying metasurfaces could bring a wealth of opportunities to this field, as they may expand the set of mathematical operators that can be encoded in an optical structure.

We believe experimental efforts into amplifying scattering metasurfaces have so far been lacking because it is challenging to achieve significant optical gain, to control optical gain, and to deal with the fact that gain may amplify not just signals of interest but also noise. In summary, amplifying metasurfaces remain an open experimental challenge, despite offering promise as a route to ultrafast control of metasurface functionality, as visualized in Fig 1.6(b).

1.3.3 Metasurface distributed feedback lasers

A large body of literature is devoted to the study of periodic light-emitting metasurfaces that function as flat lasers [29–31, 126–138]. These lasing devices operate on the distributed feedback (DFB) principle, a concept experimentally known already since the invention in 1971 by Kogelnik and Shank [139] for dielectric polymer systems.

In DFB lasers, the gain is typically realized in a dielectric medium that is formed into a 1D or 2D waveguide that is periodically corrugated in refractive index, forming at the same time a diffraction-based cavity mode and a diffractive output channel for the laser radiation [140]. Commonly, DFB lasers are designed by lattice constant to operate on the second order Bragg diffraction condition, meaning that the gain window is matched with a stopgap edge at the Γ point ($\mathbf{k}_{||} = 0$), see Fig. 1.4(c). This leads to laser emission in the normal direction [141]. However, similar laser cavities can be created on other high-symmetry points in the BZ, resulting in off-normal emission [142–144]. For instance, Fig. 1.6(c) shows lasing from three K-points of a hexagonal DFB laser. Thus, one can overlap a cavity condition of a high-symmetry point of choice with the gain energy window of the dye of choice, and tune lasing emission both in energy and angle.

Research in DFB lasing can be classified in four fields: Organic polymer slab lasers [139, 141, 145], photonic crystal slab lasers [142, 146–149], surface-plasmon polariton (SPP) lasers [150, 151], and, finally, Mie-resonant [31, 136–138] or plasmonic [29, 30, 126–135] light-emitting metasurface lasers. This thesis reports new insights in plasmonic metasurface lasers, a field in which the groups of Odom (Northwestern), Törmä (Aalto), Norris (ETH Zurich), and AMOLF have made distinct contributions since the first report of Suh et al. in 2012 [127]. Plasmonic lattice lasers received interest for their combination of rich plasmon polariton band structures, localized fields that imply Purcell enhancements and complex gain dynamics [69, 129], and the very strong feedback due to large scattering cross-sections. As such, the field closely relates to studies into lattice plasmon-exciton-polariton condensation, a phenomenon which is claimed to be achieved when using both high dye concentrations and high pump fluences [152, 153]. Plasmonic metasurface lasers have unique properties, such as being exceptionally robust against disorder [130], and requiring only very few unit cells to cross threshold (of the order of $5 - 10$, as opposed to > 1000 for polymer DFB lasers [132, 154]). What is more, dark-mode lasing emission comes in typical donut-shaped vortex beams [145, 147, 148, 151], which currently receive much interest in the study of quasi-BIC phenomena and polarization-topology [31, 134, 137, 138].

1.4 This thesis

This thesis is motivated by the prospect of realizing and understanding amplifying scattering and lasing metasurfaces at optical frequencies. Such prospects bring many experimental and theoretical questions. From the experimental viewpoint, such an endeavor requires methods to control optical gain in space and time, and to then perform microscopy on the metasurface at hand within the ultrashort time span afforded by the gain medium. Conceptually, for amplifying scattering metasurfaces one can ask how much control optical gain can offer to modulate metasurface response, and what gain levels are required. For instance, can you create conditions for perfect amplification, similar to known conditions for perfect absorption in metasurfaces? In the spirit of light emitting metasurfaces as photonic simulators of condensed matter systems, one can also ask how band structures, lattice symmetries, and boundary conditions placed on where a system amplifies and where not, express in lasing behavior. This thesis develops a new ultrafast spectroscopy and microscopy method to study such systems (Chapter 2), examines the physics of perfect amplification (Chapter 3), and studies various new aspects of metasurface lasing (Chapters 4, 5, 6) in light of band structure, mode competition and spontaneous symmetry breaking, and boundary conditions. The thesis is organized as follows:

Chapter 2 describes our experimental push towards amplifying scattering metasurfaces. We elaborate on the combination of pump-probe and Fourier microscopy techniques that enables ultrafast metasurface response modification. We test our methods by showing gain-induced grating efficiency modulation in a 1D grating covered with a gain medium.

In **Chapter 3**, we theoretically investigate singular response in amplifying reflection metasurfaces. Particularly, we study the Salisbury screen geometry – metal ground plate separated from a dense plasmonic array – with the inclusion of optical gain either in the spacer or in the metasurface. We show that gain can induce both perfect absorption and amplification singularities. In fact, in specially designed systems, we find that the absorption and amplification singularities can co-exist in parameter space.

Chapter 4 entails the first experimental report of spontaneous symmetry breaking in metasurface lattice lasers. We design lasing condition to occur at the K-points of hexagonal plasmonic lattices, and our single-shot experiment enables the capture of a spontaneous symmetry breaking between two decoupled and degenerate modes K and K'. From Fourier-space images we map statistics on parity symmetry breaking in relative amplitude, while real-space images provide the information to determine relative phase. We finally establish a new type of phase space geometry for symmetry breaking order parameters, as we map relative amplitude and phase events on the surface of the unit sphere.

In **Chapter 5**, we study metasurface lasing and spontaneous symmetry

breaking upon imparting boundary conditions in the gain field. We dynamically structure the gain field by encoding structure in the pump beam by means of a digital micromirror device. Although spontaneous symmetry breaking in the M-point laser can be easily biased by structured gain, spontaneous symmetry breaking between K and K' modes is very robust to experimental bias. The reason is that they are degenerate not just in energy, but also in spatial profile. Furthermore, we show that we can create two (or more) separate closely spaced lattice lasers at will, and we show that amplitude and phase synchronization signatures in Fourier and real space images arise from coupling.

Finally, in **Chapter 6**, we study light-emitting plasmonic metasurfaces with very dense particle spacing. Strong near-field interactions provide routes to study plasmon versions of exotic band structure dispersions, which, however, lie far beyond the light line. In fluorescence band structure measurements, we make the K-point dispersion of a dense metasurface visible by superlattice perturbations in a technique called bandfolding. We validate band structure measurements with a T-matrix simulation based on the reciprocity principle. Importantly, the folded K-points exhibit one of the highest quality factors reported in the field of plasmon lattice resonances, despite the high areal density of lossy plasmons. Based on full-wave simulations, we assign the high quality factor to interference mechanisms reminiscent of quasi-BICs.

Chapter 2

Pump-probe Fourier microscopy

In this chapter, we report on the design and commissioning of a femtosecond pump-probe microscopy setup that can perform pump-probe spectroscopy, real-space imaging and Fourier imaging. The setup is designed for pump-probe studies of plasmonic and dielectric metasurfaces with optical gain, and operates with visible / NIR pump and probe beams. We show the capability to perform synchronized single-shot real-space and Fourier-space imaging on amplifying metasurfaces, and demonstrate that the setup can measure band structures of nanophotonic lattices using the white-light probe beam. Moreover the setup has a digital micromirror device placed in the pump beam, giving a route to spatially program the pump-light distribution on the sample. We highlight some of these capabilities on amplifying plasmon lattices. Furthermore, we present a first study on ultrafast control of diffraction by means of optical pumping of a gain medium. This is realized in simple one-dimensional line gratings of metal strips in a dye-doped polymer. We find that optical pumping achieves 15% reflection modulations, and that gain can induce both enhancement and suppression of diffraction. We replicate this behavior in a simple Fraunhofer diffraction calculation. Our new experimental setup provides opportunities for active response control of PT-symmetry breaking metasurfaces and metasurfaces with perfect absorption/amplification singularities.

2.1 Introduction

A main driver for the research presented in this thesis is the idea that one could use amplification, i.e., optical gain, as a resource to expand the functionality of metasurfaces. As we argue in Chapter 1, amplifying metasurfaces can, on the one hand, be envisioned as systems that locally amplify incident wavefronts upon transmission or reflection [90], enabling the study of PT-symmetry in scattering systems [94] and of scattering singularities in metasurface perfect absorption [95]. On the other hand, one can consider amplifying metasurface lasers, for which supplied pump energy energizes the gain medium, which is followed by emission of laser radiation of which the spectral and spatial properties are tailorable by the metasurface geometry [29–31, 126–138].

To study amplifying metasurfaces, an extensive experimental inspection toolbox is needed. For optical excitation to energize the gain medium, one requires an ultrafast pump-probe setup with a time resolution matched to the picosecond timescale of gain media, and with the ability to map the scattering and emission behavior in real and momentum space. Such time-resolved real- and Fourier-space microscopy would provide access to probing the interplay of gain, geometry, and symmetry in metasurface responses. This chapter reports on the design and commissioning of such a setup, which allows studying metasurface lasing (Chapters 4, 5), amplifying metasurface tuning near singularity conditions (Chapter 3) and band structures physics of plasmon metasurfaces (Chapter 6). The experimental toolbox that we present in this chapter consists of four components:

Pump-probe microscopy This component has controllable delay and pump power, using a green pump beam for metasurface excitation, and a white-light supercontinuum as probe beam. This technique offers access to probe the ultrafast (gain) dynamics of the metasurface.

Fourier- and real-space microscopy This component enables mapping of both wavelength and angular emission/reflectance spectra, notably providing high-NA Fourier images, and band structures in fluorescence and in white-light reflectance.

Single-shot synchronized acquisition This part ensures that every individual laser shot gets captured in a single camera exposure frame. This allows to study phenomena in metasurfaces where the signal changes (randomly) from shot-to-shot, e.g. due to mode competition or spontaneous symmetry breaking (Chapter 4 of this thesis), and to obtain single-shot metasurface band structures in gain.

Spatially structured pump fields For this part we place a digital micromirror device (DMD) in a real-space plane of the pump beam, allowing to reconfigure the spatial distribution of the gain applied on the sample. In

this way, we dynamically control gain-geometry of metasurface lasers (Chapter 5). What is more, the response function of amplifying metasurfaces can be spatially programmed.

In this Chapter, we first discuss the experimental techniques and technical aspects of the newly build pump-probe Fourier microscopy in Sections 2.2 and 2.3. In Sections 2.4 and 2.5, we show results obtained with the setup for amplifying plasmonic metasurfaces and for amplifying 1D gratings.

2.2 Experimental techniques

Fourier microscopy

In introductory geometrical optics, lenses are described with the *thin lens approximation*: The thickness of the lens is taken negligible compared to the radii of curvature of the surfaces, and ray tracing follows a simple geometrical rule wherein the lens is an infinitely extended refracting plane perpendicular to its optical axis. Image formation of an object at a distance z_o from a lens of focal length f occurs at an image position z_i, as measured from the lens determined by $\frac{1}{z_i} + \frac{1}{z_o} = \frac{1}{f}$. A special case is when the object is in the focus of the lens $z_o = f$, when $z_i = \infty$ so that the image is projected onto infinity, see Fig 2.1(a). This geometry relates to the special property of lenses that they Fourier transform a real-space (x, y) object in the front focal plane) to an angular representation of (k_x, k_y) in the so-called back-focal plane (BFP). All rays that emerge from the sample plane toward the far-field with the same angle θ are projected onto a single point in the back-focal plane. Reviewing Fig 2.1(a), we notice that rays with large angle θ (when the lens has high numerical aperture, NA) become problematic as the required lens size diverges as $\tan\theta$. Very high-NA microscope objectives instead are designed

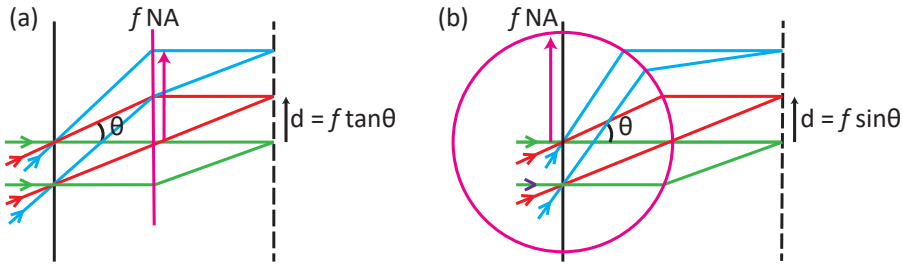

Figure 2.1: Ray evolution in lenses and objectives. Thin lens approximation (a) used for lenses with low numerical aperture. For large θ, the back-focal-plane distance $d = f\tan\theta$ blows up. Therefore, microscope objectives with high NA are designed to obey the Abbe sine condition (b), where non-paraxial rays reflect from a hypothetical reference sphere with radius fNA and d is proportional to $\sin\theta$.

to obey the *Abbe sine condition*, where (non-paraxial) rays bend off from a hypothetical reference sphere centered at the object with radius fNA, instead of a hypothetical plane (see Fig. 2.1(b)). Mathematically, the sine condition means that all rays at angle θ at the object side are focused at a distance $f \sin\theta$ from the optical axis in the back focal plane, removing the divergence. In essence, the objective performs a coordinate transformation from spherical (in the sample plane) to cylindrical coordinates (in the BFP), and the Abbe sine condition demands that the objective provides a direct map of (parallel) momentum space $k_{||} \propto \sin\theta$. In this transformation one should be aware that the intensity from an isotropic spherical source is no longer homogeneous in cylindrical coordinates: the Jacobian causes a $1/\cos\theta$ brightening towards the edge of the BFP, sometimes referred to as (part of the) objective apodization function. In an imaging system of magnification M, the Abbe sine condition says that the object plane wave spectrum k and image plane wave spectrum k_i are scaled by M: $k_i \sin\theta_i = k \sin\theta/M$: Image magnification by a factor M is accompanied by a decreased angular spectral content by the same factor, ensuring that in any microscope, the optics downstream of the objective can be viewed as paraxial.

A sketch of a standard microscope imaging system is displayed in Fig 2.2(a). Modern microscope objectives lenses are *infinity corrected*, which means that they have best (lowest aberration) performance when the object is placed in the front focal plane of the objective. Thus the objective creates an image

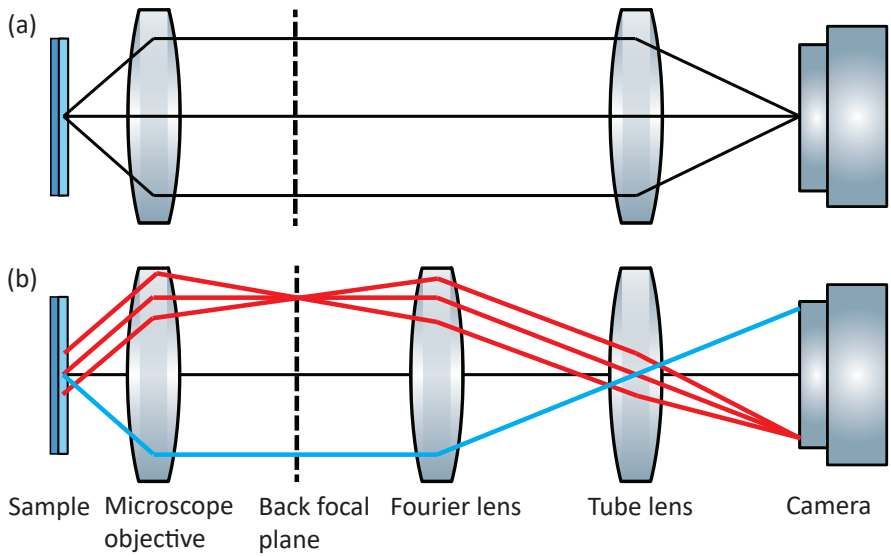

Figure 2.2: Fourier microscopy. (a) Regular real-space microscope. (b) Fourier-space microscope.

at infinity and no intermediate image plane exists in the microscope, unlike the geometry of older microscopes. The so-called tube lens, which creates an image in the detector plane, can thus be placed at arbitrary distance from the microscope objective, as long as the detector (often a camera) is a distance from the tube lens that equals the focal length f_{tube} of the lens. The microscope magnification M thus equals the ratio of focal lengths. Fig 2.2(b) shows the same microscopy arrangement but with an extra lens placed in this setup, with its focal plane precisely at the BFP of the objective lens. We refer to this lens as the *Fourier lens*. In the geometrical optics picture of Fig 2.2(b), one sees that rays emerging from any given spot in the BFP are now transformed into parallel rays towards infinity by the Fourier lens, and then focused on the detector plane by the tube lens. Inserting the Fourier lens therefore turns the microscope from a real-space imaging device into a system that maps the BFP of the objective lens onto the camera chip, providing a direct method to inspect the Fourier (k_x, k_y) content radiated from the sample. In a practical setup, one can easily flip in and out the Fourier lens to switch between real- and Fourier-space imaging. When imaging is performed by projecting a real- or Fourier-space image onto the entrance slit of a spectrometer, one can furthermore spectrally disperse sliced data, obtaining respectively data in (y, λ) space (intensity spectra versus position on a line in real space) or in (k_y, ω) space (intensity spectra along a line in k space, for periodic systems known as a a band structure slice). The Fourier-space imaging method was first reported in the context of microscopy of single nano-objects in 2004 to study radiation patterns of single-emitters [155], and has become a cornerstone technique in the field of nanophotonics, where far-field radiation profiles of dipolar plasmon antennas [156, 157] or multipolar Mie scatterers [158] have been studied extensively, and far-field radiation of periodic photonic crystals and metasurfaces contains crucial information of the band structure of photonic Bloch waves [10, 30, 31, 61, 131, 159, 160].

Pump-probe microscopy

In the 1980s and early 1990s, many (Nobel-prize winning) inventions [161, 162] were made in the field of ultrafast laser physics that enable the experimental technique of ultrafast pump-probe spectroscopy / microscopy, sometimes also referred to as transient absorption spectroscopy [163, 164] and microscopy [165–167]. These techniques opened up a plethora of venues for the investigation of dynamic processes in biology, chemistry and physics. In nanophotonics, this includes the study of photophysical materials (quantum dots [168], quantum wells [169], organic fluorophores [170]), plasmonic and dielectric nanoparticles [171, 172], photonic crystals [173], 2D materials [174], plasmon lattice lasers [129] and resonant plasmonic/dielectric metasurfaces [175–177].

Fig 2.3 shows the basic principle of ultrafast pump-probe experiments. The

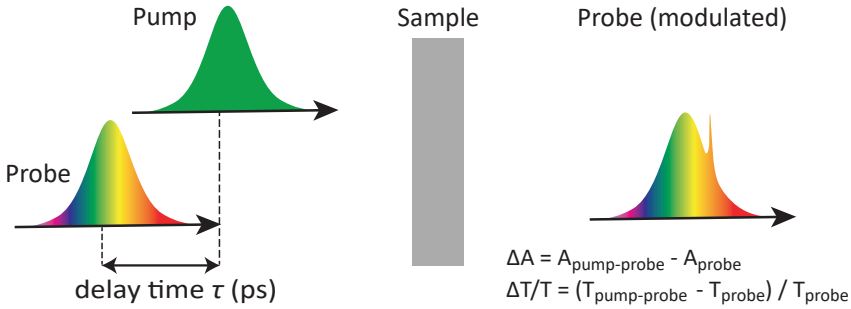

Figure 2.3: Pump-probe spectroscopy. A green femtosecond pulse energizes dipole emitters in the sample. The white-light probe arrives later with a delay time $\Delta\tau$ and experiences a change in absorption (as measured by reflection R or transmission T).

sample under study is illuminated with two fs laser pulse trains with a specific time delay τ between pump pulses and probe pulses. First, the *pump* arrives, which excites the sample material. Subsequently, the *probe* beam arrives and experiences a photoinduced change in reflection, transmission, absorption or scattering due to the pump. The setup constructed in this work is most akin to transient absorption spectroscopy in which the probe spectrum is generally broadband (white light), as this allows to spectroscopically study different nonlinear phenomena over a range wavelengths. The signal of interest in pump-probe studies is typically the *transient transmission* or *reflection*, which are defined as

$$\begin{aligned} \Delta T/T &= (T_{\text{pump-probe}} - T_{\text{probe}})/T_{\text{probe}} \\ \Delta R/R &= (R_{\text{pump-probe}} - R_{\text{probe}})/R_{\text{probe}} \end{aligned} \tag{2.1}$$

and can be subsequently related to transient absorption. The probe signal in the presence of the pump is thus referenced to the signal in absence of the pump. Therefore, it is common to periodically modulate the pump pulse train at a subharmonic frequency of the probe pulse train using choppers or acousto-optic modulators [167]. Such an approach ensures that measurements with and without probe are taken in immediate succession. By scanning a movable retroreflector (delay stage) placed in the beam track of either the pump or the probe, the transient signal is measured as a function of the delay time τ between the pump pulse and the probe pulse, revealing time dynamics of the transient optical response.

In the transient absorption field, which focuses on the temporal dynamics of ensembles of, e.g., absorbing and emitting molecules, three main nonlinear effects are commonly referred to [163, 166]. These are (1) *ground-state bleaching*, where absorption of probe photons is reduced immediately after pumping, occurring when a sizable fraction of the molecules at hand are already in a higher energy state due to absorption of pump light, (2) *stimulated emission*,

or optical gain (see Introduction) wherein the probe light is enhanced upon, e.g., transmission due to stimulated emission by the collective of pumped molecules, and (3) *excited-state absorption*, wherein pump light can induce absorption if excited molecules can absorb probe photons to enter even higher energy states. Each effect is typically strongest in a specific spectral domain. Usually, ground-state bleaching (1) occurs on the blue side of the fluorescence peak [163], stimulated emission effects (2) more or less overlap with the fluorescence spectrum [178], and excited-state absorption (3) is to the red side of the fluorescence peak for conjugated polymers [179]. Besides the aforementioned three effects, many other nonlinear processes can be seen. For instance, refractive-index modulation (e.g., upon free carrier excitation in semiconductors), harmonic generation, coherent Raman scattering, two photon absorption and cross-phase modulation, all with different signatures in spectrum and delay time [167]. This thesis focuses on probe intensity modulation via optical gain from stimulated emission.

Various detection mechanisms exist for transient signals in pump-probe experiments. These include monochromators and single pixel detectors, spectrometers with 1D pixel arrays to measure spectra, or 2D pixel arrays to map, e.g., spectra as a function of spatial coordinates [167]. In many cases, the transient signals are comparatively small $\Delta T/T = 10^{-4}$ – 10^{-7} [163, 167]. Such sensitivities are often achieved by lock-in detection of the transient signal referenced to the pump modulation frequency at very high repetition rates (ranging from kHz till 100 MHz) to reduce shot noise. In this work, we combine pump-probe microscopy and spectroscopy with Fourier imaging, collecting (k_x, k_y) and (ω, k_y) maps as a function of gain (controlled by the pump field). For that, we rely on CMOS camera operation, as in refs [180–183], which means that high repetition rate lock-in detection schemes are not possible. Since CMOS cameras have a limited dynamic range (per-pixel shotnoise on a 16-bit camera is only just sub-percent), samples should have high enhancement signal, which we expect for strongly interacting resonances in metasurfaces with gain, such as plasmon lattices operated just below the plasmon lattice lasers threshold [30].

2.3 The setup

2.3.1 Pump-probe laser system

An overview of the pump-probe Fourier microscope setup constructed in this work is shown in Fig 2.4. The setup is driven by a Light Conversion Pharos PH-1 Ytterbium-based solid-state laser, providing 1030 nm wavelength pulses of 225 fs length. This laser provides 16 W at a maximum pulse repetition rate of 1 MHz, but can be divided down with an internal pulse picker. We typically operate the system at 20-40 Hz for camera-based pump-probe measurements.

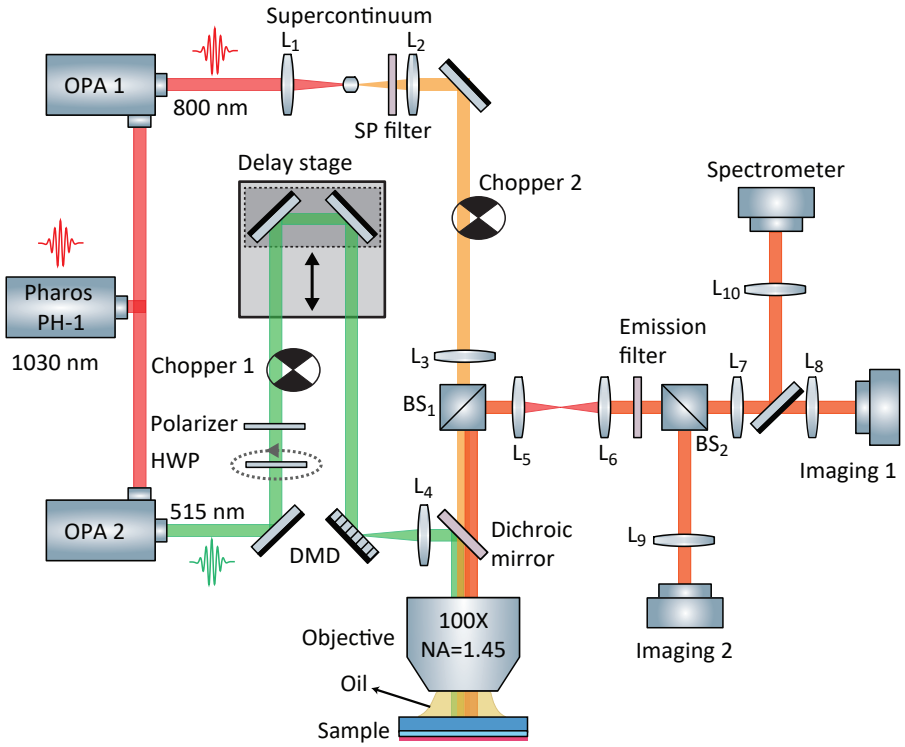

Figure 2.4: The single-shot pump-probe Fourier microscope setup, with pump beam shaping capability. From OPA 1, a 800 nm fs pulse is used to generate a white-light supercontinuum as probe for $\Delta R/R$ measurements. From OPA 2 we obtain the green 515 nm wavelength pump, and guide it through the motorized delay stage to control pump-probe delay time $\Delta\tau$. The digital micromirror device imparts an amplitude mask on the pump field in the sample plane. Choppers are placed both in pump and probe beams, as this pulse train modulation produces all four single-shot pump-probe combinations. We use high-NA immersion objective for light incoupling and sample imaging - with camera's Imaging 1 and 2 we record fluorescent emission and probe reflection in Fourier- and real-space simultaneously. With the spectrometer we record band structures. All lenses are Thorlabs achromatic doublets with AB or A coating (e.g. AC254-200-AB).

The 1030 nm beam is split in equal parts and routed to two non-collinear optical parametric amplifiers (LightConversion Orpheus-F), labeled OPA1 for the probe and OPA2 for the pump. We use OPA1 to output a 800 nm beam of diameter ≈ 3 mm with 60 fs pulses, which are weakly focused with L_1 (focal length $f = 10$ cm). With an NA of about 0.03, a spot size of approximately 10 µm is created inside a sapphire crystal (Eksma Optics 550-7126. Diameter: 12.7 mm, thickness: 6 mm), to generate a supercontinuum. After a set of two 750 nm shortpass filters (Thorlabs FESH0750) blocks residual 800 nm light, lens L_2 ($f = 20$ cm) makes a collinear beam of ≈ 8 mm diameter. For the pump beam,

we bypass the actual OPA, and instead extract the second harmonic of the 1030 nm Pharos beam to obtain a 515 nm pump beam for material excitation. We control the pump power by rotating a motorized multi-order halve wave plate (Thorlabs WPMH05M-514) placed before a Glan-Taylor linear polarizer (Thorlabs GL5-A in mount SM05PM5).

2.3.2 Controlling input beams

In both pump and probe beams, we place rotating chopper blades (Thorlabs. Controller: MC2000B-EC, blade: MC1F2) to modulate the pump and probe pulse trains (more details in Sec 2.3.4). The pump laser is guided onto a software-controlled movable retroreflector that acts as a delay stage (Newport. Power supply: DL-PS, delay line kit: DL-BKIT2U-S-M, stage: DL125) and that we use in a double-pass configuration. Thereby the effective range of the pump-probe delay is 500 mm, four times the mechanical range $x_{\text{stage}} = 125$ mm of the stage. In time this amounts to a pump-probe delay range of 1.67 ns. The step resolution of the stage is 75 nm, leading to 1 fs resolution. To control the pump-field geometry, we can send the pump via a digital micromirror device (Texas Instruments. Evaluation module: DLP LightCrafter Single DLPC900 EVM, controller: DLPC900, chip: DLP6500, see Sec 2.3.5). We place the DMD behind the delay stage and before reflecting the pump beam from a 520 nm dichroic mirror (Semrock Di02-514-25x36) towards a high-NA oil objective (Nikon CFI Plan Apochromat lambda 100×, NA = 1.45). It is mounted in an inverted microscope geometry in a homebuilt frame, where the inverted geometry provides convenient handling of the immersion oil as well as sample access. In a typical experiment, we illuminate the sample with both pump and probe beams in epi-illumination, for which we place lenses L_3 ($f = 20$ cm) and L_4 ($f = 25$ cm) with their focal point on the back focal plane of the objective, creating ≈ 60 µm collinear beams in the sample plane. The digital micromirror device is placed in the focal point of L_4, so that it is imaged onto the sample plane with 100× magnification. The non-polarizing beamsplitter (Thorlabs CCM1 BS013/M) between L_3 and the dichroic mirror separates incoming probe from reflected probe, at the cost of an overall reduction of the white-light signal by a factor four.

2.3.3 Imaging PL and white-light reflectance

Regarding the detection path, the beamsplitter BS_1 separates the incoming and outgoing beams. It should be understood that the beamsplitter in principle directs not just reflected white light (probe) to the detectors but also fluorescence signal generated in the sample by the pump, as well as residual pump light at 515 nm. We block out all 515 nm pump light with either a 514 nm notch filter (Thorlabs NF514-17) or 550 nm longpass filter (Thorlabs FELH0550). The setup has an imaging camera for Fourier imaging (camera 1,

Thorlabs CS2100M-USB), for real-space imaging (camera 2, Bassler acA 1920-40 um), and a spectrometric imaging path for Fourier-space and real-space spectra. The tube lenses for these are respectively L_8 ($f = 20$ cm), L_9 ($f = 20$ cm) and L_{10} ($f = 15$ cm). While camera 2 always records real space, the other two paths are switched to Fourier mode by the Fourier lens L_7 ($f = 20$ cm), which images the objective BFP via a 1:1 telescope L_5:L_6 ($f = 15$ cm). The telescope ensures an intermediate real-space image plane for spatial filtering, if required. By means of beamsplitter BS_2 (Thorlabs CCM1 BS013/M), the setup ensures that both Fourier- and real-space can be recorded simultaneously for a single laser shot (see Sec 2.3.4). By flipping up the mirror just in front of lens L_8, one can choose to direct the Fourier image via tube lense L_{10} to the entrance slit of a simple, compact Andor spectrometer unit (base unit: Andor Shamrock 163i, 163 mm focal length, with a 300 lines/mm grating (SR1-GRT-0300-0500) and a 25 µm fixed-width slit) to which we mounted a monochrome CMOS camera (Ximea MC124MG-SY-UB), to obtain spectrally resolved Fourier images (k_y, ω).

2.3.4 Signal synchronization

A synchronized single-shot experiment – where imaging acquisition runs synchronous to the laser repetition rate – is necessary for proper pump-probe measurements, to correct for overall fluctuations of pump and probe beams, and to be sensitive to shot-to-shot variations in signal. For that reason, the pump-probe setup is designed for fully synchronized single-shot operation.

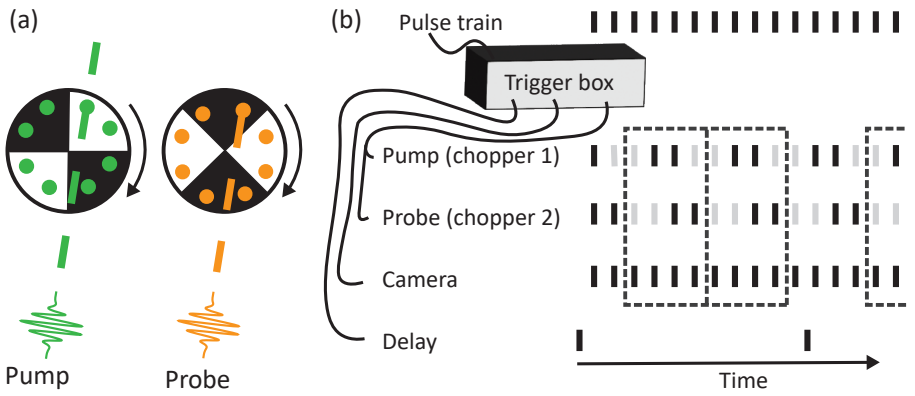

Figure 2.5: Two-chopper modulation of pump and probe pulse trains. (a) The choppers consecutively block and allow two pulses, and rotate $\pi/2$ out of phase. (b) Trigger box synchronization scheme. The chopper modulation ensures all four pump-probe shot combinations are passed to the camera in succession, together forming a completely referenced pump-probe measurement. For better signal to noise ratios these sets of four can be repeated at each specific delay position.

The Pharos PH-1 pulse picker provides an electronic signal synchronous with the laser output. This is fed to an in-house designed and constructed trigger box that is the hardware central command system to receive, delay and pass electronic triggers during a full measurement sequence. The trigger box sends electronic triggers to each of the cameras with a delay time specifically chosen to remove the so-called rolling shutter effect (a typical source of artefacts with CMOS cameras, which depends on frame rate and chosen region of interest). The trigger box also triggers the chopper rotation and movement of the delay stage after a series of camera shots. In a regular transient absorption experiment, only the pump beam is modulated [167], such that differential probe beam transmission/reflection is measured by comparing two subsequent measurements: with and without pump beam. In such a scheme, one does not have access to background signals (in absence of pump and probe) or signal from fluorescence (pump only). Therefore, we implemented a different scheme, namely the modulation of both pump and probe beam, with two choppers rotated 90° out of phase with respect to each other, and at a frequency that is 1/4th of the laser repetition rate, as is visualized in Fig 2.5. This configuration ensures that, repetitively, two shots are blocked and two pass. Due to the phase difference, this scheme generates four single-shot pump-probe combinations: background (no pump, no probe), only pump (generating fluorescent signal), only probe and pump-probe.

2.3.5 Structured pump field for asymmetric gain

An integral part of our setup design is the inclusion of the digital mirror device (DMD) in the pump beam, which we envision can be used for diverse purposes such as offering finely spatially textured pump fields to metasurfaces, or offering homogeneously illuminated patches of pump field with spatially sharp and controllable boundaries, a technique commonly applied for instance in studies of polariton condensates [184, 185]. With the DMD in the pump beam placed in the sample plane via the epi-lens, one can tailor boundary conditions in gain at will. The pixel size of the DMD is 7.56 μm, or 75.6 nm in the sample plane, covering about 2.5 pixels per diffraction limited length of $\lambda/2\mathrm{NA} \approx 180$ nm.

2.4 Amplifying plasmonic metasurfaces: Band structures and lasing

Two-dimensional (2D) lattices of plasmonic nanoparticles embedded in gain media receive considerable attention. On the one hand, diffractive lattices of plasmon particles show distributed feedback (DFB) lasing, which is an experimentally mature field [30, 126–135, 143]. On the other hand, active plasmon versions of seminal (PT-symmetric) tight-binding Hamiltonians [92,

96–102, 186] have been proposed by many workers as photonic realizations of seminal solid-state physics problems, but still remain theoretical promises. The combined capabilities of our new setup offer important opportunities in both fields. The present section serves to illustrate the setup possibilities, without going into the full physics implications of the observations.

Example results taken with our single-shot Fourier microscope from a plasmonic lattice are shown in Fig 2.6. Panel (a) shows a sketch of the amplifying plasmonic metasurface. We fabricate hexagonal lattices of plasmonic nanoparticles (80 nm diameter, 30 nm height) on glass substrates by means of e-beam exposure and lift-off (SEM image of the lattice shown in panel b). Then, we cover the lattice in a dye-doped polymer layer of 450 nm thickness, supporting one transverse electric (TE) and one transverse magnetic (TM) waveguide mode (for details of the fabrication recipe we refer to the Appendix of Chapter 4). Upon exciting the sample with the 515 nm pump, dye molecules in the slab emit incoherent fluorescent radiation, which we collect from the substrate side in our inverted setup. For a

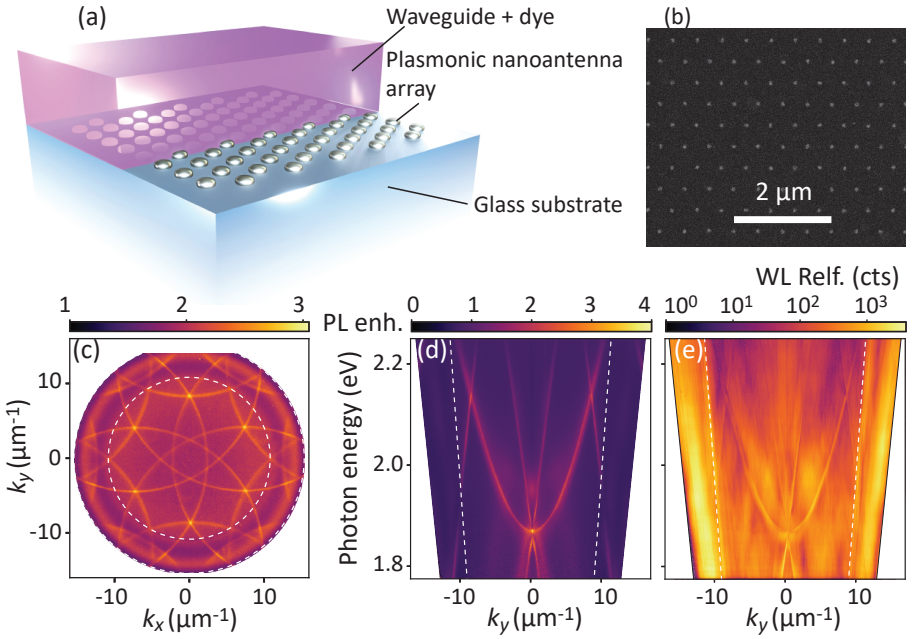

Figure 2.6: Plasmonic light-emitting metasurface band structures. (a) Sketch of an amplifying plasmonic lattice (image courtesy of R. Kolkowski). (b) SEM image of a plasmon lattice with pitch 500 nm. (c) Multi-shot recorded Fourier (k_x, k_y) image of PL enhancement, with waveguide mode circles repeated at reciprocal lattice points, intersecting at the K-points. White dashed lines represent NA $= 1$. (d) Multi-shot dispersion (ω, k_y) image of PL enhancement, and (e) of white light reflection counts, each showing the band structure with high-symmetry point intersections at Γ and K.

hexagonal plasmon lattice of pitch 500 nm, panel (c) shows a Fourier image of photoluminescence (PL) enhancement, taken with a 580 nm bandpass filter (Thorlabs FB580-10) placed before the tube lens. We obtain *PL enhancement* by normalizing the data to PL from an unpatterned sample region. Owing to the Abbe sine condition, the Fourier image is a direct image of momentum space, representing PL enhancement as a function of NA, which is expressed in parallel momentum as NA $= |\mathbf{k}_{||}|/|\mathbf{k}_0|$, with $\mathbf{k}_0$ the free space wavevector. The center of the Fourier image corresponds to angles normal to the sample, along the microscope optical axis. We perform calibration of the $k_{||}$ axis through the fact that in PL, the NA $= 1$ ring is sharply defined, allowing us to fit it with a ring, the result of which we overplot as a dashed white line. We recognize a set of high-signal circular bands: These bands are diffractively outcoupled TE waveguide modes that were excited by fluorescence, or, equivalently, the bands represent the TE waveguide in a repeated zone scheme explained in Chapter 1, Sec. 1.2.3. For this specific wavelength, a threefold intersection of bands coincides with the special K-points, the corners of the first Brillouin zone, at about $k_{||} = 8.5$ μm^{-1}. Panel (d) displays a measured frequency-dispersed PL enhancement, showing the (ω, k_y) band structure of the plasmon lattice. Also here, we notice that the dispersion coarsely follows free photon lines in the repeated zone scheme (meaning weak band perturbations from scatterer polarizabilities [30, 131]), except near the Γ and K high-symmetry points at 1.85 eV and 2.15 eV. Here, different Bloch modes interact to form photonic stopgaps with bright and dark modes on either side (especially so for the Γ-point). The same dispersion but recorded in a white-light reflection experiment is shown in Fig 2.6(e). The data is in units of counts (cts) and not normalized to reflection from a perfect reflector. This measurement is taken by focusing the white-light supercontinuum to the sample at laser repetition rate 1 kHz and camera exposure time 9 s. Such high number of shots are here required because we fill the whole (k_x, k_y) image, but we have access to a limited photon budget in a single white-light pulse. However, only photons along the k_y line are necessary to record the (ω, k_y) dispersion image, and therefore we resolve this problem by replacing the epi-lens (L_3 in Fig 2.4) with a cylindrical lens (e.g. Thorlabs LJ1277L2-A), ensuring that all photons in the shot are projected along the vertical slice on the NA, leading to decent white-light reflection SNR even in a single-shot white-light dispersion image.

Our setup's capability to simultaneously resolve single-shot Fourier- and real-space images is important for studying shot-to-shot variations in lasing behavior. Chapter 4 in this thesis is dedicated to spontaneous symmetry breaking in degenerate K-point lasers, expressing as dramatic variations between single-shot images. Figure 2.7 shows example results of simultaneously recorded single-shot Fourier images (top row) and real-space images (bottom row). Unique about these images is that we have shaped the pump beam that excites the gain medium, using the DMD device. Panels (a)

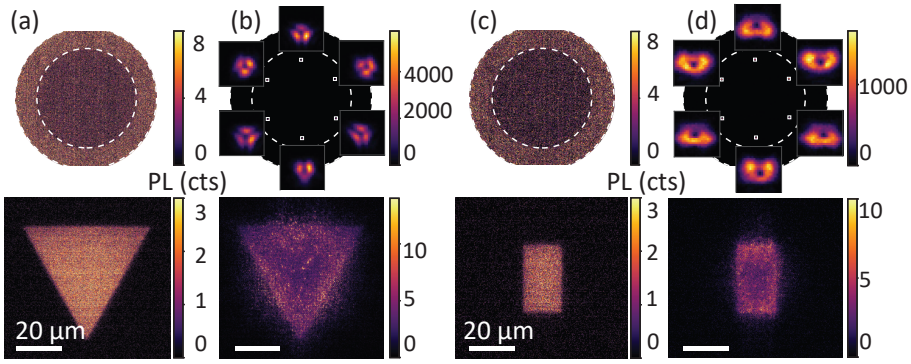

Figure 2.7: Simultaneous real- and Fourier-space single-shot recordings of plasmon lattice lasing. (a) For a 58 µm triangle pump below threshold, the system radiates incoherent fluorescence. (b) The pump fluence crossed the lasing threshold and the Fourier image displays coherent lasing from the six K-point modes. (c,d) Single-shot lasing results when pumped with a (30×17 µm) rectangle .

and (c) are taken at pump fluences below threshold and display clear DMD-generated shapes of a triangle and rectangle, respectively, in the real space. The Fourier images are isotropically filled with (weak) fluorescence. In these gently pumped single shots, the fluorescence count rate amounts to just a few photons per pixel, not enough for the repeated zone scheme circles to stand out against the shot noise. Above the threshold fluence, 2D DFB lasing occurs at the K-points, as shown in panels (b) and (d). A standout observation is that the lasing spots are donut-like with a central dark spot, and that the spot size and shape depends strongly on the real-space gain profile. This is the topic of Chapter 5.

Figure 2.8 illustrates an important outlook on possible uses of our setup. Ultimately, we envision to probe how metasurface band structures change upon reaching significant gain. For instance, one could obtain (ω, k_y) band structures of the Dirac-cone dispersion around the K-point (panels a and b) in a single-shot pump-probe experiment, and observe how bands, their loss tangents (widths), and avoided crossings change when pumping just below lasing threshold. Panels (a) and (b) compare fluorescent (many shots) and white-light probe band structures (many shots) near a K-point in absence of a pump, highlighting that it should in principle be possible to perform such pump-probe experiments. So far, to our knowledge, literature has not reported on band structures in nanophotonic systems with optical gain signal, but instead focused on PL, reflection or transmission. We argue the study of band structures in gain, or even in differential amplification, would be highly relevant. For instance, many studies on photonic crystals analyze strong resonant interaction of Bloch modes at high symmetry points with optical gain [76, 79, 84, 85, 187–190]. Another rich, emerging idea in the metasurface com-

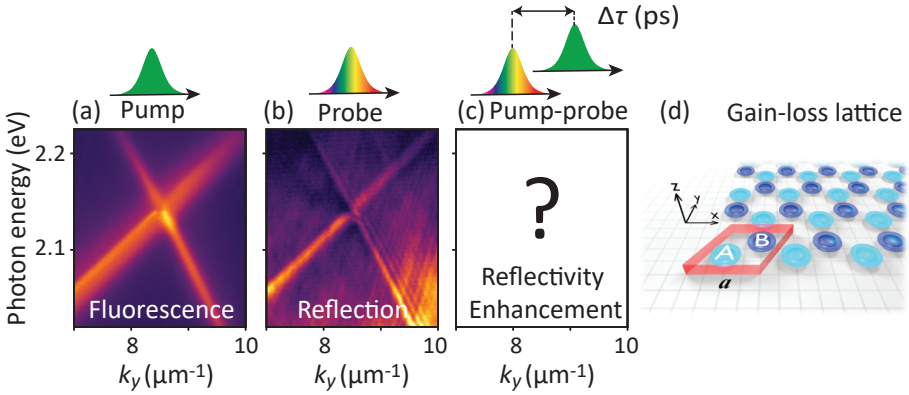

Figure 2.8: Outlook for amplifying plasmonic metasurfaces. (a,b) Our experiment enables not only to measure metasurface dispersions in PL or in R (same multi-shot data as Fig 2.6(d,e)), but also (panel c) to record band structures in *reflectivity enhancement*. (d) Then, when we only pump one sublattice (by DMD) in a plasmon honeycomb lattice, we form a gain-loss metasurface of which we can record PT-symmetry broken dispersions in reflectivity enhancement at the Dirac cone (image courtesy of R. Kolkowski).

munity is to think of metasurface response as due to complex-frequency zeros and poles in the scattering matrix. Studying how such poles and zeros can be brought on the real frequency axis, and can be engineered in k-space is the domain of the field of perfect absorption, and of optical gain singularities. The setup at hand could resolve such questions in space and time, while the DMD in the pump field could locally structure the gain, e.g., to form gain-loss PT-symmetric metasurfaces [92, 96–102, 186].

2.5 Amplifying 1D grating: Gain-enabled grating efficiency control

We explore pump-probe measurements on a very simple amplifying photonic structure: A one-dimensional (1D) grating. We demonstrate ultrafast grating efficiency modulation by means of optical gain. 1D gratings have countless applications in optics as dispersive elements, e.g. for spectroscopy, and the physics of optimizing their diffraction efficiency has been a topic of study for over a century [191]. More recently, actively controlling grating efficiency has received attention, with various methods. Some works focused on mechanically changing grating elements or the relative position of stacked binary gratings [192–194], while others changed the refractive index of an embedding active medium, for instance by thermal heating [195], liquid medium replacement in optofluidic realisations [196], electrically switching liquid crystal materials [197, 198], or by optically writing and rewriting pat-

terns in materials that show refractive index changes due to photodeformation [199]. In all above works, one drawback that stands out is the diffraction efficiency modulation speed, which typically lies in ms timescales. In this section, we study ultrafast tuning of diffraction efficiency using the new ultrafast pump-probe Fourier microscope, anticipated to achieve modulation speeds of a few ps. We consider the spectrally resolved diffraction efficiency of a simple metallic strip grating on glass, embedded in a thin thin polymer slab doped with dye molecules that provide gain by stimulated emission [178, 179, 200–202]. With the single-shot pump-probe Fourier microscope described in Sec. 2.3, we can measure modulation of diffraction efficiency in multiple orders simultaneously, which we here apply to the zeroth and $\pm 1^{\mathrm{st}}$ orders. We reproduce the main results with a Fraunhofer diffraction calculation with gain.

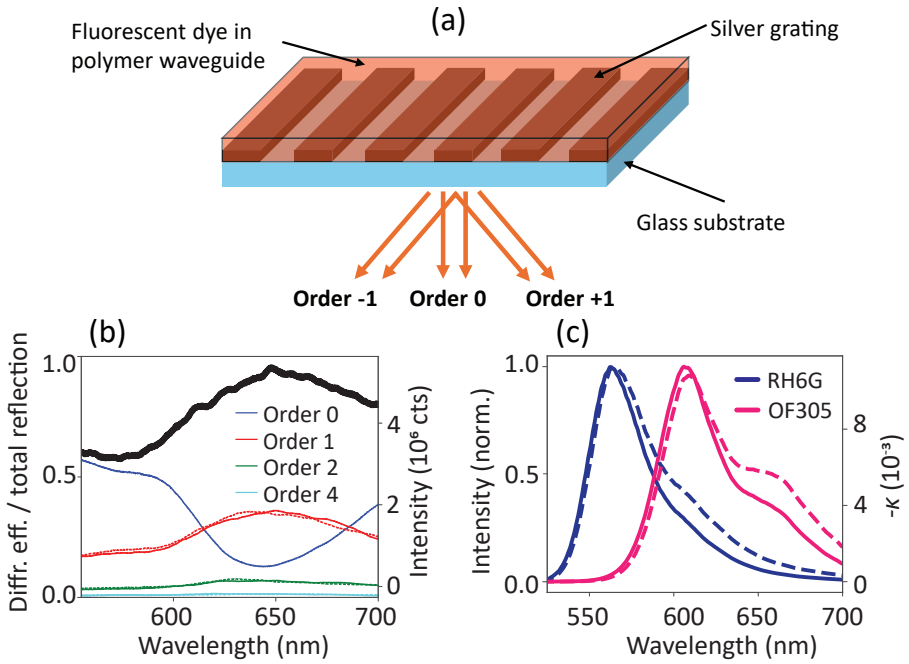

Figure 2.9: Amplifying 1D grating. (a) Sketch of sample geometry consisting of 50 nm tall silver strips on glass, embedded in dye-doped polymer. (b) Measured grating diffraction efficiencies normalized to total reflection (R_j/R_Σ) for $h = 660$ nm and duty cycle $d_c = 1/3$. Solid (dotted) lines are positive (negative) orders 1,2,4. (c) Measured, normalized fluorescence spectra, and estimated κ spectra.

2.5.1 Experiment

Fig 2.9 illustrates the main features of the 1D grating sample under study. We fabricate Ag line gratings on 170μm thick microscope cover slips using UV lithography, thin film evaporation of 50 nm Ag, and lift-off. The grating pitch is chosen as 2.5 μm and we have gratings with two duty cycles, namely 1/2 and 1/3rd (metal). Thin, dye doped, dielectric layers are then spincoated on top, resulting in the geometry sketched in Fig 2.9(a). We investigate two gain media, namely 3.5wt% rhodamine 6G (Radiant Dyes) mixed with SU8-3005 (Kayaku Advanced Materials) in cyclopentanone (ratio 2:1), spincoated at 3000 rpm for 60 s followed by $90°$ 2 min bake, or 5 wt% Oracet FL Red 305 (SunChemical, dye formally sold as BASF Lumogen F305) mixed with PMMA-A8 (Sigma Aldrich) in anisole (ratio 3:1), spincoated at 1500 rpm for 60 s, followed by a $150°$ 2 min bake. The resulting gain layers have thicknesses as measured in a profilometer that are $h_{\text{SU8}} = 510$ nm and $h_{\text{PMMA}} = 660$ nm. We project the white-light probe on the sample in epi-illumination, i.e., wide field illumination that is collimated and at normal incidence $k_{||} = 0$. A typical measurement of the white-light reflectance spectrum in the absence of gain (probe only, no pump) is shown in Fig 2.9(b) (solid black curve, sums all recorded orders), taken from the OF305:PMMA sample with duty cycle 1/3rd. In the same plot, we show measured diffraction efficiencies of various diffraction orders j, normalized to the total reflected intensity (R_Σ) as R_j/R_Σ.

Figure 2.9 shows fluorescence spectra for the Rh6G:SU8 sample (peaking just red of 570 nm) and the Oracet:PMMA sample (emission peak at 620 nm). The gain coefficient as a function of wavelength can be estimated from the fluorescence spectrum through the following set of equations relating the imaginary part of the refractive index κ, the gain coefficient g_0 and the cross-section of stimulated emission σ_e [178, 203]

$$n = n_r + i\kappa \quad \text{with} \quad \kappa = -\frac{g_0\lambda}{4\pi} \quad \text{where} \quad g_0 = N\sigma_e = C\lambda^4 f_n(\lambda).$$

Here the function $f_n(\lambda) = \text{QE} \cdot L(\lambda)/\int L(\lambda)d\lambda$ is the normalized emission spectrum and the quantum efficiency QE of the dyes at hand is taken as 0.9. The multiplicative prefactor C (unit m^{-4}) depends on the number density N of the dye molecules. Fig 2.9(c) shows derived imaginary refractive index functions alongside the measured normalized fluorescent emission spectra of RH6G:SU8 and OF305:PMMA as dotted curves, assuming $C = 10^{23}$ m^{-4} (choice of values in relation to experiments will be discussed below). The expected gain curves are slightly redshifted compared to the emission spectra.

To measure gain in diffraction orders 0 and ± 1, we operate in pump-probe mode and record single-shot spectra in reflection in Fourier space, where each order displays its own spectrum that we can separately analyze. From one complete set of four single-shot pump-probe measurements (see Fig 2.5), we

calculate enhancement G by subtracting fluorescence [84]

$$G = \frac{I_{\text{pump-probe}} - I_{\text{fluo}}}{I_{\text{probe}} - I_{\text{background}}}. \tag{2.2}$$

To have access to higher signal-to-noise ratio we measure G about 100 times (requiring 400 single-shots) for each step increment of the delay stage. For the choice of pump-probe illumination conditions, the fluorescence and white-light spot sizes are about 60 μm in the sample plane and carefully overlapped. We ensure that the walk-off of the pump spot is below 1 μm as the delay stage is swept over the full $x_{\text{stage}} = 0 - 125$ mm stage range (of which we only use a few percent for the presented data). As incoming pump fluence we measure 5 μmJ/cm^2. The resulting CMOS recorded fluorescence intensity generated by the pump light and in absence of the probe pulse is about 1 μJ/cm^2. This value is similar to the signal strength of the reflected white-light pulse. This might seem sub-optimal from the point of view that fluorescence light is a background in the pump-probe measurement. However, in our view, choosing the optimum pump and probe intensity is subtle. For the pump, too low pump fluence will provide little amount of excited molecules for stimulated emission, whereas too high fluence will lead to saturation of the dye. For the white-light probe, too low intensity will lead to poor signal to noise ratios. However, when the white light is too intense, it might deplete the available excited states for stimulated emission. From this point of view, choosing a ratio of probe intensity to the angle-integrated fluorescence of order unity is reasonable, since at unit dye quantum efficiency, the angle-integrated fluorescence is a good metric for the total energy stored in the gain medium.

Pump-probe measurements of grating diffraction efficiency changes are displayed in Fig 2.10. Both Oracet F 305 in PMMA (panels a,b) and rhodamine 6G in SU8 (panels c,d), show significant 10% intensity modulations as a function of pump-probe delay. We discuss three qualitatively different delay time regions – named U, W, and V – in the spectrum-delay maps. In region U, the probe pulse comes before the pump pulse. Therefore, there is no pump-induced change in the probe ($G = 1$). Region W contains a complicated structure. At any given wavelength, the efficiency shows a rapid modulation, taking place on a ≤ 1 ps time scale. The onset of this dynamics occurs earlier for shorter wavelengths than for red wavelengths, leading to a diagonal feature in the pump-probe diagrams that spreads over a ca. 10 ps time window. Several aspects of our experiment may give rise to picosecond dynamics. First, upon excitation with the 515 nm pump, the dye molecules will be excited into higher vibrational levels of the first electronic excited state, tending to relax in the lowest vibrational levels of the first electronic excited state on picosecond time scales. The fact that gain is initially available at blue wavelengths, and subsequently at redder wavelengths could be a result of this vibrational relaxation. Aside from molecular processes on picosecond

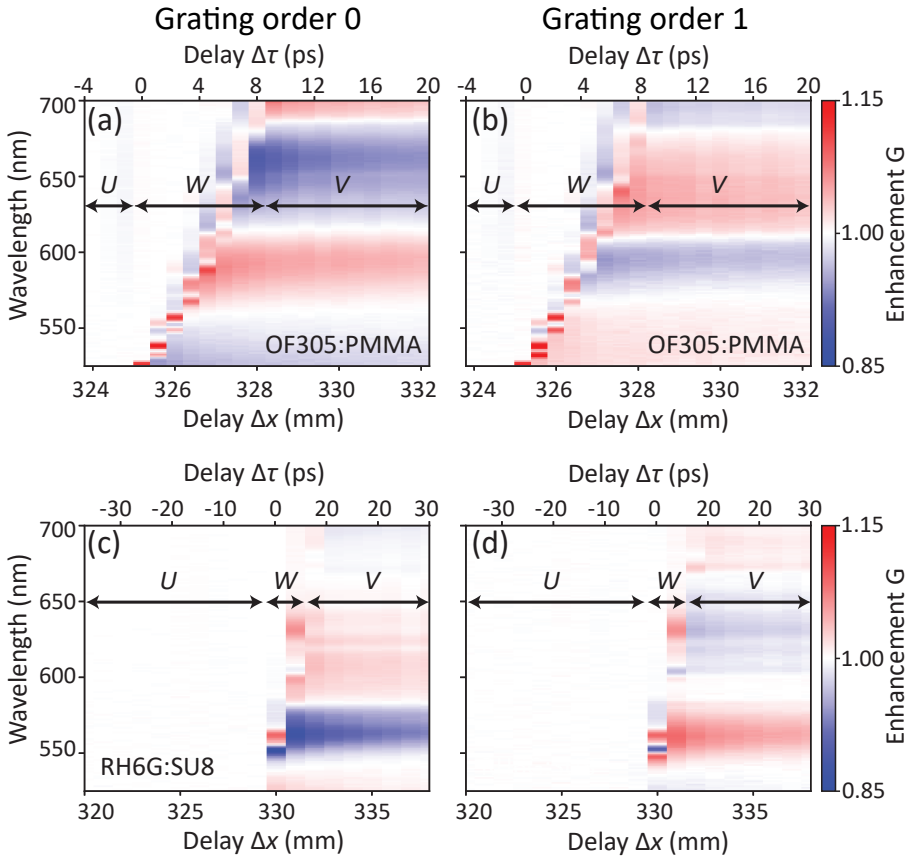

Figure 2.10: Measured enhancement spectra as a function of pump-probe delay. (a,b) Enhancement maps of diffraction order 0 and 1 for Oracet F 305 in PMMA with $d_c = 1/3$, with delay time regions U, W and V indicated. Various crosscuts through these datamaps, both horizontal and vertical, are presented later in this section. (c,d,) Enhancement maps for rhodamine 6G in SU8, $d_c = 1/2$. To construct enhancement maps, single-shot gain (Eq (2.2)) is measured 100 times per delay step, and subsequently averaged, in order to improve SNR. We obtain further SNR improvement by spectral camera hardware binning (2×2) and software binning of the vertical wavelength axis (8 pixels). These SNR-improving strategies are generally applied within this section.

time scales, one could also suspect so-called 'femtosecond coherent artefacts' that are not due to the dye, but to the experimental setup. For instance, the combination of temporal chirp in the white-light probe pulse (if blue arrives earlier than red wavelengths) in combination with molecule-enabled nonlinear processes of two-photon absorption and cross-phase modulation have been reported to lead to artefacts [204–206]. In most reports, however, the dynamics play out within a few picoseconds and do not extend over 10 ps. While this might be explainable by operating in a different wavelength window (525 – 700 nm in our experiment, vs. 300 – 400 nm in Refs. [205, 206], or generating more temporal chirp in our white-light continuum, we have not made a detailed study of whether this effect is due to the setup or the sample. Instead we focus on the longer time behavior, in the regime labeled V.

In the regime V, i.e., 10 ps after initial excitation, diffraction efficiencies are modified strongly but the induced change does not depend strongly anymore on the time delay. In this time regime, the excited fluorophores have thermalized to lower vibrational levels, while they have not yet had time to decay by fluorescence (which occurs on nanosecond time scales). Therefore, we expect the stimulated emission cross-section of the sample to be highest, hence leading to probe amplification. Strikingly, though, both gain systems exhibit not only enhancement of probe intensity, but also de-enhancement, varying with the spectral region and varying with the diffraction order that one examines. For instance, OF305:PMMA shows for the zeroth diffraction order enhancement of around 8% around $\lambda = 590$ nm, but de-enhancement of 10% at 660 nm, and then enhancement again at 700 nm. Qualitatively, the 1st order shows the opposite spectral enhancement.

Figure 2.11 displays crosscuts through the 2D enhancement data of Fig 2.10. In panels (a-e), enhancement spectra taken at various time delays are shown for the very first recorded single-shot results (as calculated through Eq. (2.2)) in a time-series of 100 consecutive pump-probe measurements. Despite the fact that single-shot data contain much more noise, the salient features both in time regions V (panels a-c: ps spectral time dynamics) and W (panel d: opposite enhancement curves for order 0 and 1) clearly appear also in the single-shot pump-probe measurements. Panels (e-h) display the result when averaged over 100 frames, significantly lowering the noise. Finally, in panels (i) and (j) we show horizontal crosscuts through the dataset for order 0 and 1 respectively. These line plots as a function of time delay, taken at wavelengths 590 nm and 660 nm, show that enhancement modulations decay with decay time in the order of 10 ps (from exponential fits).

The behavior that excitation can cause both enhancement and de-enhancement, with opposite spectral signatures in the different orders (region V), is also seen in Fig 2.12, where the pump probe delay is fixed at $x_{\text{stage}} = 327.6$ mm (where the probe modulation is strongest in region V), and the pump fluence is varied. From a fluence of 0.5 mJ/cm^2 the effect of the pump appears, increasing in magnitude over the full fluence sweep up to 3

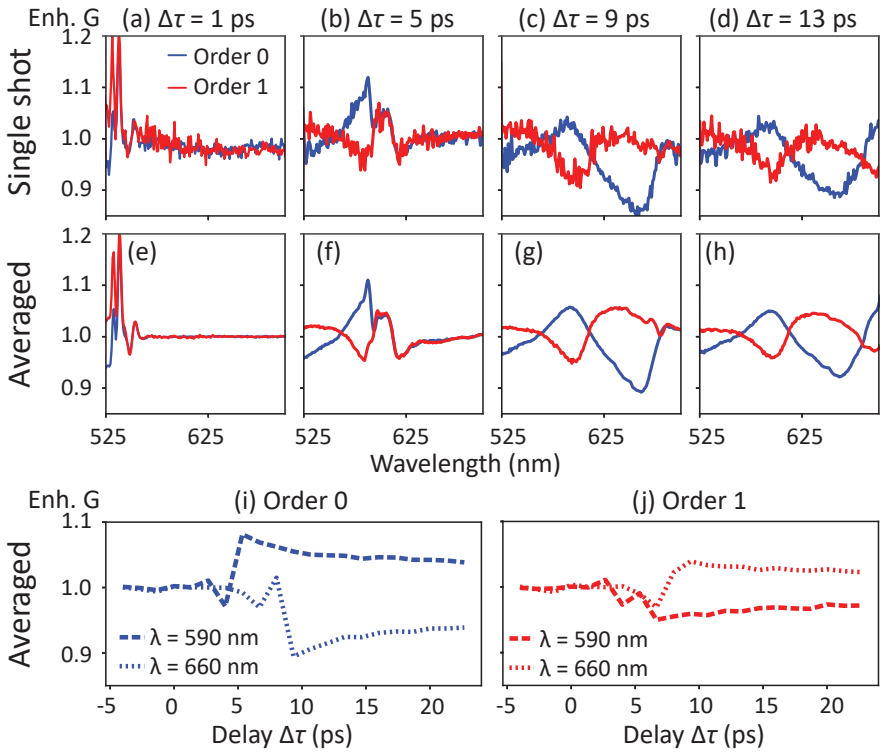

Figure 2.11: Single-shot and many-shot crosscuts through enhancement maps (a-d) Single-shot enhancement spectra (retrieved from the OF305:PMMA sample), taken at various delay times. (e-h) Enhancement spectra at same $\Delta\tau$ as (a-d), but averaged over 100 subsequent single-shot gain measurements, significantly improving SNR. (i,j) horizontal crosscuts (averaged over 100 subsequent shots), showing enhancement curves with 10s of ps decay times.

mJ/cm^2. This suggest that even at highest pump powers, the dye is not yet fully saturated in absorption. Maximum enhancements and de-enhancements of 10% and 15% are recorded in the 0th order.

On a final note, from the measurements it is not evident that there is a net gain, i.e., a net enhancement of the probe, which would directly evidence that the observed behavior is truly attributable to stimulated emission and not to other ultrafast effects (ground level depletion, excited-state absorption). We do not have access to the full closed photon balance since we only measure reflection and collect neither transmission nor guided photons. Integrating only the reflection orders we find there is net enhancement by 1-2% when integrating over the spectral gain window of OF305:PMMA. We also observe a small transient absorption at wavelengths larger than 680 nm, with faster decay time than the stimulated emission signal, which we interpret as a sig-

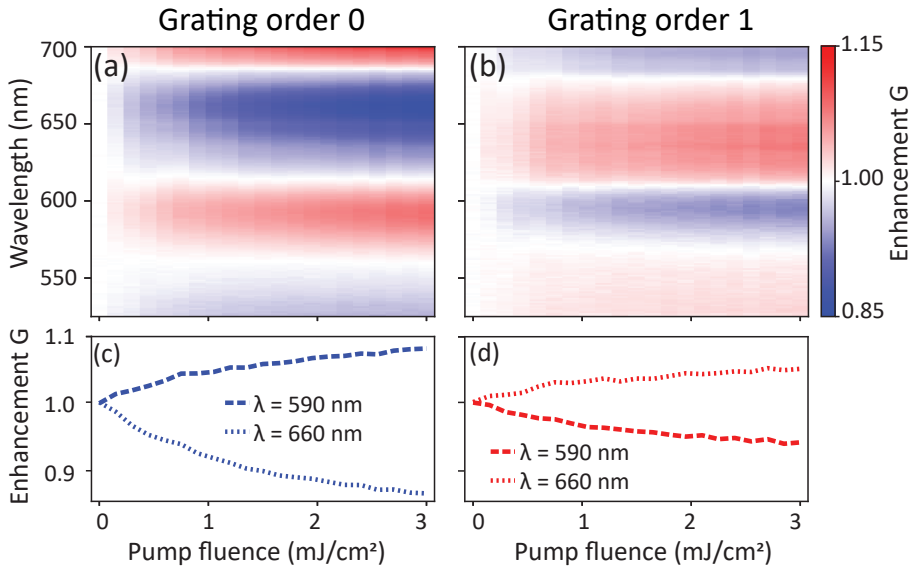

Figure 2.12: Multi-shot enhancement spectra as a function of pump power. (a,b) Enhancements in order 0 and 1. (c,d) Horizontal crosscuts through enhancement data, with wavelength choices indicated in legend. The results show the average of 100 single-shot gain measurements, taken at $x_{\text{stage}} = 327.6$ mm.

nature of excited-state absorption [179].

2.5.2 Calculation

We use a simple one-dimensional grating model to explain how optical gain can induce enhancement and de-enhancement in the different diffraction orders, seen in region V in previous section. The 1D geometry for the model is shown in Fig 2.13. We assume plane waves coming in from the glass substrate at normal incidence, and examine locally the reflection at the structure to assess the local amplitude and phase pickup upon reflection. Next, we Fourier transform the resulting modified plane wave to determine diffraction efficiencies. For regions where the plane wave reaches the silver grating, we assume that the local reflection is set by the Fresnel coefficient for a glass-silver-air multilayer for the same silver thickness. For the regions without silver, we assume that there is no reflection at the glass-polymer interface (since the index contrast is negligible), and that instead the wave is reflected at the polymer-air interface (height h). Thereby in the aperture plane (just below the glass surface), the silver and the dielectric parts of the unit cell imply an amplitude and phase pickup of

$$\text{Silver:} \quad r_m e^{i\phi_m} \qquad \text{Dielectric:} \quad r_d e^{i\frac{2\pi}{\lambda}2(n_d+i\kappa)h} \tag{2.3}$$

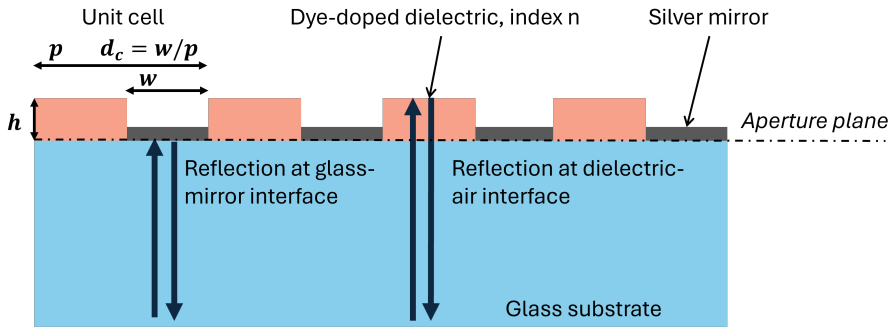

Figure 2.13: Geometry for the Fraunhofer diffraction calculation. We consider a normally incident plane wave arriving at the grating from the glass slide. The unit cell of pitch p consists of a metal grating bar (width w and duty cycle $d_c = w/p$) and a dielectric gain bar, and we assess locally at the aperture plane the amplitude and phase pickup upon reflection from metal-glass and dielectric-air interfaces. Fourier transforming the modified plane wave provides diffraction efficiencies.

For the reflectivity of the 50 nm Ag mirror on glass ($n = 1.45$), assuming a wavelength of 600 nm and $n_{\text{Ag}} = 0.06 + 4.15i$, we find absolute reflectivity $r_m = 0.98$, and angle $\phi_m = -2.46$ rad. For the dielectric-air interface we use $r_{d,\text{PMMA}} = 0.20$ ($n_{d,\text{PMMA}} = 1.49$) and $r_{d,\text{SU8}} = 0.22$ ($n_{d,\text{SU8}} = 1.58$). The exponential terms in the right hand formula account for the propagation phase associated with traversing the polymer height h both up and down, given the polymer refractive index n_d. Gain and loss are contained in the propagation factor, added by including them as an imaginary part of n_d.

To calculate diffraction efficiencies per order, we use the aperture function $t(x)$ of the 1D grating, which is the spatial convolution of an infinite Dirac comb $\text{Ш}_p(x)$ at the grating periodicity p, with the aperture function of the unit cell $t_{\text{uc}}(x)$, defined as

$$\text{Ш}_p(x) = \sum_{j=\infty}^{\infty} \delta(x - jp) \tag{2.4}$$

$$t_{\text{uc}}(x) = r_m e^{i\phi_m} \text{rect}\left[\frac{x - w/2}{w}\right] + r_d e^{i\frac{2\pi}{\lambda}2(n_d + i\kappa)h} \text{rect}\left[\frac{x - (p+w)/2}{(p-w)}\right] \tag{2.5}$$

where the function "rect(x/w)" is a block function that is zero everywhere except within a block of width w centered at the origin, where the function equals unity. According to the Fraunhofer approximation, the Fourier transform of the real-space aperture function $t(x) = \text{Ш}_p(x) \star t_{\text{uc}}(x)$ provides the angle-resolved far field. With the convolution theorem we express the Fourier transform of the aperture function as the product of the real-space δ-comb and that of the unit cell aperture function

$$\mathscr{F}[\text{Ш}_p(x) * t_{\text{uc}}(x)](k_x) = \mathscr{F}[\text{Ш}_p(x)](k_x) \cdot \mathscr{F}[t_{\text{uc}}(x)](k_x) \tag{2.6}$$

The Fourier transform of the real-space Dirac comb is simply a Dirac comb in reciprocal space that enumerates the set of grating diffraction orders (spaced by $2\pi/p$ in momentum space), while the unit cell aperture function transforms to

$$\begin{aligned}\mathscr{F}[t_{\text{uc}}(x)](k_x) = r_m e^{i\phi_m}\ e^{ik_x w/2}\ w\text{sinc}\left[\frac{k_x w}{2}\right] \\ + r_d e^{i\frac{2\pi}{\lambda}2(n_d+i\kappa)h}\ \ e^{ik_x(p+w)/2}\ (p-w)\text{sinc}\left[\frac{k_x(p-w)}{2}\right]\end{aligned} \tag{2.7}$$

where one recognizes the fact that the Fourier transform of a block of width w and unit height equates to $w\text{sinc}(k_x w/2)$, while the additional phase slips arise from the Fourier shift theorem. We define the duty cycle (referring to the metal strips of width w) as $d_c = w/p$, and evaluate at grating order j under normal incidence, by substituting $k_x = j\frac{2\pi}{p}$. The reflection intensity per diffraction order, R_j, has three contributions, namely from the metal, from the dielectric, and a cross term

$$\begin{aligned}R_j &= R_{j,m} + R_{j,d} + R_{j,\text{cross}} \\ R_{j,m} &= r_m^2 d_c^2 \text{sinc}^2(\pi j d_c)) \\ R_{j,d} &= r_d^2(1-d_c)^2\text{sinc}^2(\pi j(1-d_c))e^{2g_0 h} \\ R_{j,\text{cross}} &= 2r_d r_m d_c(1-d_c)\text{sinc}(\pi j d_c)\text{sinc}(\pi j(1-d_c))e^{g_0 h}\cos\left[\frac{2\pi}{\lambda}2n_d h + j\pi - \phi_m\right]\end{aligned} \tag{2.8}$$

For comparison with experiment, we examine calculated diffraction order efficiencies from Eq. (2.8) and derived enhancements of diffraction upon application of gain, through $G = R_{j,\text{gain}}/R_{j,\text{nogain}}$. Fig 2.14 displays as dotted red/orange lines a catalog of calculated diffraction efficiencies normalized to the total reflected intensity, i.e. R_j/R_Σ, in absence of gain. Enhancements that arise when gain is introduced are indicated as solid lines. The three rows depict metal duty cycles $d_c = 4/5$, $1/2$ and $1/5$, and the columns show results for increasing dielectric layer thickness. For $d_c = 4/5$, order 0 efficiency R_0/R_Σ is close to unity, and the $\pm$1st order diffraction efficiency is only a few percent, because at this duty cycle the width of the metal is so large that the system is almost a mirror. For smaller metal duty cycles, the 1st diffraction order becomes more apparent. For instance at duty cycle $1/2$, the $\pm$1st orders each take up to 25% of total reflected power. Generally, the efficiencies show an oscillatory dependence on wavelength, where the zeroth and 1st order anti-correlate. The oscillatory dependence redshifts with increasing height of the dielectric, and is attributable to the thin film interference in the dielectric embodied in the $\cos[4n_d k_0 h]$ dependence. This oscillatory dependence particularly occurs in the cross term $R_{\pm1,\text{cross}}$, which carries the interference between the diffracted light from the metal grating and from the dielectric bars.

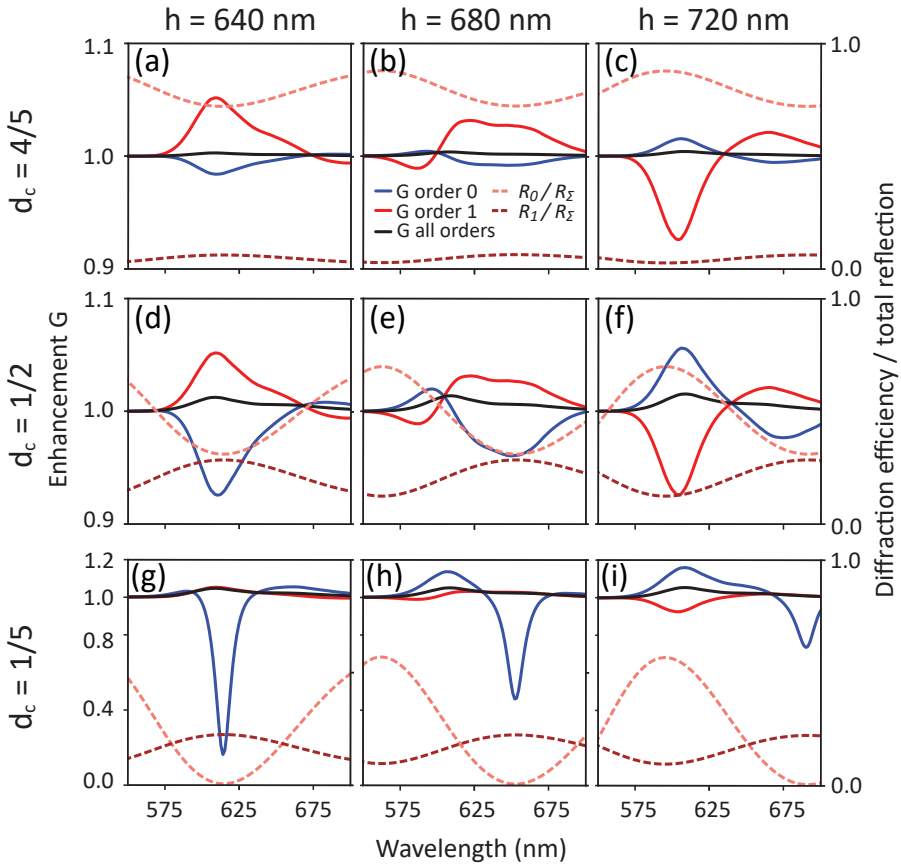

Figure 2.14: Catalog of calculation results from the 1D grating model. Each figure's right axis represents diffraction efficiency normalized to total reflection, of which the dotted red and orange lines indicate orders 0 and 1 (R_0/R_Σ and R_1/R_Σ in the legend). The left axis represents enhancement G, to which the solid lines correspond: Blue is enhancement in order 0, red in order 1 and black is total enhancement in reflection. Rows indicate duty cycles, columns increasing gain layer thicknesses. Considered duty cycles are $d_c = 4/5$ (a-c), $d_c = 1/2$ (d-f), and $d_c = 1/5$ (g-i).

Turning to gain-induced diffraction enhancements, we remind the reader that the gain in our modeling is spectrally dependent, with the gain region for Oracet F 305 from 570 to 700 nm, peaking at 620 nm. For the $h = 640$ nm grating, the model predicts that the zeroth order is suppressed, while the first order is enhanced by the gain. As the metal duty cycle reduces, the suppression of the zero order becomes stronger, although the absolute enhancement of the 1st order does not grow accordingly. Notably, the gain-induced enhancement qualitatively follows the peaks and troughs of the diffraction efficiency in the respective orders. Commensurate with that observation, there is a reversal in behavior at $\lambda = 680$ nm, to the red of which the 1st order is suppressed. As the height of the dielectric increases, the behavior of enhancement/suppression redshifts along with the spectral behavior of the diffraction efficiencies. This means that at the largest height, $h = 740$ nm, the dominant effect is a strong suppression of the 1st order diffraction, and an enhancement of the zeroth order. For all duty cycles, the total gain (i.e., the gain in all orders summed together, light blue curve) is relatively insignificant, much smaller than the (de-)enhancements in order 0 and ± 1.

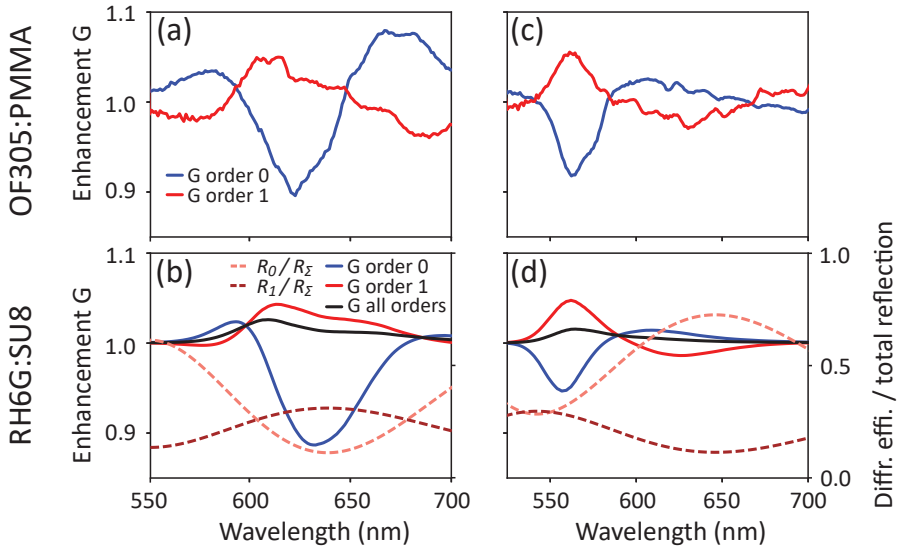

Figure 2.15: Comparing experiment with model. (a) Measurement of OF305:PMMA, $h = 660$ nm and $d_c = 1/3$, $\Delta\tau = 10$ ps. (b) Calculation, same duty cycle, but height $h = 665$ nm and peak gain coefficient $g_0 = 2200$ cm^{-1}. Right axis and dotted lines correspond to diffraction efficiency normalized to total reflection (R_0/R_Σ and R_1/R_Σ), while left axis and solid lines corresponding to enhancements G (blue order 0, red order 1, black total reflection enhancement). (c) Measurement of RH6G:SU8 with $h = 510$ nm, $dc = 1/2$, $\Delta\tau = 10$ ps. (d) Calculation with $h = 530$ nm and $g0 = 2500$ cm^{-1}. For the calculations, heights are chosen slightly off from measured layer thicknesses (with 10s of nm error), in order to improve similarity.

Having obtained basic intuition for the intensity enhancement spectra of a 1D grating with a layer of gain dielectric, we now turn to a comparison of experimental results and model. Fig 2.15 shows experimental data selected as wavelength-crosscuts from the delay-spectrum enhancement maps of Fig 2.10, in panels (a) for Oracet F 305 in PMMA and (c) for rhodamine 6G in SU8. Panels (b,d) show calculations for both systems, for layer thickness taken as measured on a bare layer. The main wavelength dependence and the anti-symmetric spectral behavior between orders 0 and 1 are captured by the model. Given the simplicity of the model, this is a remarkable correspondence. At long wavelengths, particularly for the Oracet F 305 case, there are nonetheless significant differences. One likely explanation is that other nonlinear ultrafast processes may have contributed in the pump-probe experiment, such as excited-state absorption [179].

A critical point of discussion regards the value of the gain coefficient. For parameter C we used values $1.1 \cdot 10^{23}$ m^4 (OF305:PMMA) and $1.42 \cdot 10^{23}$ m^4 (RH6G:SU8), chosen such that the magnitude of the enhancements is of the same order as in experiments. However, these values convert to gain coefficients of order $2200 - 2500$ cm^{-1}. These values are one order of magnitude higher than for dyes in polymer slabs in literature [69], as well as what was previously measured by S. Kovaios in our group: Vertical stripe length (VSL) method on slabs of Rh6G-doped SU8 evidenced modal gain coefficients of up to 90 cm^{-1} for 2D slab waveguided modes. The discrepancy may in part be explained by the fact that (1) there is large difference in excitation pulse length between the VSL test and our work (namely 500 ps with vertical stripe length method as opposed to 200 fs in our pump-probe experiment), (2) differences in dye concentration, and (3) the fact that the vertical stripe length measurement pertained to a modal gain coefficient for the 2D slab waveguide modes, and values are reduced from the bulk value due to incomplete mode overlap with the gain medium. On the contrary, one might question the simplicity of our grating model. Therefore, for validation, we perform full-wave COMSOL simulations for our 1D grating model at different gain levels inserted as imaginary part of refractive index (value of κ). The simulations confirm all main features of the model: Field plots show that the metal lines are mainly reflective, while the dielectric part is mainly transmissive. The model also shows similar oscillatory behavior for the diffraction orders, and similar reflection efficiencies. The COMSOL simulation also displays physics not contained in the model: Spectral Fano lineshapes of modest amplitude, superimposed on the gently oscillating efficiency curves, which we ascribe to standing surface plasmon polariton resonances that span the width of the grating lines. Indeed, field plots show near-field signatures of surface-plasmon polariton modes that form standing waves. Upon introduction of gain we find similar physics as in the simple model: Gain-induced spectral enhancements and de-enhancements occur that directly correlate with the passive-grating efficiency, and that show opposite behavior for the 0th and $\pm$1st orders. Moreover,

numerically, the simulation also requires gain coefficients of 2100 cm^{-1} (κ circa 0.01) to obtain 15% diffraction efficiency modulations in the different spectral regions. This is a striking confirmation of our simple model by the simulation, although it does not explain the origin of the discrepancy with reported gain coefficients. To summarize, with our methodology we record gain coefficients which are an order of magnitude higher than expected on basis of literature and VSL measurements in our group.

A final point of discussion is the possibility that cross-linkage of the polymer may occur during intense femtosecond pumping, which could change the slab thickness and thereby effective mode index [207]. We believe this an unlikely explanation, since we obtain similar results for both SU8 and PMMA gratings which have very different behavior when viewed as (two-photon) resists.

2.6 Discussion

We have commissioned a new setup that successfully combines two highly important techniques in optics and nanophotonics: Pump-probe microscopy with Fourier microscopy, providing access to angular resolved studies of ultrafast processes. Our main objective is to study and control effects from optical gain, such as metasurface lasing and resonant white-light amplification. In this chapter, we report a condensed portfolio of results on plasmonic lattices with diffractive pitch. In multi-shot mode, band structures both in fluorescence and white-light reflection display e.g. the conical Dirac cone dispersions around the K-point. Single-shot experiments offer insight into spontaneous symmetry breaking between degenerate modes K and K', and the DMD-structured pump field provides active far-field output control. As such, the setup is an experimental push forward to achieving locally patterned gain-loss plasmon metasurfaces with PT-symmetry physics at the K-point dispersions.

As a first test of pump-probe control of diffraction by means of optical gain, we presented an ultrafast study on simple amplifying 1D gratings. We measure significant gain-induced modulations in grating efficiencies: Diffraction orders can experience up to 15% amplification in one part of the spectrum but de-amplification in another part, and we found that the behavior in the zeroth and first order anti-correlates. These result are all captured in a simple Fraunhofer diffraction calculation. While we presented these measurements and the model to show a successful commissioning of our single-shot pump-probe setup, as applied to amplifying photonic systems, two surprises stand out from examining both the data and the theory. These are (1) that gain can lead to suppression as well as amplification of scattering, and (2) that the enhancements are comparatively modest, even when gain is large. In this regard, we note that pump fluences are close to those used in Chapters 4 and

5 where the same material systems are brought to lasing, and so the induced gain can indeed be deemed 'large'. The simple model expressions in Eq. (2.8) show that gain does not simply provide an overall enhancement, because the diffraction physics contains interference terms (R_{cross}). This means that minor tuning of parameters can lead to dramatic differences in response. For instance, if within the simple grating model we take a system of 20% duty cycle, and a larger layer thickness of 1000 nm, singular behavior (diverging diffraction efficiency) can occur, but only at specific gain values. This notion of 'critical gain', wherein amplification disappears when the gain is both too small and too large relative to a specific value at which a gain singularity occurs, resembles the physics of 'perfect absorption' (vanishing instead of diverging response). In the metasurface community, resonant systems with weakly absorbing layers have been well studied, and it has been shown that perfect absorption can only occur upon precise matching of radiative and absorptive loss coefficients [95]. The analog of perfect absorption in the case of amplifying systems is theoretically studied in Chapter 3.

Chapter 3

Absorption and amplification singularities in plasmon metasurface etalons with gain

Passive reflective metasurfaces can possess perfect absorption conditions: Singular scattering anomalies at which all impinging light is absorbed. Perfect absorption is a common yet powerful metasurface design option with applications in energy harvesting, sensing, and more. Less common is the inclusion of optical gain to the system, which can give rise to a singular condition for perfect amplification. In this Chapter, we analyze absorption and amplification singularities in plasmon antenna metasurface etalons with gain with a simple transfer matrix model. Our etalon follows the Salisbury screen design: A metal ground plate spaced by dielectric medium from an array of resonant plasmonic scatterers. We include frequency dispersive models for gain media and discuss the limitations of time reversal symmetry arguments for relating gain singularity conditions (reflectivity poles) to the well known perfect absorption conditions (reflectivity zeros) of metasurface etalons. We show that for metasurface etalons with both gain and loss, gain can induce both perfect absorption and gain singularities, and we describe topological constraints on their creation and annihilation. Our findings have implications for the fields of non-Hermitian photonics, parity-time symmetric scattering systems, and dynamically controllable active metasurface pixels.

3.1 Introduction

Reflective metasurfaces are of considerable interest for their ability to control the reflection amplitude, phase, and absorption of optical waves [18, 116, 118, 119, 208–214]. A common geometry is inspired by the radio frequency concept of Salisbury and Dallenbach screens: Thin (patterned) layers at a carefully chosen distance from a metal ground plate that achieve perfect absorption of impinging waves [118, 215, 216]. In optics this motif of metasurfaces at quarter wavelength (or similar) distances from a mirror has led to advances in reflective metasurface pixels [119, 208, 211, 213], and has been used to turn intrinsically weakly absorbing layers like two-dimensional (2D) materials into effective photodetectors [217–219]. The seminal paper of Chong et al. relates perfect absorption to complex frequency plane analysis of the scattering matrix of photonic structures in terms of zeros and poles: The scattering matrix eigenvectors with eigenvalues 0 and ∞ [113]. In fact, according to Krasnok et al. [95] the scattering response of a system is completely determined by such zeros and poles. By adding losses, one can bring zeros from the upper half complex frequency plane onto the real frequency axis. Conversely, poles correspond to scattering resonances, and when brought to the real frequency axis by gain engineering, they become amplification singularities [80, 220, 221]. This understanding explains Salisbury and Dallenbach screens, more general cases of coherent perfect absorption (CPA) [95, 117, 120, 121, 222–227], as well as of CPA lasing [80, 95, 114, 120, 220, 228–230]. Zeros and poles furthermore have a topological character that expresses in the phase response [121]. Recently, active tuning of metasurface response through the control of zeros and poles has received interest in numerical studies. One focus has been on the active control over absorption singularities using thermo- or electro-optical mechanisms [231, 232], while another has been on amplification singularity tuning by means of optical gain [91, 122]. However, actively tuned singular response of a plasmon metasurface Salisbury screen with optical gain has received little attention.

In this work, we theoretically study perfect absorption (zeros) and amplification singularities (poles) in amplifying plasmon antenna metasurface etalons, extending the Salisbury-screen analogon for perfect absorption in such structures [118] to gain. The philosophy of the work is highlighted in Figure 3.1: While a passive metasurface etalon (panel a) may host pairs of reflection zeros, we will show that the introduction of gain can give rise both to zeros and poles, and we analyze topological constraints on these singularities. We develop a transfer matrix model [233] for metasurface etalons with loss and gain, and address the emergence of zeros and poles in dependence of (1) whether gain/loss is included in the spacer layer or in the metasurface, and (2) in the lattice case, how the gain is included in the meta-atoms. Furthermore, we emphasize the importance of the numerical models used for loss and gain. An appealing viewpoint comes from the

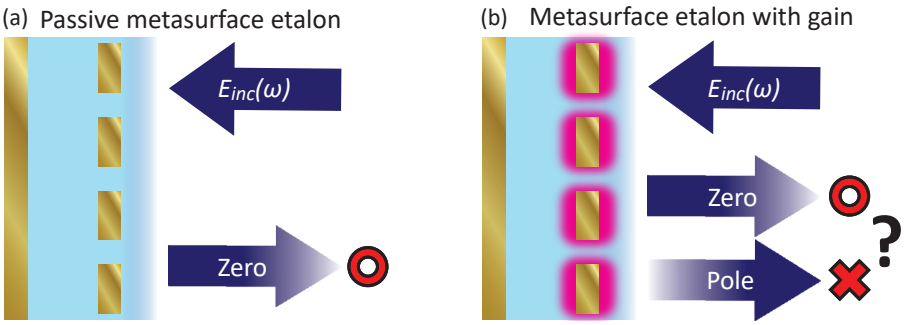

Figure 3.1: Singular reflection in metasurface etalons with loss and gain. (a) For a lossy, plasmon metasurface in front off a mirror, hybridization between the plasmon resonance and etalon resonances leads to pairs of perfect absorption conditions: Zeros in reflection accompanied by phase singularities in a parameter space spanned by frequency and etalon spacing. (b) When optical gain is included both reflection zeros (○) and reflection poles (×) can arise.

field of time-reversal and Parity-Time (PT) symmetry, where nonresonant imaginary refractive index (n'') of equal magnitude but opposite sign are associated with time-reversal, i.e., an interchange of loss and gain properties. This viewpoint implies simple relations between perfect absorption and gain singularity conditions. However, we argue that the physics is crucially affected by the need to account for the physical frequency dispersion in gain media: A correct gain dispersion means that gain and loss *are not* time-reversed equivalents through sign-inversion of the imaginary part of the dielectric response. Finally, we argue that Salisbury screens with gain and loss can show real-frequency zeros and poles that are very close in parameter space, which may be interesting for dynamically controllable amplitude and phase metasurface pixels with very large dynamic range.

3.2 Model

In this work, we consider semi-analytical modeling of amplifying metasurface etalons in which plasmon particle lattices are held in front of a mirror, and in which gain is introduced, either in the dielectric spacer or in the particle lattice. We start by reviewing simple physical models for loss and gain materials and scatterers, before recapitulating the transfer matrix method to calculate the stack response.

3.2.1 Model for loss materials and scatterers

The canonical model for a plasmonic particle with loss [35] starts with the Drude model for the free electron plasma, yielding the complex-valued di-

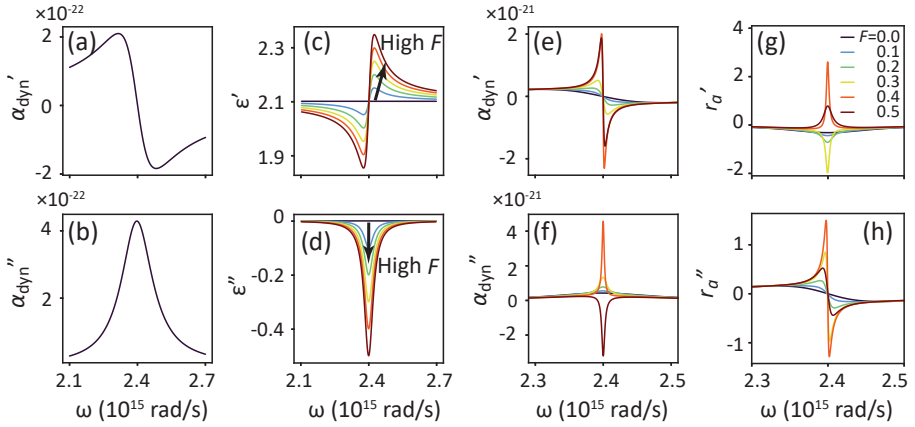

Figure 3.2: Response functions of lossy and gainy constituents of the plasmon metasurface etalons with gain. (a,b) Plot of Eq. (3.4): Real and imaginary part of the dynamic polarizability of a single plasmon rod of $V = 3 \cdot 10^{-23}$ m^3 (Lorentz model fitted to COMSOL simulation from Ref. [121]). (c,d) Plot of Eq. (3.5): Real and imaginary permittivity of a model dielectric medium with a Lorentzian gain resonance frequency $\omega_g = \omega_p = 2.4 \cdot 10^{15}$ rad/s, line width $\gamma_p = 0.01\omega_g$ and population inversion parameter $F = (0, 0.1, 0.2, 0.3, 0.4, 0.5)$. Note how compared to the plasmon dispersion not only the imaginary but also the real part is flipped in sign. (e,f) Plot of Eq. (3.4) with Eq. (3.5). Dynamic polarizability of a plasmon antenna coupled to a resonant gain bath according to the model of Manjavacas [234], effectively forming a combination of resonances (a,b) and (c,d). For increasing gain the sign of the metal dispersion remains, but from $F = 0.5$, $\mathrm{Im}(\alpha_{\mathrm{dyn}})$ flips sign. (g,h) Plot of Eq. (3.7): Reflectivity r_a of a subdiffractive ($a = 350$ nm) gain plasmonic metasurface in glass for increasing pump strength. $\mathrm{Re}[r_a]$ flips sign as the singularity condition between $F = 0.3$ and $F = 0.4$ is traversed.

electric constant

$$\epsilon_{\mathrm{Drude}}(\omega) = \epsilon_\infty - \frac{\omega_p^2}{\omega^2 + i\omega\gamma_p}, \tag{3.1}$$

where ω_p is the plasma frequency, and γ_p the Ohmic damping rate. When substituted into the Rayleigh expression for the quasi-static electric dipole polarizability of a subwavelength sphere of dielectric constant ϵ and radius r, in a host of dielectric constant ϵ_{host} (we use the convention $\mathbf{p} = 4\pi\epsilon_{\mathrm{host}}\epsilon_0\alpha\mathbf{E}$ so that polarizabilities have units of volume), one finds

$$\alpha_0(\omega) = r^3 \frac{\epsilon(\omega) - \epsilon_{\mathrm{host}}}{\epsilon(\omega) + 2\epsilon_{\mathrm{host}}} \tag{3.2}$$

displaying the well-known localized surface plasmon resonance at $\epsilon(\omega) = -2\epsilon_{\mathrm{host}}$. When $\epsilon_\infty = \epsilon_{\mathrm{host}}$, this resonance is exactly Lorentzian

$$\alpha_0 = \frac{V\omega_0^2}{\omega_0^2 - \omega^2 - i\omega\gamma}. \tag{3.3}$$

The particle resonance frequency $\omega_0 = \omega_p/\sqrt{3\epsilon_{\text{host}}}$ and damping rate follow straightforwardly from the Drude parameters, while the oscillator strength is quantified by V (units of volume, equal to r^3 for the Rayleigh sphere). For strong scatterers, scattering into the far-field comes with an additional loss channel. It is well known in literature [37, 38] that a self-consistent theory for multiple scattering requires to include a radiation damping factor $i2/3k^3$

$$\alpha_{\text{dyn}}(\omega) = \frac{1}{1/\alpha_0 - i2/3k^3}, \tag{3.4}$$

where $k = n\omega/c$ is the wave number of the light in the medium surrounding the scatterer ($n = \sqrt{\epsilon_{\text{host}}}$) [37, 38]. The resulting 'dynamic' polarizability satisfies the optical theorem, meaning that scattering equals extinction at zero Ohmic damping, while at non-zero Ohmic damping the extinction exceeds scattering, with the deficit equal to absorption. In this work we start with parameters from [121], which make Eqs. (3.2), (3.4) accurately fit finite element simulations of extinction and scattering of single nanorod plasmon antennas in glass ($n = 1.45$) for polarization along the long axis of the rods. These parameters in terms of Eq. (3.3) read $\omega_0 = 2.4 \cdot 10^{15}$ rad/s, damping rate $\gamma_p = 9.3 \cdot 10^{13}$ s^{-1} and $V = 6.9 \cdot 10^{-23}$ m^3 for Au nanorods ($100 \times 50 \times 40$ nm^3) in glass. We will vary V to control oscillator strength. Figure 3.2(a,b) show the resulting dynamic polarizability of the lossy plasmon particles. The real part shows the typical dispersive line shape, indicating the typical π phase slip in scattering that occurs upon crossing the resonance. The imaginary part is a positive Lorentzian line shape, and through the relation $\sigma_{\text{ext}} = 4\pi k \text{Im}\alpha_{\text{dyn}}$ directly indicates the resonance in the extinction cross section.

3.2.2 Extension to gain materials

To describe amplifying instead of lossy scatterers, it is tempting to simply reverse the sign of the damping rate, or equivalently complex conjugate ϵ. While such a transformation has been argued to be equivalent to time reversal [92, 102, 235–238], we note that special care is required because scattering by a gainy particle is not the time-reverse of scattering by a lossy particle. Scattering redistributes light from a single input port (a plane wave) over all outgoing ports (outgoing spherical wave) at a rate given by the radiation damping term $i2/3k^3$. Time-reversing material loss into gain does not also redefine the input and output ports in a scattering problem, meaning that the radiation damping term does not change sign. Given these subtleties, it is useful to inspect gain susceptibility models and review the ramifications for scattering.

A common model in the laser community [65] to describe an inverted population of atoms in a dielectric medium, is to add the susceptibility χ_{gain} of an ensemble of atoms in inversion to the background permittivity $\epsilon_b(\omega)$ as

$$\epsilon(\omega) = \epsilon_b(\omega) + \chi_{\text{gain}}(\omega) \tag{3.5}$$

with a resonant Lorentzian lineshape

$$\chi_{\text{gain}}(\omega) = F\frac{\gamma_g}{\omega - \omega_g + i\gamma_g}, \tag{3.6}$$

where ω_g is the resonant frequency of the gain medium, γ_g its line width, and F quantifies the density of excited atoms (population inversion controlled by pump strength in experiments). This model has been proposed for 3- or 4-level gain atoms [65, 69, 234, 239–241]. Figure 3.2(c,d) plots Lorentzian susceptibility model χ_{gain} for atoms in glass, with $\omega_g = \omega_p = 2.4 \cdot 10^{15}$ rad/s and $\gamma_p = 0.01\omega_g$ for various pump strengths F. Importantly, the gain not only makes the imaginary part of the permittivity/polarizability negative, but also affects the dispersion in the real part of the response function. We note that a Drude scatterer can be transformed into an amplifying resonant scatterer with valid gain dispersion (as Fig 3.2(c,d)) not by $\gamma \to -\gamma$, as an intuitive time-reversal argument would suggest, but instead by $V \to -V$. Ref. [241] explains this behavior on basis of a quantum mechanical microscopic model of a 3-level atom upon pumping, from which the authors derive the classical dynamic polarizability of an atomic scatterer with gain. Below inversion, the atom dynamic polarizability displays a lossy Lorentzian polarizability, much like a plasmonic particle (panel a,b). Upon reaching population inversion, the atom becomes transparent. Crossing through transparency, the polarizability goes through zero, flipping sign both in its imaginary and real part. The sign flip in the imaginary part indicates negative extinction cross sections, i.e., amplification. The scattering cross sections $\sigma_{\text{scatt}} = 8\pi/3k^4|\alpha_{\text{dyn}}|^2$ instead remain positive.

Several works have proposed including gain into lossy plasmonic scatterers [69, 92, 102, 234, 242–247]. We follow the description of Manjavacas [234], which implements gain by taking the dielectric constant of a nanoparticle as $\epsilon(\omega) = \epsilon_{\text{Drude}}(\omega) + \chi_{\text{gain}}(\omega)$, and evaluating Eq. (3.2) and Eq. (3.4). Figure 3.2(e,f) plot the real and imaginary part of the polarizability at various gain levels F. For low gain values, the polarizability is similar to that of the lossy plasmonic particle, sharpening with increasing gain as the intrinsic Drude loss is compensated. The dispersion then goes through a condition of strong scattering and strong positive extinction, to a regime of negative extinction (net gain). For such a compound particle, the dispersion in the real part of polarizability does *not* flip sign.

Finally, we review how to convert the single particle polarizability into metasurface reflectivity. To calculate r_a for periodic arrays of identical scatterers, one can use Ewald lattice summation techniques that include retarded multiple scattering interactions in the point dipole approximation [38, 248]. For lattices consisting of identical scatterers specified by quasi-static polarizabilities α_0, arranged in unit cells of area A, the reflectivity in the non-

diffractive regime reads

$$r_a(\omega) = \frac{2\pi ik}{A} \frac{1}{1/\alpha_0(\omega) - \frac{2\pi ik}{A}}. \tag{3.7}$$

Interestingly, Eq. (3.7) replaces the single nanoparticle radiation damping correction that is appropriate for the single scatterer (Eq. (3.4)) with a collective lattice damping term $2\pi ik/A$. This lattice damping term increases with antenna density and signifies superradiant damping for coherently radiating dipole arrays. [121]. In the limit of high areal density, the reflectivity approaches a perfect mirror $r_a(\omega) = -1$. In Fig. 3.2 (g,h), we examine complex reflectivity of a plasmonic metasurface with gain included in α_0, according to the approach of Manjavacas [234]. The real value of r_a (Fig. 3.2(g)) becomes increasingly negative with more gain, until it reaches the singular condition $\alpha_0 = A/2\pi ik$ (between $F = 0.3$ and 0.4), at which point the gain compensates the Ohmic and lattice radiation loss. At this point the reflectivity flips sign to large positive amplitudes, before converging to zero with further increase of F. Panel (h) shows that near the singularity condition, the Lorentzian curve of $\mathrm{Im}(r_a)$ has the steepest slopes.

3.2.3 Metasurface etalon transfer matrix model

To describe the complete response of the composite system from the single material response just described, we use a transfer matrix method laid out in Ref. [233]. We consider normally incident radiation only. The transfer matrix method, as introduced in the seminal work of Ref. [249], relates parallel electric and magnetic (E, H) fields at the front side of a stack of a dielectric layer ($z = 0$) with those at the back side ($z = d_{\text{stack}}$) via multiplication of characteristic matrices of individual layers: $M_{\text{stack}} = M_N \cdot M_{N-1} ... M_2 \cdot M_1$ (with $m = 1, 2, ...N$ enumerating the layers from front to back). From the stack matrix M_{stack}, the complex reflection and transmission amplitudes follow as

$$\begin{pmatrix} t \\ ikt \end{pmatrix} = M_{\text{stack}} \begin{pmatrix} 1+r \\ ik(1-r) \end{pmatrix}. \tag{3.8}$$

Our stack will be composed of transfer matrices M_d for homogeneous layers of index n and thickness d, and a transfer matrix for the metasurface M_{meta}. M_d is well known in literature, but M_{meta} should depend on r_a and merits careful attention. For non-diffractive metasurfaces, M_{meta} is obtained by assuming a zero thickness layer with reflection coefficient r_a, and also assuming that both slabs immediately neighboring the metasurface have identical refractive index [233]. Explicitly, M_d and M_{meta} [233] read:

$$M_d = \begin{pmatrix} \cos kd & \frac{1}{k}\sin kd \\ -k\sin kd & \cos kd \end{pmatrix} \quad \text{and} \quad M_{\text{meta}}(r_a) = \begin{pmatrix} 1 & 0 \\ \frac{2ikr_a}{1+r_a} & 1 \end{pmatrix}. \tag{3.9}$$

The model does not allow for any diffraction channels, so we only consider lattices with subdiffractive pitches. We retrieve r_a from Eq. (3.7).

While we use the transfer matrix method for all calculations in this work, we note that for a simple two layer etalon (one mirror, one metasurface) one can extract an analytical Fabry-Perot formula [121, 226, 250]

$$r_{\text{FPI}} = \frac{r_a + r_m(1+2r_a)e^{2ik_0nd}}{1 - r_a r_m e^{2ik_0nd}}. \tag{3.10}$$

Here, r_m denotes the back reflector reflection coefficient. In this work, we use glass-backed gold mirrors with $n = 0.25 + 3.46i$ and thickness 50 nm or 20 nm, and dielectric spacers of varying thickness and index $n = 1.45$. Solving Eq. (3.8) with proper M_d, these values yield reflection coefficients $r_m = -0.5935 - 0.6502i$ and $-0.3066 - 0.5126i$, respectively. Eq. (3.10) has been used in literature to explain the topological constraints on perfect absorption conditions in absorbing metasurface etalons [121].

3.3 Results

3.3.1 Gain equivalent of lossy metasurface

We now discuss the response of Salisbury screens that include optical gain. We examine increasingly complex scenarios for metasurface etalons with gain, focusing on singular responses. The simplest case is presented in Figure 3.3: Reflectivity of a standard etalon where a lossy mirror is separated by a transparent spacer from a layer composed of nanoparticles, whose response are defined by the Lorentzian Drude model (Eq. (3.3)). We compare the standard case of loss, modeled by positive oscillator strength V shown in panels (a-d), with the simplest self-consistent model of amplification of equivalent magnitude, set by negative volume, $V \to -V$, in panels (e-h). Parameters are chosen to closely resemble the standard plasmonic Salisbury screen in Ref. [121], sketched in Fig. 3.1(a). The left three columns of Fig. 3.3 show reflectivity amplitude in a phase space (ω, d) spanned by etalon spacing d and frequency ω, with different panels corresponding to successively higher antenna density (plots labeled with lattice pitch $a = \sqrt{A}$, assuming square lattices). The rightmost column displays reflectivity phase. Throughout this work we use color scales for $|r_a|$ that are linear from 0 to 1 (blue to white), and logarithmic for $|r_a| > 1$ (white to red, clipped at $r_a = 10^2$). Panels (a-d) show the case of a standard lossy metasurface Salisbury screen. The response is dominated by the hybridization of the antenna resonance at $2.4 \cdot 10^{15}$ rad/s with etalon resonance conditions, especially visible in (c): At thicknesses of approximately 250, 500 and 750 nm, hyperbolic white features curve from top slightly rightward towards bottom. In between these etalon conditions, the reflectivity amplitude drops with increasing antenna density, signifying

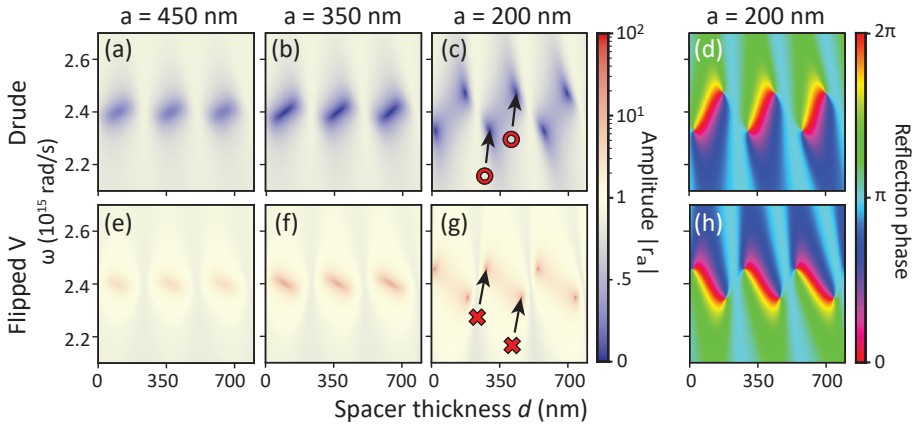

Figure 3.3: Transfer matrix calculations in (ω, d) space of an etalon with a regular Drude metasurface vs. its amplifying equivalent. (a-c) Reflectivity amplitude for metasurfaces of increasing particle density (decreasing square arrays of pitch a, listed as plot titles), assuming standard lossy plasmon particles. At $a = 200$ nm, absorption zeros around the plasmon resonance appear, two of which are pointed out with a red $\circ$ for clarity. In reflection phase ((d), referenced to same structure without particles) the pairs of zeros appear as phase singularities of opposite topological charge ± 1. (e-g) Response for the amplifying equivalent structure ($V \to -V$ in Eq. (3.2)). Amplification singularity pairs occur at $a = 200$ nm (indicated with $\times$). However, note that the response does not simply exchange loss for gain, as also the dispersion around ω_0 is inverted. Evaluated for $V = 3 \cdot 10^{-23}$ m^3 and Au mirror thickness 50 nm.

absorption. At $a = 200$ nm, the value of r_a has become large enough that points of perfect absorption occur. They arise in pairs, and coincide with singularities in the reflection phase shown in panel (d) (phase referenced to the phase pickup in absence of the particles). In the parameter space spanned by $\omega - d$, phase singularities arise in pairs of opposite charge ± 1, indicating a 2π phase increment over a (counter)clockwise loop around the singular points. These charges highlight the topological nature of the singularity conditions.

Next, we turn to the amplifying counterpart ($V \to -V$) in Fig. 3.3(e-h), the geometry of which is sketched in Fig. 3.1(b). At first glance, it appears that as loss is replaced by gain, the absorption features in reflection are replaced by enhanced reflection. At low antenna density, the reflectivity enhancement is modest (mimicking the finite absorption in panels (a,b)), while above a threshold antenna density, the gain metasurface etalon displays poles in reflectivity. These emerge as the counterparts of perfect absorption in (c), and likewise correspond to phase singularities (compare panel h and d). While qualitatively the results for gain are clearly analogous to the case of loss (points of singular behavior, arising in pairs, exchanging zeros for poles), there is one striking difference: For pairs of perfect absorption the red-shifted (blue-shifted) singularity appears for spacing larger (resp. smaller) than the etalon

condition, but in the case of gain this ordering is reversed. Associated with that, the phase map (h) is mirrored in the line $\omega = \omega_0$, meaning that for a given pair of singularities, not only the frequency ordering is flipped, but also the topological charges. This evidences that poles and zeros are not simply interchanged when going from a lossy polarizability to an equivalent gainy polarizability.

The explanation is that the entire polarizability flips sign, i.e., both the real and imaginary parts, as opposed to complex conjugating which is common in some branches of literature on amplifying nanophotonics, PT-symmetry and CPA-lasing [69, 95, 113–115, 120]. In the framework of the Salisbury screen, the approach $\gamma \to -\gamma$ (leading to an amplifying but unphysical polarizability) would interchange perfect absorption for perfect amplification points, *without* rearranging the location of the singularities in phase space. The fact that a correct gain dispersion also changes the real part of the response function is well-known in other fields, such as the field of anomalous dispersion in gain media [239, 240], where the effect is responsible for superluminal light propagation.

3.3.2 Gainy spacers in lossy etalons

Next, we explore systems that simultaneously have both gain and loss. A first system one could envision is a standard Salisbury screen (lossy plasmonic particles), but imbuing the spacer medium with gain. We study the dependence of the Salisbury screen response on the imaginary part of the refractive index of the glass spacer layer in Fig. 3.4, ignoring dispersion in the gain. As a starting point we take the case of Fig. 3.3(b): A Salisbury screen made with a plasmon lattice that is not quite dense enough to create points of perfect absorption if the spacer has neither gain nor loss (reproduced as panel Fig. 3.4(d)). To the left of panel (d), in panels (a-c) we consider increasing loss, and to the right in panels (e-g) increasing gain. Spacer loss/gain is modeled through a non-dispersive imaginary refractive index n'', while a constant $n' = 1.45$ defines the real part. For increasing spacer loss, we already notice for $n'' = 0.05$ that absorption singularity-pairs emerge. Their frequency separation increases with the amount of spacer loss (n'') and also with spacer thickness d. The latter effect is to be contrasted with Salisbury screens with lossless spacer: If there are singularities, they occur at all successive etalon orders and at identical frequencies, see Fig 3.3(c,d)). Turning to the case of gainy spacers in Fig 3.4(e-g), amplification singularities appear for $n'' = -0.15$. Amplification is strongest at the etalon resonance conditions, and pockets of absorption persist. It is obvious that zeros and poles cannot simply be interchanged when $n'' \to -n''$. Indeed, it is immediately obvious that there is no time-reversal symmetry when inverting the sign of n'' in the spacer while maintaining constant particle losses.

For standard plasmonic Salisbury screens, the topological origin of perfect

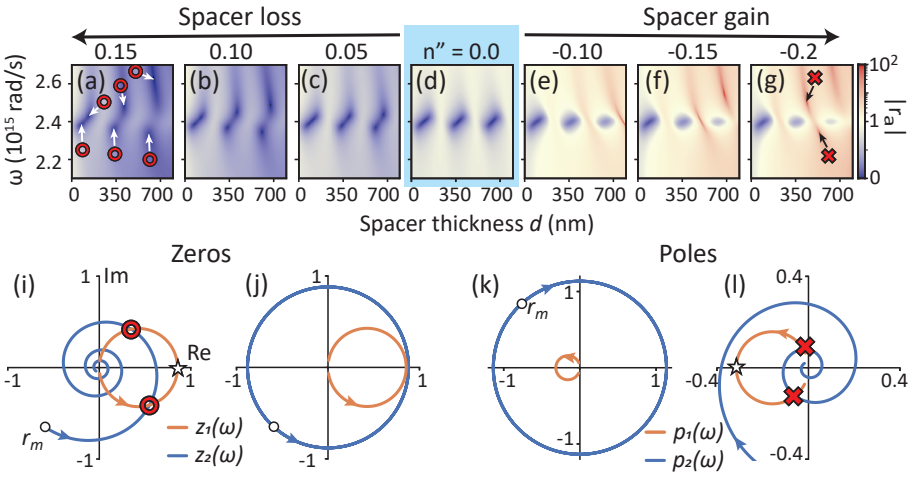

Figure 3.4: Response of metasurface etalons with non-dispersive loss or gain in the dielectric spacer. The metasurface comprises standard lossy plasmon antennas. (a-h) Evolution with increasing loss resp. gain of the reflection amplitude. The reference case $n'' = 0$ corresponds to panel (d). Absorption singularities appear for $n'' \geq 0.05$, and are highlighted in (a) with red ○. Reflection poles only appear for $n'' \leq -0.15$, indicated in (g) with red × for $n'' = -0.2$. (i-j) resp. (k-l) Complex-plane construction of conditions for reflection zeros resp. poles. Orange (blue) curves correspond to z_1 and p_1 (resp. z_2, p_2). Panel (i) shows how a spacer absorption of $n'' = 0.15$ generates intersections, i.e. perfect absorption points that do not exist (owing to insufficient antenna density, at the chosen $a = 350$ nm) in the case of zero spacer loss (panel j). Similarly, panel (l) shows the generation of amplification singularity conditions that only exist for sufficient spacer gain (here, $n'' = -0.2$). Evaluated for pitch $a = 350$ nm, $V = 3 \cdot 10^{-23}$ m^3 and Au mirror thickness 50 nm. Open black circles in (i,j) resp. (k,l) indicate r_m resp. $1/r_m$ (starting point of z_2 resp. p_2 at $d = 0$), while the asterisks indicate z_1 resp. p_1 at scatterer resonance $\omega = \omega_0$. Zeros and pole conditions are indicated by the red circles and crosses.

absorption points and the necessity for them to occur in pairs [121] can be explained by the simple Fabry-Perot interference model Eq. (3.10). This analysis generalizes to the zeros and poles of amplifying metasurface etalons. Zeros arise from the numerator, and occur when the complex-valued quantities

$$z_1(\omega) = \frac{-r_a(\omega)}{1 + 2r_a(\omega)} \quad \text{and} \quad z_2(\omega, d) = r_m e^{2ik(\omega)nd} \tag{3.11}$$

are equal. Complex functions $z_1(\omega)$ and $z_2(\omega, d)$ are plotted in Fig. 3.4(j) for a lossless spacer. The quantity z_1 is solely dependent on the metasurface. When sweeping frequency ω, z_1 traces a circle in the complex plane, starting at the origin for zero frequency, returning to it at infinite frequency, while reaching its point farthest from the origin when $\omega = \omega_0$, where z_1 intersects the real axis. The circle grows in radius with increasing oscillator strength V, reaching infinite radius when $r_a(\omega_0) = -1/2$. At even stronger scattering the circle appears on the other side of the imaginary axis. The quantity z_2 instead

does not depend on the metasurface, but only on the combination of spacer and mirror. For a lossless spacer, it simply traces out a circle in the complex plane of radius r_m centered on the origin, both as function of frequency ω, and as function of etalon spacing d. For the lossless example at hand, there is no crossing between z_1 (orange curve), and z_2 (blue curve) and thus no zero reflection points are expected. For somewhat larger oscillator strength (increased radius r_a), intersections will occur in pairs and are revisited when increasing the etalon thickness d for each revolution over the blue circle.

We now discuss the generalization to lossy spacers. While the metasurface term z_1 is left unchanged, the term z_2 now changes from a circle of radius r_m to a spiral that spirals inward as the radius decreases with frequency ω and etalon spacing d. One turn of the spiral is traversed when $n'k_0d$ corresponds to a 2π phase increment, while the change in radius per turn of the spiral is governed by n''. In panel (i), the spiral starts at the point r_m corresponding to just the mirror, and displays already the first round trip a first pair of intersections, while the second turn generates a second pair, etcetera. The intersections correspond to points of zero reflection: The frequency at which they occur can be read off from z_1, since each point on the orange circle corresponds to a unique frequency. The matched etalon spacing d can then be read off from z_2, since each point on z_2 corresponds to a unique value of the product ωd. The first two intersections with z_2 occur at frequencies comparatively close to the plasmon resonance. The intersections at the next higher etalon orders occur increasingly far from resonance. All these observations are in line with the transfer matrix calculations of panel (a). In the case of amplification, the spiral grows outwards, meaning that perfect absorption conditions do not occur.

A similar analysis can be made for poles in the reflectivity, for which we analyze the denominator of the Fabry-Perot interference formula. Setting the denominator to zero is equivalent to satisfying the condition $p_1(\omega) = p_2(\omega, d)$ for two complex valued quantities

$$p_1(\omega) = r_a(\omega) \quad \text{and} \quad p_2(\omega, d) = 1/(r_m e^{2ik(\omega)nd}), \tag{3.12}$$

where again p_1 only depends on the metasurface response, and p_2 only depends on the mirror and spacer. Now p_1 travels a clockwise circle in the complex plane with increasing frequency (panel k), centered on the negative real axis and touching the origin. Again, the furthest point of p_1 from the origin occurs at plasmon resonance. For $n'' = 0$, the term p_2 (a circle of radius $1/r_m$) has a much larger radius than p_1, and the system is very far from emergence of amplification singularities. As gain is introduced, the term p_2 turns from a circle into an inward spiral. This causes the occurrence of crossings, i.e., reflection poles. The large mismatch in radius between p_1 and p_2 means that significant gain or path length is required: In this example, crossings only occur at the second round trip. Higher-order intersections do occur, but only at points very far detuned from plasmon resonance, out of the frequency range considered in our plots. Again, all observations are in line

with the (ω, d) map in panel (h). To summarize, when the time-symmetry is explicitly broken, i.e., introducing loss/gain in the spacer while keeping plasmon losses unchanged, very different conditions for generating zeros and poles are predicted.

3.3.3 Both loss and gain in metasurfaces

We finally proceed to the scenario of metasurface etalons with lossless spacers and a loss-gain metasurface, modeled according to the model of Manjavacas, where the permittivity function reads $\epsilon(\omega) = \epsilon_{\text{Drude}}(\omega) + \chi_{\text{gain}}(\omega)$ [234]. Importantly, Re(α) does not immediately flip sign upon increasing population inversion (Fig. 3.2 g,h). We take antenna volumes $V = 2 \cdot 10^{-23}\text{m}^{-3}$ and assume the gain resonance ω_g to overlap with the plasmon resonance ω_0, and take a line width $\gamma_g = 0.01\omega_g$. Figure 3.5 considers dense ($a = 250$ nm, panels a-e) and dilute ($a = 400$ nm, panels f-j) lattices. For the dense lattice at hand, Figure 3.5(a) shows that in the absence of gain, absorption singularity pairs exist at frequencies quite far away from plasmon resonance. Increasing the gain parameter F brings the pairs closer to the resonance, until they disappear for $F = 0.4$. For the dilute lattice without gain, no absorption singularities exist (panel f), but as F increases (panels (g-j)), first two absorption singularities emerge (just below $F = 0.1$). They annihilate at $F = 0.3$, when two gain singularities have emerged. Again, we can explain the singularity behavior by searching for intersections of the functions z_1 and z_2 in panels (a-e) and pole functions p_1 and p_2 in panels (k-o), for zeros and poles respectively. While for the loss/gain spacer case the terms z_2 and p_2 (blue curves) were modified by loss/gain, now the changes occur in the metasurface terms z_1 and p_2 (orange curves).

Focusing on the absorption zeros, if one starts with the dilute metasurface, the circle generated by z_1 is too small to generate an intersection with the term z_2 (blue circle of radius r_m). Upon pumping, loss compensation causes the metasurface response z_1 to grow in radius, creating a pair of intersections (compare panels k,l,m). Optical gain thus causes pairs of reflection zeros that will occur at all etalon orders. For further increasing gain, the singularities disappear (panel n), owing to the fact that z_1 shrinks again. It should be noted that the sharp, non-trivial dispersion causes the z_1 locus to deviate from the circular shapes that occur for simple Lorentzian antennas. Turning to the occurrence of poles, one notices a similar evolution, with the locus of p_1 growing in radius in k, reaching a condition where two singularities originate in pairs (panel s), while the gain singularities disappear for even stronger pumping. For both the zero and pole construction, the trajectories of z_1 resp. p_1 change the orientation at which they cross through the real axis at critical F values. For the reflection zeros, this is associated with Re$[r_a]$ crossing the value $1/2$ (flipping the sign of z_1), while for the poles, this reversal occurs when Re$[r_a]$) changes sign, which happens when the metasurface by itself (in

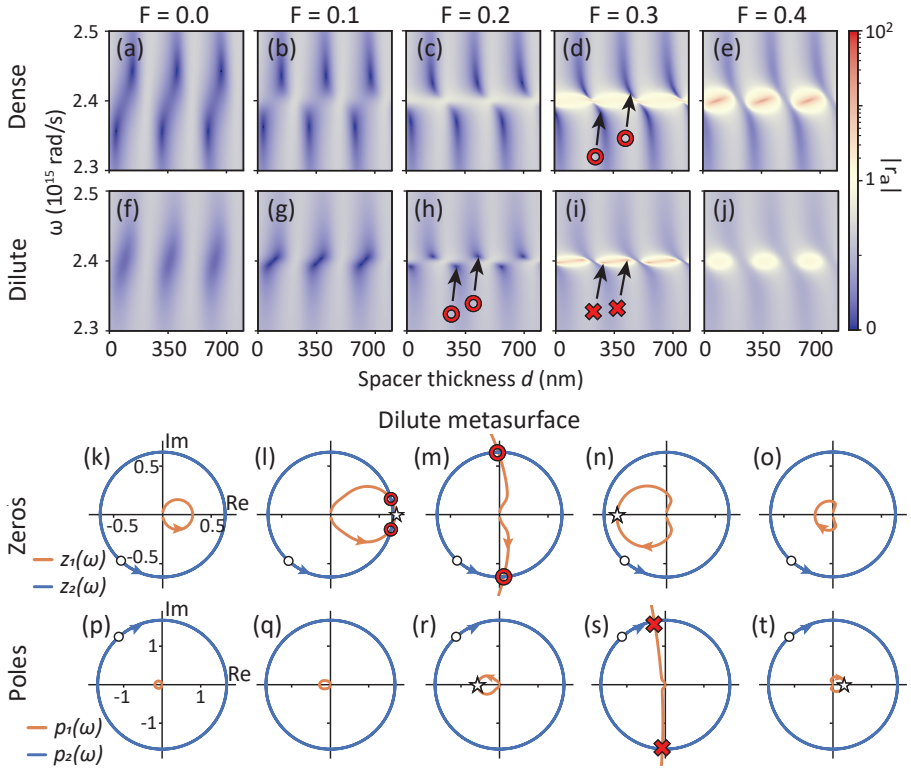

Figure 3.5: Response of metasurface etalons with gain-plasmon antennas, following the model of Manjavacas [234]. The spacer is lossless. (a-e) Reflectivity amplitude for a dense metasurface ($a = 250$ nm) as function of increasing gain parameter F. For $F = 0$ the absorption singularity pairs are far from the plasmon resonance. For increasing F the absorption singularities ○ approach the plasmon resonance ω_0, and ultimately disappear. (f-j) Reflectivity amplitude of a dilute metasurface etalon ($a = 400$nm), without absorption singularities in absence of gain. Absorption singularities are induced by gain (○ in panel h), and ultimately are replaced by amplification singularities at larger gain (× in panel i). (k-o) Geometrical construction in the complex plane for reflectivity zeros and poles. Orange (blue) curves correspond to z_1 and p_1 (resp. z_2, p_2). Intersections signify the occurrence of zeros (panel m) and poles (panel s). Evaluated for $V = 2 \cdot 10^{-23}$ m^3 and Au mirror thickness 20 nm. Open black circles in (k-o) resp. (p-t) indicate r_m resp. $1/r_m$ (starting point of z_2 resp. p_2 at $d = 0$), while the asterisks indicate z_1 resp. p_1 at scatterer resonance $\omega = \omega_0$. Zero and pole conditions are indicated by the red circles and crosses.

absence of the back reflector) goes through its gain singularity (Fig. 3.2(g)). In summary, in this type of metasurface etalon, the addition of gain can induce both perfect absorption points and amplification singularities. Singularities require a critical gain: They disappear both when gain is too low and when gain is too large.

For the system with loss and gain, one may wonder if zeros and poles can coexist – or even coalesce – in (ω, d) space. In Fig. 3.6, we focus on a small region in (ω, d) space, and very small increments of F around the emergence of gain singularities. For $F = 0.26$, the reflectivity amplitude plot (panel a) displays two perfect absorption points, as substantiated by the two oppositely charged phase singularities in the reflection phase (panel d). Here, z_1 and z_2 intersect, but not p_1 and p_2. When increasing gain only very slightly to $F = 0.27$, also p_1 intersects p_2 near resonance, and two amplification singularities co-exist together with the perfect absorption points (panels b, e). Another increment in gain pushes the gain singularities away from each other, while on a trajectory in between the gain singularities, the two absorption singularities approach and annihilate ($F = 0.28$, panels c,f). The co-existence of two types of singularities in parameter space is reminiscent of Ref. [220]. One can ask if this behavior is generic, or if one can construct conditions in which

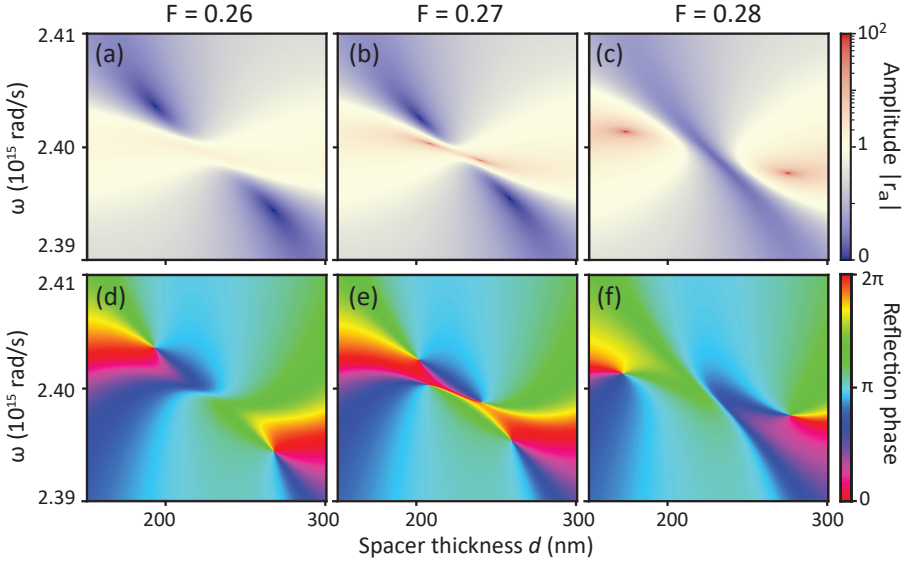

Figure 3.6: Birth and annihilation of absorption and amplification singularities. We consider the dilute ($a = 400$ nm) amplifying metasurface etalon of Fig. 3.5. (a-c) and (d-f) Reflection amplitude and phase in a small part of $\omega - d$ parameter space for small increments of gain F. At $F = 0.27$ (panel b,e), both absorption and gain singularities are present, while in panels (a,d) and (c,f) only zeros resp. only poles occur. Evaluated for $V = 2 \cdot 10^{-23}$ m^3 and Au mirror thickness 20 nm.

the creation of the amplification singularity pair exactly coincides with the annihilation of the absorption singularity pair. Mathematically, the poles and zeros can only exactly coincide in the case of an etalon with a perfect mirror $|r_m| = 1$, and when at the same time $r_a = -1$. The latter solution from Eq. (3.7) implies a static polarizability $\alpha_0(\omega) = \infty$, which requires not only the usual particle plasmon resonance condition ($Re[\epsilon(\omega) + 2\epsilon_{\text{host}}] = 0$) to be fulfilled, but also perfect compensation of the plasmon loss by the gain [251, 252]. While the perfect mirror condition can never be strictly achieved, for very high reflectivity mirrors and antenna's operated near the polarizability singularity condition, the zero and pole may approach each other very closely in parameter space.

3.4 Discussion

We analyzed the physics of absorption and amplification singularities in reflectivity (in (ω, d) space) of plasmonic metasurface etalons with amplifying constituents. Several observations stand out. First, replacing plasmon antennas with pure gain counterparts is not simply a time-reversal operation in which loss singularities become gain singularities. Two aspects are at play. First, for pure gain antennas not only the imaginary part of polarizability dispersion flips sign, but also the real part. Hence singularities appear at the same equivalent oscillator strenght ($|V|$), but not at the same $\omega - d$ combinations. Second, time-reversing a scattering experiment is generally not equivalent to swapping loss and gain rates, as radiation loss is not inverted in sign. A further set of peculiar observations is that (A) gain can induce perfect absorption, and (B) if gain induces poles in reflection, these conditions of singular reflection only occur at isolated (pairs of) $\omega - d$ points, (C) these generally do not persist indefinitely as gain is increased. The observation that one requires critical gain, and that *more* gain removes singular response, is reminiscent of the physics of critical coupling: Loss, gain, and coupling rates need to be all carefully matched to obtain singular response.

One has to acknowledge that in this conceptual theory work we have used gain parameters that cannot be readily obtained in optics (our values imply gain coefficients up to $g = 2 \cdot 10^4$ cm^{-1}). Nonetheless, we argue that the phenomena may be realizable in experiments. Firstly, high gain parameters can be achieved by, for instance, using perovskite quantum dots [69]. Perovskite Mie scatterers that demonstrate resonant net gain and room temperature lasing have been demonstrated in literature [253], which quotes $g = 3 \cdot 10^4$ cm^{-1} as material gain coefficient. Secondly, our model ignores near field enhancement effects that can increase gain. Lastly, one could envision using waveguiding geometries and local density of states enhancements to make better use of material gain. Indeed, these mechanisms are routinely used in plasmon lattice lasers that show modest lasing thresholds (mJ/cm^2) at material gain

coefficients $g \sim 100$ cm^{-2}. We thus envision that in such systems, just below lasing threshold, application possibilities could open up as amplitude and phase tunable metasurface pixels, where each amplifying metasurface etalon forms a single pixel. The possibility to bring the absorption and amplification singularity pairs extremely close to each other in parameter space, means this system can be actively tuned to switch between extreme amplitude enhancement and de-enhancement in a very small window of parameters (F, ω, d). An open question is what the actual experimental fingerprint will be if you address the reflection poles in experiment. We have evaluated a purely linear model which should break down at the reflection pole conditions: The actual description would need to include nonlinear effects such as gain dynamics, saturation and depletion of the gain, as well as noise [69]. Temporal pulse shaping in the spirit of *virtual gain* might sidestep some of these issues, by accessing the scattering matrix at frequencies away from the real axis [95, 254]. Also, the nonlinear dynamics could open interesting perspectives for these systems as nonlinear, or self-oscillating optical elements [255].

Chapter 4

Spontaneous symmetry breaking in plasmon lattice lasers

Spontaneous symmetry breaking (SSB) is key for our understanding of phase transitions and the spontaneous emergence of order. In this work, we report that for a two-dimensional (2D) periodic metasurface with gain, SSB occurs in the lasing transition. We study diffractive hexagonal plasmon nanoparticle lattices, where the K-points in momentum space provide two modes that are degenerate in frequency and identically distributed in space. Using femtosecond pulses to energize the gain medium, we simultaneously capture single-shot real-space and k-space images of laser emission. By combining k- and real-space, we resolve the two order parameters for which symmetry breaking simultaneously occurs: Spatial parity and U (1) (rotational) symmetry breaking, evident respectively as random relative mode amplitude and phase. The methodology reported in this work is generally applicable to 2D plasmonic and dielectric metasurfaces and opens numerous opportunities for the study of SSB and the emergence of spatial coherence in metaphotonics.

4.1 Introduction

In nature, there exist many physical systems that can spontaneously and abruptly evolve into an asymmetric state. This phenomenon of spontaneous symmetry breaking (SSB), is observed for instance in phase transitions, such as in the emergence of ferromagnetism, superfluidity, superconductivity, and Bose-Einstein condensation. In photonics, spontaneous symmetry breaking occurs for instance at the lasing transition, marked by the emergence of a randomly manifested phase, and in degenerate resonant systems imbued with gain or nonlinearity, where SSB expresses as a random imbalance in the population of the modes. SSB has recently been studied in evanescently coupled 'photonic molecule' nanocavities [256, 257], in microcavities with degeneracy between counter-propagating modes (whispering gallery mode systems), with either gain or a Kerr nonlinearity [258–264], and in exciton-polariton microcavities and microcavity lattices [265–268]. There is a large interest in understanding and harnessing the mechanisms of SSB in photonics. Firstly, this is because photonic systems are ideal to study SSB as a general phenomenon: Nonlinear photonic resonators allow to synthesize many dynamical nonlinear differential equations with SSB behavior, and in addition one can measure system response with high precision over many decades in time. Secondly, from the application viewpoint, SSB is envisioned as key to realizing ultra-small flip-flop optical memories, optically controllable circulators and isolators, and all-optical switching [263, 269, 270].

Plasmon lattice lasers are periodically arranged lattices of plasmon nanoparticles (antennas) embedded in a gain waveguide slab. Plasmon lattice lasers were first reported in 2003 [126] and have since then been studied extensively [30, 127–135, 143]. They are akin to distributed feedback (DFB) lasers [139], but the weak feedback mechanism of a dielectric Bragg grating is replaced by that of collective plasmon modes: The plasmon lattice enables long-range interactions (nanoparticle scattering cross-sections are often larger than the unit cell), and through diffractive resonances that are delocalized over the lattice, this system generates strong features in the frequency-momentum (ω-k) space. This type of nonlocal resonance originates from the field of plasmonic surface lattice resonances. Recent work generalizes this to the so-called nonlocal metasurfaces of *irregular* periodic arrays with collective modes [22]. The plasmon surface lattice resonances have high quality factors and strong plasmonic near fields. These unique properties provide strong feedback [30], exceptional robustness to disorder [130], and ultrafast gain dynamics [129]. In the plasmon lattice system, one can tailor the unit cell resonance (controlled by antenna size and shape) and lattice symmetry at will, providing opportunities to study plasmon versions of a rich family of tight-binding Hamiltonians, such as honeycomb and kagome lattices with topological properties [53, 63, 271], bound states in the continuum modes [272], and exceptional points [92]. These works fall into the broader context

of 2D photonic simulation systems of seminal Hamiltonians in solid-state physics: For instance, topological metasurfaces and photonic crystals can realize the quantum (spin) Hall effect [273] and active photonic lattices provide a route to study $\mathcal{PT}$-symmetry breaking physics [94] and topological lasing [137, 138, 186].

In this work, we demonstrate spontaneous symmetry breaking in hexagonal plasmon lattice lasers, using the intrinsic degeneracy of Bloch modes at the K-symmetry points in reciprocal space, which are defined as the corners of the first Brillouin zone. Lasing from these points has been reported before in photonic crystal and plasmonic lattice lasers [142, 143]. However, these works did not report spontaneous symmetry breaking. In our newly developed methodology, we use a pulsed femtosecond laser as pump to bring the system to lasing in every single shot, and we simultaneously perform real-space and Fourier-space microscopy to map the relative intensity and phase of the lasing modes from shot to shot. We uncover that this system concurrently shows parity symmetry breaking, observable in the direction of light emission, and rotational SSB, i.e. $U(1)$ symmetry breaking, observable as a random choice of relative phase between the lasing modes [274]. This behavior can be reproduced with a minimal density-matrix based dynamic model, showing that the SSB origin can be attributed to the inherently stochastic noise in spontaneous emission that initiates the lasing. While conventionally studied coupled microcavity systems [256, 257, 265–268] are ideal for two-mode coupling or optical simulators of nonlinear Hamiltonians with just nearest-neighbor interactions, metasurfaces provide an even richer design space to construct symmetries, mode degeneracies, and long-range interactions. The extended 2D nature of the lattice laser also means that one can go beyond mapping only overall mode populations: Our microscopy methods resolve spatial structure in the SSB, giving direct insight into the spatial structure of the spontaneously emerging coherence. Therefore, this work opens a rich venue for studying spontaneous symmetry breaking in nanophotonic metasurfaces.

4.2 Experimental approach

Fig. 4.1 illustrates our approach. We study hexagonal periodic lattices of plasmonic nanodisks (Ag, diameter 80 nm and height 30 nm) embedded in a polymer waveguide doped with a laser dye (fabrication described in Appendix Sec. 4.6.1). This layer acts both as a gain medium and as a planar waveguide with a single transverse electric (TE) and transverse magnetic (TM) mode. The dominantly in-plane nanoantenna polarizability makes this geometry especially favorable to TE-mode distributed feedback lasing. The 500 nm lattice pitch creates a K-point lasing condition near 580 nm wavelength. The 2D hexagonal lattice provides degeneracy at the K-point both in frequency and space. The Brillouin zone has six K-points that fall apart in two decoupled

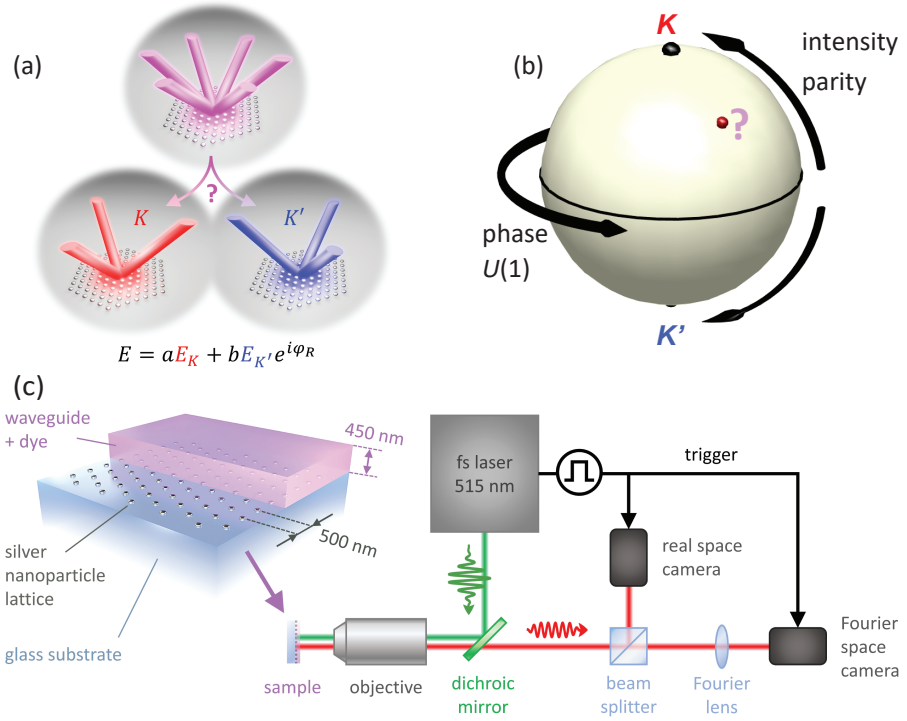

Figure 4.1: Single-shot microscopy retrieves relative intensity and phase of symmetry broken K and K' laser modes. (a) K-point lasing in hexagonal plasmon lattice lasers occurs on two decoupled modes, degenerate in frequency and space, and only differing in parity. Spontaneous symmetry breaking occurs in relative amplitude between the K and K'-mode (parity breaking), and in relative phase ($U(1)$ symmetry breaking). The phase space maps to the unit sphere (b), where the distance from the equator maps parity breaking, and the azimuth maps relative phase. (c) Plasmon lattices are embedded in a planar polymer waveguide with organic dye to provide gain. We study lasing in a high-NA microscope with single-shot real-space and Fourier-space imaging capabilities, synchronized to a 20 Hz train of pump pulses (515 nm, 250 fs).

sets (henceforth K and K' points), each consisting of three points that are internally connected by a reciprocal lattice vector. In a scalar description, at a given K-point, there exist three modes, two of which form a pair of doubly degenerate E-modes, and one is the remaining A_1 mode, which is the only mode that forms a flat band [49] required for lasing. While group theory is more involved for polarized waves, the first order TE waveguide mode still has the same separation into a degenerate doublet and one flat band [275]. The K and K' flat band modes are not only frequency-degenerate but also their local fields $E_{K,K'}(\mathbf{r})$ are exactly identical in terms of energy density ($|E_K(\mathbf{r})|^2 = |E_{K'}(\mathbf{r})|^2$). The only difference is in the mirrored wavevector content. This offers the condition for spontaneous parity symmetry breaking:

Lasing just on the K, or just on the K' condition will correspond to three instead of six far-field output spots, with mirrored orientation (Fig. 4.1(a)). Lasing of both modes in some superposition will furthermore imply the spontaneous emergence of a random relative phase φ_R, breaking $U(1)$ symmetry [67]. In this work, we visualize the phase space for such SSB on the unit sphere (Fig. 4.1(b)): Moving away from the equator represents parity breaking (pure K and K' lasing at the north and south pole respectively), while azimuth represents the relative phase.

To map the symmetry breaking both in intensity parity and in phase, we employ our newly developed simultaneous single-shot real- and Fourier-space microscopy method (Fig. 4.1(c)). The samples are pumped by 250 fs pulses at 515 nm wavelength. Emission collected by a high-NA microscope objective is split in two optical tracks, each with a camera synchronized with the 20 Hz laser pulse train. By imaging real-space in one track, while inserting a Fourier lens in the other, we obtain statistics to correlate Fourier-space and real-space output over long sequences of single-shot experiments. To assess the dispersion relation underlying the laser behavior, we collect photoluminescence (PL) enhancement Fourier and dispersion images (Figs. 5.2(a, b)) by pumping at low fluence yet high repetition rate (1 MHz). We refer to Appendix Sec. 4.6.2 for more details. The PL enhancement Fourier image (Fig. 5.2(a)) shows that exactly three circular bands cross at each K-point. These bands are the 2D slab waveguide modes folded by the lattice periodicity [10]. The intersections are also clearly visible in the dispersion (Fig. 5.2(b)). The three-fold degeneracy is consistent with the fact that K-point lasing corresponds to feedback on three reciprocal lattice vectors G that form a closed triangular loop [142]. The dispersion image, taken by projecting the $k_x = 0$ slice of the Fourier image on the entrance slit of a spectrometer, samples one of the K'-points (negative k_y), and one of the K-points (positive k_y), at an energy of 2.15 eV. From the dispersion image, we estimate the quality factor of the diffractive surface lattice resonance near the K-point as Q = 120.

To measure lasing, we operate in single-shot mode. Increasing the pump pulse energy leads to a sudden nonlinear increase in output power at the K-points, together with a very clear spectral narrowing (Figs. 4.2(e,f)). The thresholds of 1 mJ/cm^2 (50 nJ pulse energy) are consistent with earlier works on plasmon lattice lasing [30, 132, 143]. Fourier images integrated over many shots (Fig. 4.2(c)) distinctly show six high-intensity spots at the K-points. Importantly, each spot has a doughnut shape, reflecting the fact that the lasing mode is prevented from radiating directly into the far-field due to its symmetry (a dark mode). This effect is known as a symmetry-protected optical bound state in the continuum (BIC) [160], where the DFB laser will choose as laser condition the band edge of lowest loss, which is the band that is dark precisely at the K-point, as opposed to a radiatively damped band. While this is a BIC in the infinite lattice, lasing will in fact occur over a finite spatial

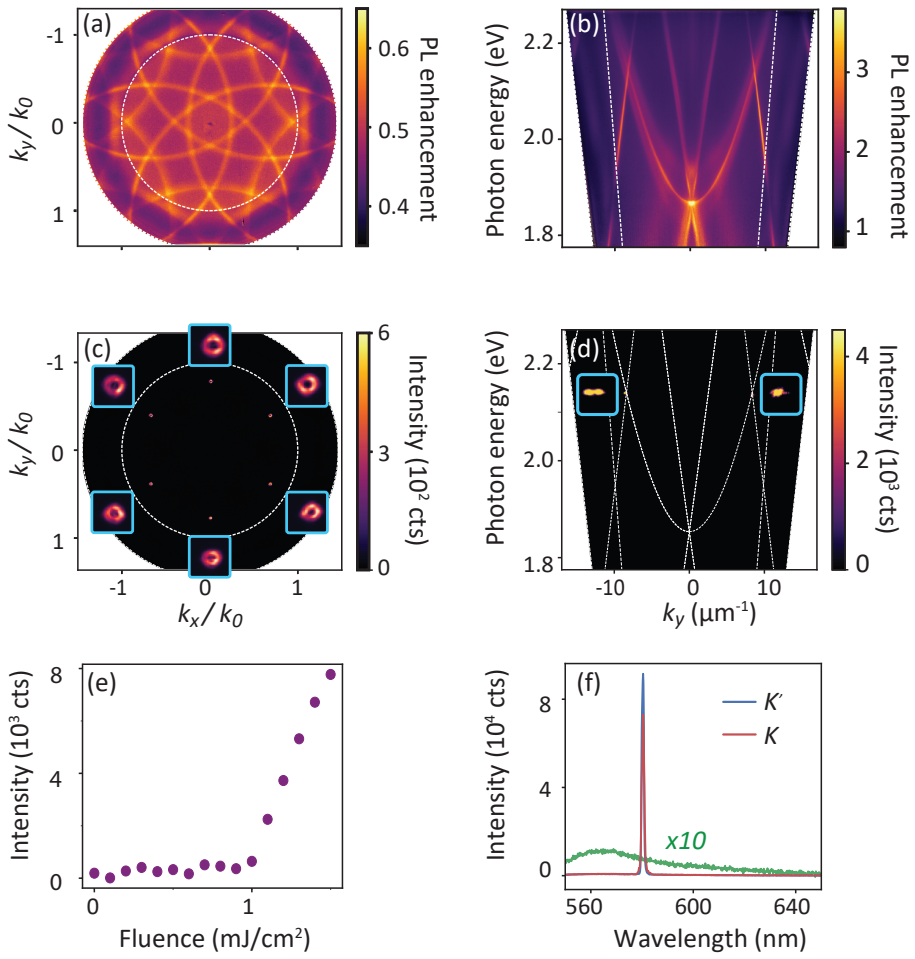

Figure 4.2: K-point lasing averaged over multiple laser shots. (a) Fourier image of photoluminescence (PL) shows the isofrequency contours of the guided mode dispersion curves that are repeated in the momentum space due to periodicity (below lasing threshold). Threeway crossings just within the NA $= 1$ circle (dashed) correspond to the K-points. (b) Below threshold PL band structure showing K-point intersections at $\hbar\omega = 2.15$ eV. (c) Above-threshold Fourier image showing lasing at the six K-points in Fourier-space, with $5\times$ enlarged beam spots as insets (averaged over 150 shots). The beam spots are doughnut-shaped due to the quasi-BIC nature of the lasing condition. (d) Lasing at the K-points in the dispersion image (six shots summed), with calculated free photon lines (insets show enlarged lasing spots). (e) Input-output power curve. (f) Above threshold, the broad fluorescence spectrum (green curve) narrows to two sharp lasing peaks. The pump fluence of the lasing spectra is $3\times$ larger than the threshold fluence. The emission wavelengths at K- and K'-points are identical.

envelope. This translates into a finite-width wave vector content around the K-points [145–147]. In current nomenclature in the field, this is considered a quasi-BIC, where the finite extent opens the BIC to radiation [31, 160]. Lastly, the dispersion image for lasing is shown in Fig. 4.2(d). Two intensity peaks from lasing, at the K- and K'-point, occur at the same wavelength (Fig. 4.2(f)), highlighting the frequency degeneracy that the hexagonal lattice symmetry guarantees for K/K' modes. The imbalance in intensity between the two spectra is due to experimental reasons which are explained in Sec. 4.6.4.

4.3 Spontaneous symmetry breaking in single-shot results

Spontaneous symmetry breaking in parity is directly evident in sequences of single-shot Fourier images. Figure 4.3(a-d) show four single-shot images taken from a run of several hundred laser shots. For each of the six K-point lasing spots, we observe very large shot-to-shot differences in intensity. Figs. 4.3(a,b,c) show three directly subsequent shots, in the first of which both K- and K'-points appear equally bright, while the next frame has hardly any K'-point emission (only three lasing spots at the K-points). The opposite, parity breaking entirely towards K' lasing, is evident in Fig. 4.3(d). In the entire data sequence, no spot patterns occur *except* linear superpositions of the K and K' triplets. Given the observation that the lasing output is intermittent with a different intensity ratio of K and K' modes in each shot, a relevant question is what the relative *phase* between the two modes is in a given realization, and how that phase is statistically distributed over all shots. Since, in the Fourier-space, the K and K' modes have no overlap, Fourier imaging can not reveal relative phase. However, the relative phase can be determined from single-shot real-space images, which we acquire simultaneously with Fourier images. Upon crossing the lasing threshold, the real-space appearance of the sample transitions from the diffuse glow of fluorescence to a structured speckled pattern that directly evidences the emergence of both spatial and temporal coherence [130]. Fig. 4.3(e) shows a typical single-shot real-space image over an area of 44×44 μm^2, while Fig. 4.3(f) shows the sum over many laser shots. In both results, the hexagonal lattice symmetry is visible. However, 2D Fourier transforms (insets) reveal a marked difference. The ensemble-averaged image *only* shows Fourier components commensurate with the lattice of particles (six sharp peaks in the Fourier-transformed images). The single-shot image instead shows additional spatial structure, evident as a 6-tuple of Fourier peaks at wave vectors *shorter* by a factor $\sqrt{3}$. These peaks point towards the emergence of *longer* range periodicities. Motivated by this observation, we apply Fourier-domain filtering (explained in Appendix Sec. 4.6.7) and examine close-ups of Fourier-filtered real-space data. Figs. 4.3(g-j) correspond directly to the

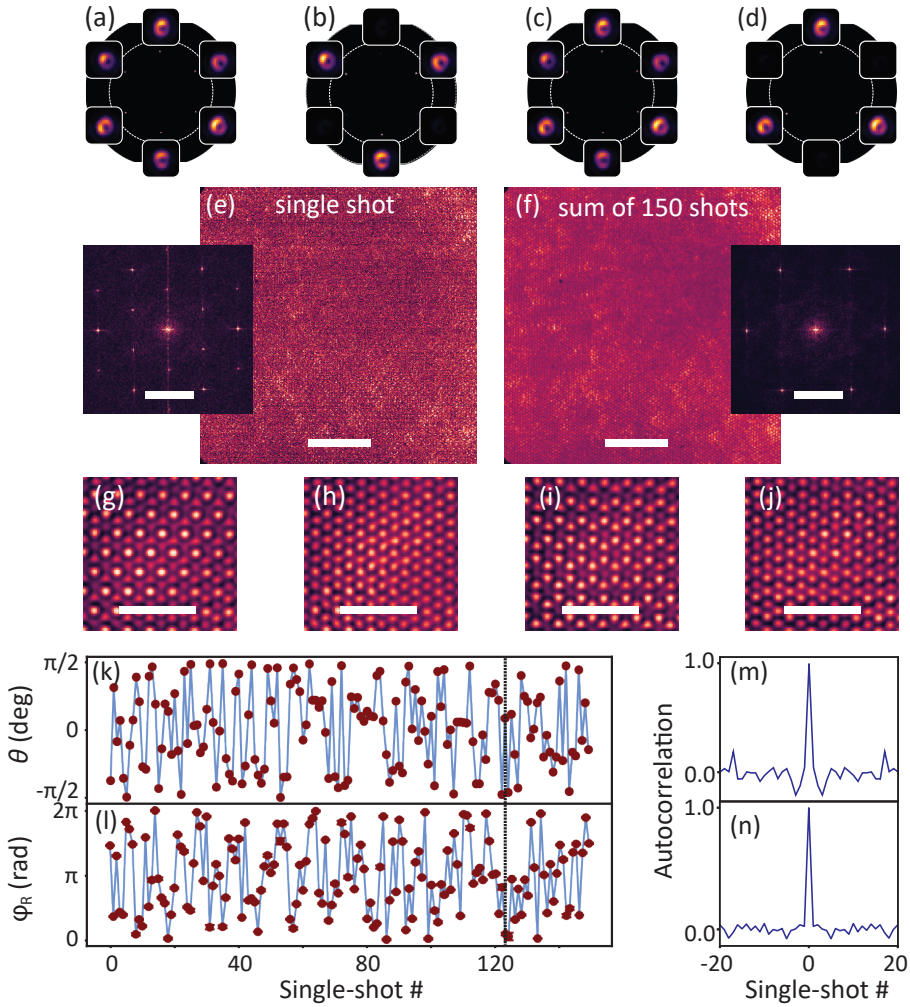

Figure 4.3: Single-shot K-point lasing and SSB in Fourier- and real-space. (a-d) Single-shot Fourier images taken from a single experiment run. Shots 1-3 (a-c) are directly subsequent to each other. (b,d) show parity breaking towards pure K/K'-point lasing, while (a,c) show cases of equal superposition. (e) Single-shot and ensemble-averaged real-space images (scale bar: 10 µm). Insets show 2D Fourier transforms (scale bar: 10 μm^{-1}). (g-j) Fourier-filtered close-ups of the real-space images (scale bar: 3 µm), corresponding to the Fourier images (a-b). (k,l) Sequence of relative amplitude (parity-breaking) and phase ($U(1)$ symmetry breaking) for a 150-shot data sequence. The dashed line highlights the location of shots (a,b,c). (m,n) Temporal autocorrelations of the data in (k,l). The traces are taken at 1.8 mJ/cm^2 pump power.

single-shot Fourier images in Figs. 4.3(a-d). Whenever only K (shot 2) or only K' (shot 4) lasing occurs, the intensity patterns are simply hexagonal with periodicity identical to the particle lattice. In stark contrast, when both K- and K'-points substantially lase (shots 1 and 3), we observe a honeycomb supercell pattern. Moreover, while shots 1 and 3 have very similar Fourier images, the spatial patterns are distinct: The shot 3 honeycomb pattern is clearly shifted horizontally and vertically compared to shot 1. This variation in spatial pattern encodes the random relative phase between K- and K'-point lasing.

To explain how we retrieve relative phase from real-space images, we consider a simple scalar coupled-mode model for $K\,/\,K'$-point Bloch modes [276, 277]. The A_1 mode at the K-point is a coherent superposition of three plane waves of identical amplitude and phase, with in-plane momentum given by the three K-points,

$$E_K(\mathbf{r}) = e^{i\mathbf{K_1}\cdot\mathbf{r}} + e^{i\mathbf{K_2}\cdot\mathbf{r}} + e^{i\mathbf{K_3}\cdot\mathbf{r}} \tag{4.1}$$

The K' field is described by the same equation but substituting the K'-points as in-plane momenta. For both of these modes individually, the local intensity distributions correspond to identical simple hexagonal patterns with peak intensities at the lattice positions. However, for superpositions $E_T(\mathbf{r}) = aE_K(\mathbf{r}) + bE_{K'}(\mathbf{r})e^{i\varphi_\mathrm{R}}$ the intensity distributions acquire a superlattice periodicity that is $\sqrt{3}$ times larger than the original lattice pitch. The relative amplitudes a and b affect the contrast, but not the topology of these honeycomb intensity patterns. The alignment of the superlattice intensity pattern relative to the underlying particle lattice depends on the relative phase φ_R (see Appendix Sec. 4.6.6 for a plot catalog). The simple coupled-mode model qualitatively rationalizes all our observations, namely: (i) Whenever lasing is purely on the K- or K'-point (shots 2 and 3), the intensity distribution is simply hexagonal. The real-space intensity distributions are identical, even though the far-field directions of lasing emission are mirrored; (ii) honeycomb patterns occur when K and K' modes both lase, and the observed spatial shift from frame to frame can be understood as shot-to-shot variations in relative phase φ_R (shots 1 and 4 in Fig. 4.3); (iii) the incoherent sum over all frames washes out this interference and is simply hexagonal (Fig. 4.3(f)). To extract the relative phase φ_R for each laser shot, we take a small section of the real-space data (as selected for Figs. 4.3(g-j)) and fit the coupled mode model, where the relative amplitude is not a free parameter, but fixed by the Fourier images (see Sec. 4.6.7 for methodology).

Figs. 4.3(k,l) report on the extracted fluctuations in parity-breaking ($K\,/\,K'$ contrast) and relative phase (random phase) in a typical measurement run. In line with Fig. 4.1(b), we quantify the $K\,/\,K'$ intensity contrast as an angle θ defined for intensity I_K in the K modes and $I_{K'}$ in the K' modes as $\tan\theta/2 = (I_K - I_{K'})/(I_K + I_{K'})$. From the time traces we conclude that both the intensity ratio and relative phase manifest randomly and independently from shot to

shot. The normalized temporal autocorrelations (Figs. 4.3(m,n)) for both the K/K' intensity ratio and the relative phase φ_{R} show no correlation beyond $\Delta n = 0$. This observation is consistent with the notion that the symmetry breaking is not from any *explicit/geometric* symmetry breaking, but is purely *spontaneous:* It arises from the inherently stochastic fluctuations in the spontaneous emission seed that initiates lasing. In the system at hand, beyond simply being degenerate in spectrum and energy density $|E_K(\mathbf{r})|^2$, the K and K' modes are even fully identical up to complex conjugation $E_K(\mathbf{r}) = E_{K'}(\mathbf{r})^*$, physically meaning time reversal. This means that overlap integrals $< f|\Delta|f >$ with geometric perturbations, say in dielectric constant $\Delta\epsilon$, waveguide height Δh, or particle polarizability $\Delta\alpha$, tend to be identical for both modes, especially for predominantly real-valued perturbations. These degeneracies imply robustness against geometric disorder in the sample and pump field. For instance, in our experiment we were unable to impart explicit symmetry breaking with linear pump polarization, even though the pump field does have near field hot spots that rotate with input polarization. To conclude, this system shows pure spontaneous symmetry breaking, which is a result of its inherent protection from explicit symmetry breaking caused by an inhomogeneous gain distribution. Therefore, we argue that this system stands out as a platform for exploring SSB in the lasing transition, as compared with systems that do not enjoy this protection (for instance, coupled cavity lasers [256]).

4.4 Order parameter visualization

To visualize how the SSB order parameters of this plasmon lattice laser sample phase space, we consider the distribution of the intensity contrast parameter θ and the phase φ_{R} in Fig. 4.4. For a run of 900 shots, we place each shot on the unit sphere in Fig. 4.4(a), while Fig. 4.4(b) and (c) report histogrammed results for each parameter individually. With regards to the parity breaking, we construct a histogram by a projection method that not only takes into account the K/K' contrast, but that also reports on whether spot patterns are strict superpositions of just K/K' lasing (see Sec. 4.6.3). In short, Fig. 4.4(b) reads as follows: If all six lasing spots are equally bright, then $c_+ = 1$ and $c_- = 0$. If instead lasing emission is just in the K (resp. K') directions, then $c_+ = \pm c_- = \sqrt{2}$. Any other linear combination of pure K- and K'-point lasing will result in a plot coordinate on the circular arc connecting these extremes and at angle $\theta/2$ relative to the x-axis. Finally, any hypothetical intensity pattern that is *not* a linear superposition of K- and K'-point lasing (e.g., if just a single laser spot would appear) will result in a coordinate interior to the circular arc. The histogram evidences that no such patterns occur, verifying that all laser shots are true linear combinations of K- and K'-point lasing. Analysis as function of pump power (see Appendix Sec.4.6.5) shows that the

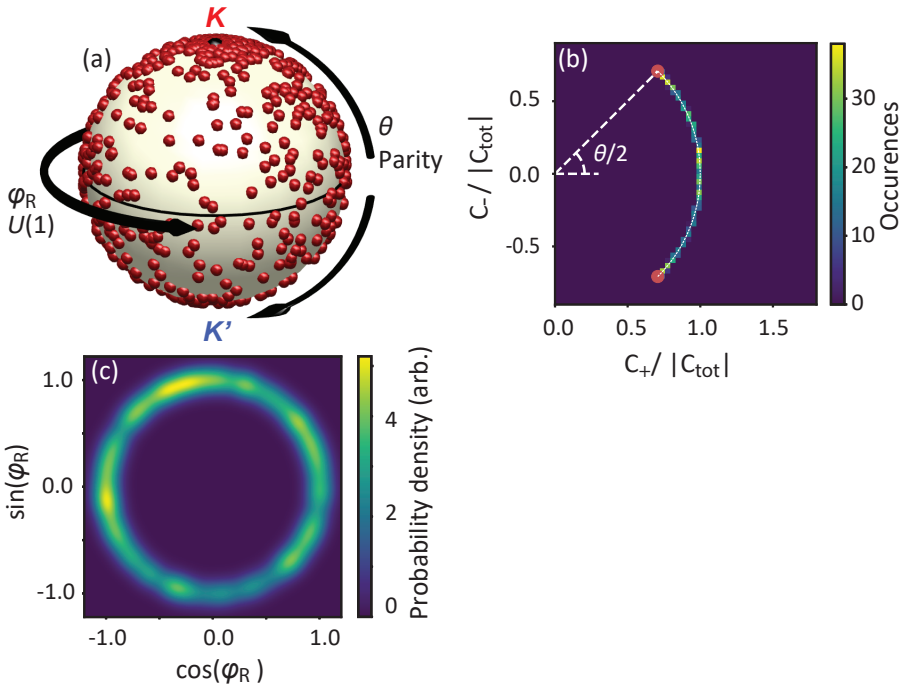

Figure 4.4: SSB order parameters θ and φ_R, mapped onto the surface of a unit sphere. (a) SSB phase space samples in a 900-shot measurement run. Each shot is plotted as a data point on the unit sphere according to its relative phase (azimuth φ_R) and relative amplitude (parity breaking, distance θ from equator). (b,c) Histograms of the parity breaking θ and random phase φ_R.

histogram is identical irrespective of how high above threshold one operates. To test whether the variation in contrast θ samples the entire interval from $-\pi/2$ to $\pi/2$ uniformly, we subject this dataset to the Kolmogorov-Smirnov (KS) test to find if the data is likely drawn from a uniform distribution. For the 150 long dataset taken at the highest power (1.8 mJ/cm2), we calculate a KS value of 0.054, evidencing that the null hypothesis at $\alpha = 5\%$ holds. While some runs marginally fail the test at this level of strictness, we view that, quantitatively, the data is in good accord with a uniform distribution in θ. For details we refer to Sec. 4.6.9.

This expression of symmetry breaking is comparable to recent results on orbital angular momentum microlasers [264], and different from the more usually reported bistability in which a system switches randomly to just one of the initially degenerate modes [256, 257]. One can ask if this difference arises from the pulsed nature of our experiment, as previous studies on bistability either used quasi-CW conditions, or pulses substantially longer than the intrinsic gain dynamics. To verify if the pumping conditions affect the

observed SSB character, we repeated the experiments with 500 ps instead of 250 fs pulses. These pulses are longer than the picosecond time scales associated with distributed feedback laser dynamics. Despite pumping the system with such long pulses, we observe the same continuous histogram. Furthermore, the fact that the real-space maps encode the relative phase rules out the possibility of rapid switching between the K and K' lasing within a single shot. Turning to the phase, Fig. 4.4(c) plots the probability density for observing $(\cos\varphi_{\mathrm{R}}, \sin\varphi_{\mathrm{R}})$. The relative phase between the K and K' is 'picked' randomly as expected for $U(1)$ symmetry breaking, where a system's phase evolves as a second order phase transition from a highly symmetric (spontaneous emission) to locking in a single phase above lasing threshold [67, 274]. We also subject the φ_{R} data to the KS test and we find that it generally passes the null hypothesis for strictness $\alpha = 5\%$. Finally, we note that breaking the parity symmetry and $U(1)$ symmetry lead to uncorrelated choices in θ and φ_{R} on the unit sphere. Although the data on the sphere suggests an accumulation of points close to the poles, this does not mean θ is biased: Drawing θ and φ_{R} independently and uniformly is not equivalent to picking points uniformly over the unit sphere (due to the $\sin\theta$ Jacobian).

One can substantiate some main aspects of the observed spontaneous symmetry breaking in a simple dynamic model that is based on a density matrix formalism developed by Ref. [186] for plasmon lattice lasing, adapted to the lattice symmetry at hand. The ingredients of this minimal model are parameters for the gain dynamics of the medium, the symmetry of k-space modes, the $|E_K(\mathbf{r})|^2 = |E_{K'}(\mathbf{r})|^2$ degeneracy, and, finally, seeding of the dynamics by amplitude and phase noise terms. Since this density matrix model was implemented by R. Kolkowski, it is not reported on further in this thesis. We refer to the supplement of Ref. [255] for the implementation and results of this model, with parameters pertinent to our experiment.

4.5 Discussion

In summary, we observe spontaneous symmetry breaking in K-point plasmon lattice lasers, where the symmetry is broken both in relative amplitude and phase between the two (K and K') lasing modes. The SSB in intensity implies a breaking of parity symmetry, while the SSB in phase is a $U(1)$ symmetry breaking. A key aspect of our work is the methodology of simultaneous single-shot Fourier- and real-space imaging, which should be contrasted to the earlier time-averaged measurements. This methodology is generally applicable to a large library of metasurface lasers with photonic lattice systems in which one can design symmetries and degeneracies at will (e.g., honeycomb, kagome lattices, topological photonic crystals) [53, 110, 134, 160]. Therefore, our work opens important new opportunities in the study of spontaneous symmetry breaking and emergence of spatial coherence.

An example of the important role of symmetry and degeneracy can already be seen in hexagonal lattices, where one can compare M-point and K-point lasing [144]. For K-point lasing, the lattice symmetry rigorously guarantees that modes are exactly co-localized in space and exactly degenerate in energy. M-point lasing is also associated to six output spots, but instead arises from three distinct modes, each engaging two M-points. These modes are degenerate in frequency, but distinct in space. Consequently, in the M-point laser, we observe three-way spontaneous symmetry breaking that is easily turned into explicit symmetry breaking by changing the pump field polarization and thereby the mode overlap with the near-field gain distribution. In this way, we can force lasing in just one out of the three modes. In contrast, we were unable to coerce K-point lasing into either the K or K' mode by changing pump geometry, reflecting the profound protection that the time reversed modes experience against explicitly imparted disorder.

Another important perspective is to study the spontaneous emergence of coherence in space. Our methods image spatial variations of the order parameters: A degree of freedom that is not present in simple coupled cavity realizations of SSB. In the reported experiment, we can for instance fit real-space patterns in boxes of just a few unit cells, and thereby assemble phase maps over the full microscope field of view (see Appendix Sec. 4.6.8). In our system, such maps show mean-squared phase excursions of order 0.2 radians relative to the randomly chosen mean phase, with spatial correlation lengths that are of order 5 μm. While the precise microscopic origin is out of the scope of this Chapter, these variations in part report on slight geometrical sample variations and in part arise from the distributed feedback lasing physics. According to Kogelnik and Shank [140], even almost index-matched polymer distributed feedback lasers show a rich spatial structure that is determined by interplay of the system band structure, the balance between gain, loss, and overall laser size [132]. It is completely open how spontaneous symmetry breaking in (nonlocal) DFB laser systems generalizes to the rich variety of nonlocal photonic systems that are currently emerging, encompassing plasmonic and dielectric metasurface lasers, photonic crystal lasers, quasi-bound state in the continuum, and topological lasers, as well as systems that show photon or exciton-polariton Bose-Einstein condensate physics [31, 136, 153, 265]. Overall, our results demonstrate a practical route to quantifying the emergence of coherence in this entire array of photonic systems. Related to the above, the collective nonlocal resonances that are typical of the plasmon lattice laser turn out to be a cornerstone in the field of nonlocal metasurfaces [22]. Therefore, we envision that our methods directly apply to this field, and we foresee interesting possibilities for spatially extended manipulation of the symmetry breaking in irregular periodic arrays.

Finally, spontaneous symmetry breaking in photonics can be associated with various applications. SSB in metasurfaces can be continuously distributed in intensity, as in this work, or can be multistable with two

or more fixed points in phase space. Also our observation that M-point lasers with SBB can be biased at will by pump polarization (as opposed to K-point lasers), shows that the multi-stability can be externally controlled. Such controllable bi- and multi-stability is a potential resource for photonic flip-flop memories. Lasers with chaotic output are also pursued as potentially high-bit rate, or triggerable, hardware random number generators [278]. In this spirit, one can also envision SSB in metasurfaces as a resource for spiking artificial neural networks. Finally, we view the methods developed in our work as laying the foundations for exploration of broken time symmetries, phase transitions, and handedness selectivity in metasurfaces coupled to active matter, such as gain media, 2D materials with valleytronic degrees of freedom, and in scenarios of strong coupling with excitons.

4.6 Appendix

4.6.1 Sample fabrication

We use 170 μm thick microscope cover slips (Menzel) as substrates. A 150 nm layer of PMMA is deposited on the substrate by spin-coating after cleaning them with base piranha. Then, we cover the PMMA with a thermally evaporated layer of 20 nm Ge, which acts as an etch mask for reactive ion etching after resist development. Over the Ge layer, we spin-coat a 65 nm layer of positive CSAR resist in which we write the structures using electron beam lithography (approximate dose of 130 $\mu C/cm^2$). The pattern is a hexagonal lattice of 500 nm period, consisting of 80 nm diameter particles. After exposure, we develop the samples for 60 s in pentyl-acetate, 6 s in O-xylene and finally 15 s in MIBK:IPA (9:1). We then etch through the Ge and PMMA layer by reactive ion etching. Finally, we evaporate a 30 nm Ag layer on the sample, and perform lift-off in a 60 °C acetone bath. This three-layer recipe from [121] has the benefit of a high resolution, defined by the thin CSAR layer, and yet a thick resist stack with high undercut for the lift-off. After fabrication of the plasmon lattice, we spin-coat a 450 nm thick layer of SU8 doped with rhodamine 6G (10 mg Rh6G in 3 mL cyclopentanone mixed with 1 mL SU8, or 0.5 wt% Rh6G) on the sample, as in [30]. The polymer refractive index is estimated at 1.6, leading to a waveguide mode index of 1.55. On basis of variable-stripe-length measurements on unpatterned films we estimate gain coefficients from 20 to 80 cm^{-1} over the relevant pump power range.

4.6.2 Optical setup

As the light source for pumping our plasmon lattice laser, we use the frequency-doubled output from a Light Conversion Pharos laser, providing 515 nm wavelength and 250 fs pulse duration. The electronic signal of the internal pulse picker is used to drive single-shot camera measurements. We direct the pump light through an epilens and a microscope objective (Nikon CFI Plan Apochromat lambda 100×, NA = 1.45), to obtain a 70 μm diameter collinear beam in the sample plane. The pump power is controlled by a motorized half-wave plate placed before a linear polarizer. The pump is filtered by a combination of a 532 nm dichroic mirror and a 550 nm longpass

filter. We image the sample plane with the same objective onto a camera chip (Bassler acA1920-40um) for real-space imaging. A beam-splitter directs 50 % of the light to another camera (Thorlabs CS2100M-USB) for Fourier-space imaging; in this track, we placed a Fourier lens in focus with the back focal plane of the objective via a 1:1 telescope. For spectrally resolved Fourier images (i.e, band structures), we direct the Fourier image through the entrance slit of a spectrometer (Andor Shamrock 163i), to which we mounted a camera (Ximea MC124MG-SY-UB). For single-shot lasing experiments, we use a repetition rate of 20 Hz, and synchronize both the Basler and Thorlabs camera to the laser, to enable simultaneous single-shot imaging in real-space and in Fourier-space. To obtain band diagrams in (k_x, k_y) space or in (ω, k_y) space, we operate in multi-shot mode with a repetition rate of 1 MHz and at low incident pulse power, thereby collecting below-threshold fluorescence. For the Fourier images below threshold, we insert a 550 nm (40 nm) bandpass filter, to select a narrow band of emission wavelengths near the lasing conditions.

4.6.3 K-point basis projection method

We convert the sequence of images into a time series of integrated intensities at each of the 6 lasing output spots, obtained by summing regions of interest (20 pixels across) around each spot. Having reduced the intensity information in the images to a vector of six intensities for each frame, we determine the projection of this 6-vector onto the subspace of lasing in superpositions of the K and the K' modes. Let I_N be the 6-vector of intensities in frame N normalized to be of unit length, where the vector elements list intensities in the consecutive K-points enumerated in clockwise order, starting from the top spot. We determine the coefficients $c_{N,+} = \langle I_N | v_+ \rangle$ and $c_{N,-} = \langle I_N | v_- \rangle$, where $v_\pm = 1/\sqrt{6}(1, \pm 1, 1, \pm 1, 1, \pm 1)$, and $\langle . | \rangle$ stands for the inner product. We normalize to $\langle I_N | I_N \rangle$. The normalized temporal autocorrelation for a parameter x is defined as $\mathrm{Mean}[(x(n+\Delta n) - \bar{x})(x(n) - \bar{x})]/\mathrm{Var}[x]$ where Δn refers to comparing the time series at Δn shots apart.

4.6.4 Spectrum of the lasing mode

The K and K' modes both form a set of three k-space points that are coupled by a reciprocal lattice vector. There exist no lattice vectors that could couple K into K' and vice versa, which ensures the energy degeneracy between modes that live at the K/K'-points. In essence, the energy degeneracy is thus a result of Bloch's theorem. Figure 4.5(b) further evidences this degeneracy. While Fig. 4.2(f) in the main manuscript shows the spectra taken in Fourier space, separating out K and K', Fig. 4.5(b)) shows spatially resolved spectroscopy, obtained by projecting a slice of the real space image onto the spectrometer slit. The spectral image is not corrected for imaging artifacts in the Andor spectrometer, and therefore there is a slight curvature in the result. Along the entire length of the field of view that is imaged (circa 44 μm) there is only a single lasing line.

What is more, we wish to explain the origin of the intensity imbalance between the spectra of K and K', seen in Fig. 4.2(f) in the main text. The imbalance has no relation to a global preference of the laser for a particular mode but is due to a trivial experimental reason: slicing k-space with a narrow spectrometer slit can lead to an

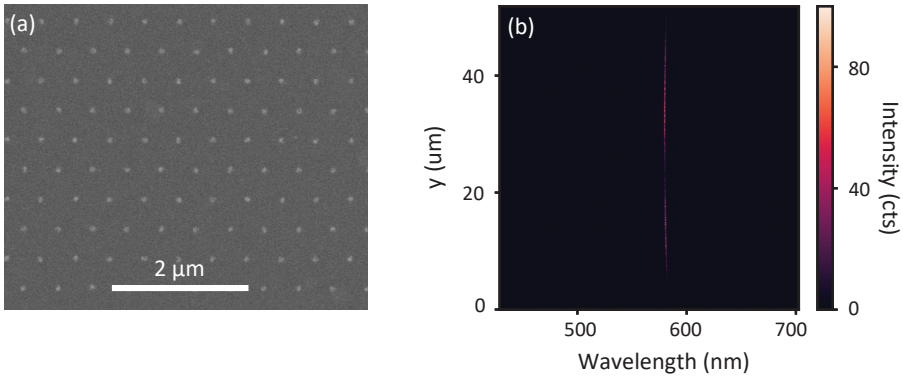

Figure 4.5: Electron microscope image and spectrum of the lasing mode. (a) SEM image of the K-point plasmonic lattice laser, showing the lattice of pitch 500 nm of silver plasmon particles with diameter 80 nm. (b) raw spectral image of K-point lasing emission, showing a single lasing line along the full length of the real-space field of view. The slight curvature is due to the spectrometer imaging optics and has not been corrected for in this image.

apparent imbalance, as can averaging over just a few shots. That there is no imbalance on average, and no global preference, is evident from the statistical analysis in Fig. 4.4 These data are extracted from full 2D Fourier imaging without any spectrometer slit to slice the data, and hence do not suffer from the artifact.

4.6.5 SSB power dependence

Spontaneous symmetry breaking generally occurs when one input parameter to a physical system is continuously changed, and crossing some threshold value, the system's energy mode reduces in symmetry. Figure 4.6(a) displays such threshold behavior for the K/K' mode laser, mapped as function of pump power. We use the parameter θ defined in the main text. Below lasing threshold, fluorescence at all K-points is equally bright ($\theta = 0$). As the pump power exceeds the lasing threshold power of 1.0 mJ/cm^2, a continuous spread becomes visible in the SSB parameter θ that expresses the relative intensity between the K and K' mode (y-axis). The spread remains uniform over the entire θ range when increasing pump power. Fig. 4.6(a) is measured with the 250 fs pump pulses also used for the main manuscript. For Fig. 4.6(b), we place the same sample in a similar fluorescence Fourier microscope but with 532 nm pump pulses of 500 ps pulse length, and we apply the same linear basis projection method to the Fourier images. For this much longer pump pulse regime, the system also shows no bifurcation, and a wide range of θ values is sampled. The spread in θ is less than in Fig. 4.6(a). We attribute this to a higher fluorescence intensity background when using 500 ps long pulses than 250 fs, which reduces K/K' contrast. This is supported by Fig. 4.6(c) that shows the histogram for 0.4 mJ/cm^2, but with fluorescence background subtracted prior to extracting θ. This recovers a more uniform distribution of θ over the full range.

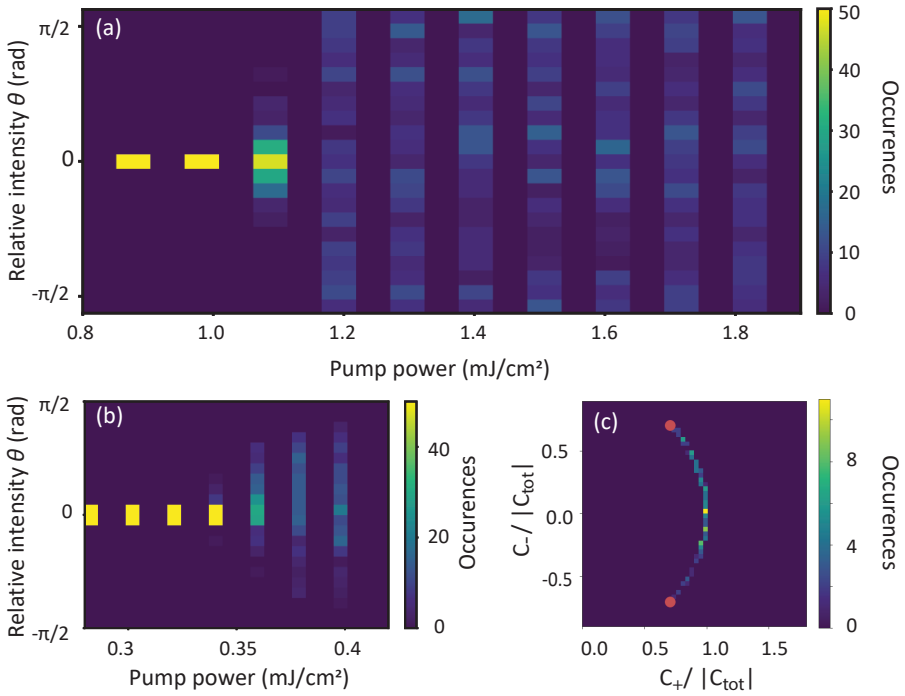

Figure 4.6: Influence of pump strength on θ, for fs and ps pulse lengths. (a) Histograms of K/K' intensity contrast parameter θ for increasing pump fluence, showing even spreads in θ for fluences well above lasing threshold. Data taken with the 250 fs pulsed laser setup described in the main text. (b) Same measurement as in (a) but taken with a setup using a laser of 500 ps pulse length. (c) Fluorescence intensity background subtracted occurrence histogram for θ, showing that the fluorescence background significantly reduces the spread in θ.

4.6.6 Coupled-mode model

From scalar coupled-mode theory, the A_1 K/K'-point Bloch mode is described by three coupled waves (see Figure 4.7(a))

$$E_K(\mathbf{r}) = e^{iK_1\cdot\mathbf{r}} + e^{iK_2\cdot\mathbf{r}} + e^{iK_3\cdot\mathbf{r}}. \tag{4.2}$$

This simple model is used to calculate local field distributions for the A_1 mode. Fig. 4.7(b,c) display the calculated intensity distributions of the K/K' modes, showing that they both form hexagonal patterns with peaks at the lattice nodes. The K/K' modes are thus spatially degenerate and are only distinguished by their opposite wavevector content. When both modes form a coherent superposition

$$E_T(\mathbf{r}) = aE_K(\mathbf{r}) + bE_{K'}(\mathbf{r})e^{i\varphi_R}, \tag{4.3}$$

the result in local intensity shows honeycomb interference patterns as visible in Fig. 4.7(d). The supercell pattern has $\sqrt{3}$ times larger pitch than the sublattice, and the

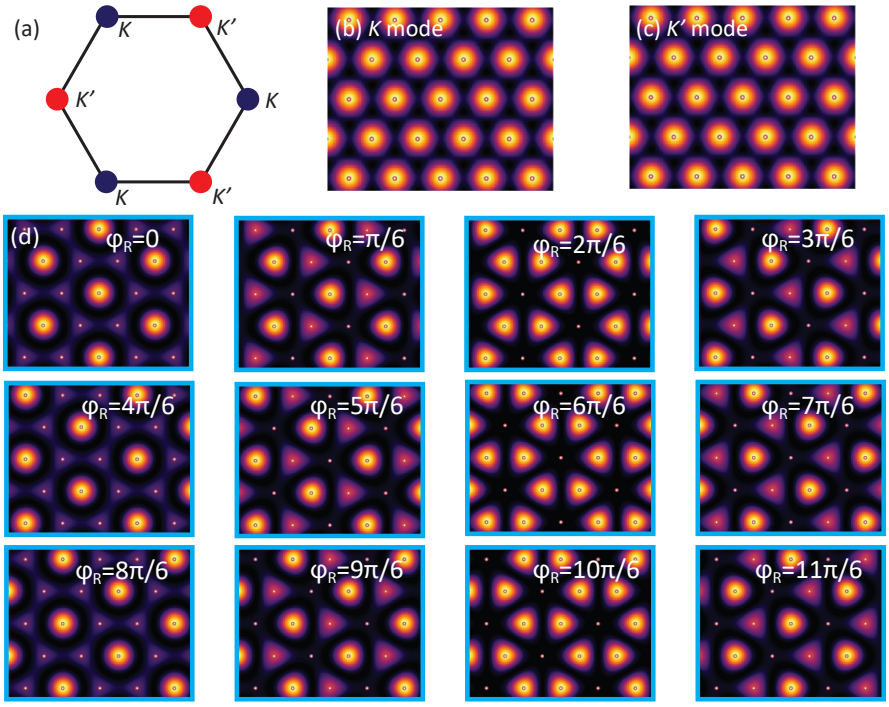

Figure 4.7: Catalogue of K/K' mode interference patterns in real space. (a) The hexagonal Brillouin zone corners comprise two sets of three reciprocal lattice vector-coupled K-points. The A-type modes of the $K\,/\,K'$ points are calculated with a coupled-wave model, they have equal intensity distributions in space, as shown in (b) (K mode) and (c) (K' mode). (d) Catalogue of local $|E_T(\mathbf{r})|^2$ for different relative phases φ_R between K and K' modes (calculated with equal K-mode amplitudes $a = b$).

structure and spatial alignment relative to the origin of the patterns vary with relative phase φ_R.

4.6.7 Real space filtering and phase fitting

In a single-shot real space image (Figure 4.8(a)), different periodic features are distinguishable, but their detailed structures are partially obscured by residual noise from scattering by fabrication disorder. We Fourier filter the real space data for fitting, as follows. The inset of Figure 4.8(a) shows the absolute value of the 2D Fourier transform F of the real space image, in which we clearly observe 19 sharp peaks (one at 0 wave vector, and the remaining 18 forming different orders spanning the honeycomb patterns across the hexagonal lattice). In the 2D FFT peaks, 6 points at $|\mathbf{k}_{//}| = 15$ $\mu\mathrm{m}^{-1}$ are the first order reciprocal lattice points of the real space lattice itself, and the remaining 12 are responsible for the superlattice periodicity. For fitting, we first define the size $l = 5.86$ μm of the real space blocks of data that we will fit the coupled-mode model to. This defines a Fourier filter width $dk = 2\pi/l$ $\mu\mathrm{m}^{-1}$. We then remove

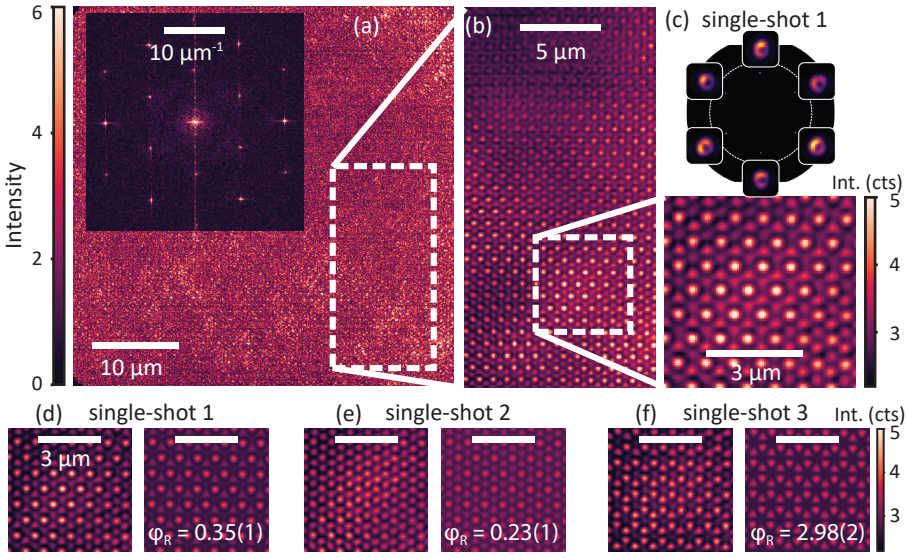

Figure 4.8: Workflow illustration of the method to extract relative phase between the K and K' mode from the real space data. (a) Raw image and FFT as inset. (b) Fourier filtered data for region as indicated in (a). (c) Close-up of area used for fitting, taken from (b). Also shown is the corresponding measured Fourier image. (d-f) show example data and fits.

high-frequency noise from the full real space image by selecting only regions of width Δk around each of the 19 sharp peaks (Gaussian filters, width dk). Inverse-Fourier transforming the masked FFT returns the filtered real space image. Intensities in real-space images in Fig. 4.8 are reported in dimensionless units. For a quantitative scale, the data in Fig. 4.8(a) corresponds to $1.4 \cdot 10^6$ camera ADU units integrated over the 44 by 44 µm^2 field of view. With a camera quantum efficiency of 70% this translates into circa $1 \cdot 10^6$ collected photons per laser shot (500 photons per square micron). The Fourier filtering suppresses the Poisson counting noise.

We then fit filtered real space intensity patterns of size $l \times l$ to the coupled-mode

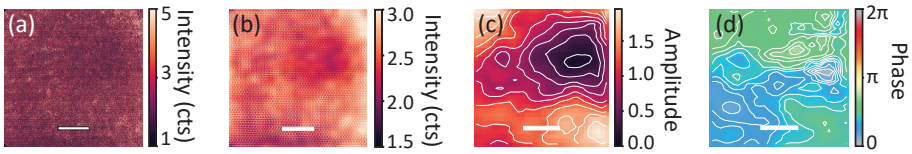

Figure 4.9: Spatial amplitude and phase landscapes of a single lasing shot. (a) The raw single-shot real space data, to which the spatial filter technique is applied to obtain (b). (c) Fitted amplitude of the periodic patterns above the fluorescence background. (d) Spatial landscape of the extracted relative phase between K and K' mode. Scale bars are 10 µm.

model with the Python SciPy minimize function using the BFGS algorithm. For all the fits, we choose the same area in the sample, and the block origin is chosen to coincide with an intensity peak in the ensemble-averaged data. This ensures a precise and common registration to the underlying particle lattice, which is needed to avoid ambiguity in fitting the phase. The fit function reads

$$|E_T(\mathbf{r})|^2 = A|(\sqrt{a}E_K(\mathbf{r}) + \sqrt{b}E_{K'}(\mathbf{r})e^{i\varphi_R})|^2 + B, \tag{4.4}$$

where the relative amplitude coefficients a and b are derived from θ, taken from the Fourier-space measurement, as: $a = (1 + \tan\theta/2)/2$ and $b = (1 - \tan\theta/2)/2$. a and b are square rooted to obtain the right units. The only free fit parameters are the overall amplitude and background counts (A and B) and the relative phase φ_R. Representative fit results are shown in Figs S4(d,e,f). We note that performing this fit in real space works best at choices of l that encompass of order 10×10 unit cells.

4.6.8 Spatial landscapes of the phase

The fitting procedure as described above can be extended to obtain a spatial phase texture over the microscope field of view. To this end, we divide the field of view into a target set of phase sampling points and for each sampling point we determine the phase by real space fitting the intensity pattern inside a small box centered at the sampling point (side length 5× larger than the sampling point distance). For successful fitting, it is important that in all images the underlying particle lattice is precisely referred to one common origin, since otherwise an error in spatial position would translate as a phase slip (see Fig. 4.7). We have found that it is advantageous to first fit the phase texture at a coarse sampling resolution, fitting larger areas at a

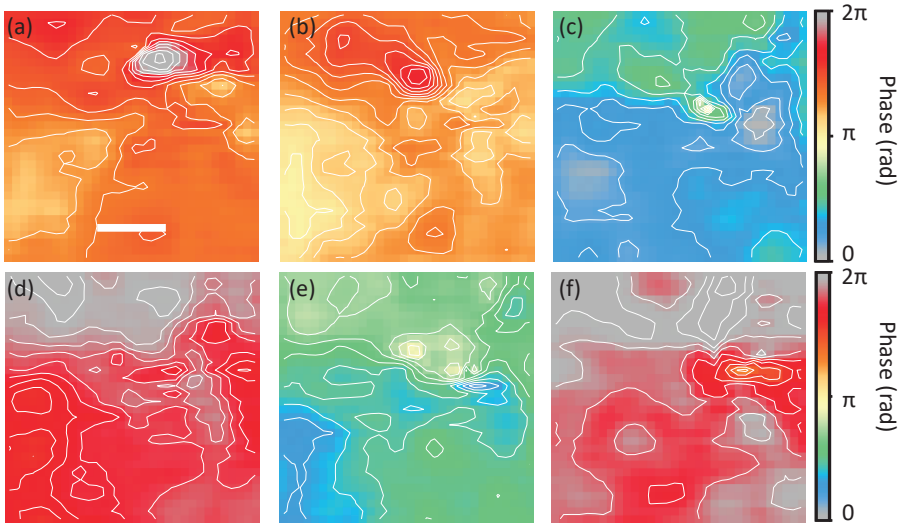

Figure 4.10: Spatial phase landscapes for six subsequent single-shots. These landscapes show random excursions from the mean spatial phase texture.

time, and subsequently using those fit results as an initial guess for fitting at refined resolutions. Generally, we find that the local phase can be fitted accurately except in two cases. First, whenever the lasing is purely K or K', the relative phase is φ_R not defined. In practice, this means that also close to pure K/K'-lasing the phase is hard to determine. Second, the amplitude maps show variations in laser intensity, including marked minima. We note that such inhomogeneities in amplitude envelopes are intrinsic to DFB lasing, and occur, for instance, in coupled mode theory descriptions from a nonlinear interplay of laser size, gain coefficient and feedback strength in coupled mode theory. At intensity minima, the contrast in the data to which the fit is performed is low. Figure 4.9 shows the results for one example frame, reporting the raw real space image, the Fourier filtered data, and the extracted phase map. For this particular example, there are phase excursions of order 0.1 to 0.2 radians around the mean. Figure 4.10 shows such phasemaps for 6 subsequent frames. Both the average phase, and the phase fluctuations vary from map to map. The spatial autocorrelation lengths are of order 5 μm.

4.6.9 Statistics of SSB parameters (Kolmogorov-Smirnov test)

Our sampling of the probability distribution typically contains of order 1000 shots (Fig. 4.4(b,c): 900 shots, combined from the six highest pump powers (each 150 shots) in Fig. 4.6(a)). Focusing on the symmetry breaking in relative intensity and phase as gauged by θ and φ_R, one can perform statistical testing to test if the data is likely drawn from a uniform distribution. A standard test is the Kolmogorov-Smirnov test (KS), which compares measured and hypothesized cumulative probability distribution functions. As an example of such an analysis, in Figure 4.11 we plot the KS test applied to data taken from the highest power dataset in Fig. 4.11(a) (150 shots). The measured cumulative distribution function matches that of a uniform distribution for θ and φ_R well, with a respective maximum deviations D = 0.054 and D = 0.046, which are smaller than the threshold value of the Kolmogorov-Smirnov test evaluated at $\alpha = 0.05$ (5%) as significance level: D = 0.11. Most runs pass the test at this level of strictness for θ and φ_R, and a few runs marginally fail the test. In our view this means that quantitatively the data is in good accord with the hypothesis of a uniform distribution. In a future study, it would be interesting to resolve if there is finer structure in phase space, e.g., in relation to how the system geometrical symmetry is broken, or how much disorder is introduced.

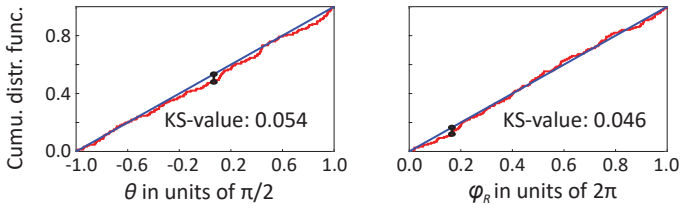

Figure 4.11: Cumulative distribution functions for Kolmogorv-Smirnov testing. The cumulative distribution functions of hypothetical perfectly uniform distribution datasets are shown in blue, and of the SSB data in red. The data is taken from the highest pump power dataset in Fig. 4.6(a). Both θ and φ_R pass the Kolmogorov-Smirnov test.

Chapter 5

Plasmon lattice lasers programmed in size, shape and symmetry

We study hexagonal plasmon lattice lasers that are programmable in size, shape, symmetry, and boundary conditions. Plasmon lattice lasers are two-dimensional (2D) lattices of plasmonic scatterers embedded in a waveguide with optical gain. At the high-symmetry points, the lattice forms delocalized plasmon modes that provide optical feedback distributed across the array, akin to distributed feedback (DFB) lasers. We project optical pump fields of various shapes onto the lattice, using a digital micromirror device, and study the diffracted output light with simultaneous real-space and Fourier-space microscopy. We focus on K-point lasing in hexagonal lattices. Firstly, we note that the 2D laser's real-space intensity envelopes display clear signatures of being in the undercoupled DFB lasing regime. What is more, we find that the vortex beams of laser emission in Fourier space strongly depend on the shape/size of the illuminated area in real space. In the acquired single-shot lasing images, we observe shot-to-shot variations in relative amplitude between the degenerate K and K' modes, indicating spontaneous parity symmetry breaking. We study the relation between real-space laser shape, k-space output, and local spatial intensity distribution in the spontaneous symmetry breaking process. Spatial shaping of the pump field also allows to create nearby coupled lasers. Finally, we show how coupled plasmon lasers synchronize in phase and amplitude in dependence of their coupling strength.

5.1 Introduction

Plasmon lattice lasers receive much interest as two-dimensional (2D) distributed feedback lasers (DFB) based on diffractive plasmon modes [30, 126, 127, 130–132, 134, 135, 143, 255]. They are periodically arranged lattices of metallic nanoparticles, embedded in an optical gain medium that often also functions as a 2D waveguide. The resonant nanoparticle polarizability offers strong and ultrafast near-field enhancements as well as large scattering cross-sections that guarantee strong optical feedback. Employed as laser cavity, plasmon lattice resonances provide much stronger feedback than typical polymer [139, 141, 145] and photonic crystal [142, 146–148] DFB lasers, and therefore plasmon lattice lasers come, for instance, with exceptional robustness to disorder [130]. An alternative viewpoint on plasmon lattice lasers is that they implement a diffractive resonant metasurface, and as such, plasmon lattice lasers are related to lasers based on lattices of Mie-resonant scatterers and lasers based on bound states in the continuum in nonlocal metasurfaces [19, 23, 31, 136–138]. Typically, lattice lasers operate on the Γ-point condition (2nd order Bragg diffraction, output normal to the laser), but recent interest emerged in plasmon lattices of hexagonal symmetry that lase from the high-symmetry K- and M-points in momentum space, for they offer a rich class of mode symmetries [143, 144, 186, 255, 279]. For instance, in hexagonal lattices the K and K' Bloch modes are time-reversed companions [186], degenerate not only in frequency but also in the spatial mode profile. In Chapter 4, we proposed this as a new venue to study spontaneous symmetry breaking physics. This exemplifies that plasmon lattice lasers give access to fundamental studies of solid-state physics phenomena occurring in 2D lattice symmetries with loss and gain.

In this Chapter, we spatially program the size, shape and symmetry of the impinging pump field, and investigate the output characteristics of the resulting lasing. Using a digital micromirror device to shape the optical pump field, we achieve spatially programming the gain. Spatial programming of gain allows us to study many highly interesting questions. First, coupled wave theory (CWT) for dielectric DFB lasers [140] predicts that lasing behavior highly depends on boundary conditions: 2D DFB lasing comes with nontrivial spatial intensity distributions that are slowly varying envelopes compared to the underlying Bloch-mode standing waves [132, 148, 280, 281]. In dependence of the ratio of gain and feedback strength, these envelopes have typical shapes – for instance, the lowest threshold modes in plasmon lattices are typically 'undercoupled', with intensity high at the laser boundaries and low in the center. Interestingly, K-mode lasers can display far-field emission into a triplet of spots, and we here examine their intensity envelopes. Second, by diffraction, the real-space profile directly relates to the far-field output. In the metasurface laser community, there is large interest in the vortex beams displayed by lattice lasers, which are associated to the

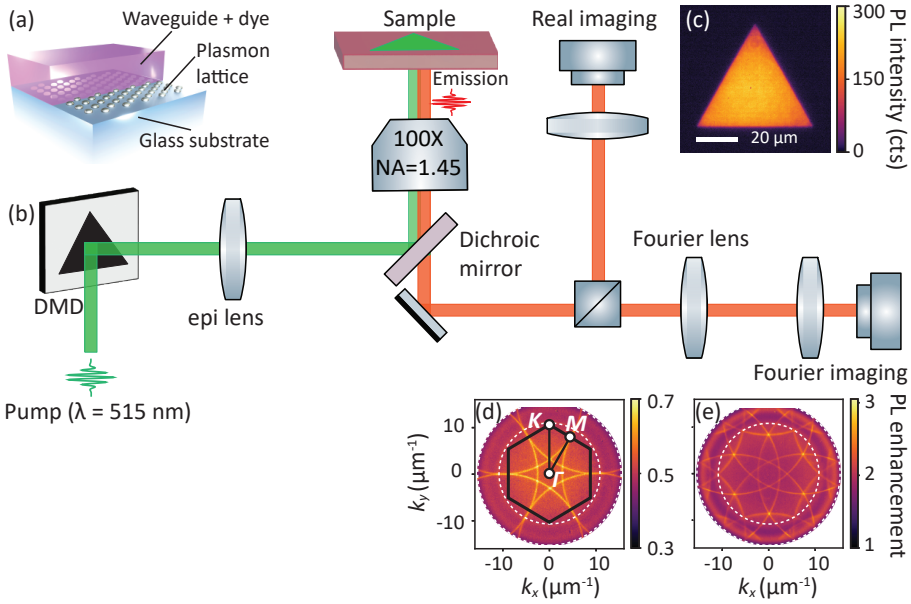

Figure 5.1: Single-shot microscopy with structured pump illumination. (a) Illustration of the plasmon lattice laser, which is a hexagonal lattice of silver nanoparticles embedded in a dye-doped slab waveguide. (b) Fluorescence microscope setup. We place a digital micromirror device (DMD) in the pump-illumination track in the focus of the epi-lens in order to project any pattern in the real-space plane of the sample. The emission signal is sent to the imaging setup where we record real- & Fourier-space images simultaneously. (c) 54 µm sized triangle projected by the DMD produces a triangle in fluorescence as recorded in real space. (d,e) Fourier images of fluorescence from the hexagonal plasmon lattice for pitches a = 375 nm and 500 nm, with bandpass filter centered at 580 nm, at which energy the repeated waveguide mode crossings occur at the M- and K-points, respectively. The first Brillouin Zone is shown in black in panel (c), with high-symmetry points M,Γ,K indicated.

so-called quasi-BIC (bound state in the continuum) nature of the lasing mode [31, 134, 255]. While finite size effects have been studied with CWT and in experiments [132, 148, 154, 281], showing signatures both in the Fourier-space vortex lasing beam and in the spatial intensity distribution, these studies have focused on *hard boundaries*, where the physical lattice actually stops. In this work, we show how the quasi-BIC vortex beams are controlled by shape and size of the pumped area. Third, we study spontaneous symmetry breaking (SSB) physics as function of boundary conditions that can be chosen to either match, or instead frustrate and reduce the symmetries of the underlying lattice. Furthermore, there is no need to restrict spatially programmed gain to contiguous domains, and we show that one can controllably study the coupling and synchronization of two and more closely spaced 2D lasers. A rich body of literature exists on coupled lasers in various forms, including

two-section 1D DFB lasers [282, 283], coupled semiconductor lasers [284, 285], and coupled photonic crystal cavity lasers [256, 286, 287]. Already systems of two coupled lasers come with a plethora of nonlinear dynamical features, such as self-pulsations, chaos, synchronization, spontaneous symmetry breaking, with rich input-output bifurcation scenarios [288, 289]. These nonlinearities are typically mapped via temporal studies of emission output. Our work presents a method to spatially control and image the nonlinear interaction dynamics of coupled lattice lasers.

5.2 Experimental approach

To create gain regions with sharply defined and controllable boundaries, we use a digital micromirror device (DMD) to structure the pump beam. This method is borrowed from programmable emission control in polariton condensate studies [184, 290], planar random lasers [291], and more recently studies of refractive index tuning to manipulate luminescent all-dielectric metasurfaces [292]. Figure 5.1 shows the concept of our set up, which is essentially a fluorescence microscope driven by a 250 fs pulsed pump laser of 515 nm wavelength (LightConversion Pharos, frequency doubled). Fig. 5.1(b) displays the setup, where we place a Texas Instruments digital mirror device (DLP6500, a 2 megapixel device with 7.6 micron pixel size) in the pump beam, imaging it through the microscope epi-illumination lens and objective (NA $= 1.45$ oil objective, Nikon CFI Plan Apochromat lambda 100x) onto the sample, at a demagnification of 100 times. This allows to project an amplitude mask formed by DMD pixel-mirrors as intensity pattern in the pump field on the sample with diffraction limited resolution $\lambda/2\text{NA} = 175$ nm (≈ 2.5 DMD pixels). Fig. 5.1(c) shows an example of the real-space illumination, visualized by recording fluorescence from a dye-doped but uncorrugated polymer slab. The emission clearly delineates a triangular shape, as encoded by the DMD, onto the pump. As in Chapter 4, our setup can operate in single-shot mode, with a camera frame rate synchronized to the repetition rate of the laser (set at 20 Hz). A beamsplitter in the imaging track ensures simultaneous capture of real-space images with one camera and Fourier-space images with the other. Single-shot recordings allow to capture shot-to-shot variation in the laser emission, originating e.g. from mode competition and spontaneous symmetry breaking [255, 264].

We study hexagonal lattices of plasmonic nanoparticle antennas, sketched in Figure 5.1(a). The nanoantennas have 80 nm diameter and 35 nm height, with a pitch of 375 nm or 500 nm. The lattice is fabricated by standard electron beam lithography followed by a lift-off procedure. We cover the lattices with an approximately 500 nm thick SU8 polymer slab, which is doped with 3.5 wt % rhodamine 6G providing the gain required for lasing. We refer to Sec.4.6.1 in the Appendix of Chapter 4 for details of sample fabrication procedures. The

choices of particle size, waveguide and gain medium are typical in the field of plasmon lattice lasers: The in-plane plasmon resonance of the particles is resonant with the gain (near 590 nm), and the waveguide supports just one transverse electric (TE) and one transverse magnetic (TM) guided mode. The fully in-plane electric field of the TE mode aligns to the main polarizability axes of the anisotropic oblate metallic nanodisks, therefore favoring diffractive coupling through the TE waveguide mode over TM guided modes [30, 131]. Figures 5.1(d,e) show Fourier images of PL enhancement from plasmon lattices with pitch 375 and 500 nm. In the extended-zone scheme representation of band-structure physics, the waveguide mode represents a circular feature in (k_x, k_y) space, repeating centered at each reciprocal lattice point of the hexagonal lattice [10]. This repeated-zone-scheme dispersion is immediately evident in the back-focal-plane images in Fig. 5.1(d) and (e). The first Brillouin zone (BZ) is hexagonally shaped and is highlighted in black (Fig. 5.1(d), with high-symmetry points Γ (center of BZ) K (corners of BZ) and M (in between corners of BZ). In panel 5.1(d), for $a = 375$ nm, repeated waveguide modes intersect at the M-points, while in Fig.5.1(e) for $a = 500$ nm an intersection occurs at the K-points. At such intersections, two or more Bloch modes couple and form a stop gap in $(\omega, k_{||})$ space, with flat bands suitable for lasing [30, 132, 140, 142]. For the amplifying plasmon lattice of pitch 500 nm, lasing occurs from the A_1 mode at the K-point [143, 255, 275–277]. In all experiments reported in this work, we vary boundary conditions only in the excited area, not in hard boundaries of the lattice. For the latter, we use 200 µm × 200 µm large fields, and stay well within this area as we project shapes in the pump field. Details on our measurement protocol can be found in the Appendix Sec. 5.8.1.

5.3 K-point lasing of single gain areas

Figure 5.2 displays real- and Fourier-space images of illuminated areas of different shape. We observe K-point lasing with different laser shapes and sizes, each example showing maps of the laser output well above the lasing threshold. In panels (a-c) we show ensemble averages (summation over 100 consecutive single-shots) of real-space and concomitant Fourier-space lasing results for hexagonal lasing areas of decreasing size. In the real-space images, we observe an intensity envelope that peaks at the triangle edges, reaching a minimum in the center. In the theory of 1D distributed feedback lasers by Kogelnik and Shank [140], such profiles are viewed as a clear signature of an undercoupled lasing system, which is typical for photonic and plasmonic lattice lasers [132, 148, 281]. For the pump fluences used in our experiment, the intensity envelopes generally maintain a signature of undercoupled shapes, see Appendix Sec. 5.8.2 for examples. These undercoupled intensity distributions have been associated by Hakala et al. [133] to lasing on a dark mode.

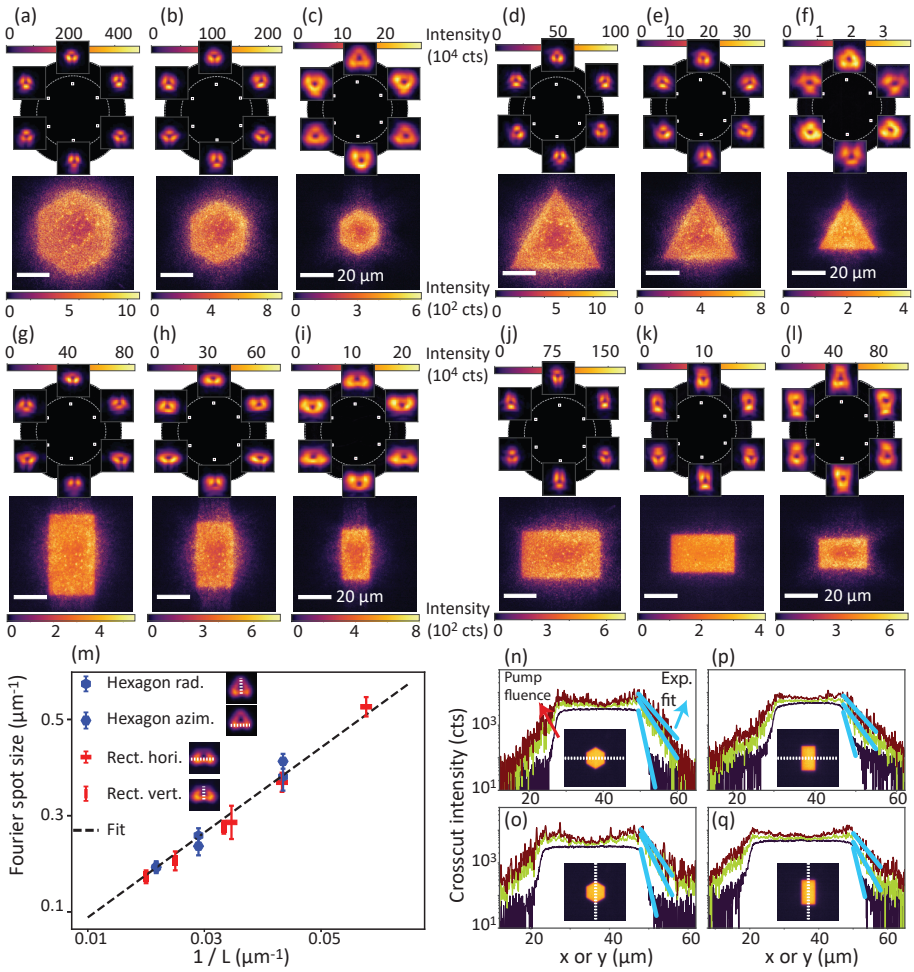

Figure 5.2: K**-point lasing with boundary conditions in gain.** (a-c) Fourier- and real-space images of K-point lasing ($a = 500$ nm) from DMD-projected hexagons of short diagonal $L = \{46, 34.5, 23\}$ µm (radius $\{26.6, 19.9, 13.3\}$ µm). (d-f) Lasing from triangles with side length $L = \{57.5, 46, 34.5\}$ µm. (g-i) Lasing from rectangles of shape $\{(28.9 \times 50), (23.1 \times 40), (17.3 \times 30)\}$ µm and (j-l) 90° rotated rectangles. Note how in all four cases, in real space, lasing is characterized by finely spaced speckle, overlayed with overall slowly varying intensity envelopes that are minimal at the center. In Fourier space, six K-point lasing spots are donut-like (extent of the square insets is $\Delta k/k_0 = 0.06$) but relate to the real space gain area symmetry by Fourier transform, and increase in size as the real-space area reduces. (m) Fourier-space lasing spot size versus the inverse of real space length L. This data is obtained by measuring size of the Fourier spots, averaging over six spots and taking standard deviation for estimation error. In blue we display radial and azimuthal line measurements in the donut-spots of hexagon pump (panels a-c). Red data highlights horizontal and vertical crosscuts through donut-spots from rectangle pump (panels g-i). Both datasets are plotted against $1/L$ with L either hexagon short diagonal or relevant rectangle side length. The relation $\Delta k \propto 1/L$ clearly holds: All data fall on the linear line fit with slope 9. *Caption continues next page.*

Figure 5.2: *Continuation of caption from previous page.* (n,o) To quantify the propagation length of laser light beyond the pumped area, we take horizontal and linear crosscuts (at $y_c, x_c = (35, 38.7)$ µm and summing 20 pixels wide) through the real-space hexagon shape in panel (c), for pump fluences $\{1.5, 2.1, 2.7\}$ mJ/cm^2. The lowest fluence (dark purple curve) belongs to fluorescence, the higher two (green/red curves) to lasing. We fit the line $y = a \exp b(x - x_1)$ to this region beyond pumped area, shown in cyan curves, and obtain $b = -1.2$ µm^{-1} for fluorescence, but $b = -0.4$ µm^{-1} for the lasing curves. The laser thus propagates about 2 to 3 µm beyond the gain boundary. (p,q) Crosscut results for the rectangular pump of panel (i), with fluences $\{1.8, 2.3, 2.8\}$ mJ/cm^2 – fitting leads to similar b-values as the hexagons shapes..

Dark-mode lasing entails Fourier-space output in form of donut-shaped intensity spots that display a minimum in their center [148]. Indeed, this is what we generally observe in all Fourier images of lasing emission, fully in line with a plethora of 2D DFB lasing studies [145–148, 151]. In current nomenclature, these donut-shaped spots are referred to as signatures of quasi-BIC modes: Lasing occurs on a stopgap edge at the K-point that correspond to radiation-forbidden Bloch modes. However, the finite extent of the lasing area opens up the possibility to radiate, manifesting as a ring of emission around the K-point. In recent works, these quasi-BIC lasing conditions have been associated with polarization vortices carrying topological charge [31, 134, 136, 160]. Interestingly, panels (a-c) in Fig. 5.2 show that as the real-space gain area reduces, in Fourier space the laser spots become larger. All features described above are also observed in panels (d-f) for triangular-shaped lasers.

Next, we project gain regions that are not commensurate with the hexagonal symmetry of the underlying lattice. We use a rectangular illumination area and show results for vertically oriented (Fig. 5.2(g-i)), and horizontally oriented areas (panels j-l). The resulting Fourier-space donuts also become rectangular shaped – this is especially visible for the smallest lasers, as boundaries here are largest compared to the overall laser area. The rectangular donut spots have their long axis oriented normal to the long axis of the rectangle in real space. This behavior follows the reasoning that the far-field emission is the Fourier transform of the real-space field at the sample plane, according to which real-space confinement causes Fourier-space broadening [132, 148, 151] through a convolution of the infinite-system output with the Fourier transform of the lasing area. The Fourier-space width Δk is thus expected to be directly proportional to the inverse of the laser size L, i.e. $\Delta k \propto 1/L$. In Fig. 5.2(m), we show that this proportionality indeed holds by plotting Fourier-space spot sizes of hexagon and rectangle lasers versus inverse laser size $1/L$. For a homogeneously radiating rectangle, the expected proportionality constant should be of order $\Delta k L \approx 2\pi$. We find constants of order 9. This difference may lie in a smaller effective radiative surfaces (likely because mainly the laser edges contribute), and likely also special polarization properties of the lasing mode. The latter also explain finer features such as the

dark lines crossing through the emission spots. Finally, we note an interesting observation in real space: Lasing emission also emerges from outside the pumped area. While the DMD provides a sharp boundary between excited and non-excited area, there is no interruption for Bloch wave propagation as the underlying lattice and waveguide continue. In these regions, the guided mode travels in the slab along the K-direction without gain while loosing energy by diffractive outcoupling. In Figures 5.2(n,o) and (p,q) we plot the real-space image intensity across the illuminated area for increasing pump fluences. Clearly, intensity persists beyond the gain boundary and decays exponentially. The lasing intensity (green and red curves), decays more gradually than the fluorescence intensity (dark purple curve), which we take as as measure for how sharply the gain region is defined. From exponential fits (cyan curves, linear on the log scale) we obtain exponents of $b = -1.2$ μm^{-1} for the fluorescence intensity decay, and $b = -0.4$ μm^{-1} for the laser intensity decay. This indicates that lasing emission propagates about 2 to 3 μm into the lattice, away from the pumped area, or about 6 to 10 unit cells of the plasmon lattice. In the theory of photonic crystals, an important length scale to quantify the behavior of light in or near stop bands is the so-called 'Bragg length', which is a metric for the distance or number of unit cells required to build up a significant Bragg reflection. This length indicates the typical distance required to build up significant optical feedback in distributed feedback lasing. The measured 6 to 10 unit cells is consistent with measures of the minimum size required for plasmon lattice arrays of finite extent (hard boundaries) to lase [132, 154].

5.4 Explicit symmetry breaking for K-point lasers

In hexagonal lattices, the K- and K'-point modes are uncoupled, but degenerate. In each mode, three wave vectors are coupled by lattice diffraction. K and K' modes are each others time inverse, and as such degenerate in eigenfrequency and near-field intensity distribution. As a result, spontaneous symmetry breaking can be observed [255]. To understand how K-point lasing and spontaneous symmetry breaking behave as a function of gain boundary conditions, we proceed by studying single-shot measurements of areas of various shapes. For increasing pump fluence, we record sequences of ≥ 100 single shots. As in Chapter 4, we observe spontaneous parity symmetry breaking in the Fourier images as a result of the two degenerate modes, one in which three K-points are coupled by diffraction, and another one lasing on the K'-points. While within a triplet of K- resp. K'-points the relative intensities are equal, every shot exhibits a random relative amplitude of the K- and K'-points. Selected shots of high-contrast K-mode lasing for various shapes are shown in Figure 5.3, top row, while the corresponding K'-mode lasing shots are shown in the bottom row. Each example is well above the lasing threshold.

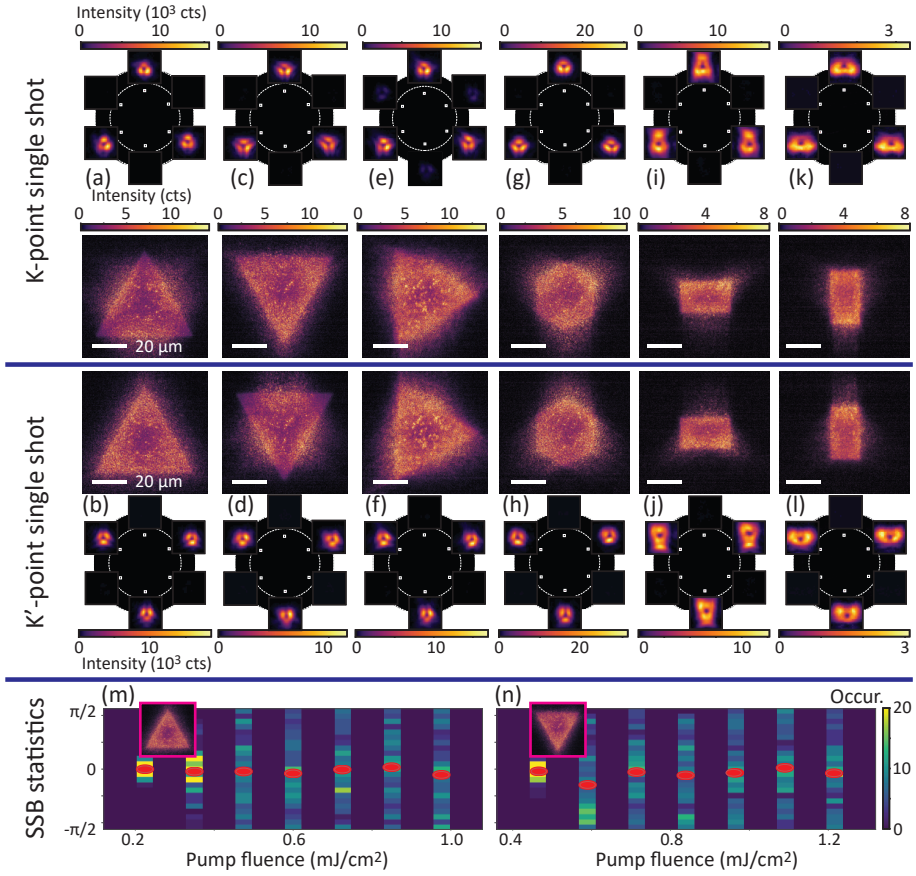

Figure 5.3: Single-shot K-point lasing and spontaneous symmetry breaking. Top row: Simultaneously recorded Fourier/real-space single lasing shots, where spontaneous symmetry breaking realizes in high contrast K-mode lasing, for a variety of boundary conditions in gain. The real-space envelope makes a triangular shape of mirrored orientation with respect to Kmode in Fourier space, besides displaying the intensity dip in the center as predicted by coupled wave theory. Second row: Single lasing shots for same pump patterns but with highest contrast in the K' mode. Again, the real-space envelope is triangular and mirrored vs. the Fourier-space mode. Note how the envelopes extend far beyond the gain boundary condition. (a-f) Triangle, side length 53 µm. (g,h) Hexagon, short diagonal 34.5 µm. (i-l) Rectangle, shape (17.3×30) µm. (m) Single-shot statistics of K/K' SSB parameter θ that traces relative amplitude, as a function of pump fluence, for the upward triangle (panels a,b), and (n) for the downward triangle (panels c,d). Note the absence of bias towards K/K' lasing, despite their symmetry being broken by the geometry of the gain field.

Independently of the shape of the pumped area, we observe that the real-space intensity envelope is directly linked to the Fourier-space output of the laser: The real-space intensity envelope creates triangular patterns, where the areas of bright emission are in location exactly opposite to the emitting lasing wave vectors. Panels (a,b,g,h) in Figure 5.3 show this for triangularly shaped lasers. For K-point lasing (panels a,b), the real-space envelopes are brightest at the sides of the triangle: The top left, top right and bottom of the lasing field; vice versa, for K'-point lasing the corners of the triangle are brightest. This behavior is not due to the choice of the pumped area in relation to the mode that lases: The hexagonal gain area in (d,j) whose geometry is fully symmetric with K/K' lasing in Fourier space shows the same behavior. We note that this behavior shows that the parallel momenta of the involved Bloch modes, mapped as the Fourier-space output spots, are oppositely oriented to the in-plane directions, in which the gain builds up upon propagation. Moreover, our experiment addresses the important question whether boundary conditions in gain might bias the SSB in relative amplitude. Fig. 5.3(m,n) display for up/down oriented triangles the recorded statistical spread of relative K/K' amplitudes expressed in parameter θ, defined by $\theta = 2\arctan(\frac{I_K - I_{K'}}{I_K + I_{K'}})$ (I_K and $I_{K'}$ are summed K/K' point intensities), which we compute for every shot in the time trace. Thus, when explicitly breaking the K/K' parity symmetry by aligning triangular real-space gain areas with either K or K' orientation, we do not recognize any bias towards K- or K'-point lasing in the single-shot time traces. We also observe absence of explicit symmetry breaking for all other recorded examples, as shown in the Appendix Sec. 5.8.3. In Chapter 4, we argued that the K and K' mode are each others time-reverse counterparts (related by complex conjugation) and share a fully identical real-space amplitude mode profile – this means that incoherent pumping in whichever domain shape inherently does not break K/K' symmetry.

5.5 Explicit symmetry breaking for M-point lasers

The property that spontaneous symmetry breaking cannot be programmed by boundary conditions, established from Figure 5.3, is specific for K/K'-point lasing, and intrinsic to their time reversal relation. Experiments on M-point lasers show that this property is not shared by other SSB conditions. The M-point band intersection falls within the rhodamine 6G gain window when the pitch $a = 375$ nm (see Fig. 5.1(d)). While K-points present a degenerate doublet of modes that each couple three reciprocal lattice vectors, there are three sets of two M-points, with pairs of M-points connected by a reciprocal lattice vector. The three modes are degenerate in frequency but not in space as each mode forms in real space a 1-dimensional standing wave pattern normal to their specific M axis. Under fully symmetric gain conditions, mode competition between the three modes expresses a SSB in relative amplitude. We

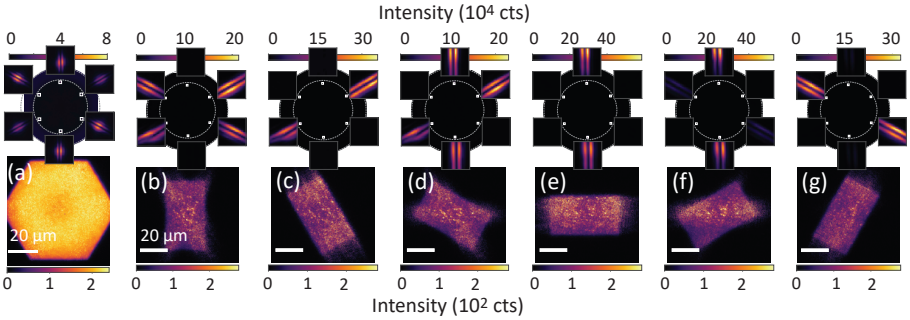

Figure 5.4: DMD-controlled M-point lasing. (a) 20-shot average Fourier- and real-space lasing from the M-points, in a symmetric pumping scheme (LCP-polarized pump forming hexagonal shape in real space with short diagonal 69 µm). Spontaneous symmetry breaking between the three frequency-degenerate M-modes leads to mode competition and fluctuations of 15%. (b-g) Active switching between M-modes by rotating a rectangular pump shape (50×28.9) µm, by which we impart bias by overlapping the gain with the spatially distinct mode profiles belonging to the three M-modes. The square lasing spot insets in the Fourier images have size $k_{||}/k_0 = 0.1$.

show this in panel (a) of Figure 5.4, where a hexagonally shaped pump that is left circularly polarized (LCP) creates Fourier space output that is almost completely symmetrically distributed on average over the three modes. SSB in amplitude is evident from shot-to-shot variations in intensity of about 15%.

The fact that M-point lasing is essentially 1-dimensional, is evident from the stripe nature of the lasing output. One can now bias one of the M modes by aligning the illuminated area as an elongated rectangle along the pair of M-points of interest, since their real-space mode profiles are not degenerate in space (as is the case for the K/K' laser). In Figure 5.4(b-g), the pump is still LCP polarized but a rectangular gain area is used, the long axis of which we rotate in steps of 30 degrees. This either ensures mode overlap with two M-point modes (panels b,d,f), or with a single M mode (c,e,g). As a consequence, the system is forced to either show SSB between just two instead of three modes, or lasing on just a single M mode. We note that experimental results presented in Fig. 5.4 are not fully symmetric in the contrast which can be achieved by equalizing, or selecting, the three M-modes. For the SSB in Figure 5.4(a), one M-point mode is favored less, and the same effect is seen in panel (f). We argue that these asymmetric results are due to minor asymmetries in the lattice geometry or experiments, to which the M-modes are very sensitive. This finding shows that our method can be used to obtain deeper insight in, and control over, mode competition and spontaneous symmetry breaking in amplifying photonic lattices.

5.6 Synchronization of coupled triangular K-point lasers

We now set up a system in which two nearby lasers couple, studying K-point lasing for two closely spaced triangular gain shapes of side length 33 μm. The hypothesis is that the two triangles, each pumped to lasing, couple with each other, since emission from one laser may travel to the other via the waveguide slab that separates them. As before, we record many single-shot lasing sequences to observe spontaneous symmetry breaking. We show selected salient events of high-contrast K-point lasing in the top row of Figure 5.5 and those of K'-point lasing in the bottom row. From left to right, we increase the separation distance by moving the left triangle up-left and the right triangle down-right, along the K-axis diagonal. In Fig. 5.5(a), we study K-point lasing for a separation distance of D = 5 μm. We firstly observe that the Fourier image donut spots are elongated normal to the diagonal spanned by the two triangles. Secondly, we find the real-space envelope forms a supermode that follows the borders of the right triangle but anti-aligns with those of the left triangle. The supermode comes with a central intensity dip, and the intensity pattern (bright at the edges, dim at the center), is that of a single undercoupled laser, with the shape of the enclosing parallelogram. In Fourier space, the emission appears as elongated donut spots, with elongation axis perpendicular to the long axis of the enclosing parallelogram, consistent with the notion that the laser more or less operates as if it had one large contiguous shape. We obtain fully symmetric behavior for high-contrast K'-mode lasing in Fig. 5.5(d) (i.e., identical once mirrored through the horizontal). Increasing the separation distance to D = 10 μm, Fig. 5.5(b,e), we observe fringes in the K-point donut spots along the separation diagonal. The interference fringes in the far-field emission evidence that the two triangles deliver output that adds coherently in the far field. The fringe pattern can indeed be understood from the simple interference between two coherently emitting, spatially separated, triangular patches. Importantly, for the 100-long single-shot time traces, the fringe pattern in each of the 6 output beams hardly varies from shot to shot, which indicates that the relative phase at which both lasers radiate is locked. We substantiate this claim further by measuring relative phase between K/K' lasing at the border of each triangle from the precise patterns resolved to within the microscope resolution limit, and precisely registered to the particle lattice (as in the Appendix of Chapter 4, Sec. 4.6.6). The real-space images, however, display a clear difference from the 'supermodes' belonging to K/K' lasing that we observe in Fig. 5.5(a,d) for the smaller separation. At the larger separation, each shape clearly forms its own spatial intensity distribution with a dip in the center of each triangle, suggesting that the spatial distribution in each triangle is much like in separate undercoupled DFB lasers. Finally, the results for K'-point lasing are again the mirror image of the K-point lasing

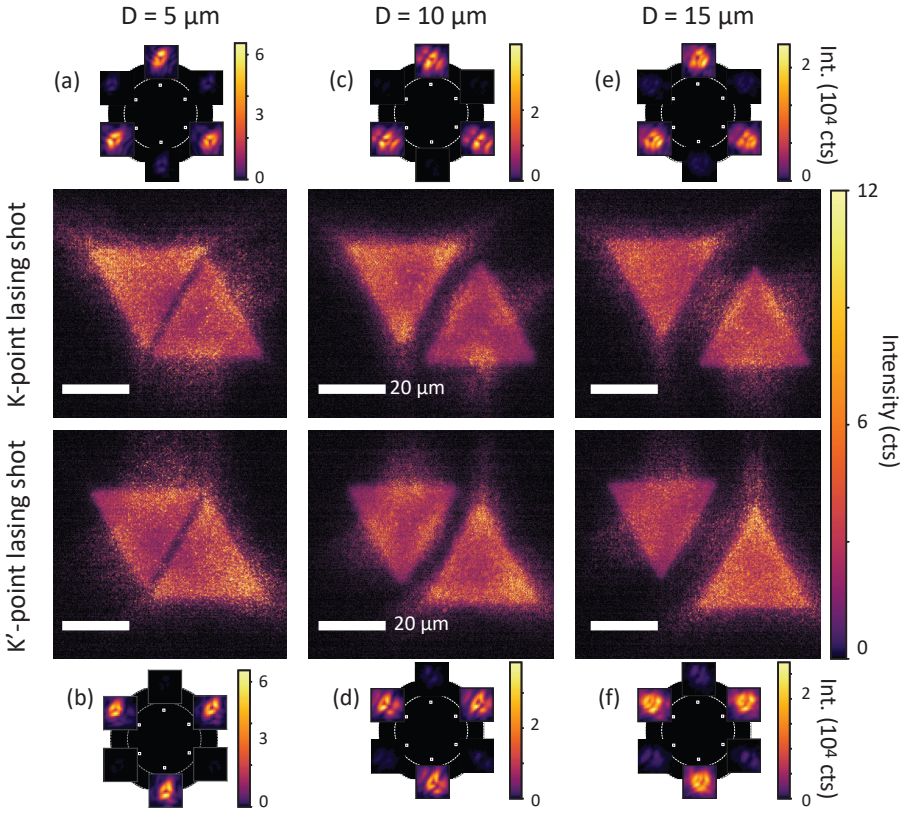

Figure 5.5: Closely spaced triangle lasers with K/K' supermodes in real space. (a-c) Examples of single-shot K-point lasing (Fourier/real space recorded simultaneously) of two triangle lasers as function of separation distance, while (d-f) display examples of K'-point lasing. The triangles have 34.5 µm side length. In the Fourier images, fringes in the donut spots indicate phase synchronization between two triangles, whereas the real space shows supermodes that strongly depend on D, and which are mirror-symmetric between K- and K'-mode lasing. The Fourier image insets extent over $k_{||}/k_0 = 0.06$.

case, both for the real-space envelopes and the Fourier-space output. Finally, for the largest separation recorded, D = 15 µm, Fig. 5.5 (c) and (f) show that the donut-shaped output spots in Fourier space have more closely spaced fringes, consistent with the larger laser separation, and fringe contrast is lower than for D = 10 µm. While this lower contrast might be due to our k-space resolution, it could also hint at a lower mutual coherence. We further observe that this system shows a stronger outcoupling of laser light from the unpumped gap as compared to the D = 10 µm system. We suspect that outcoupling from the gap nontrivially scales with gap width, associated with the phase offset between the lasers as well as the propagation phase accrued on crossing the

gap.

Regarding the synchronization between the two lasers, one can ask if a more complete analysis that does not rest on inspection of just a few laser shots is possible. For instance, to ascertain whether the relative K/K' amplitudes are always locked to each other in each of the two lasers, or whether the two lasers instead are subject to spontaneous symmetry breaking independently. While our Fourier-space imaging approach can not disentangle which triangle contributes which amplitude to the output, we note that the single-shot real-space analysis in Fig. 5.3 shows that for single contiguous shapes, high contrast K/K' lasing comes with distinct triangular real-space mode envelopes. In order to answer if SSB in K/K' relative amplitude occurs in lockstep for the two coupled lasers, we argue that one needs to search for intensity pattern correlations across the time series in the real-space envelopes. This problem is perfectly addressed by the singular value decomposition (SVD) method, a technique widely used to reduce dimensionality in correlated datasets [293–295]. We structure our $N_{\text{ims}} = 100$ long time traces of single-shot real space images of 1100 by 800 pixels ($n_{\text{pixels}} = 880000$) in an array $\boldsymbol{A}$ of shape ($N_{\text{ims}} \times n_{\text{pixels}}$). We then factorize $\boldsymbol{A}$ by the SVD method (Python, numpy implementation of svd): $\boldsymbol{A} = \boldsymbol{U} \cdot \boldsymbol{S} \cdot \boldsymbol{V}^T$, where $\boldsymbol{U}$ ($N_{\text{ims}} \times N_{\text{ims}}$) and $\boldsymbol{V}^T$ ($N_{\text{ims}} \times n_{\text{pixels}}$) are left-hand and right-hand orthonormal eigenvectors (T denotes transpose

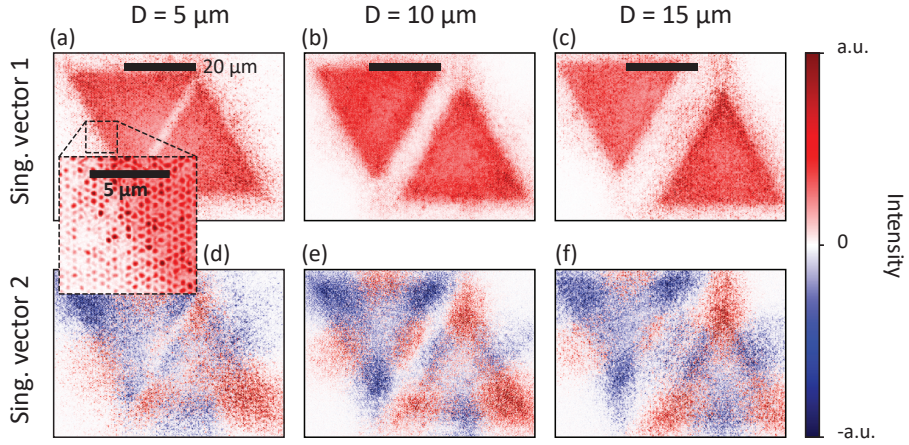

Figure 5.6: Amplitude synchronization of coupled lasers revealed by singular value decomposition (SVD). For increasing separation distance D, (a-c) display the first singular vectors in a SVD analysis on 100-long time series of single-shot real-space images. Note how these capture the microscopic real-space intensity mode of the hexagonal lattice. (a) The real-space envelope extends over the full parallelogram shape formed by the two closely spaced lasers. In panel (b) and (c), on the other hand, the separation is large enough for the two shapes to come with their own undercoupled spatial intensity distribution (intensity dip in center of envelope). (d-f) Second singular vectors that enable the formation of K/K' supermodes.

operation), and $\boldsymbol{S}$ is a diagonal matrix of singular values arranged in decreasing order. The singular vectors (rows in $\boldsymbol{V}^T$) and their associated weights (singular values in $\boldsymbol{S}$) reveal how much the image intensity data is correlated along a time trace of single lasing shots: The singular values represent the weights with which the singular vectors contribute as basis vectors that span the data. The first singular vector relates to the ensemble-averaged intensity, and the following $N_{\text{ims}} - 1$ vectors quantify variations relative to that average, specific to each shot in the time trace.

Figure 5.6 shows the first two singular vectors obtained from our SVD analysis on coupled lasers (in the Sec. 5.8.5 of the Appendix, we also study SVD on single triangle). The first singular vector for D = 5 μm is shown in panel (a). When viewed at high resolution (inset in panel (a)), one can make out a hexagonal fine structure at the periodicity of the lattice ($a = 500$ nm), as reported earlier for the average behavior of K/K'-point lasing [255]. Importantly, the intensity envelope is that of an undercoupled laser of the shape of the circumscribing parallelogram (bright at the edge, less bright in the center), with a stripe of zero intensity at the gap. The second singular vector (Fig. 5.6(d)) shows the most common variation relative to the average: In each triangular lasing shape, it shows two 'downward-pointing' triangles in blue and 'upward-pointing' triangles in red. We interpret this as due to the real-space envelopes associated to K/K'-point symmetry breaking and evidenced in Figure 5.3. Higher-order singular vectors have much smaller singular values and do not show patterns of the opposite symmetry: While singular vector 2 has mirror anti-symmetry relative to the centerline of the gap, no singular vector is found that is mirror symmetric. Therefore, we argue that the two coupled lasers are locked in their SSB behavior. Fig. 5.6(b) and (c) show the evolution of the singular vectors with increased separation. For larger separations, the dominant pattern (lowest order vector) shows that both triangular lasers have intensity envelopes more like single lasers (intensity minima on the inside of the triangles, instead of in-between). The next singular vector shows the same behavior as for the D = 5 μm case, indicating that SSB in the two lasers still dominantly occurs in lockstep, and not independently. In the Appendix (Sec. 5.8.5), we tabulate for the three separation distances the first 6 singular vectors, together with plots of the 100 singular values. While the dominant ones describe the intensity envelopes, the higher-order vectors correspond to fluorescence and imaging shot noise. While for the smaller separations we find no singular vector of opposite symmetry to singular vector 2, for the case D = 15 μm we do find a singular vector of opposite symmetry to singular vector 2. In the 100-shot time series at hand, for instance, it occurs 16 times that this contribution dominates over s_2, meaning that the real-space envelope indicates K-point lasing in one triangle, but K'-point lasing in the other. We thus conclude from our SVD analysis that for $D \leq 10$ μm, the two lasers are always entrained in their K/K'-point SSB, but that this is not necessarily so for D = 15 μm. This indicates that our

experimental method is appropriate to study laser synchronization as function of coupling, which we control by separation distance.

5.7 Discussion

We demonstrate spatially programmable pumping of plasmon DFB lasers and study how various geometries in the pump field affected laser emission in Fourier and real space. For time-averaged measurements, we find that lasers formed by single areas of various geometries (triangular, hexagonal, rectangular) generate spatial intensity distributions with peaks along the boundaries and minima in the center, indicative of undercoupled lasers. The associated donut-like Fourier-space lasing spots increase in size as the laser area reduces and reflect the geometry of the area, in line with the intuition that far-field emission is the Fourier transform of the source distribution at the sample. When recorded in a single-shot fashion, K/K'-point symmetry breaking in relative amplitude generates unique spatial intensity distributions that form triangular mode envelopes of opposite orientation to the triangle of output points spanned in Fourier space. This behavior is irrespective of gain field geometry. Spatial programming can also be used to generate coupled lasing systems at will, as evidenced by our study of two closely spaced but oppositely oriented triangular lasers with varying separation distance. From high contrast fringe patterns in the k-space output, that hardly vary from shot to shot, we conclude that in this system two waveguide-coupled lasers synchronize in phase. From singular value decomposition analysis on real-space images, we conclude the lasers also synchronize in K/K' amplitude. The spatial information that we have access to in this method makes this platform stand out against previous literature that mostly focuses on time-resolved experiments. Such dynamic and spatial lattice laser response control is favorable for applications, and shows the proposed method as a rich playground for studying SSB in amplifying photonic lattice systems. Drawbacks of the method mainly arise from the sample materials: For instance, our studies suffer from cross-linkage of the SU8 polymer upon high-energy fs pumping, which changes the waveguide properties, and from bleaching of the rhodamine that might influence laser dynamics. Such problems can be easily resolved by choosing a less photo-sensitive gain-waveguide material such as quantum dots or a halide-perovskite medium.

We have experimentally observed special triangular spatial intensity distributions for the K/K'-point modes. Although theoretical reproduction of such patterns was beyond the scope of this work, we deem this feasible for instance by CWT methods for hexagonal Γ-point laser as shown in Ref. [296], but adapted to K-point Bloch modes instead. The spontaneous symmetry breaking can be addressed via a density-matrix approach formulated in Refs. [186] and [255]. We envision such numerical endeavors can shed light on rich

unexplored nonlinear dynamics both in time and space of (coupled) lattice lasers. Our work opens opportunities for a large variety of interesting studies. For instance, one could also envision programming through the gain landscape multi-particle hexagonal lattices (honeycomb, kagome), dense band-folded plasmon lattices [279], superlattices of longer periodicity, as well as gain landscapes that are continuously graded in the gain strength.

5.8 Appendix

5.8.1 Measurement protocol

To obtain measurements for various shapes and sizes in main Figs 5.2-5.5, we followed a specific protocol. Before exploring any new pump shape geometry, we navigate to a fresh, previously unpumped patch in the 200×200 um lattice area. If we measure a single shape geometry but for a series of sizes, we start measuring the smallest and then also in the same area measure the ever larger shapes. In runs where we measure two coupled triangular lasers, in a pristine region we first measure the shortest separation

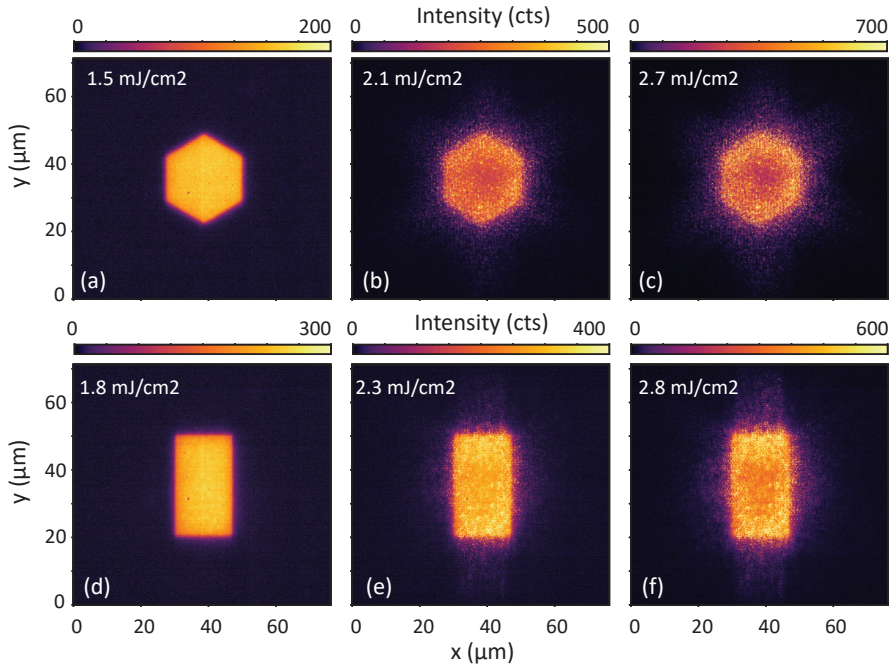

Figure 5.7: Evolution of real space intensity distributions with pump fluence. (a-c) Hexagons of short diagonal 23 um. (e-f) Rectangles of shape (17.3 × 30). At the lowest fluence the signal is due to fluorescence, not lasing. At the intermediate fluence both fluorescence and lasing contribute comparably.

distance, and then measure the larger separations while staying in the same area.

5.8.2 Real-space distributions as function of pump fluence

In coupled wave theory for DFB lasers, the amount of gain influences the nature of the lasing modes (undercoupled, critically coupled, overcoupled). What is more, at higher fluences, various mode envelope solutions may exist above threshold and compete for the gain. In Fig. 5.7, we study the evolution of the real space intensity envelopes with increasing pump fluences. For the both the hexagons (panels a-c) and rectangles (panels d-f) we observe undercoupled envelopes, that do not drastically change their profile for higher gain.

5.8.3 SSB statistics

In Figure 5.8, we tabulate the parity SSB statistics for single-shot time traces for the pump geometries of main Fig. 5.3. This SSB is expressed in the parameter θ that projects the relative amplitude between K and K' lasing on the interval $-\pi/2 < \theta < \pi/2$. We plot θ as a function of pump fluence for $\geq$ 100 shots per fluence interval. SI Fig. 5.8 shows results for a pumped hexagon (panel a), right-oriented triangle (b), upward triangle (c) and downward triangle (d). None of the shape geometries display a significant tendency towards K or K' lasing.

5.8.4 Relative phase fit for coupled lasers

When we project two L = 35 μm triangular lasers with separation distances D = 10 μm and D = 15 μm, clear fringe features appear in the Fourier-space donut-spots (main Fig. 5.5. We attribute the appearance of fringes in far-field emission to mutual coherence between the lasers, and since the fringe pattern does not significantly vary

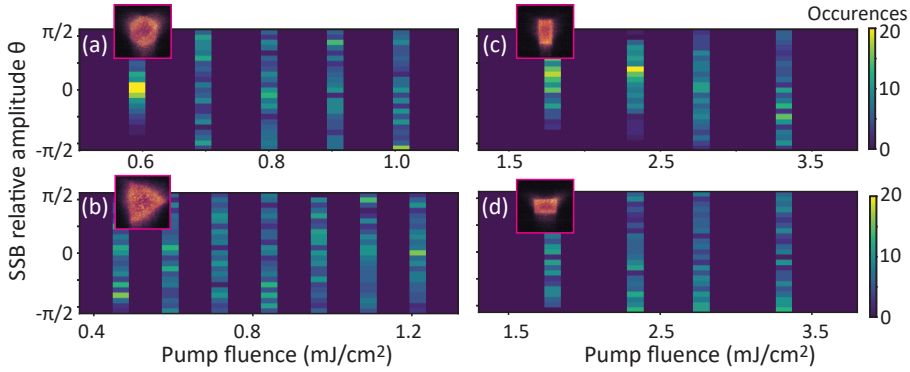

Figure 5.8: Statistics of spontaneous symmetry breaking in relative amplitude. Single-shot time traces of the SSB parameter θ that traces the relative phase between K and K', for the (a) single hexagon (short diagonal 34.5 μm), (b) rotated triangle (side length 53 μm), and (c,d) vertical and horizontal (17.3×30).

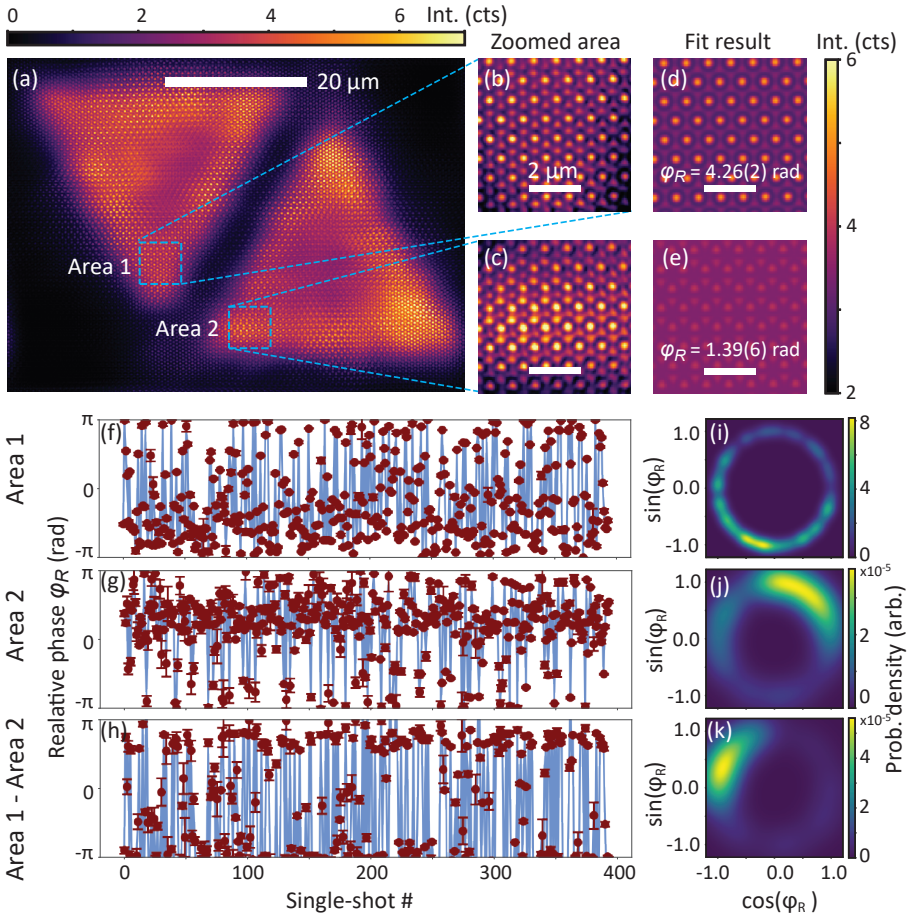

Figure 5.9: Relative phase between K and K' measured on the border of each triangle. (a) Fourier-filtered real-space image, same data as main Fig. 5.5, D = 10 µm. (b,c) Enlargements of two blue areas in (a). (d,e) Fit results to extract relative phase φ_R. (f,g) 400-long time series of fitted φ_R from area 1 and 2, hinting at phase bias to values near $-2\pi/3$ and $\pi/3$, respectively. (h) Difference in measured φ_R, biasing towards $-\pi$. (i-k) Probability density plots of φ_R as projected on the unit circle.

within the recorded time trace of single-shot lasing, we argue that the two lasers synchronize with a definite, reproducible phase. We substantiate this claim by measuring the relative phase between K and K' on a border area of both triangles, a bias in the difference between the two measured phases signifies phase-locking. To measure phase for triangle separation D = 10 μm, we follow the protocol laid out in detail in Sec. 4.6.7 in the Appendix of Chapter 4. First, we Fourier-filter the real-space image and find that the fast-Fourier transform displays 25 components. We mask the Fourier components with a Gaussian filter of width 1.07 μm^{-1}, before inverse-fast Fourier transform the image back to the real space, see single-shot example in Fig. 5.9. The Gaussian width corresponds to a real-space resolution of 5.86 μm or 100 pixels. In panels (b,c,) we show enlargements of 5.86 μm large square areas selected in panel (a). Here, the microscopic detail of the filtered real-space image displays the superlattice patterns that we recognize from Chapter 4 as interference between the plane-wave triplets of K and K'. In Sec. 4.6.7, we explain that by fitting the plane waves of the K and K' modes, $E_T(\mathbf{r}) = aE_K(\mathbf{r}) + bE_{K'}(\mathbf{r})e^{i\varphi_R}$, to the hexagon/honeycomb superlattice patterns, one can retrieve relative phase φ_R. The results are shown in Figure 5.9(d,e). We apply this method to a time-trace of 400 single shots, extracting φ_R in both regions. Already in these time series, clear bias in φ_R is visible for both areas: Area 1 tends towards $-2\pi/3$ (panel f) whereas area 2 towards $\pi/3$ (panel g). Their difference is close to $-\pi$ (h). The phase bias in the time series is better visualized by projecting the phase on the unit circle (See Chapter 4 Fig. 4.4). In these projections, shown in Fig. 5.9(i-k), the phase fit error sets the width of the unit circle and the resulting histogram displays a probability density of measured phases. Clearly, the biased behavior is also reflected in these density histograms.

5.8.5 SVD of real-space intensity distributions

We apply the singular value decomposition method to the real-space lasing images in order to find similarities in SSB behavior among the single shots within the time trace. We first study single triangularly shaped lasers in Figure 5.10 of side lengths L = 58 μm (first six singular vectors shown in panels a-f), L = 46 μm (panels g-l), L = 35 μm (panels m-r). For a time series of 100 shots, it turns out that the first six singular vectors compose most of the signal of the lasing emission and fluorescence background, as indicated by the singular value plots in panels (s-u). The singular values drop in significance after about 6 indices. Only the first few vectors play a role in generating the signal content of single-shot data, all remaining vectors are required to compose random (shot) noise of fluorescence and lasing speckle. From the singular vector plots in Fig. 5.10, it can be seen that as the triangle area gets smaller, the boundaries and corners become increasingly sharp. What is more, from the enlarged insets for L = 46 μm, panels (g-i), one can see hexagonal intensity patterns on a microscopic level in high resolution. Vectors 3 and 4 (panels i,j) show hexagonal features in both negative (blue) and positive (red) intensities, these are likely used to generate the hexagonal/honeycomb superlattice patterns that we also observe after Fourier filtering (See Fig. 5.9).

Finally, in Figure 5.11, we provide a tabular overview of singular vectors and values corresponding to the coupled-triangle results shown in main Fig. 5.5. We perform SVD on 100-long single-shot sequences. Panels (a-f) show singular vectors for separation distance D = 5 μm, together with enlarged insets highlighting microscopic,

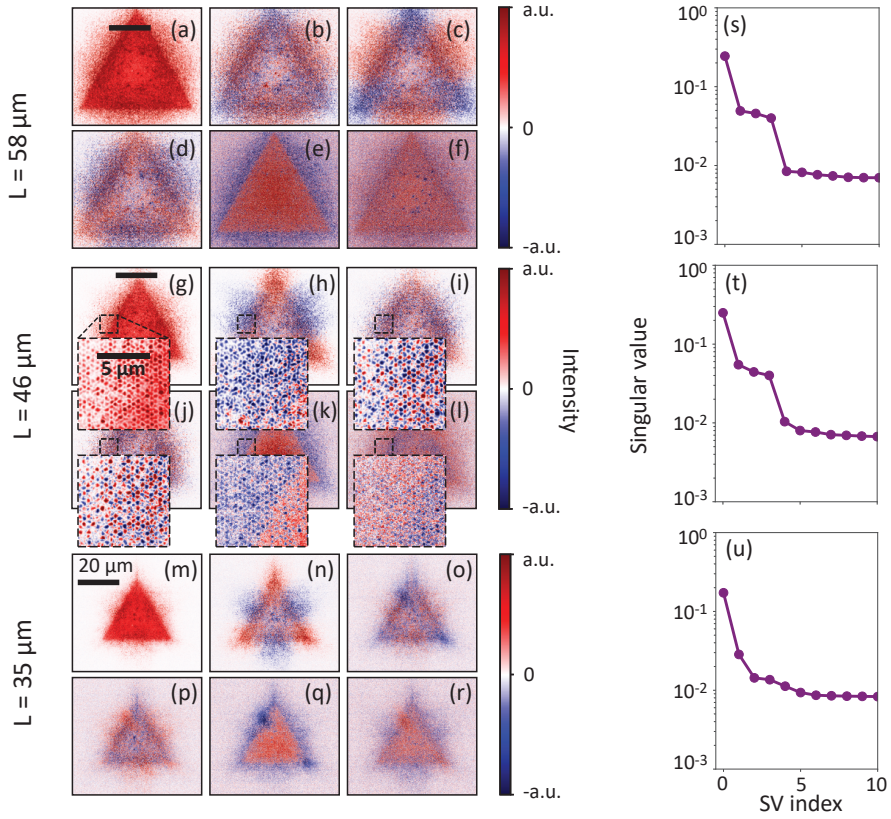

Figure 5.10: Singular value decomposition results for single triangular lasers. (a-f) First six singular vectors in the SVD method applied on a single-shot real-space lasing image of a L = 58 µm triangle triangle. (g-l) First six singular vectors for a 46 µm triangle, together with six enlarged images in which hexagonal features on a microscopic level are visible. (m-r) Singular value decomposition results for a L = 35 µm. (s-u) First ten singular values associated to vectors displayed in left.

hexagonal details. Panel (a) represents the ensemble average of the sequence, and shows signature of undercoupled lasing (intensity dip in center) throughout the total shape of two lasers combined. In contrast, when D = 10 µm or 15 µm, Fig. 5.11(g) and (m) show the undercoupled signature in both lasers *individually*. Moreover, importantly, for D = 5 µm and D = 10 µm only one singular vector composes the typical triangular intensity distribution associated to K/K' lasing, namely panels (b) and (h) respectively. This is not the case anymore when D = 15 µm, since Fig. 5.11(q) shows a pattern that allows K-lasing in one triangle and at the same time K' lasing in the other.

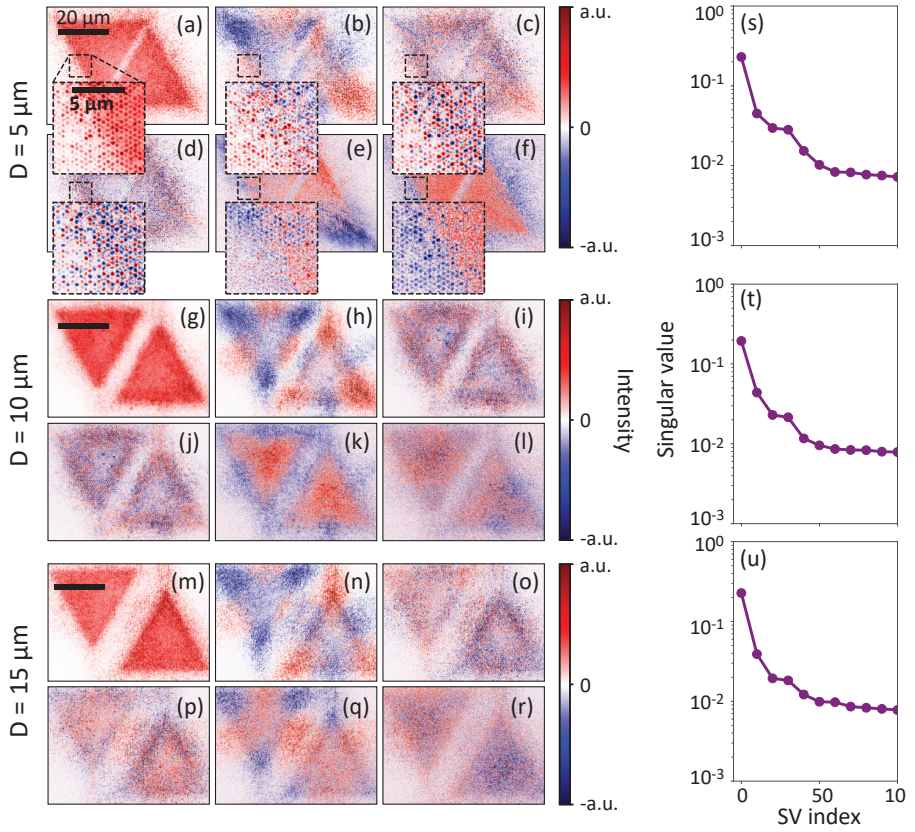

Figure 5.11: Overview of SVD results for coupled triangular lasers, with side length L = 35 µm and increasing separation distance. (a-f) First six singular vectors for D = 5 µm, with enlarged areas that display microscopic detail. (g-l) Singular vectors for D = 10 µm.. (m-r) Singular vectors for D = 15 µm. (s-u) Singular values for the three separation distances.

Chapter 6

Accessing beyond-light line dispersion and high-Q resonances of dense plasmon lattices by bandfolding

Dense plasmon lattices are promising as experimentally accessible implementations of seminal tight-binding Hamiltonians, but the plasmonic dispersion of interest lies far beyond the light line and is thereby inaccessible in far-field optical experiments. In this work, we make the guided mode dispersion of dense hexagonal plasmon antenna lattices visible by bandfolding, induced by perturbative scatterer size modulations that introduce supercell periodicity. We present fluorescence enhancement experiments and reciprocity-based T-matrix simulations for a systematic variation of perturbation strength. We evidence that folding the K-point into the light cone gives rise to a narrow plasmon mode, achieving among the highest reported quality factors for plasmon lattice resonances in the visible wavelength range, despite a doubled areal density of plasmon antennas. We finally show K-point lasing and spontaneous symmetry breaking between the bandfolded K and K' modes, signifying that intrinsic symmetry properties of the dense plasmon lattice are maintained and can be observed upon band folding.

6.1 Introduction

Two-dimensional (2D) periodic photonic systems, such as photonic crystals, plasmonic lattices, metasurfaces, and waveguide arrays, are an interesting arena to study the effects of symmetry and symmetry breaking on wave interactions. For instance, the interaction of light with periodically arranged photonic systems can simulate a plethora of classical solid-state tight-binding Hamiltonians, where control over photonic design allows for versatile control of interaction strengths, symmetries, and defects. This freedom of design combines advantageously with the ability to perform high-resolution imaging of photonic systems in real space and k-space, as well as in the spectral and temporal domain. Example achievements include topological Dirac cone band structures with photonic Hall edge state effects [51, 53, 54, 107, 273], exotic topologies due to Parity-Time (PT) symmetric lattices [92, 94, 186], and, more recently, photonic Landau levels in strained crystals [297, 298]. In another strand of nanophotonics research, the focus is on the interplay of symmetries and resonant scattering. For instance, Mie-resonant meta-atoms, as well as plasmonic nanoparticles, give access to Fano-resonances and bound states in the continuum (BIC) physics [20]. These resonances have implications for strong light-matter interaction, nonlinear optics, and nanolasers. For instance, 2D lattices with gain are studied in the context of plasmon lattice lasers[29, 30, 127, 132, 135, 143, 255], PT-symmetry [92, 94, 102], BIC-based lasers, and topological lasing [136, 138, 186].

In the context of 2D periodic lattices of resonant scatterers, there is particular interest in lattices with short interparticle distances with respect to free space radiation wavelength, i.e., subwavelength pitch. For instance, many theoretical reports [92, 97, 104, 106–108, 186] have addressed plasmon particle lattices with strong $1/r^3$ near-field interactions as possible classical analogs of tight-binding Hamiltonians. Short distances provide strong nearest-neighbor interactions and, at the same time, forbid diffractive coupling to the radiation continuum. This should be contrasted to the limit of large periodicities. In this limit, the physics is not dominated by nearest-neighbor interactions but by surface lattice resonances (SLR) – collective oscillations in which localized resonances (either plasmonic or Mie resonances) hybridize with grating anomalies. According to theory, dense plasmonic lattices imbued with gain can be designer realizations of non-Hermitian Hamiltonians with physics typical for the field of PT (parity-time) symmetry breaking and topology [92, 102, 186]. For instance, in kagome plasmon lattices, plasmonic interactions are expected to express in optical angular momentum-coupled chiral topological edge modes [110]. In active honeycomb lattices, symmetry-broken unit cells are predicted to lead to topological chiral lasing [186]. At PT-symmetry breaking conditions in such lattices, K-point Dirac cones are expected to evolve into rings of exceptional points [92], where the mode structure becomes pseudo-chiral. Despite these interesting theory proposals, experimentally dense plas-

monic lattices have hardly been addressed. Experiments on plasmon lattices have largely focused on the opposite regime, i.e. large periodicities, diffractive resonances, and the benefits of surface lattice resonances (SLRs) for sensing, light emission, and lasing [30, 127, 135, 143, 255]. In such conventional plasmon lattice scenarios, the band structure of interest can be directly mapped by far-field Fourier microscopy in a high numerical aperture microscope. A key practical obstacle towards studying dense, strongly interacting lattices is that the proposed physics pertains to deeply subwavelength pitches, resulting in Brillouin zones that extend well beyond the light line. Since the lattice modes of interest have wave vectors that lie far beyond the light line, they cannot be accessed using standard far-field microscopy.

In this Chapter, we explore the band structures of dense plasmonic lattices beyond the light line through a technique called band folding [92, 102]. The core idea is the following: Starting from a dense lattice of subwavelength pitch, one applies a periodic supercell of slight perturbations in particle size. The reciprocal lattice vectors of the supercell then fold the original beyond-the-light line dispersions back into the light cone. Band folding has been applied to surface plasmon polaritons [299–301] and photonic crystal slabs [302–311], and is currently receiving attention in the community of dielectric metasurfaces as a route to creating quasi-BICs by symmetry breaking [20, 312–314]. In this work we perform a systematic simulation and experimental study of the effect of band folding on the full band structure of dense plasmon metasurfaces, studying both fluorescence and gain scenarios. While there are studies of plasmonic lattices with bipartite unit cells [134, 248, 315–323] and superlattice perturbations [324, 325] only [326] investigated beyond-the-light-line physics of a dense plasmon lattice. We demonstrate that it is indeed possible to fold beyond-the-light-line dispersions into the observable light cone and identify the role of the strength of the supercell perturbation. Our experiments show that in certain folding scenarios, cancellation mechanisms occur in the radiative damping of modes that are reminiscent of reported mechanisms for the formation of BICs in dielectric metasurfaces [20], and that give rise to surprisingly high Q-factor resonances. For instance, we find that perturbed dense lattices can exhibit Q-factors that are 4 to 5 times higher than dilute reference lattices with the same supercell despite having twice the areal density of lossy metal particles. At these conditions, we show plasmon lattice lasing. Folding strategies that leave the original degeneracy of symmetry points intact are furthermore shown to preserve the property of spontaneous symmetry breaking in the lasing behavior, showing that it is possible to preserve main characteristics of the mode structure of the dense lattice despite the folding perturbation. Our work offers a practical route for studying plasmonic counterparts of topological and PT-symmetric Hamiltonians.

6.2 Bandfolding strategies

The main idea of band folding is conceptually visualized in Figure 6.1: The sublattice is periodically perturbed such that diffractive interactions become observable in the far field. As starting point (panel a), we consider a subdiffractive hexagonal lattice, meaning that the lattice constant $a = 160$ nm is not large enough for diffractive coupling of far-field radiation to in-plane surface lattice resonances. The lattice vectors of the dense hexagonal lattice are: $a_1 = (a\sqrt{3}/2, a/2)$ and $a_2 = (0, a)$, and the reciprocal lattice vectors: $G_1 = (\frac{2\pi}{\sqrt{3}a}, \frac{2\pi}{a})$ and $G_2 = (\frac{4\pi}{\sqrt{3}a}, 0)$. To illustrate the basic concept of folded band structures and observables in such a system, we evaluate the minimal coupled-dipole model [10, 38] to calculate "extinction" band structures Fig 6.1(b,c,d). The model (see Sec. 6.7.1 in Appendix for details) ignores both multipole scattering and stratified dielectric surrounding. In the calculated band structure of the dense lattice, Fig 6.1(b), we observe a strongly damped band that is blueshifted compared to the single particle resonance at the Γ-point, redshifting towards the light-cone, as the lattice is subject to radiative damping by plasmon hybridization [121]. Beyond the light cone, sharp bands arise. Here, the collective modes have no radiation damping, and the loss of the resulting guided lattice modes is determined by the mode overlap of the field with the absorptive particles. Band crossings occur at the first order K-points, i.e., beyond the observable light line. Figure 6.1(c) reports a concomitant optical observable, namely far-field reflectivity. The area beyond the light cone is not accessible, while within the light cone, the superradiantly damped dispersion is evident. Next, we implement bandfolding by periodically perturbing the dense lattice. By decreasing particle diameters in every other unit cell, along just the y direction (Fig. 6.1(a)), we form a rectangular superlattice with reciprocal lattice vectors that should fold the beyond-the-light-line dispersion back inside the light line, Fig 6.1(d). Indeed, a replica of the bands near the guided K-point, that were originally only visible beyond the light line (panel c), now become clearly visible in the calculated reflectivity. The perturbation strength controls the contrast of this feature. This simple calculation highlights that bandfolding gives access to beyond-light line dispersion features. At the same time, the model points at a complication to anticipate in folding experiments: The bands in Fig 6.1(d) have asymmetric, Fano-type lineshapes due to mixing of the folded features with direct reflectivity signal.

Aside from choosing the perturbation strength, a nontrivial choice is that of folding periodicity. Two main considerations are pertinent. The first question is how far beyond the light line one wishes to access the dispersion relation. In essence, this consideration requires matching the mode index of the band to be folded with the supercell periodicity, i.e., with the reciprocal lattice vector offered by the perturbation. The second consideration is the symmetry reduction of the superlattice compared to the underlying structure

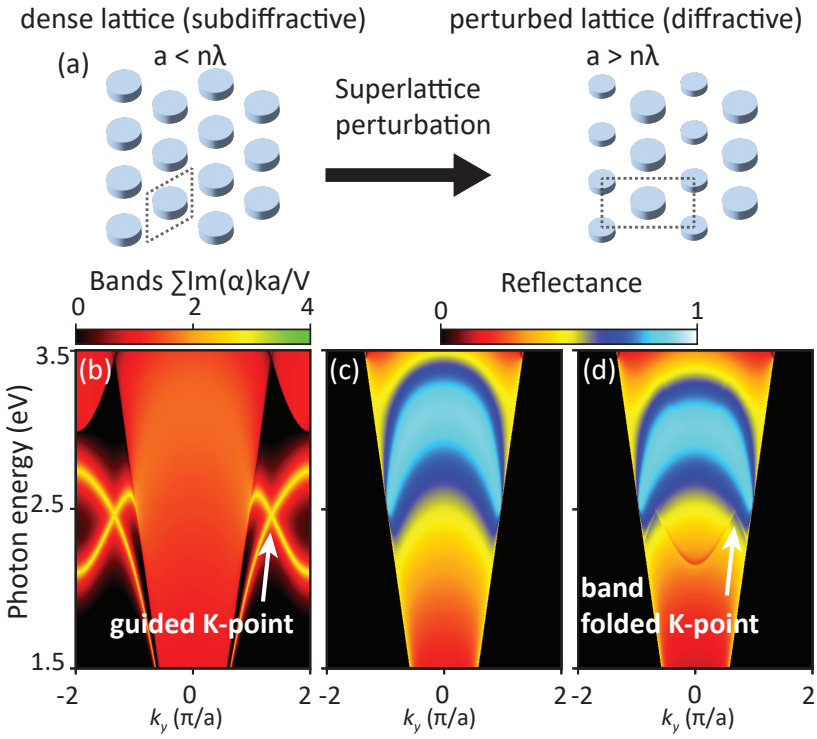

Figure 6.1: Bandfolding by supercell perturbation. (a) The dense lattice has subdiffractive pitch, so we perturb the lattice by antenna size modulations that introduce a supercell with diffractive period. (b) Band structure for a dense plasmon lattice ($a = 160$ nm) as visualized by the sum of the imaginary part of the effective eigenpolarizabilities dressed with lattice interactions in a simple point dipole model – a metric that generalizes the notion of extinction. To bring out only the in-plane band structure, we assume oblate plasmonic ellipsoids (diameter in xy-plane 112 nm, volume $V = 3 \cdot 10^{-22}$ m^3). The K-points are in the guided regime well beyond the light line, not accessible from the far field. (c) Reflectance of the dense lattice shows no photonic bands within the far field radiation cone, except for the broad, superradiantly damped collective plasmon mode at the energy of around 3 eV. (d) Bandfolding induced by perturbing particles of the supercell (12% decrease in x-y diameter). Bloch modes around the K-point become visible due to bandfolding.

that one tolerates. For instance, in the example of Fig. 6.1, a rectangular supercell is used, which evidently reduces the symmetry relative to that of the hexagonal lattice. An excellent and general overview of symmetry considerations for folding has been reported by Overvig et al. [20], on the basis of group representation theory and in the context of designing bound states in the continuum modes. Here, we limit ourselves to discussing practical constraints on supercell periodicity. In Figure 6.2, we display four elementary examples of band folding symmetries that bring a guided K-point mode into the light line, taking the case of hexagonal lattices as an illustrative example. In typical plasmonic and dielectric metasurface scenarios, one could envision that the dispersion of the dense lattice (no superlattice perturbation) is, to first order, like that of a waveguide of mode index n_{eff}, which is repeated at every reciprocal lattice vector. This description is common in the description of, e.g., plasmon lattices in waveguides [10], and also applies to, e.g., perforated dielectric membranes [275]. While plasmon hybridization or photonic crystal effects will generally shift bands, we use this nearly-free-photon repeated zone scheme dispersion to illustrate the considerations for folding strategies.

A first folding strategy (Fig. 6.2(a)) is to introduce a rectangular supercell (lowering the lattice group symmetry of C_6 to C_2), with pitch along y equal to that of the dense lattice, but along x larger than that of the dense lattice by $\sqrt{3}$. A second strategy (panel d) maintains the C_6 symmetry upon perturbation, by choosing as superlattice a hexagonal lattice with twice the pitch of the original. Fig 6.2(b,e) shows the Brillouin zones of the dense lattice (hexagon spanned by red circles) and the superlattice (smaller grey polygon). The dotted line is the light cone set by the index of the surrounding medium. For the rectangular strategy, the three beyond-the-light-line K-points (top one at $k = (0, 4\pi/3a)$ $\mu\mathrm{m}^{-1}$) are repeated by reciprocal lattice vectors of the supercell at a single Δ-point ($k = (0, -2\pi/3a)$ $\mu\mathrm{m}^{-1}$) inside the light line, while the K'-points fold toward Δ'. This is in contrast to the second strategy, second row of Fig 6.2, where, after folding, there are three K-points and three K'-points inside the light line (Fig 6.2(e)). In both superlattice symmetries, the original property that the diffractively coupled K-points are uncoupled from the K'-points remains intact upon folding. Band diagrams in Figs 6.2(c,f) show the dispersion of the dense lattice – visible as the thicker set of black lines – repeated by the superlattice periodicity (replicas indicated as thinner lines).

An important observation from Figure 6.2 is that a given folding strategy only works for a particular range of mode indices. Raising the mode index essentially rescales the frequency axis, moving down the band crossings while maintaining them at the same k-space coordinate. Evidently, at some point this will drop the replica (blue circle in Fig. 6.2(c,f)) below the light cone of the surrounding medium. For the scenarios at hand, this occurs at a mode index contrast above 2. Instead, one needs a smaller superlattice reciprocal lattice vector or, equivalently, a larger supercell. This is demonstrated in the third row of Fig 6.2: The strategy with a rectangular supercell that is effective up

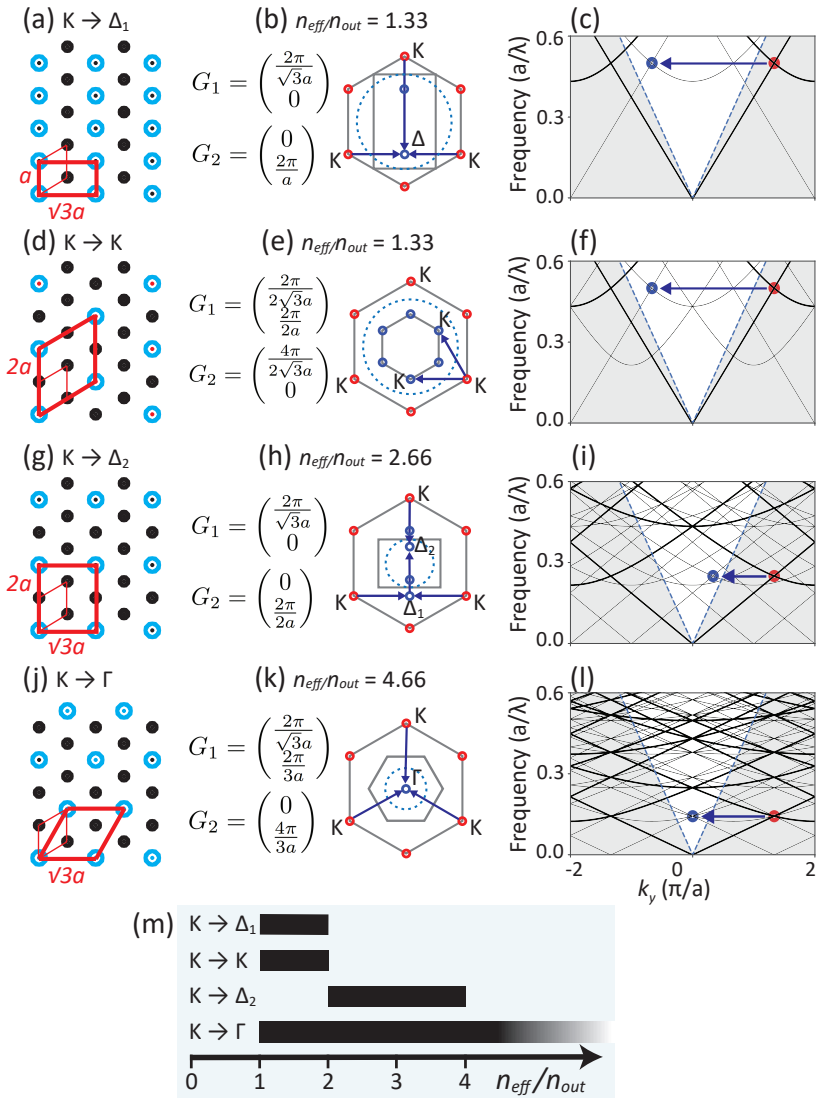

Figure 6.2: Different bandfolding strategies, all starting from a hexagonal dense lattice of lattice constant a. Panel (a) Rectangular superlattice ($\sqrt{3}a$ long in the x-direction) reducing the symmetry from C_6 to C_2. (b) Reciprocal lattice vectors of the rectangular superlattice repeat three guided K-points (corners of the first Brillouin zone indicated with red circles) at the Δ-point (blue circle). Blue dotted circle: Slab light cone. (c) Folded free-photon dispersion for an effective mode index $n_{\text{eff}}/n_{\text{out}} = 1.33$. Bands of the dense lattice (thick black lines) repeat upon superlattice perturbation (thin black lines). (d,e,f) Folding strategy where C_6 symmetry is preserved and 6 K-points emerge inside the light line. (g,h,i) Rectangular superlattice with large lattice constants, required when dealing with larger mode indices. (j,k,l) Strategy that folds K and K' onto each other and onto the Γ-point. (m) Overview of which folding strategies to choose depending on the effective mode index n_{eff} relative to the outside medium n_{out}.

to a 4× larger mode index than that of the surrounding medium. This folding strategy retains the property that the triplet of K-points, and the triplet of K'-points each fold to distinct special points of the rectangular superlattice ($\Delta_{1,2}$-points). Fig 6.2(m) summarizes these considerations: Any mode index at hand needs to be matched to a specific supercell choice, to ensure that one actually folds into the light cone. The one exception is if the superlattice folds the K-points toward the Γ-point, which by construction is always in the light cone. This occurs when the superlattice is hexagonal but rotated by 90 degrees and with $\sqrt{3}$ larger pitch than the dense lattice. With this folding, the K and K' become coupled. This folding design is common in the field of topological photonic crystals [54, 298].

6.3 Measurement of realistic dense plasmonic lattices

We perform fluorescence-based, spectrally resolved Fourier microscopy experiments on dense metasurfaces with folding perturbations. Using electron beam lithography and a liftoff process, we fabricate plasmonic metasurface arrays of constituent cylindrical shaped particles, each 35 nm high but with varying diameters (see Sec. 6.7.4, with fabrication procedure and SEM images). The silver particle arrays on glass are embedded in a 450 nm dye-doped polymer waveguide layer via spin coating with SU8, which is doped with 0.5 wt% rhodamine 6G. As a basis, we take the typical sample structure employed in studies of plasmon-enhanced fluorescence and lasing [28, 29,

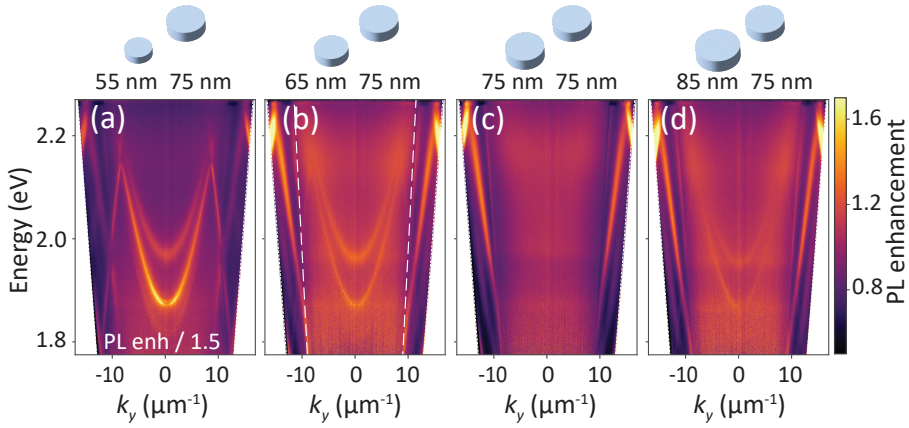

Figure 6.3: Measured fluorescence enhancement band structures of dense plasmonic lattices, for the unperturbed hexagonal dense lattice in (c), and rectangular supercell diameter perturbations in (a), (b) and (d).

327] but designed with subwavelength pitch. This standard geometry has particle lattices fabricated on glass, embedded in a 2D polymer layer that functions both as a waveguide and as a host for the active medium. The waveguide thickness is generally chosen such that in absence of particles, it behaves as a 2D waveguide with a single transverse electric (TE) and a single transverse magnetic (TM) mode. These guided modes dominate the waveguide's local density of states (LDOS), which is beneficial for capturing fluorescence and facilitating lattice resonance formation. As we deal with a mode index of 1.55 on top of glass ($n = 1.45$), our effective mode index contrast is $n_{\mathrm{eff}}/n_{\mathrm{out}} = 1.07$. Therefore we choose the first folding strategy in Fig 6.2(a,b,c). Using an inverted microscope, we excite the dye polymer layer with a 250 fs pulsed pump laser at 515 nm wavelength, with a 1 MHz repetition rate. The back focal plane of the objective is projected onto an imaging spectrometer slit to map the dispersion diagram. The dispersion diagrams are shown as photoluminescence enhancement (PLE), obtained by normalizing the data to similar dispersion diagrams measured on sample area without a metasurface. Experimental details can be found in Sec. 6.7.2.

Three sample geometries are relevant in our experiment. These are, firstly, the unperturbed sub-diffractive hexagonal lattice, referred to as the 'dense lattice' from here on, secondly, the rectangular diffractive reference lattice, referred to as 'empty superlattice', and, lastly the perturbed lattice that should show band folding, which we will refer to as 'dense perturbed lattice'. In Figure 6.3(a)-(d), we observe the progression of fluorescence band structures as we systematically perturb the superlattice particle's diameter from 55 nm to 85 nm in 10 nm increments while keeping the other particle's diameter fixed at 75 nm. We find that at zero perturbation, the dense lattice case, no bands are visible except for quasi-guided modes at an effective mode index of around 1.2. These quasi-guided modes are not particularly related to the plasmon antenna resonances, as they already occur in a simple multilayer model for a polymer waveguide on a thin reflector. Upon introducing superlattice perturbation, folded bands emerge in the dense perturbed lattices, and higher perturbation strength corresponds to increased contrast. In the Appendix (Sec. 6.7.7), all salient band structure features are reproduced and explained by full-wave simulations with the open-source software code *treams*, based on the T-matrix method by Beutel, Fernandez-Corbaton and Rockstuhl [64], where we employ reciprocity [328–331] to relate plane wave far-field angular emission to absorption calculations of incident waves. Note that we do not mean physical absorption by the dye molecules, but instead numerical absorption in the polymer with a small value of non-dispersive $\kappa = 0.006$. As Ref. [328] discusses, this absorption is used as the time inverse of emission in reciprocity-based calculations. From the simulations we learn that the parabolic bands derive from interaction of the particles with the TM waveguide mode (parabola in k-space with minimum at 2.0 eV, no observable stop band) and bandgapped TE bands (lower energy compared to TM band).

The TE modes have the brightest intensity in measured band structures, as the waveguide field aligns with the mainly in-plane nanoparticle polarizability tensor. Polarization-resolved measurements with a linear polarizer crossed to the spectrometer slit confirm the TE/ TM mode assignment from theory (data shown in Appendix Sec. 6.7.5). On a final note, in Sec. 6.7.9, we report band structure measurements for band folding through the second strategy displayed in Fig. 6.2 (row 2, K folds to K). Importantly, we find that dispersions near the K-points are very similar to the bandfolded dispersions near the Δ-points, observed in Fig. 6.4. This means that different folding strategies may be employed to image the same truly guided mode, and that deformation of the original guided dispersion is limited.

A most remarkable feature of the folded band structure arises near the folded K-points, and becomes apparent when analyzing the spectral width of the folded bands. Figure 6.4 shows the dispersion diagrams for the dense perturbed lattice, with the superlattice particle diameter of 55 nm, reproduced from Figure 6.3(a), alongside that of the empty rectangular superlattice (Fig. 6.4(b) versus (f)). Close-ups near the Δ-points / folded K-points reveal a marked difference: In the dense perturbed lattice, there is a clear gap around 2.15 eV at $k_y = 8.5$ μm^{-1}. Additionally, the lower band appears dark right at the special point. This contrasts with the empty superlattice (panel g): At the Δ-point, bands cross, but no avoided crossing or dark area is observed. In a purely free photon picture, i.e., at zero scattering strength, the location of the rectangular lattice bands and the folded dense hexagonal lattice bands would simply overlap at the Δ-point. The difference thus points at the much stronger particle interactions in the dense lattice, which become visible upon bandfolding. To quantify the sharpness of the bands, we evaluate the quality (Q) factors by fitting double-Lorentzian curves to vertical crosscuts through the dispersion data (see Appendix for the fitting procedures), where even the smallest recorded widths of 1.7 nm are still a factor 4 above our spectral resolution. In Figure 6.4(d) and (h), we plot the extracted Q-factors as a function of in-plane momentum k_y for the dense perturbed lattice and empty superlattice, with blue circular and green triangular markers representing the lower and higher energy bands. The fitted center frequencies extracted from the fitting analysis are overlaid on the zoomed ω-k plots in Figure 6.4(c), and (g), displaying only every eighth marker for visual clarity. Remarkably, the Q-factor reaches values as high as Q = 330 near the Δ-point. In comparison, the empty superlattice does not exhibit a Q-increase near the special point, with a maximum Q-factor of only around 110, which is typical for standard diffractive plasmon lattices [255]. This observation is both counterintuitive and surprising: Despite containing twice the amount of metal per unit cell, the dense lattice displays a Q-factor up to three times that of the empty superlattice. Additionally, a Q-factor of 330 is exceptionally high. While reported record Q-factors [332] for plasmon lattice resonances are on the order of 10^3, such high Q-factors are only achieved at

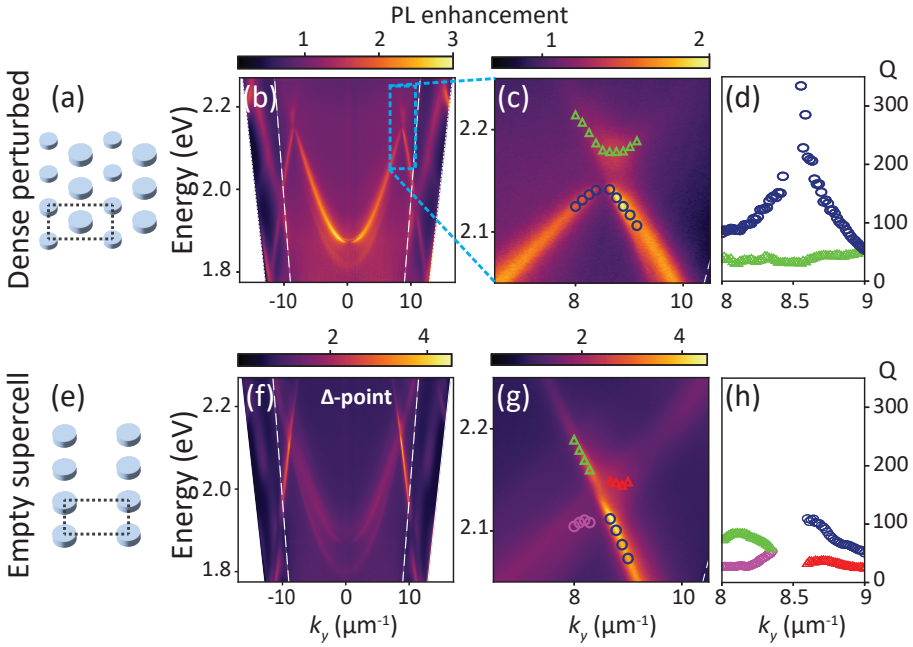

Figure 6.4: Quality factor analysis for bands near the folded K-point / Δ-point. (a) The dense perturbed lattice geometry and (b) its measured fluorescence enhancement band structure, where a linear polarizer with horizontal orientation was placed in front of the spectrometer slit. (c) Zoomed image of the crossing of Bloch modes with the dark spot at the Δ-point. (d) Measured quality factors were obtained by fitting Lorentzian lineshapes through vertical crosscuts in panel (c), with a maximal value of Q=330. The green triangles and blue circles highlight Q-factors along different dispersion branches. (e-h) Results for the rectangular empty superlattice. The dense perturbed lattice shows up to 3 times higher Q near Δ-points than the empty superlattice, despite twice as much metal in the system.

telecom wavelengths (where metal loss is minimized) and observing them usually requires coherent illumination with a very small angular spread, addressing very large metasurface areas. In contrast, our measurement stems from incoherent emission from randomly located and mutually incoherent dipole sources within a relatively small metasurface footprint of only 100 μm across and emitting at 590 nm, where the particle albedo is low. Similar to Ref. [333], our measured Q-factor of 330 near the Δ-point is among the highest measured in the visible wavelength range [255, 315, 334], and is especially remarkable at this large areal density of metal.

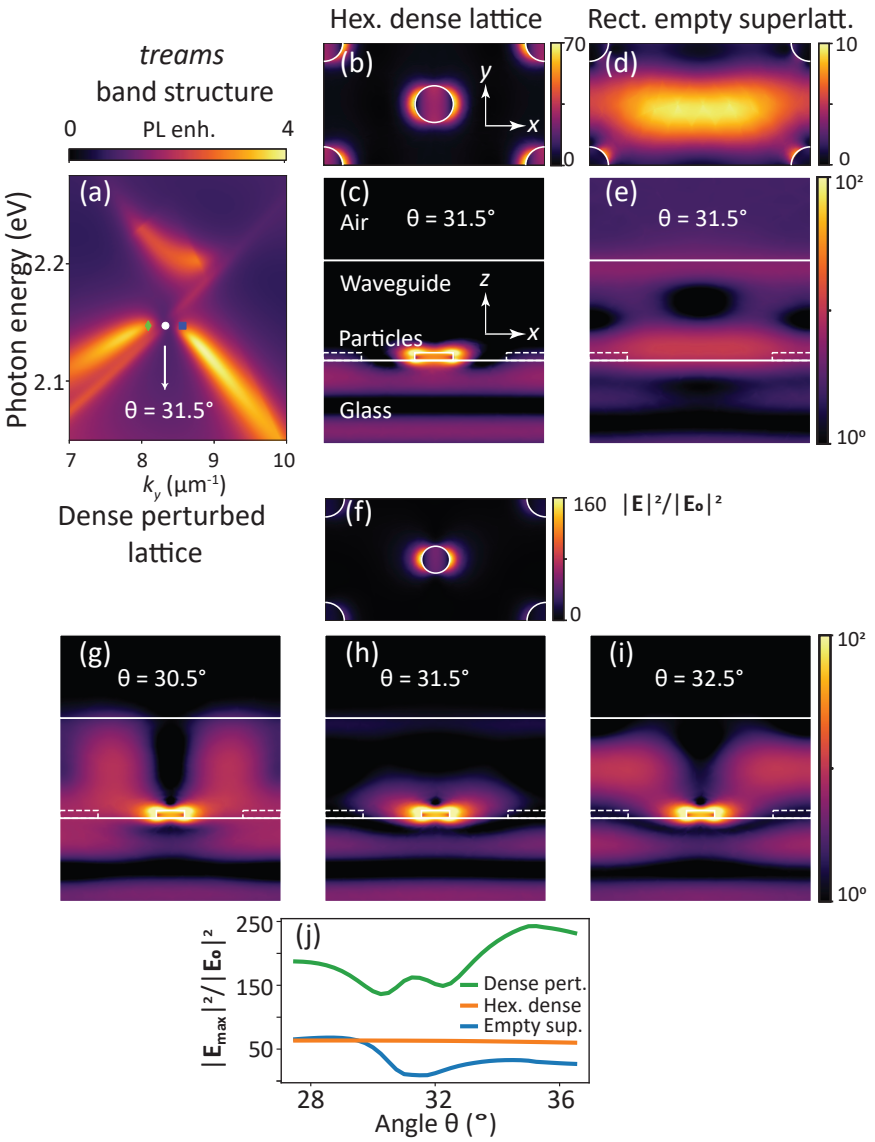

Figure 6.5: Simulations for understanding the dark feature at the folded K-point. (a) T-matrix based *treams* simulation of band structure near the dark spot for the bandfolded K-point. COMSOL simulation of near-field intensity enhancement ($|\mathbf{E}|^2/\ |\mathbf{E}_0|^2$) in the xy and xz planes (cuts midway through the central particle) for (b,c) a hexagonal dense lattice and (d,e) a rectangular superlattice at θ = 31.5° incidence angle at fixed wavelength $\lambda = 577.5$ nm (E = 2.15 eV). (f) Intensity in the xy plane for a perturbed dense lattice at θ = 31.5°. Intensity in the xz plane for incidence angles: (g) θ = 30.5°, (h) θ = 31.5°, and (i) θ = 32.5°. (j) Field intensity enhancement maximum ($|\mathbf{E_{max}}|^2/|\mathbf{E_0}|^2$ as function of θ for hexagonal dense lattice, rectangular empty superlattice, and dense perturbed lattice in orange, blue, and green, respectively. The specific chosen angles are marked and overplotted on the dispersion diagram in panel (a).

6.4 Origin of the dark feature at the folded K-point

To understand the origin of the observed narrow dark mode at the Δ-point, we examine near-field distributions obtained from full-wave simulations (COMSOL). We employ a similar setup to the experiment, driving the structure with plane waves incident from the glass side. Importantly, as a starting point, we require a simulation of a fluorescence band structure near the Δ-point to pinpoint which exact (k_y, ω) plane waves to use in COMSOL simulations to match the Δ-points precisely. For that, we use the *treams* reciprocity code, which is benchmarked against COMSOL to be accurate to within sub-percent levels for angle- and frequency-resolved PLE maps, providing an 850-fold computing speed improvement. The result is shown in Figure 6.5(a), where we clearly see the dark spot at Δ, as in the experiment (Fig. 6.4(c)). We pick three radiation angles (in glass, n = 1.465), $\theta = (30.5, 31.5, 32.5)^\circ$ that tune through the dark Δ-point, at which we perform the COMSOL simulations of near-field distributions (at a wavelength of 577.5 nm ($\sim$ 2.15 eV)). At an incidence angle of θ = 31.5°, the in-plane wavevector ($k_{||}$) closely matches the Δ-point ($2\pi/3a$) at a wavelength of 577.5 nm. In Figures 6.5 (b) and (c), for the dense hexagonal unit cell, the field is primarily concentrated near the particles, and there is no coupling into the waveguide mode. This is consistent with the fact that a sub-diffractive lattice provides no wave vector matching. In stark contrast, the empty rectangular supercell (Figures 6.5(d) and (e)) at this angle shows a field intensity distribution ($|\mathbf{E}|^2 / |\mathbf{E}_0|^2$, normalized to $\mathbf{E}_0$ the field strength of the incident wave) which is typical for diffractive grating coupling from the far field into the waveguide [28, 327]. Notably, Fig. 6.5(f-i) for the dense perturbed lattice shows a delicate cancellation mechanism for waveguide coupling, only at the Δ-point. The reciprocal lattice of this perturbed structure equals that of the empty rectangular superlattice, meaning that waveguide coupling is wave vector allowed. However, right at the Δ-point, coupling to the waveguide mode nearly disappears. As shown in Fig. 6.5(h), although the field within the waveguide is significantly diminished at this angle, it is prominently enhanced right at the central particle in the unit cell. We interpret this formation of a high-Q mode with a strongly enhanced near field in the spirit of reported mechanisms behind the formation of bound states in the continuum. The dominant radiative loss for waveguide SLRs occurs within the waveguide mode. For the dense lattice at zero perturbation strength, this loss channel is strictly forbidden at all wave vectors, which can be viewed in real space terms as a destructive interference between the radiation from the center particle in the unit cell and that from the corner particles spanning the rectangular supercell. Upon perturbation, this destructive interference becomes imperfect and persists most prominently at the Δ-point. It is important to note that this does not represent a strict (quasi)-

BIC mechanism, as out-of-plane radiation loss is not canceled. Additionally, as the angle is scanned through the Δ-point, the near field in the vertical cross cuts changes, forming a distinct two-lobe pattern in the phosphor layer at a 32.5-degree incidence (Fig. 6.5(h)). This shows that both TE and TM waveguide modes are engaged, with mode coupling occurring due to the plasmon particles.

To highlight the different field localizations, we compare the maximum localized field intensity enhancement $|\mathbf{E_{max}}|^2/|\mathbf{E_0}|^2$ in the XY plane, attained just outside the central particle, at different input angles of incidence θ, while scanning through the Δ-point as shown in Figure 6.5(j). The empty rectangular superlattice (blue curve) shows a dip in the maximum local field enhancement at the Δ point, indicating that the field delocalization over the waveguide reduces the near-field intensity. In contrast, the dense hexagonal lattice (orange curve) maintains a nearly constant maximum field enhancement across all angles, suggesting that the field is more uniformly distributed regardless of the incidence angle. This behavior aligns with the absence of a waveguide coupling condition. The dense perturbed lattice achieves a maximum field enhancement of nearly 250, approximately four times higher than in the other cases, commensurate with the higher Q. This distinct behavior of the perturbed case highlights the influence of symmetry and mode interactions on field enhancement and coupling efficiency. This observation is consistent with theoretical works by Refs. [248, 326, 335], which predict that bipartite plasmon lattices can be engineered to achieve significantly enhanced near fields and high-Q modes.

6.5 Plasmon lasing and spontaneous symmetry breaking

Finally, we show that it is possible to study plasmon lasing in dense lattices, appearing as laser emission at the band folded K-point guided modes. In our setup, we have access to femtosecond pulsed pumping (515 nm) and we can capture Fourier-space emission maps in a single-shot fashion with a camera synchronized to the pump laser repetition rate (20 Hz) [255]. At low fluences, we observe fluorescence in Fourier space, as shown in the previous figures. However, when crossing a pump threshold fluence, we observe lasing in spectrally resolved input-output curves, and the Fourier images start to acquire hallmark features of spatial coherence. Examples of these Fourier images are shown in Figure 6.6 for the same perturbation series as in Fig 6.3. Input-output curves of the lasing for the various perturbation cases are shown in Appendix Sec. 6.7.8. In the unperturbed case, Fig. 6.6(c), we observe that the below-threshold diffuse fluorescence image, which has spatially uncorrelated shot noise, is replaced by a high contrast, spatially correlated speckle pattern [130], which evidences the emergence of coherence. On basis of the emission

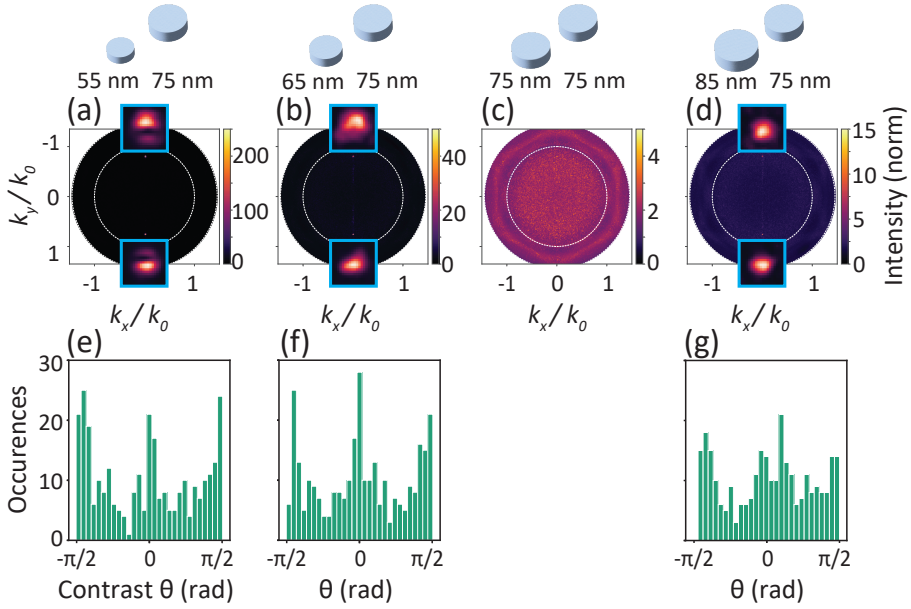

Figure 6.6: Fourier-space images of lasing from bandfolded K-points. Panels (a,b,d) when the dense lattice is diameter-perturbed with a rectangular superlattice, lasing spots appear at the two Δ-points. Panel (c) above threshold, the unperturbed dense lattice displays random speckle patterns as opposed to uncorrelated Poisson statistics typical of fluorescence – a telltale sign of lasing. (e,f,g) The perturbed cases show random fluctuations due to spontaneous symmetry breaking in relative intensity between Δ and Δ'. (e-g) Histograms for time traces of 300 single-shot lasing measurements of the parameter θ, that maps the relative intensity of the two competing modes. Occurrences bunch toward pure Δ and Δ' lasing (at $\theta = \pi/2$ and $-\pi/2$), and to $\Delta + \Delta'$ lasing at $\theta = 0$. The lasing data is normalized by fluorescent signal from a bare waveguide slab (as in a PL enhancement experiment).

wavelength (measured as 579 nm), we attribute it to lasing at the K-points. Since the K-points are beyond the light cone, they are not directly visible. However, laser light is scattered out by residual disorder, e.g. from small particle size fluctuations, filling the back focal plane with speckle. In contrast, for nonzero perturbation, Figs 6.6(a,b,d), the K-point lasing emission is folded into the light cone, and lasing spots appear exactly at the two Δ-points, i.e., at the folded K-points. Insets in Figs 6.6(a,b,d) show enlargements of the lasing spots. Particularly the 55 nm – 75 nm dense perturbed lattice (Fig 6.6(a)) displays the typical donut beam, observed in many plasmonic and dielectric DFB laser works [31, 146, 255], pointing at the quasi-BIC nature of the lasing condition. Polarization topology of the vortex beam could reveal the quasi-BIC nature of the lasing mode involved, and therefore in future experiments we aim to measure polarization in Fourier space using a single-shot Stokes polarimetric setup. We have also observed lasing from dense perturbed lattice

where the M-point is folded towards the Γ-point, with lattice constant $a = 210$ nm (see Sec. 6.7.8). To our knowledge, the dense plasmon lattices investigated in our work are the densest plasmon lattices so far reported to show lasing: Standard Γ-point lasers with rhodamine-doped polymer waveguide layer have pitch of around 390 nm [30], and recently [336] reported high-index InP layers with Au lattice with pitch of 270 nm.

In Chapter 4, we reported that diffractive plasmon lattice lasers of hexagonal symmetry present spontaneous symmetry breaking. In hexagonal lattices, the K- and K'-points feature Bloch modes that are, by construction, degenerate in eigenfrequency and have identical mode patterns up to time-reversal / phase conjugation. Upon crossing the lasing threshold, we found spontaneous symmetry breaking both in relative amplitude between K and K' lasing (parity symmetry) and in relative phase ($U(1)$ symmetry) for such diffractive K-point lasers. This also occurs in dense lattices. In the single-shot lasing experiments with the dense perturbed lattices, large variations in intensity between the Δ- and Δ'-points are apparent from shot to shot. This is in line with the notion of spontaneous symmetry breaking between the guided K- and K'-points, since the three K-points, that together constitute one of the lasing modes, fold to the Δ-point, while the three K'-points, that constitute the other lasing mode, together fold onto the Δ'-point (Fig 1d). In the absence of the folding perturbation, the single-shot lasing data shows speckle patterns that vary from shot to shot, indicating that spontaneous symmetry breaking occurs also for beyond-light line operation.

We map the single-shot spontaneous symmetry breaking in relative intensity between Δ and Δ' in the same phase space as reported in Chapter 4. To this end, from the summed pixel intensities of the two lasing spots, I_Δ and $I_{\Delta'}$, we calculate the parity symmetry breaking parameter θ as: $\theta = 2\arctan(\frac{I_\Delta - I_{\Delta'}}{I_\Delta + I_{\Delta'}})$, which maps contrast between K/K' lasing in terms of the polar angle of a unit sphere. The resulting histograms of occurrences of θ are presented in Figs 5(e,f,g), and can be read as follows: At $\theta = 0$, the Δ and Δ'-point are equally bright, whereas at $\theta = \pm\pi/2$, lasing is purely into Δ- respectively Δ'-points. In all three perturbation cases, the spontaneous symmetry breaking leads to continuous distributions in the phase space, as in the diffractive lattice studied in Chapter 4. Lasing and spontaneous symmetry breaking for the folding strategy of Fig 6.2(d) (which preserves the dense lattice symmetry and repeats 6 K-points inside the light line) is reported in the Appendix, Sec. 6.7.9. These observations show that band folding is an effective strategy to observe salient features of beyond-light line Bloch modes.

6.6 Discussion

In this work, we have shown experimentally and by T-matrix calculations that the dispersion relation of guided modes of dense plasmon lattices can

be accessed by bandfolding, induced by introducing a supercell periodicity by slight modulations in particle diameter. We measure Q-factors of over 300 at the folded K-point of the dense perturbed lattice, three times higher than that of the rectangular empty superlattice. This observation highlights that radiation cancellation mechanisms, that have been well studied in the context of quasi-BIC formation by symmetry breaking [20], also arise in dense multipartite plasmon lattices [337]. We can observe lasing from both the purely guided K-points in a dense plasmon lattice, and from band folded K-points. Yet, our work also highlights subtleties in the bandfolding strategy. First, the chosen supercell must be matched to the effective mode index of interest to ensure that the special points of interest actually fold into the light cone. Second, the strength of the perturbation is a trade-off between making the features of interest sufficiently strongly visible (favoring raising the perturbation to raise the outcoupling strength) and avoiding changing the underlying band structure. Third, we observe that interpretation of the folded band structures is hard for two reasons. On the one hand, the band structures of the empty supercell is qualitatively similar to the folded bands of the dense lattices, with the dense nature of the folded lattices mainly expressing as larger mode splittings. On the other hand, the folded band structure is observed on top of the original scattering response that occurs within the light cone, giving rise to Fano resonances in observables (Fig. 6.1(d)). This work offers opportunities to experimentally study dense plasmon lattices with gain.

6.7 Appendix

6.7.1 Coupled dipole model

We employ the Ewald lattice summation technique for point dipole lattices as reported in [10, 38, 62]. We calculate the *in-plane* band structure (only E fields in x and y directions) by taking scatterers with negligible out-of-plane polarizability. For the polarizability we assume silver ellipsoids with aspect ratio $(x, y, z) = (2.431, 2.431, 1)$, and use experimental permittivity data of silver presented in Ref. [338].

6.7.2 Optical setup

We use the frequency-doubled output of a Light Conversion Pharos laser as pump, with 515 nm wavelength and 250 fs pulse duration. Through an epi-lens and microscope objective (Nikon CFI Plan Apochromat lambda 100×, NA=1.45) we illuminate the sample with a 70µm diameter collinear beam. Pump input power is set by rotating halve-wave plate placed in front of a linear polarizer, and we reject it from the emission signal through a combination of 532 nm dichroic mirror and a 550 nm long pass filter. To create a Fourier image on our detection camera (Thorlabs CS2100M-USB), an insertable Fourier lens can be placed in focus of the back-focal-plane of the objective, via a 1:1 telescope. For single-shot lasing measurements, the electronic signal of the lasers's pulse picker drives the camera. For fluorescence (below threshold) band

structure measurements, we operate at a repetition rate of 1 MHz (multi-shot mode) but at low pump pulse power.

6.7.3 Near field calculations

We use the finite element method (FEM) as implemented in COMSOL Multiphysics 5.2.0 to perform a three-dimensional simulation of the fabricated structure in response to far-field plane wave excitation. The computational domain spans the unit cell in the periodicity plane and extends a few wavelengths into both the substrate and superstrate. We apply Bloch-Floquet boundary conditions at the edges of the unit cell and periodic port conditions at the top and bottom along the illumination direction. Additionally, we employ perfectly matched layers (PMLs) on the exterior boundaries of the ports to absorb any unwanted reflections. The particles are meshed with a nominal element size of 5 nm, while other layers are meshed at 1/6th of the wavelength in that material, and the PMLs are meshed using a sweep distribution method.

6.7.4 Sample preparation

For electron beam lithography and lift off we spin 160 nm PMMA 495-A8 on base-piranha cleaned glass, deposit a 20 nm layer of Germanium (Ge) through thermal evaporation, and then spin a 60 nm CSAR AR-P 6200:09 layer that acts as high-resolution e-beam resist. We expose the CSAR layer using a Raith Voyager 50 KeV at a nominal dose of 140 $\mu C/cm^2$. Once the CSAR resist layer is developed, we etch the Ge and PMMA layers using SF_6 and O_2 plasma after developing the resist layer. This provides for high-resolution holes in the Ge, yet a wide opening in the PMMA that is conducive to liftoff. We then evaporate 35 nm silver (Ag) at a deposition rate of 0.1 nm/s and perform a liftoff process in warm acetone. Scanning electron microscope (SEM) images of the samples are shown in Fig 6.7. Finally, we apply a roughly 0.45 μm thick SU8-based polymer film, doped with 0.5 wt% rhodamine 6G, which functions as the fluorescent waveguide layer.

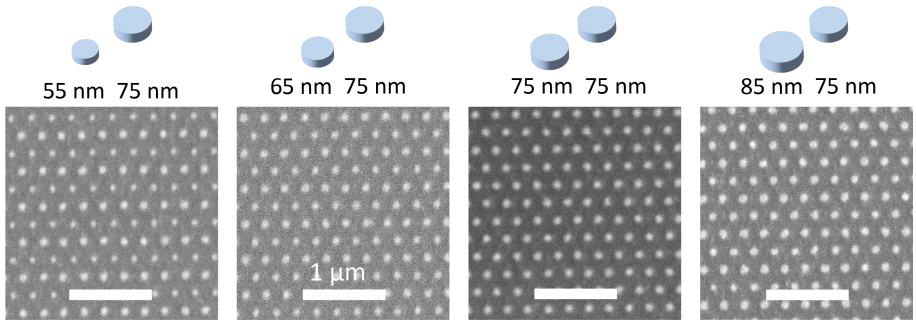

Figure 6.7: SEM images. Scanning electron micrographs of unperturbed (c) and perturbed (a,b,d) dense hexagonal lattices.

6.7.5 Enhancement in 0 and 90 degree polarization

Additional to the fluorescence enhancement band structure measurements in the main manuscript (Fig. 6.3), we record perturbation sweeps in s and p scattering planes by placing a polarizer in front of the spectrometer slit. The results are shown in Fig. 6.8, showing that different bands appear based on polarizer orientation. The TE/TM mode assignment in the main text is based on the assignment rules explained in [131, 132], which are accurate near the $k_{||} = 0$ line.

6.7.6 Lorentzian fits for Q calculation

The measured fluorescence enhancement spectra display narrow bands near the high symmetry points (Fig.6.4(c)). To calculate the quality factors, we take crosscuts along the energy axis near these dispersions and fit curves that are parametrized as the sum of two Lorentzian peaks, plus allowing for a linearly sloping background. The fit proceeds using the Python package lmfit (Levenberg-Marquardt algorithm). The model fits the Lorentz center frequencies, widths, and peak amplitudes. We start the fit procedure for crosscuts well away from the high symmetry point, and then fit crosscuts increasingly close to the symmetry point using the fitted parameters from the previous

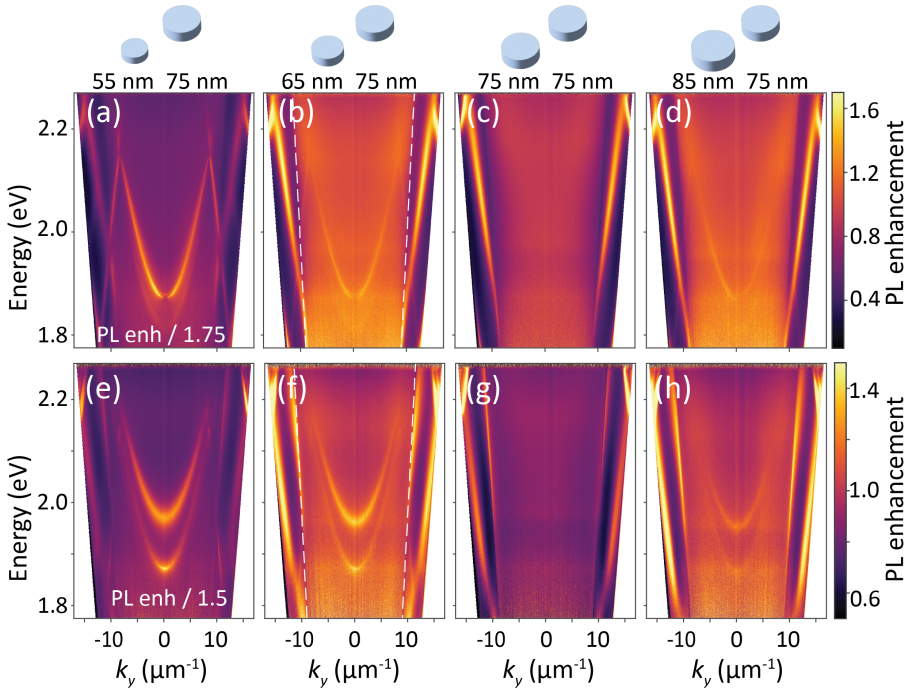

Figure 6.8: Polarization dependent measurements. Fluorescence enhancement band structure measurements with linear polarizer placed in front of spectrometer slit. (a-d) Polarizer oriented horizontally. (e-h) Polarizer oriented vertically.

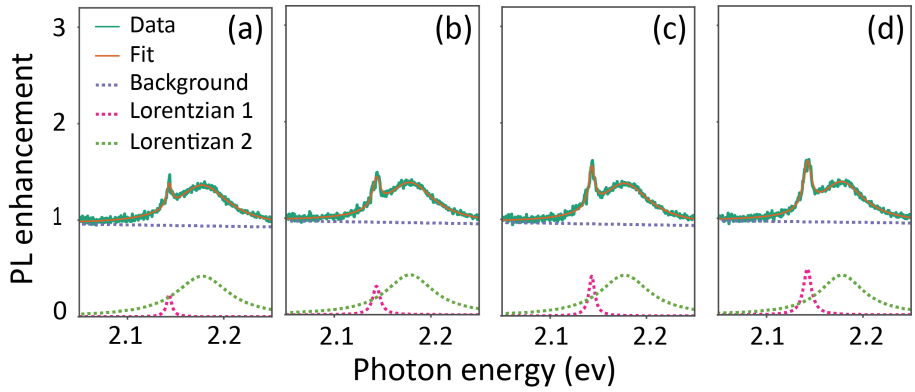

Figure 6.9: Lorentzian peak fitting. Four vertical crosscuts through the fluorescence enhancement band structure measurement (main Fig. 6.4(b,c)), from $k_y = 8.55$ µm^{-1} (a) until $k_y = 8.60$ µm^{-1} (d), each with two fitted Lorentzian peaks and linear background. (a) Q = 334, (b) Q = 228, (c) Q = 285, (d) Q = 212.

cross cut as starting guesses for the next. Example fits that allow to judge the quality of fit are shown in Figure 6.9. The smallest fitted spectral width corresponds to Q=334 in Fig 6.9(a), where $\lambda = 578.6$ nm and spectral width $d\lambda = 1.73$ nm. This width is still a factor 4 higher than our instrument's spectral resolution resolution (Andor Shamrock 163i, with 300 lines per mm grating and 25 µm wide slit).

6.7.7 Band structure simulations using *treams*

We utilize full-wave simulations to predict fluorescence band diagrams of dense plasmonic lattice structures without any of the following approximations: Nearly-free photon dispersion, absence of multipolar interactions, absence of substrates, and perturbative nature of the supercell. We use the open-source software code *treams* based on the T-matrix method by Beutel, Frenandez-Corbaton and Rockstuhl [64]. To calculate the emission properties, we use reciprocity to relate plane wave incident calculations of absorption to far-field angular emission. According to the Helmholtz reciprocity principle, light absorption at a given position originating from the far field is reciprocally linked to the emission of light from the same position toward the far field at the same angle and polarization [328–331]. By employing this method, we can estimate angularly resolved far-field emission and the radiative part of the system's local density of optical states (LDOS). The *treams*-method combines the single object T-matrix with Ewald lattice summation to solve for the two-dimensional periodic arrangement of particles and then employs a multilayer S-matrix formalism to consider stratification, thereby accounting for the layered dielectric system in which the particles are embedded. To set up *treams* we first use the finite element solver JCMsuite to calculate the T-matrices of individual scatterers within a homogeneous medium of index equal to that of the polymer. We assume a 450 nm thick polymer with a refractive index of $n = 1.6$ on glass (n=1.465) and air (n=1) above. To implement the reciprocity method, we assume a numerically very small tracer loss (k = 0.006) in the polymer, excluding

the 35 nm thick layer containing the particles, which must remain lossless for technical reasons. We calculate the volume-integrated absorption enhancement in the polymer layer as a proxy for photoluminescence enhancement (PLE). To map out the dispersion diagrams, we use two linear polarizations (s- and p-polarization) to illuminate from the glass side at various polar angles with $k_x = 0$ for different wavelengths. We plot the polarization averaged absorption, normalized to a reference calculation without particles, as a metric for photoluminescence enhancement (PLE). Benchmarking with FEM simulations with periodic boundary conditions demonstrates better than percent level agreement while achieving an 850-fold speed up.

To obtain a library of T-matrices as function of wavelength and size for nanocylinders we use JCMsuite, which has built-in features to evaluate the multipole decomposition of the scattered field. The refractive index of the cylinder is modeled using Drude's model $\varepsilon(\omega) = \varepsilon_\infty - \omega_p^2/\omega(\omega + i\gamma)$ for silver (Ag) with $\epsilon_\infty = 5.43 + 0.55i$, $\omega_p = 1.39 \cdot 10^{16}$ rad/s, and $\gamma = 8.21 \cdot 10^{13}$ rad/s [339]. Since the T-matrix calculation involves expanding plane waves into vector spherical wave functions, the surrounding environment of the cylinder is considered lossless. We consider multipole order of cylinders up to ($l_{\text{max}} = 5$), i.e., up to the 32 pole or triacontadipolar response. For the lattice sum, we consider propagating diffraction orders (G_{max}) up to a maximum radius of 5 times the reciprocal lattice vector in the reciprocal space.

First, we present the calculated dispersion diagrams for two reference particle array configurations, as illustrated in Figure 6.10. The first configuration is the unperturbed sub-diffractive hexagonal lattice, referred to as the "dense lattice" from here on, shown in panels (a) and (b). The second configuration is the rectangular diffractive reference lattice, named the "empty superlattice" in Fig. 6.10(c) and (d). Following this, we discuss the dispersions that involve band folding, specifically in "dense perturbed lattices," which are shown in Fig. 6.10(e), (f), (g), and (h). The first Brillouin Zone of the dense hexagonal lattice ($a = 250$ nm) in Figure 6.10(a), has the KK-points at its corners just outside the light cone of the glass (outer dotted circle), rendering them inaccessible and truly guided. Thus, there are also no dispersive bands within the air light line in the predicted PL enhancement (Figure 6.10b). A weak but broad dark band, with slight dispersion near 2.1 eV, indicates the absorptive plasmon resonance. Somewhat surprisingly, a set of bands emerges at intermediate wave vectors (effective index $n = 1.2$, i.e., quasiguide modes). They can be understood using an effective medium picture: Similar modes arise in systems where a thin metal partial reflector is placed between the glass and the waveguiding polymer.

Figure 6.10(c) shows the 1st BZ for the rectangular empty superlattice, which is itself rectangular and entirely situated within the light line of the glass substrate (indicated by the dotted outer circle). At this large periodicity, the folded waveguide mode dispersion that falls within the frequency range of interest appears as parabolic bands centered at the Γ points, as shown in Fig. 6.10(d). Also shown are band crossings at the so-called Δ-points, which are situated between the Γ- and X-points. The underlying guided modes are those of the 2D polymer layer, which supports a single transverse electric (TE) and transverse magnetic (TM) polarized mode, with an average mode index of around 1.54 [50]. Colored arrows indicate the contribution of both fundamental TM (green arrow, around 2 eV) and TE modes. The TM waveguide mode has a weak in-plane electric field and is not strongly scattered by the anisotropic, oblate aspect ratio cylindrical plasmonic particles, which primarily have in-plane polarizability. This results in the TM feature being only weakly visible. In contrast, the TE mode is dom-

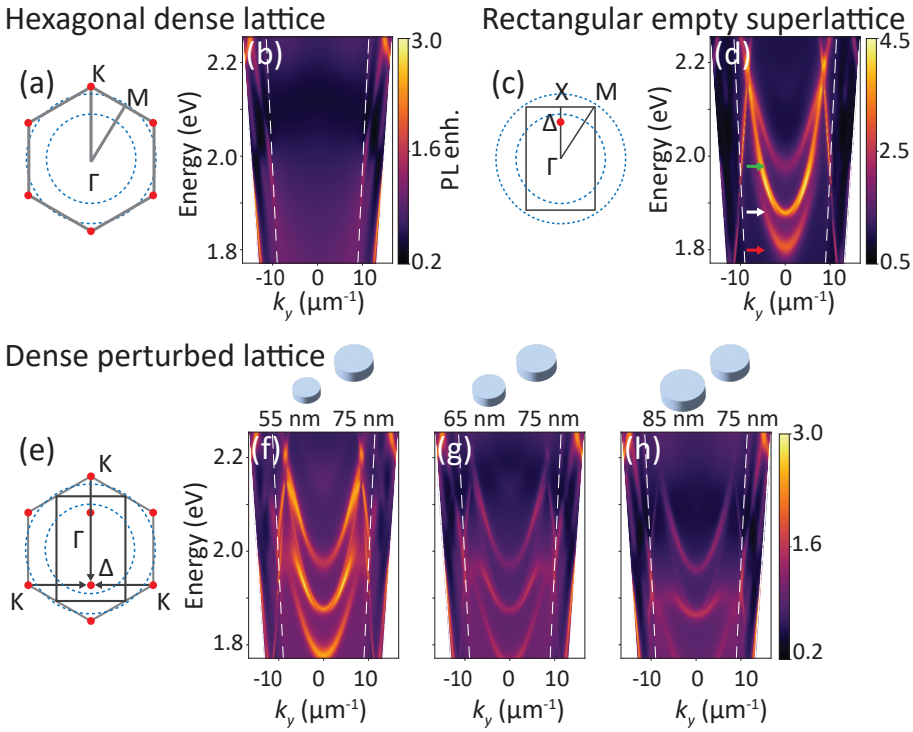

Figure 6.10: ***treams*-simulated band structures.** Reciprocal lattice and simulated dispersion band diagrams using reciprocity for (a-b) a hexagonal dense lattice and (c-d) a rectangular empty lattice, both with a lattice constant of 250 nm and 75 nm diameter nanocylinders. Green arrow: TM waveguide modes. White and red arrow: TE bands. In the bottom panel (e-h), the dense perturbed lattice features two particles per unit cell: One with a fixed diameter of 75 nm and the other with varying diameters of (f) 55 nm, (g) 65 nm, and (h) 85 nm (as shown in the insets).

inantly polarized in the plane of the particles. Consequently, the TE band experiences mode splitting, as indicated by the white and red arrows.

Having established the main features expected for the dense lattice and for the empty superlattice, we now examine the folded band structure of the dense perturbed lattice: The hexagonal system where we introduce a perturbation in the particle diameter for every other row. The results of weak superlattice perturbations with a diameter difference of only 10 nm are shown in Figure 6.10(f-g). The folded bands appear as expected and are only visible as faint features due to the weak perturbation. When the perturbation strength is increased to a 20 nm diameter difference, as illustrated in Fig. 6.10(e), the folded bands become more prominent and exhibit higher contrast. Compared to the rectangular supercell, we observe that the folding does not introduce entirely new bands *per se*; rather, the folded bands of the hexagonal dense lattice qualitatively resemble the bands of the rectangular empty superlattice, as seen in Fig. 6.10(d). However, a closer inspection shows that the band splittings

are significantly different and generally larger. This difference can be qualitatively attributed to the fact that the dense perturbed lattices contain a higher polarizability, which leads to increased scattering per unit cell. Finally, it is important to note that with larger diameter differences, the perturbation not only folds the bands but also changes the band splitting. This is particularly notable with perturbed particles that are enlarged to 85 nm, which display a much larger band splitting compared to cases with smaller perturbations.

6.7.8 Lasing for dense perturbed lattices

Input-output curves. In the main manuscript, we claim the results of Fig. 6.6 are actual lasing output, and as evidence we display in Appendix Fig. 6.11 input-output curves of the lasing wavelength (579 nm), as measured with the spectrometer (exposure time 300 ms, reprate is 20 Hz, so 15 single shots in one camera capture, with 2x2 software pixel binning).

Densest plasmon lattice laser. We show lasing not only from band folded K-points in dense perturbed lattices (Fig. 6.6) of pitch 250 nm, but also for the same perturbation geometry but pitch 210 nm. In this configuration, two M-points fold toward the Γ-point. In terms of antenna areal density this is the densest plasmon lattice laser reported in literature, to the best of our knowledge.

6.7.9 Different folding strategy: Folding from K to K

Fluorescence enhancement band structures. In the main manuscript Figs. 6.3 and 6.3, we displayed measured results for band folding strategy where three K-points are folded to one Δ-point (and K' to Δ'), explained in detail in to the first row of Fig. 6.2. Here, in Fig. 6.13, we show it is also possible to employ the second folding strategy, where K folds towards K of the supercell (panels (a,b)). The first

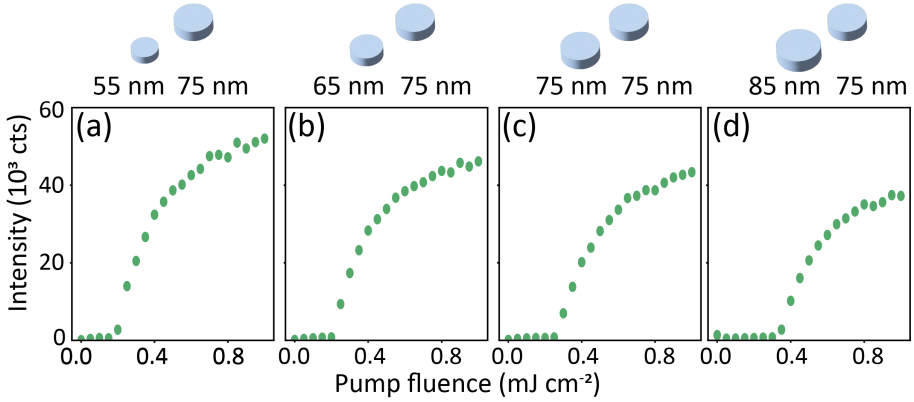

Figure 6.11: Lasing input-output curves. Input-output curves for the dense lattice (c), and the various dense perturbed lattices (a), (b), (d).

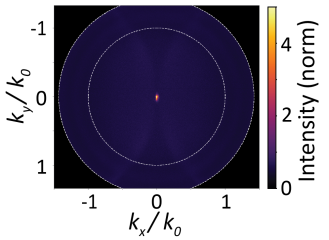

Figure 6.12: Densest plasmon lattice laser. Densest lattice laser at the Γ-point (folded from the M-point). The pitch is 210 nm.

row of experimental band structure data, panels (c-f), shows polarization averaged fluorescence enhancement. As expected, we observe no photonic Bloch modes for the dense lattice, panel Fig. 6.13(e)(same data as Fig. 6.3(c)). Also in this folding strategy, when we apply superlattice perturbations, the measured band structures contain signal of folded photonic bands, their contrast depending on perturbation strength. The contrast of the bands is less pronounced, which might be attributed to the fact that in this case, half of the metal is perturbed, compared with K-Δ folding. In Fig. 6.13(c), dispersions near the Γ-point immediately draw attention, where large band splitting occurs both in the parabolic and linear bands. However, more importantly, inspecting panel (c) and (d), it is evident that the dispersions near the K-point are very alike those bandfolded dispersions near the Δ-point in Fig. 6.3. This is further highlighted by the results in the second and third rows of experimental data are measurements with a polarizer placed before the spectrometer slit, either horizontally oriented (Fig. 6.13(g-j)) or vertically oriented (panels (l-0)): Again, the dispersions near K are very similar to bandfolded dispersions near Γ in Fig. 6.8. This important observation highlights the fact that one can employ different folding strategies to uncover the same beyond-the-light line dispersions. Also in this dataset, a dark spot is observed at the bandfolded K-point, especially visible in panel Fig. 6.13(g).

Lasing and spontaneous symmetry breaking. We study lasing and spontaneous symmetry breaking (SSB) for the K to K bandfolding strategy. Starting with the dense lattice, Fig. 6.14(c) (same data as main Fig. 6.6(c)), the spatially coherent random speckle patterns find their origin in truly guided K-mode lasing. Upon applying superlattice diameter perturbations, the guided K-modes are bandfolded to the K dispersions of the dense perturbed lattices, which support lasing radiation to the far-field. For 10 nm perturbations, Fig. 6.14(b) and (d), the lasing signal is slightly brighter than that of the speckle pattern, but for the 55 nm - 75 nm perturbation case (panel (a)), very sharp lasing intensity peaks are observed.

For each sample we recorded 300 single-shots of lasing output, and we found similar behavior as we reported in Chapter 4 for a diffractive plasmon lattice K-point laser [255]. That is, from shot to shot, the relative intensity between the K and K' laser modes varies randomly, which we attribute to an incomplete bifurcation in a spontaneous symmetry breaking event. With the same methods as described in Chapter 4, we project the intensity data to a subspace of lasing in superpositions of the K and K' modes. The six-vector of lasing intensities in the 6 output spots I (obtained by summing intensity in a small area around each K'-point) is projected on vectors that span K/K', to produce coefficients: $C_+ = \langle I|v_+\rangle$ and $C_- = \langle I|v_-\rangle$ with $v_\pm = 1/\sqrt{6}(1, \pm 1, 1, \pm 1, 1, \pm 1)$. The resulting histograms of Fig. 6.14(e-g) show all

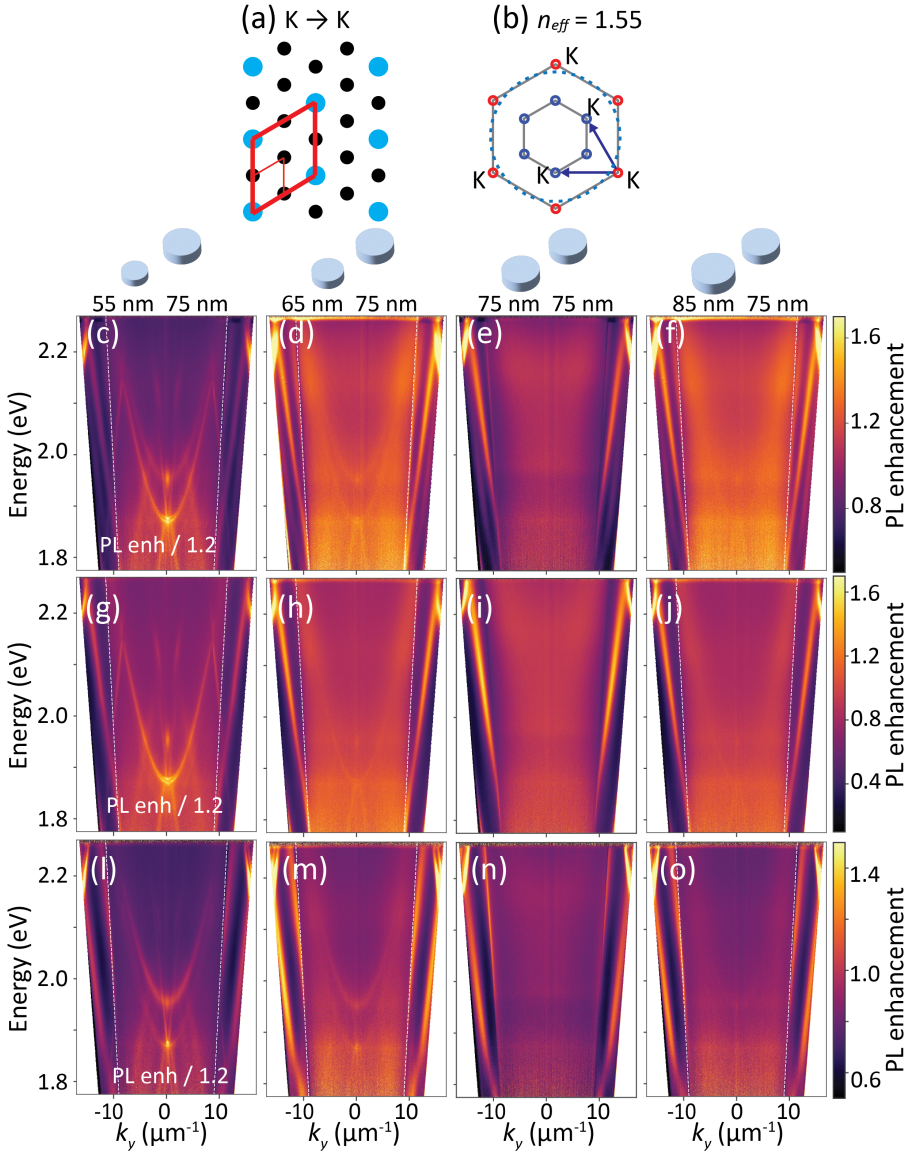

Figure 6.13: Measurements of bandfolding from K to K. (a) Folding strategy where K folds to K, obtained by applying diameter perturbations of double period along the symmetry axes of the hexagonal dense lattice. (b) Three K-points of the dense lattice fold toward three K-points of the dense perturbed lattice. K' folds towards K'. (c-f) Fluorescent enhancement band structures containing emission in all polarization states. (g-j) Band structures with horizontally oriented polarizer in front of spectrometer slit. (l-0) Band structures with vertically oriented polarizer.

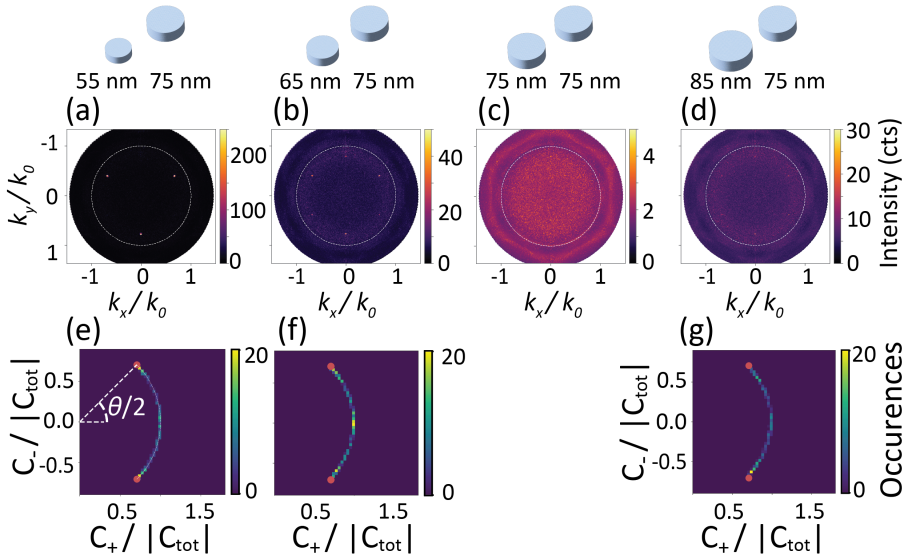

Figure 6.14: Lasing and spontaneous symmetry breaking for bandfolding from K to K. (a-d) lasing data for various superlattice diameter perturbations. (e-g) histograms of parity symmetry breaking, with parameter θ as measure for contrast of K/K' mode lasing. The lasing spot signals are fluorescence background subtracted, by subtracting a same-sized patch directly next to each spot, to generate the histogram plots.

datapoints lie on the arc between the two points $C_+ = \pm C_- = \sqrt{1/2}$ (indicated by red dots). The angle θ of a datapoint on the arc is the spontaneous parity symmetry breaking parameter, and maps to the surface of the unit sphere as polar coordinate. The fact that no datapoints occur within the arc means that the system does not lase in other spot combinations than those corresponding to superpositions of K/K' modes. What is more, in Fig. 6.14(e) as in main Fig. 6.6(e-g), bunching towards the center and towards edges of the arc is observed, which indicates the system either favors K+K' lasing or pure K/K' lasing.

References

[1] J. C. Maxwell, *VIII. A Dynamical Theory of the Electromagnetic Field*, Phil. Trans. R. Soc. **155**, 459 (1865).

[2] H. Amano, N. Sawaki, I. Akasaki, and Y. Toyoda, *Metalorganic Vapor Phase Epitaxial Growth of a High Quality Gan Film Using an Aln Buffer Layer*, Appl. Phys. Lett. **48**, 353 (1986).

[3] W. S. Boyle, and G. E. Smith, *Charge Coupled Semiconductor Devices*, Bell Syst. Tech. J. **49**, 587 (1970).

[4] E. Fossum, *Cmos Image Sensors: Electronic Camera-On-A-Chip*, IEEE Trans. Electron Devices. **44**, 1689 (1997).

[5] K. Kao, and G. Hockham, *Dielectric-Fibre Surface Waveguides for Optical Frequencies*, Proc. Inst. Electr. Eng. **113**, 1151 (1966).

[6] G. Wetzstein, A. Ozcan, S. Gigan, S. Fan, D. Englund, M. Soljačić, C. Denz, D. A. B. Miller, and D. Psaltis, *Inference in Artificial Intelligence with Deep Optics and Photonics*, Nature **588**, 39 (2020).

[7] A. Karabchevsky, A. Katiyi, A. S. Ang, and A. Hazan, *On-Chip Nanophotonics and Future Challenges*, Nanophotonics **9**, 3733 (2020).

[8] L. Novotny, and B. Hecht, *Principles of Nano-Optics* (Cambridge University Press, Cambridge, United Kingdom, 2012), 2nd ed.

[9] A. V. Kildishev, A. Boltasseva, and V. M. Shalaev, *Planar Photonics with Metasurfaces*, Science **339**, 1232009 (2013).

[10] A. Vaskin, R. Kolkowski, A. F. Koenderink, and I. Staude, *Light-Emitting Metasurfaces*, Nanophotonics **8**, 1151 (2019).

[11] J. B. Pendry, D. Schurig, and D. R. Smith, *Controlling Electromagnetic Fields*, Science **312**, 1780 (2006).

[12] C. M. Soukoulis, and M. Wegener, *Past Achievements and Future Challenges in the Development of Three-Dimensional Photonic Metamaterials*, Nat. Photonics **5**, 523 (2011).

[13] N. Yu, and F. Capasso, *Flat Optics with Designer Metasurfaces*, Nat. Mater. **13**, 139 (2014).

[14] H.-T. Chen, A. J. Taylor, and N. Yu, *A Review of Metasurfaces: Physics and Applications*, Rep. Prog. Phys. **79**, 076401 (2016).

[15] N. Yu, P. Genevet, M. A. Kats, F. Aieta, J.-P. Tetienne, F. Capasso, and Z. Gaburro, *Light Propagation with Phase Discontinuities: Generalized Laws of Reflection and Refraction*, Science **334**, 333 (2011).

[16] X. Ni, S. Ishii, A. V. Kildishev, and V. M. Shalaev, *Ultra-thin, planar, Babinet-inverted plasmonic metalenses*, Light Sci. Appl. **2**, e72 (2013).

[17] K. Chen, Y. Feng, Z. Yang, L. Cui, J. Zhao, B. Zhu, and T. Jiang, *Geometric Phase Coded Metasurface: From Polarization Dependent Directive Electromagnetic Wave Scattering to Diffusion-Like Scattering*, Sci. Rep. **6**, 35968 (2016).

[18] N. Yu, F. Aieta, P. Genevet, M. A. Kats, Z. Gaburro, and F. Capasso, *A Broadband, Background-Free Quarter-Wave Plate Based on Plasmonic Metasurfaces*, Nano Lett. **12**, 6328 (2012).

[19] A. C. Overvig, S. C. Malek, and N. Yu, *Multifunctional Nonlocal Metasurfaces*, Phys. Rev. Lett. **125**, 017402 (2020).

[20] A. C. Overvig, S. C. Malek, M. J. Carter, S. Shrestha, and N. Yu, *Selection Rules for Quasibound States in the Continuum*, Phys. Rev. B **102**, 035434 (2020).

[21] A. Chen, and F. Monticone, *Dielectric Nonlocal Metasurfaces for Fully Solid-State Ultrathin Optical Systems*, ACS Photonics **8**, 1439 (2021).

[22] A. Overvig, and A. Alù, *Diffractive Nonlocal Metasurfaces*, Laser Photonics Rev. **16**, 2100633 (2022).

[23] R. Kolkowski, T. K. Hakala, A. Shevchenko, and M. J. Huttunen, *Nonlinear Nonlocal Metasurfaces*, Appl. Phys. Lett. **122**, 160502 (2023).

[24] J. Le Gall, M. Olivier, and J.-J. Greffet, *Experimental and Theoretical Study of Reflection and Coherent Thermal Emissionby a Sic Grating Supporting a Surface-Phonon Polariton*, Phys. Rev. B **55**, 10105 (1997).

[25] J.-J. Greffet, R. Carminati, K. Joulain, J.-P. Mulet, S. Mainguy, and Y. Chen, *Coherent Emission of Light by Thermal Sources*, Nature **416**, 61 (2002).

[26] C. Wiesmann, K. Bergenek, N. Linder, and U. Schwarz, *Photonic Crystal LEDs – Designing Light Extraction*, Laser Photonics Rev. **3**, 262 (2009).

[27] D. Costantini, A. Lefebvre, A.-L. Coutrot, I. Moldovan-Doyen, J.-P. Hugonin, S. Boutami, F. Marquier, H. Benisty, and J.-J. Greffet, *Plasmonic Metasurface for Directional and Frequency-Selective Thermal Emission*, Phys. Rev. Appl. **4**, 014023 (2015).

[28] G. Lozano, D. J. Louwers, S. R. Rodríguez, S. Murai, O. T. Jansen, M. A. Verschuuren, and J. Gómez Rivas, *Plasmonics for Solid-State Lighting: Enhanced Excitation and Directional Emission of Highly Efficient Light Sources*, Light Sci. Appl. **2**, e66 (2013).

[29] W. Zhou, M. Dridi, J. Y. Suh, C. H. Kim, D. T. Co, M. R. Wasielewski, G. C. Schatz, and T. W. Odom, *Lasing Action in Strongly Coupled Plasmonic Nanocavity Arrays*, Nat. Nanotechnol. **8**, 506 (2013).

[30] A. H. Schokker, and A. F. Koenderink, *Lasing at the Band Edges of Plasmonic Lattices*, Phys. Rev. B **90**, 155452 (2014).

[31] S. T. Ha, Y. H. Fu, N. K. Emani, Z. Pan, R. M. Bakker, R. Paniagua-Domínguez, and A. I. Kuznetsov, *Directional Lasing in Resonant Semiconductor Nanoantenna Arrays*, Nat. Nanotechnol. **13**, 1042 (2018).

[32] E. Hutter, and J. H. Fendler, *Exploitation of Localized Surface Plasmon Resonance*, Adv. Mater. **16**, 1685 (2004).

[33] P. Zijlstra, M. Orrit, and A. Femius Koenderink, in *Nanoparticles: Workhorses of Nanoscience*, edited by C. de Mello Donegá (Springer, Berlin, Heidelberg, 2014), pp. 53–98, ISBN 978-3-662-44823-6.

[34] A. F. Koenderink, *On the Use of Purcell Factors for Plasmon Antennas*, Opt. Lett. **35**, 4208 (2010).

[35] C. Bohren, and D. R. Huffman, *Absorption and Scattering by Small Particles* (John Wiley & Sons, New York, United States, 1983).

[36] N. W. Ashroft, and N. D. Mermin, *Solid State Physics* (Saunders College

Publishing, New York, United States, 1976).

[37] P. de Vries, D. V. van Coevorden, and A. Lagendijk, *Point Scatterers for Classical Waves*, Rev. Mod. Phys. **70**, 447 (1998).

[38] F. J. García de Abajo, *Colloquium: Light Scattering by Particle and Hole Arrays*, Rev. Mod. Phys. **79**, 1267 (2007).

[39] N. Katsarakis, T. Koschny, M. Kafesaki, E. N. Economou, and C. M. Soukoulis, *Electric Coupling to the Magnetic Resonance of Split Ring Resonators*, Appl. Phys. Lett. **84**, 2943 (2004).

[40] I. Sersic, M. Frimmer, E. Verhagen, and A. F. Koenderink, *Electric and Magnetic Dipole Coupling in Near-Infrared Split-Ring Metamaterial Arrays*, Phys. Rev. Lett. **103**, 213902 (2009).

[41] B. Wang, P. Yu, W. Wang, X. Zhang, H.-C. Kuo, H. Xu, and Z. M. Wang, *High-Q Plasmonic Resonances: Fundamentals and Applications*, Adv. Opt. Mater. **9**, 2001520 (2021).

[42] S. Kruk, and Y. Kivshar, *Functional Meta-Optics and Nanophotonics Governed by Mie Resonances*, ACS Photonics **4**, 2638 (2017).

[43] K. Koshelev, and Y. Kivshar, *Dielectric Resonant Metaphotonics*, ACS Photonics **8**, 102 (2021).

[44] Y. Kivshar, *The Rise of Mie-Tronics*, Nano Lett. **22**, 3513 (2022).

[45] Q. Zhao, J. Zhou, F. Zhang, and D. Lippens, *Mie Resonance-Based Dielectric Metamaterials*, Mater. Today **12**, 60 (2009).

[46] L. Wang, S. Kruk, K. Koshelev, I. Kravchenko, B. Luther-Davies, and Y. Kivshar, *Nonlinear Wavefront Control with All-Dielectric Metasurfaces*, Nano Lett. **18**, 3978 (2018).

[47] C. Zou, J. Sautter, F. Setzpfandt, and I. Staude, *Resonant Dielectric Metasurfaces: Active Tuning and Nonlinear Effects*, J. Phys. D: Appl. Phys. **52**, 373002 (2019).

[48] F. Bijloo, K. Murzyn, F. van Emmerik, A. J. den Boef, P. M. Kraus, and A. F. Koenderink, *Near-Unity All-Optical Modulation of Third-Harmonic Generation with a Fano-Resonant Dielectric Metasurface*, Nano Lett. **24**, 12942 (2024).

[49] K. Sakoda, *Optical Properties of Photonic Crystals*, Springer Series in Optical Sciences (Springer-Verlag, Heidelberg, Germany, 2005), 2nd ed.

[50] H. P. Urbach, and G. L. J. A. Rikken, *Spontaneous Emission from a Dielectric Slab*, Phys. Rev. A **57**, 3913 (1998).

[51] F. D. M. Haldane, and S. Raghu, *Possible Realization of Directional Optical Waveguides in Photonic Crystals with Broken Time-Reversal Symmetry*, Phys. Rev. Lett. **100**, 013904 (2008).

[52] K. Sakoda, *Universality of Mode Symmetries in Creating Photonic Dirac Cones*, J. Opt. Soc. Am. B **29**, 2770 (2012).

[53] G. Weick, C. Woollacott, W. L. Barnes, O. Hess, and E. Mariani, *Dirac-Like Plasmons in Honeycomb Lattices of Metallic Nanoparticles*, Phys. Rev. Lett. **110**, 106801 (2013).

[54] L.-H. Wu, and X. Hu, *Scheme for Achieving a Topological Photonic Crystal by Using Dielectric Material*, Phys. Rev. Lett. **114**, 223901 (2015).

[55] M. S. Dresselhaus, G. Dresselhaus, and A. Jorio, *Group Theory* (Springer-Verlag, Heidelberg, Germany, 2008).

[56] W. M. Robertson, G. Arjavalingam, R. D. Meade, K. D. Brommer, A. M. Rappe, and J. D. Joannopoulos, *Measurement of Photonic Band Structure in a Two-Dimensional Periodic Dielectric Array*, Phys. Rev. Lett. **68**, 2023 (1992).

[57] K. Sakoda, *Transmittance and Bragg Reflectivity of Two-Dimensional Photonic Lattices*, Phys. Rev. B **52**, 8992 (1995).

[58] P. Paddon, and J. F. Young, *Two-Dimensional Vector-Coupled-Mode Theory for Textured Planar Waveguides*, Phys. Rev. B **61**, 2090 (2000).

[59] B. Zhen, C. W. Hsu, L. Lu, A. D. Stone, and M. Soljačić, *Topological Nature of Optical Bound States in the Continuum*, Phys. Rev. Lett. **113**, 257401 (2014).

[60] C. W. Hsu, B. Zhen, A. D. Stone, J. D. Joannopoulos, and M. Soljačić, *Bound States in the Continuum*, Nat. Rev. Mater. **1**, 1 (2016).

[61] H. M. Doeleman, F. Monticone, W. den Hollander, A. Alù, and A. F. Koenderink, *Experimental Observation of a Polarization Vortex at an Optical Bound State in the Continuum*, Nat. Photonics **12**, 397 (2018).

[62] S. Zou, N. Janel, and G. C. Schatz, *Silver Nanoparticle Array Structures That Produce Remarkably Narrow Plasmon Lineshapes*, J. Chem. Phys. **120**, 10871 (2004).

[63] A. Abass, S. R.-K. Rodriguez, J. Gómez Rivas, and B. Maes, *Tailoring Dispersion and Eigenfield Profiles of Plasmonic Surface Lattice Resonances*, ACS Photonics **1**, 61 (2014).

[64] D. Beutel, I. Fernandez-Corbaton, and C. Rockstuhl, *treams – a t-matrix-based scattering code for nanophotonics*, Comput. Phys. Commun. **297**, 109076 (2024).

[65] A. E. Siegman, *Lasers* (University Science Books, Mill Valley, United States, 1986).

[66] J. R. Lakowicz, *Principles of Fluorescence Spectroscopy* (Springer US, Boston, United States, 2006).

[67] R. Graham, and H. Haken, *Laserlight — First Example of a Second-Order Phase Transition Far Away from Thermal Equilibrium*, Z. Physik **237**, 31 (1970).

[68] M. T. Hill, and M. C. Gather, *Advances in Small Lasers*, Nat. Photonics **8**, 908 (2014).

[69] A. Krasnok, and A. Alù, *Active Nanophotonics*, Proc. IEEE **108**, 628 (2020).

[70] *Scrutinizing Lasers*, Nat. Photonics **11**, 139 (2017).

[71] N. Mohammadi Estakhri, and A. Alù, *Wave-Front Transformation with Gradient Metasurfaces*, Phys. Rev. X **6**, 041008 (2016).

[72] L. Kang, R. P. Jenkins, and D. H. Werner, *Recent Progress in Active Optical Metasurfaces*, Adv. Opt. Mater. **7**, 1801813 (2019).

[73] T. Cui, B. Bai, and H.-B. Sun, *Tunable Metasurfaces Based on Active Materials*, Adv. Funct. Mater. **29**, 1806692 (2019).

[74] A. M. Shaltout, V. M. Shalaev, and M. L. Brongersma, *Spatiotemporal Light Control with Active Metasurfaces*, Science **364**, eaat3100 (2019).

[75] M. R. Shcherbakov, P. P. Vabishchevich, A. S. Shorokhov, K. E. Chong, D.-Y. Choi, I. Staude, A. E. Miroshnichenko, D. N. Neshev, A. A. Fedyanin, and Y. S. Kivshar, *Ultrafast All-Optical Switching with Magnetic Resonances in Nonlinear Dielectric Nanostructures*, Nano Lett. **15**, 6985 (2015).

[76] E. Schwoob, H. Benisty, C. Weisbuch, C. Cuisin, E. Derouin, O. Drisse, G. H. Duan, L. Legouézigou, O. Legouézigou, and F. Pommereau, *Enhanced Gain Measurement at Mode Singularities in InP-Based Photonic Crystal Waveguides*, Opt. Express **12**, 1569 (2004).

[77] A. Guo, G. J. Salamo, D. Duchesne, R. Morandotti, M. Volatier-Ravat, V. Aimez, G. A. Siviloglou, and D. N. Christodoulides, *Observation of PT-Symmetry Breaking in Complex Optical Potentials*, Phys. Rev. Lett. **103**, 093902 (2009).

[78] C. E. Rüter, K. G. Makris, R. El-Ganainy, D. N. Christodoulides, M. Segev, and D. Kip, *Observation of Parity–Time Symmetry in Optics*, Nat. Phys. **6**, 192 (2010).

[79] S. Ek, P. Lunnemann, Y. Chen, E. Semenova, K. Yvind, and J. Mork, *Slow-Light-Enhanced Gain in Active Photonic Crystal Waveguides*, Nat. Commun. **5**, 5039 (2014).

[80] Z. J. Wong, Y.-L. Xu, J. Kim, K. O'Brien, Y. Wang, L. Feng, and X. Zhang, *Lasing and Anti-Lasing in a Single Cavity*, Nat. Photonics **10**, 796 (2016).

[81] B. Peng, S. K. Özdemir, F. Lei, F. Monifi, M. Gianfreda, G. L. Long, S. Fan, F. Nori, C. M. Bender, and L. Yang, *Parity–Time-Symmetric Whispering-Gallery Microcavities*, Nat. Phys. **10**, 394 (2014).

[82] L. Chang, X. Jiang, S. Hua, C. Yang, J. Wen, L. Jiang, G. Li, G. Wang, and M. Xiao, *Parity–Time Symmetry and Variable Optical Isolation in Active–Passive-Coupled Microresonators*, Nat. Photonics **8**, 524 (2014).

[83] Y. A. Vlasov, K. Luterova, I. Pelant, B. Hönerlage, and V. N. Astratov, *Enhancement of Optical Gain of Semiconductors Embedded in Three-Dimensional Photonic Crystals*, Appl. Phys. Lett. **71**, 1616 (1997).

[84] F. Raineri, G. Vecchi, C. Cojocaru, A. M. Yacomotti, C. Seassal, X. Letartre, P. Viktorovitch, R. Raj, and A. Levenson, *Optical Amplification in Two-Dimensional Photonic Crystals*, Appl. Phys. Lett. **86**, 091111 (2005).

[85] R. Sapienza, M. Leonetti, L. S. Froufe-Pérez, J. F. Galisteo-López, C. Conti, and C. López, *Optical Amplification Enhancement in Photonic Crystals*, Phys. Rev. A **83**, 023801 (2011).

[86] S. Xiao, V. P. Drachev, A. V. Kildishev, X. Ni, U. K. Chettiar, H.-K. Yuan, and V. M. Shalaev, *Loss-Free and Active Optical Negative-Index Metamaterials*, Nature **466**, 735 (2010).

[87] S. Wuestner, A. Pusch, K. L. Tsakmakidis, J. M. Hamm, and O. Hess, *Overcoming Losses with Gain in a Negative Refractive Index Metamaterial*, Phys. Rev. Lett. **105**, 127401 (2010).

[88] N. Meinzer, M. Ruther, S. Linden, C. M. Soukoulis, G. Khitrova, J. Hendrickson, J. D. Olitzky, H. M. Gibbs, and M. Wegener, *Arrays of Ag Split-Ring Resonators Coupled to Ingaas Single-Quantum-Well Gain*, Opt. Express **18**, 24140 (2010).

[89] P. Berini, and I. De Leon, *Surface Plasmon–Polariton Amplifiers and Lasers*, Nat. Photonics **6**, 16 (2012).

[90] O. Hess, J. B. Pendry, S. A. Maier, R. F. Oulton, J. M. Hamm, and K. L. Tsakmakidis, *Active Nanoplasmonic Metamaterials*, Nat. Mater. **11**, 573 (2012).

[91] Y.-R. Zhang, J.-Q. Yuan, Z.-Z. Zhang, M. Kang, and J. Chen, *Exceptional Singular Resonance in Gain Mediated Metamaterials*, Opt. Express **27**, 6240 (2019).

[92] R. Kolkowski, S. Kovaios, and A. F. Koenderink, *Pseudochirality at Exceptional Rings of Optical Metasurfaces*, Phys. Rev. Res. **3**, 023185 (2021).

[93] S. K. Özdemir, S. Rotter, F. Nori, and L. Yang, *Parity–Time Symmetry and Exceptional Points in Photonics*, Nat. Mater. **18**, 783 (2019).

[94] M.-A. Miri, and A. Alù, *Exceptional Points in Optics and Photonics*, Science **363**, eaar7709 (2019).

[95] A. Krasnok, D. Baranov, H. Li, M.-A. Miri, F. Monticone, and A. Alú, *Anomalies in Light Scattering*, Adv. Opt. Photon. **11**, 892 (2019).

[96] M. Botey, R. Herrero, and K. Staliunas, *Light in Materials with Periodic Gain-Loss Modulation on a Wavelength Scale*, Phys. Rev. A **82**, 013828 (2010).

[97] A. Szameit, M. C. Rechtsman, O. Bahat-Treidel, and M. Segev, *Pt-Symmetry in Honeycomb Photonic Lattices*, Phys. Rev. A **84**, 021806 (2011).

[98] H. Benisty, A. Degiron, A. Lupu, A. D. Lustrac, S. Chénais, S. Forget, M. Besbes, G. Barbillon, A. Bruyant, S. Blaize, and G. Lérondel, *Implementation of Pt Symmetric Devices Using Plasmonics: Principle and Applications*, Opt. Express **19**, 18004 (2011).

[99] H. Ramezani, T. Kottos, V. Kovanis, and D. N. Christodoulides, *Exceptional-Point Dynamics in Photonic Honeycomb Lattices with Pt Symmetry*, Phys. Rev. A **85**, 013818 (2012).

[100] M. Turduev, M. Botey, I. Giden, R. Herrero, H. Kurt, E. Ozbay, and K. Staliunas, *Two-Dimensional Complex Parity-Time-Symmetric Photonic Structures*, Phys. Rev. A **91**, 023825 (2015).

[101] A. Cerjan, A. Raman, and S. Fan, *Exceptional Contours and Band Structure Design in Parity-Time Symmetric Photonic Crystals*, Phys. Rev. Lett. **116**, 203902 (2016).

[102] R. Kolkowski, and A. F. Koenderink, *Lattice Resonances in Optical Metasurfaces with Gain and Loss*, Proc. IEEE **108**, 795 (2020).

[103] C. Yan, and O. J. F. Martin, *Periodicity-Induced Symmetry Breaking in a Fano Lattice: Hybridization and Tight-Binding Regimes*, ACS Nano **8**, 11860 (2014).

[104] L. Wang, R.-Y. Zhang, M. Xiao, D. Han, C. T. Chan, and W. Wen, *The Existence of Topological Edge States in Honeycomb Plasmonic Lattices*, New J. Phys. **18**, 103029 (2016).

[105] C. A. Downing, and G. Weick, *Topological Collective Plasmons in Bipartite Chains of Metallic Nanoparticles*, Phys. Rev. B **95**, 125426 (2017).

[106] P. Qiu, R. Liang, W. Qiu, H. Chen, J. Ren, Z. Lin, J.-X. Wang, Q. Kan, and J.-Q. Pan, *Topologically Protected Edge States in Graphene Plasmonic Crystals*, Opt. Express **25**, 22587 (2017).

[107] C.-R. Mann, T. J. Sturges, G. Weick, W. L. Barnes, and E. Mariani, *Manipulating Type-I and Type-II Dirac Polaritons in Cavity-Embedded Honeycomb Metasurfaces*, Nat. Commun. **9**, 2194 (2018).

[108] M. Honari-Latifpour, and L. Yousefi, *Topological Plasmonic Edge States in a Planar Array of Metallic Nanoparticles*, Nanophotonics **8**, 799 (2019).

[109] F. Fernique, and G. Weick, *Plasmons in Two-Dimensional Lattices of Near-Field Coupled Nanoparticles*, Phys. Rev. B **102**, 045420 (2020).

[110] M. Proctor, M. Blanco de Paz, D. Bercioux, A. García-Etxarri, and P. Arroyo Huidobro, *Higher-Order Topology in Plasmonic Kagome Lattices*, Appl. Phys. Lett. **118**, 091105 (2021).

[111] L. Feng, Y.-L. Xu, W. S. Fegadolli, M.-H. Lu, J. E. B. Oliveira, V. R. Almeida, Y.-F. Chen, and A. Scherer, *Experimental Demonstration of a Unidirectional Reflectionless Parity-Time Metamaterial at Optical Frequencies*, Nat. Mater. **12**, 108 (2013).

[112] B. Zhen, C. W. Hsu, Y. Igarashi, L. Lu, I. Kaminer, A. Pick, S.-L. Chua, J. D. Joannopoulos, and M. Soljačić, *Spawning Rings of Exceptional Points Out of Dirac Cones*, Nature **525**, 354 (2015).

[113] Y. D. Chong, L. Ge, H. Cao, and A. D. Stone, *Coherent Perfect Absorbers: Time-Reversed Lasers*, Phys. Rev. Lett. **105**, 053901 (2010).

[114] Y. D. Chong, L. Ge, and A. D. Stone, *PT-Symmetry Breaking and Laser-Absorber Modes in Optical Scattering Systems*, Phys. Rev. Lett. **106**, 093902 (2011).

[115] S. Longhi, *PT-Symmetric Laser Absorber*, Phys. Rev. A **82**, 031801 (2010).

[116] N. I. Landy, S. Sajuyigbe, J. J. Mock, D. R. Smith, and W. J. Padilla, *Perfect Metamaterial Absorber*, Phys. Rev. Lett. **100**, 207402 (2008).

[117] R. Alaee, M. Farhat, C. Rockstuhl, and F. Lederer, *A Perfect Absorber Made of a Graphene Micro-Ribbon Metamaterial*, Opt. Express **20**, 28017 (2012).

[118] C. M. Watts, X. Liu, and W. J. Padilla, *Metamaterial Electromagnetic Wave Absorbers*, Adv. Mater. **24**, OP98 (2012).

[119] A. Pors, and S. I. Bozhevolnyi, *Plasmonic Metasurfaces for Efficient Phase Control in Reflection*, Opt. Express **21**, 27438 (2013).

[120] D. G. Baranov, A. Krasnok, T. Shegai, A. Alù, and Y. Chong, *Coherent Perfect Absorbers: Linear Control of Light with Light*, Nat. Rev. Mater. **2**, 1 (2017).

[121] A. Berkhout, and A. F. Koenderink, *Perfect Absorption and Phase Singularities in Plasmon Antenna Array Etalons*, ACS Photonics **6**, 2917 (2019).

[122] M. Chen, Z. Li, X. Tong, X. Wang, and F. Yang, *Manipulating the Critical Gain Level of Spectral Singularity in Active Hybridized Metamaterials*, Opt. Express **28**, 17966 (2020).

[123] A. Cordaro, H. Kwon, D. Sounas, A. F. Koenderink, A. Alù, and A. Polman, *High-Index Dielectric Metasurfaces Performing Mathematical Operations*, Nano Lett. **19**, 8418 (2019).

[124] A. Cordaro, B. Edwards, V. Nikkhah, A. Alù, N. Engheta, and A. Polman, *Solving Integral Equations in Free Space with Inverse-Designed Ultrathin Optical Metagratings*, Nat. Nanotechnol. **18**, 365 (2023).

[125] H. Zhou, C. Zhao, C. He, L. Huang, T. Man, and Y. Wan, *Optical Computing Metasurfaces: Applications and Advances*, Nanophotonics **13**, 419 (2024).

[126] J. Stehr, J. Crewett, F. Schindler, R. Sperling, G. von Plessen, U. Lemmer, J. Lupton, T. Klar, J. Feldmann, A. Holleitner, M. Forster, and U. Scherf, *A Low Threshold Polymer Laser Based on Metallic Nanoparticle Gratings*, Adv. Mater. **15**, 1726 (2003).

[127] J. Y. Suh, C. H. Kim, W. Zhou, M. D. Huntington, D. T. Co, M. R. Wasielewski, and T. W. Odom, *Plasmonic Bowtie Nanolaser Arrays*, Nano Lett. **12**, 5769 (2012).

[128] T. B. Hoang, G. M. Akselrod, A. Yang, T. W. Odom, and M. H. Mikkelsen, *Millimeter-Scale Spatial Coherence from a Plasmon Laser*, Nano Lett. **17**, 6690 (2017).

[129] W. Wang, N. Watkins, A. Yang, R. D. Schaller, G. C. Schatz, and T. W. Odom, *Ultrafast Dynamics of Lattice Plasmon Lasers*, J. Phys. Chem. Lett. **10**, 3301 (2019).

[130] A. H. Schokker, and A. F. Koenderink, *Statistics of Randomized Plasmonic Lattice Lasers*, ACS Photonics **2**, 1289 (2015).

[131] A. H. Schokker, F. van Riggelen, Y. Hadad, A. Alù, and A. F. Koenderink, *Systematic Study of the Hybrid Plasmonic-Photonic Band Structure Underlying Lasing Action of Diffractive Plasmon Particle Lattices*, Phys. Rev. B **95**, 085409 (2017).

[132] K. Guo, and A. F. Koenderink, *Spatial Intensity Distribution in Plasmonic Particle Array Lasers*, Phys. Rev. Appl. **11**, 024025 (2019).

[133] T. K. Hakala, H. T. Rekola, A. I. Väkeväinen, J.-P. Martikainen, M. Nečada, A. J. Moilanen, and P. Törmä, *Lasing in Dark and Bright Modes of a Finite-Sized Plasmonic Lattice*, Nat. Commun. **8**, 13687 (2017).

[134] R. Heilmann, G. Salerno, J. Cuerda, T. K. Hakala, and P. Törmä, *Quasi-BIC Mode Lasing in a Quadrumer Plasmonic Lattice*, ACS Photonics **9**, 224 (2022).

[135] J. M. Winkler, M. J. Ruckriegel, H. Rojo, R. C. Keitel, E. De Leo, F. T. Rabouw, and D. J. Norris, *Dual-Wavelength Lasing in Quantum-Dot Plasmonic Lattice Lasers*, ACS Nano **14**, 5223 (2020).

[136] A. Kodigala, T. Lepetit, Q. Gu, B. Bahari, Y. Fainman, and B. Kanté, *Lasing Action from Photonic Bound States in Continuum*, Nature **541**, 196 (2017).

[137] B. Bahari, A. Ndao, F. Vallini, A. El Amili, Y. Fainman, and B. Kanté, *Nonreciprocal Lasing in Topological Cavities of Arbitrary Geometries*, Science **358**, 636 (2017).

[138] P. St-Jean, V. Goblot, E. Galopin, A. Lemaître, T. Ozawa, L. Le Gratiet, I. Sagnes, J. Bloch, and A. Amo, *Lasing in Topological Edge States of a One-Dimensional Lattice*, Nat. Photonics **11**, 651 (2017).

[139] H. Kogelnik, and C. V. Shank, *Stimulated Emission in a Periodic Structure*, Appl. Phys. Lett. **18**, 152 (1971).

[140] H. Kogelnik, and C. V. Shank, *Coupled-Wave Theory of Distributed Feedback Lasers*, J. Appl. Phys. **43**, 2327 (1972).

[141] G. A. Turnbull, P. Andrew, M. J. Jory, W. L. Barnes, and I. D. W. Samuel, *Relationship between Photonic Band Structure and Emission Characteristics of a Polymer Distributed Feedback Laser*, Phys. Rev. B **64**, 125122 (2001).

[142] M. Notomi, H. Suzuki, and T. Tamamura, *Directional Lasing Oscillation of Two-Dimensional Organic Photonic Crystal Lasers at Several Photonic Band Gaps*, Appl. Phys. Lett. **78**, 1325 (2001).

[143] R. Guo, M. Nečada, T. K. Hakala, A. I. Väkeväinen, and P. Törmä, *Lasing at K Points of a Honeycomb Plasmonic Lattice*, Phys. Rev. Lett. **122**, 013901 (2019).

[144] X. G. Juarez, R. Li, J. Guan, T. Reese, R. D. Schaller, and T. W. Odom, *M-Point Lasing in Hexagonal and Honeycomb Plasmonic Lattices*, ACS Photonics **9**, 52 (2022).

[145] G. Heliotis, R. Xia, G. A. Turnbull, P. Andrew, W. L. Barnes, I. D. W. Samuel, and D. D. C. Bradley, *Emission Characteristics and Performance Comparison of Polyfluorene Lasers with One- and Two-Dimensional Distributed Feedback*, Adv.

Funct. Mater. **14**, 91 (2004).

[146] M. Imada, A. Chutinan, S. Noda, and M. Mochizuki, *Multidirectionally Distributed Feedback Photonic Crystal Lasers*, Phys. Rev. B **65**, 195306 (2002).

[147] E. Miyai, K. Sakai, T. Okano, W. Kunishi, D. Ohnishi, and S. Noda, *Lasers Producing Tailored Beams*, Nature **441**, 946 (2006).

[148] Y. Liang, C. Peng, K. Sakai, S. Iwahashi, and S. Noda, *Three-Dimensional Coupled-Wave Analysis for Square-Lattice Photonic Crystal Surface Emitting Lasers with Transverse-Electric Polarization: Finite-Size Effects*, Opt. Express **20**, 15945 (2012).

[149] K. Hirose, Y. Liang, Y. Kurosaka, A. Watanabe, T. Sugiyama, and S. Noda, *Watt-Class High-Power, High-Beam-Quality Photonic-Crystal Lasers*, Nat. Photonics **8**, 406 (2014).

[150] F. van Beijnum, P. J. van Veldhoven, E. J. Geluk, M. J. A. de Dood, G. W. 't Hooft, and M. P. van Exter, *Surface Plasmon Lasing Observed in Metal Hole Arrays*, Phys. Rev. Lett. **110**, 206802 (2013).

[151] V. T. Tenner, M. J. A. d. Dood, and M. P. v. Exter, *Two-Mode Surface Plasmon Lasing in Hexagonal Arrays*, Opt. Lett. **43**, 166 (2018).

[152] M. Ramezani, A. Halpin, A. I. Fernández-Domínguez, J. Feist, S. R.-K. Rodriguez, F. J. Garcia-Vidal, and J. G. Rivas, *Plasmon-Exciton-Polariton Lasing*, Optica **4**, 31 (2017).

[153] T. K. Hakala, A. J. Moilanen, A. I. Väkeväinen, R. Guo, J.-P. Martikainen, K. S. Daskalakis, H. T. Rekola, A. Julku, and P. Törmä, *Bose–Einstein Condensation in a Plasmonic Lattice*, Nat. Phys. **14**, 739 (2018).

[154] D. Wang, M. R. Bourgeois, J. Guan, A. K. Fumani, G. C. Schatz, and T. W. Odom, *Lasing from Finite Plasmonic Nanoparticle Lattices*, ACS Photonics **7**, 630 (2020).

[155] M. A. Lieb, J. M. Zavislan, and L. Novotny, *Single-Molecule Orientations Determined by Direct Emission Pattern Imaging*, J. Opt. Soc. Am. B **21**, 1210 (2004).

[156] I. Sersic, C. Tuambilangana, and A. F. Koenderink, *Fourier Microscopy of Single Plasmonic Scatterers*, New J. Phys. **13**, 083019 (2011).

[157] A. F. Koenderink, *Single-Photon Nanoantennas*, ACS Photonics **4**, 710 (2017).

[158] A. G. Curto, T. H. Taminiau, G. Volpe, M. P. Kreuzer, R. Quidant, and N. F. van Hulst, *Multipolar Radiation of Quantum Emitters with Nanowire Optical Antennas*, Nat. Commun. **4**, 1750 (2013).

[159] N. L. Thomas, R. Houdré, M. V. Kotlyar, D. O'Brien, and T. F. Krauss, *Exploring Light Propagating in Photonic Crystals with Fourier Optics*, J. Opt. Soc. Am. B **24**, 2964 (2007).

[160] Y. Zhang, A. Chen, W. Liu, C. W. Hsu, B. Wang, F. Guan, X. Liu, L. Shi, L. Lu, and J. Zi, *Observation of Polarization Vortices in Momentum Space*, Phys. Rev. Lett. **120**, 186103 (2018).

[161] D. Strickland, and G. Mourou, *Compression of Amplified Chirped Optical Pulses*, Opt. Commun. **56**, 219 (1985).

[162] D. E. Spence, P. N. Kean, and W. Sibbett, *60-Fsec Pulse Generation from a Self-Mode-Locked Ti:sapphire Laser*, Opt. Lett. **16**, 42 (1991).

[163] R. Berera, R. van Grondelle, and J. T. M. Kennis, *Ultrafast Transient Absorption*

Spectroscopy: Principles and Application to Photosynthetic Systems, Photosynth. Res. **101**, 105 (2009).

[164] D. Zigmantas, T. Polívka, P. Persson, and V. Sundström, *Ultrafast Laser Spectroscopy Uncovers Mechanisms of Light Energy Conversion in Photosynthesis and Sustainable Energy Materials*, Chem. Phys. Rev. **3**, 041303 (2022).

[165] E. M. Grumstrup, M. M. Gabriel, E. E. M. Cating, E. M. Van Goethem, and J. M. Papanikolas, *Pump–Probe Microscopy: Visualization and Spectroscopy of Ultrafast Dynamics at the Nanoscale*, Chem. Phys. **458**, 30 (2015).

[166] D. Davydova, A. de la Cadena, D. Akimov, and B. Dietzek, *Transient Absorption Microscopy: Advances in Chemical Imaging of Photoinduced Dynamics*, Laser Photonics Rev. **10**, 62 (2016).

[167] M. C. Fischer, J. W. Wilson, F. E. Robles, and W. S. Warren, *Invited Review Article: Pump-probe Microscopy*, Rev. Sci. Instrum. **87**, 031101 (2016).

[168] T. Guenther, C. Lienau, T. Elsaesser, M. Glanemann, V. M. Axt, T. Kuhn, S. Eshlaghi, and A. D. Wieck, *Coherent Nonlinear Optical Response of Single Quantum Dots Studied by Ultrafast Near-Field Spectroscopy*, Phys. Rev. Lett. **89**, 057401 (2002).

[169] N. Erhard, S. Zenger, S. Morkötter, D. Rudolph, M. Weiss, H. J. Krenner, H. Karl, G. Abstreiter, J. J. Finley, G. Koblmüller, and A. W. Holleitner, *Ultrafast Photodetection in the Quantum Wells of Single AlGaAs/GaAs-Based Nanowires*, Nano Lett. **15**, 6869 (2015).

[170] J. Cabanillas-Gonzalez, G. Grancini, and G. Lanzani, *Pump-Probe Spectroscopy in Organic Semiconductors: Monitoring Fundamental Processes of Relevance in Optoelectronics*, Adv. Mater. **23**, 5468 (2011).

[171] K. Imura, T. Nagahara, and H. Okamoto, *Imaging of Surface Plasmon and Ultrafast Dynamics in Gold Nanorods by Near-Field Microscopy*, J. Phys. Chem. B **108**, 16344 (2004).

[172] O. L. Muskens, N. Del Fatti, and F. Vallée, *Femtosecond Response of a Single Metal Nanoparticle*, Nano Lett. **6**, 552 (2006).

[173] P. Colman, P. Lunnemann, Y. Yu, and J. Mørk, *Ultrafast Coherent Dynamics of a Photonic Crystal All-Optical Switch*, Phys. Rev. Lett. **117**, 233901 (2016).

[174] S. Ahmed, X. Jiang, F. Zhang, and H. Zhang, *Pump–Probe Micro-Spectroscopy and 2D Materials*, J. Phys. D: Appl. Phys. **53**, 473001 (2020).

[175] A. Schirato, M. Maiuri, A. Toma, S. Fugattini, R. Proietti Zaccaria, P. Laporta, P. Nordlander, G. Cerullo, A. Alabastri, and G. Della Valle, *Transient Optical Symmetry Breaking for Ultrafast Broadband Dichroism in Plasmonic Metasurfaces*, Nat. Photonics **14**, 723 (2020).

[176] M. R. Shcherbakov, S. Liu, V. V. Zubyuk, A. Vaskin, P. P. Vabishchevich, G. Keeler, T. Pertsch, T. V. Dolgova, I. Staude, I. Brener, and A. A. Fedyanin, *Ultrafast All-Optical Tuning of Direct-Gap Semiconductor Metasurfaces*, Nat. Commun. **8**, 17 (2017).

[177] M. Maiuri, A. Schirato, G. Cerullo, and G. Della Valle, *Ultrafast All-Optical Metasurfaces: Challenges and New Frontiers*, ACS Photonics **11**, 2888 (2024).

[178] U. Scherf, S. Riechel, U. Lemmer, and R. F. Mahrt, *Conjugated Polymers: Lasing*

and Stimulated Emission, Curr. Opin. Solid State Mater. Sci. **5**, 143 (2001).

[179] T. Pauck, R. Hennig, M. Perner, U. Lemmer, U. Siegner, R. F. Mahrt, U. Scherf, K. Müllen, H. Bässler, and E. O. Göbel, *Femtosecond Dynamics of Stimulated Emission and Photoinduced Absorption in a PPP-type Ladder Polymer*, Chem. Phys. Lett. **244**, 171 (1995).

[180] S. Bourquin, R. P. Prasankumar, F. X. Kärtner, J. G. Fujimoto, T. Lasser, and R. P. Salathé, *High-Speed Femtosecond Pump Probe Spectroscopy with a Smart Pixel Detector Array*, Opt. Lett. **28**, 1588 (2003).

[181] T. Pezeril, C. Klieber, V. Shalagatskyi, G. Vaudel, V. Temnov, O. G. Schmidt, and D. Makarov, *Femtosecond Imaging of Nonlinear Acoustics in Gold*, Opt. Express **22**, 4590 (2014).

[182] Y.-H. Kim, and P. T. C. So, *Three-Dimensional Wide-Field Pump-Probe Structured Illumination Microscopy*, Opt. Express **25**, 7369 (2017).

[183] O. Denk, K. Zheng, D. Zigmantas, and K. Žídek, *Compressive Imaging of Transient Absorption Dynamics on the Femtosecond Timescale*, Opt. Express **27**, 10234 (2019).

[184] P. Cristofolini, A. Dreismann, G. Christmann, G. Franchetti, N. G. Berloff, P. Tsotsis, Z. Hatzopoulos, P. G. Savvidis, and J. J. Baumberg, *Optical Superfluid Phase Transitions and Trapping of Polariton Condensates*, Phys. Rev. Lett. **110**, 186403 (2013).

[185] A. Dreismann, P. Cristofolini, R. Balili, G. Christmann, F. Pinsker, N. G. Berloff, Z. Hatzopoulos, P. G. Savvidis, and J. J. Baumberg, *Coupled Counterrotating Polariton Condensates in Optically Defined Annular Potentials*, Proceedings of the National Academy of Sciences **111**, 8770 (2014).

[186] J.-S. Wu, V. Apalkov, and M. I. Stockman, *Topological Spaser*, Phys. Rev. Lett. **124**, 017701 (2020).

[187] J. P. Dowling, M. Scalora, M. J. Bloemer, and C. M. Bowden, *The Photonic Band Edge Laser: A New Approach to Gain Enhancement*, J. Appl. Phys. **75**, 1896 (1994).

[188] K. Sakoda, *Enhanced Light Amplification Due to Group-Velocity Anomaly Peculiar to Two- and Three-Dimensional Photonic Crystals*, Opt. Express **4**, 167 (1999).

[189] A. Askitopoulos, L. Mouchliadis, I. Iorsh, G. Christmann, J. J. Baumberg, M. A. Kaliteevski, Z. Hatzopoulos, and P. G. Savvidis, *Bragg Polaritons: Strong Coupling and Amplification in an Unfolded Microcavity*, Phys. Rev. Lett. **106**, 076401 (2011).

[190] J. Grgić, J. R. Ott, F. Wang, O. Sigmund, A.-P. Jauho, J. Mørk, and N. A. Mortensen, *Fundamental Limitations to Gain Enhancement in Periodic Media and Waveguides*, Phys. Rev. Lett. **108**, 183903 (2012).

[191] N. Bonod, and J. Neauport, *Diffraction Gratings: From Principles to Applications in High-Intensity Lasers*, Adv. Opt. Photon. **8**, 156 (2016).

[192] B. A. Grzybowski, D. Qin, and G. M. Whitesides, *Beam Redirection and Frequency Filtering with Transparent Elastomeric Diffractive Elements*, Appl. Opt. **38**, 2997 (1999).

[193] M. Stürmer, M. C. Wapler, J. Schmitt, F. Völklein, and U. Wallrabe, *Phase Gratings with Tunable Diffraction Efficiency*, Opt. Express **24**, 23765 (2016).

[194] J. I. Trisnadi, C. B. Carlisle, and R. Monteverde, *Overview and Applications of Grating-Light-Valve-based Optical Write Engines for High-Speed Digital Imaging*, in

MOEMS Display and Imaging Systems II (SPIE, 2004), vol. 5348, pp. 52–64.

[195] M. Riahi, H. Latifi, A. Madani, and A. Moazzenzadeh, *Design and Fabrication of a Spatial Light Modulator Using Thermally Tunable Grating and a Thin-Film Heater*, Appl. Opt. **48**, 5647 (2009).

[196] A. Groisman, S. Zamek, K. Campbell, L. Pang, U. Levy, and Y. Fainman, *Optofluidic 1x4 Switch*, Opt. Express **16**, 13499 (2008).

[197] F. Fan, A. K. Srivastava, V. G. Chigrinov, and H. S. Kwok, *Switchable Liquid Crystal Grating with Sub Millisecond Response*, Appl. Phys. Lett. **100**, 111105 (2012).

[198] A. Ryabchun, and A. Bobrovsky, *Cholesteric Liquid Crystal Materials for Tunable Diffractive Optics*, Adv. Opt. Mater. **6**, 1800335 (2018).

[199] D. E. Lucchetta, A. Di Donato, G. Singh, A. Tombesi, and R. Castagna, *Optically Tunable Diffraction Efficiency by Photo-Mobile Holographic Composite Polymer Material*, Opt. Mater. **121**, 111612 (2021).

[200] B. J. Schwartz, F. Hide, M. R. Andersson, and A. J. Heeger, *Ultrafast Studies of Stimulated Emission and Gain in Solid Films of Conjugated Polymers*, Chem. Phys. Lett. **265**, 327 (1997).

[201] M. Yan, L. J. Rothberg, F. Papadimitrakopoulos, M. E. Galvin, and T. M. Miller, *Spatially Indirect Excitons As Primary Photoexcitations in Conjugated Polymers*, Phys. Rev. Lett. **72**, 1104 (1994).

[202] M. Yan, L. J. Rothberg, E. W. Kwock, and T. M. Miller, *Interchain Excitations in Conjugated Polymers*, Phys. Rev. Lett. **75**, 1992 (1995).

[203] G. van Soest, *Experiments on Random Lasers*, Ph.D. thesis, Universiteit van Amsterdam (2001).

[204] B. Dietzek, T. Pascher, V. Sundström, and A. Yartsev, *Appearance of Coherent Artifact Signals in Femtosecond Transient Absorption Spectroscopy in Dependence on Detector Design*, Laser Phys. Lett. **4**, 38 (2007).

[205] G. Auböck, C. Consani, R. Monni, A. Cannizzo, F. van Mourik, and M. Chergui, *Femtosecond Pump/supercontinuum-Probe Setup with 20 kHz Repetition Rate*, Rev. Sci. Instrum. **83**, 093105 (2012).

[206] B. Baudisch, *Time Resolved Broadband Spectroscopy from Uv to Nir*, Ph.D. thesis, Ludwig-Maximilians-Universität München (2018).

[207] M. Pauls, J. Brunne, U. Wallrabe, and R. Grunwald, *A Reflective Tunable Blazed-Grating for High Energy Femtosecond Laser Pulses*, in *2012 International Symposium on Optomechatronic Technologies (ISOT 2012)* (2012), pp. 1–2.

[208] X. Liu, T. Starr, A. F. Starr, and W. J. Padilla, *Infrared Spatial and Frequency Selective Metamaterial with Near-Unity Absorbance*, Phys. Rev. Lett. **104**, 207403 (2010).

[209] K. Aydin, V. E. Ferry, R. M. Briggs, and H. A. Atwater, *Broadband Polarization-Independent Resonant Light Absorption Using Ultrathin Plasmonic Super Absorbers*, Nat. Commun. **2**, 517 (2011).

[210] Y. Yao, R. Shankar, M. A. Kats, Y. Song, J. Kong, M. Loncar, and F. Capasso, *Electrically Tunable Metasurface Perfect Absorbers for Ultrathin Mid-Infrared Optical Modulators*, Nano Lett. **14**, 6526 (2014).

[211] Y. Ra'di, C. Simovski, and S. Tretyakov, *Thin Perfect Absorbers for Electromagnetic*

Waves: Theory, Design, and Realizations, Phys. Rev. Appl. **3**, 037001 (2015).

[212] F. Huang, S. Drakeley, M. G. Millyard, A. Murphy, R. White, E. Spigone, J. Kivioja, and J. J. Baumberg, *Zero-Reflectance Metafilms for Optimal Plasmonic Sensing*, Adv. Opt. Mater. **4**, 328 (2016).

[213] B. Sima, K. Chen, X. Luo, J. Zhao, and Y. Feng, *Combining Frequency-Selective Scattering and Specular Reflection through Phase-Dispersion Tailoring of a Metasurface*, Phys. Rev. Appl. **10**, 064043 (2018).

[214] F. Ding, Y. Yang, R. A. Deshpande, and S. I. Bozhevolnyi, *A Review of Gap-Surface Plasmon Metasurfaces: Fundamentals and Applications*, Nanophotonics **7**, 1129 (2018).

[215] W. W. Salisbury, *Absorbent Body for Electromagnetic Waves* (1952).

[216] R. Fante, and M. McCormack, *Reflection Properties of the Salisbury Screen*, IEEE Trans. Antennas Propag. **36**, 1443 (1988).

[217] Y. Cai, J. Zhu, and Q. H. Liu, *Tunable Enhanced Optical Absorption of Graphene Using Plasmonic Perfect Absorbers*, Appl. Phys. Lett. **106**, 043105 (2015).

[218] J. R. Piper, and S. Fan, *Total Absorption in a Graphene Monolayer in the Optical Regime by Critical Coupling with a Photonic Crystal Guided Resonance*, ACS Photonics **1**, 347 (2014).

[219] S. Kim, M. S. Jang, V. W. Brar, K. W. Mauser, L. Kim, and H. A. Atwater, *Electronically Tunable Perfect Absorption in Graphene*, Nano Lett. **18**, 971 (2018).

[220] C. Hang, G. Huang, and V. V. Konotop, *Tunable Spectral Singularities: Coherent Perfect Absorber and Laser in an Atomic Medium*, New J. Phys. **18**, 085003 (2016).

[221] W. Y. Cui, J. Zhang, Y. Luo, X. Gao, and T. J. Cui, *Dynamic Switching from Coherent Perfect Absorption to Parametric Amplification in a Nonlinear Spoof Plasmonic Waveguide*, Nat. Commun. **15**, 2824 (2024).

[222] J. Zhang, K. F. MacDonald, and N. I. Zheludev, *Controlling Light-With-Light without Nonlinearity*, Light Sci. Appl. **1**, e18 (2012).

[223] M. Kang, Y. D. Chong, H.-T. Wang, W. Zhu, and M. Premaratne, *Critical Route for Coherent Perfect Absorption in a Fano Resonance Plasmonic System*, Appl. Phys. Lett. **105**, 131103 (2014).

[224] M. A. Kats, and F. Capasso, *Optical Absorbers Based on Strong Interference in Ultra-Thin Films*, Laser Photonics Rev. **10**, 735 (2016).

[225] C. Menzel, J. Sperrhake, and T. Pertsch, *Efficient Treatment of Stacked Metasurfaces for Optimizing and Enhancing the Range of Accessible Optical Functionalities*, Phys. Rev. A **93**, 063832 (2016).

[226] R. Alaee, M. Albooyeh, and C. Rockstuhl, *Theory of Metasurface Based Perfect Absorbers*, J. Phys. D: Appl. Phys. **50**, 503002 (2017).

[227] R. Colom, E. Mikheeva, K. Achouri, J. Zuniga-Perez, N. Bonod, O. J. F. Martin, S. Burger, and P. Genevet, *Crossing of the Branch Cut: The Topological Origin of a Universal 2π-Phase Retardation in Non-Hermitian Metasurfaces*, Laser Photonics Rev. **17**, 2200976 (2023).

[228] P. Bai, K. Ding, G. Wang, J. Luo, Z.-Q. Zhang, C. T. Chan, Y. Wu, and Y. Lai, *Simultaneous Realization of a Coherent Perfect Absorber and Laser by Zero-Index Media*

with Both Gain and Loss, Phys. Rev. A **94**, 063841 (2016).

[229] B. Baum, H. Alaeian, and J. Dionne, *A Parity-Time Symmetric Coherent Plasmonic Absorber-Amplifier*, J. Appl. Phys. **117**, 063106 (2015).

[230] Z. Gu, N. Zhang, Q. Lyu, M. Li, S. Xiao, and Q. Song, *Experimental Demonstration of PT-Symmetric Stripe Lasers*, Laser Photonics Rev. **10**, 588 (2016).

[231] M. Elsawy, C. Kyrou, E. Mikheeva, R. Colom, J.-Y. Duboz, K. Z. Kamali, S. Lanteri, D. Neshev, and P. Genevet, *Universal Active Metasurfaces for Ultimate Wavefront Molding by Manipulating the Reflection Singularities*, Laser Photonics Rev. **17**, 2200880 (2023).

[232] M. Li, L. Michaeli, and H. A. Atwater, *Electrically Tunable Topological Singularities in Excitonic Two-Dimensional Heterostructures for Wavefront Manipulation*, ACS Photonics **11**, 3554 (2024).

[233] A. Berkhout, and A. F. Koenderink, *A Simple Transfer-Matrix Model for Metasurface Multilayer Systems*, Nanophotonics **9**, 3985 (2020).

[234] A. Manjavacas, *Anisotropic Optical Response of Nanostructures with Balanced Gain and Loss*, ACS Photonics **3**, 1301 (2016).

[235] M. A. K. Othman, V. Galdi, and F. Capolino, *Exceptional Points of Degeneracy and Pt Symmetry in Photonic Coupled Chains of Scatterers*, Phys. Rev. B **95**, 104305 (2017).

[236] X. Chen, W. Yue, R. Tao, P. Yao, and W. Liu, *Scattering Phenomenon of PT-Symmetric Dielectric-Nanosphere Structure*, Phys. Rev. A **94**, 053829 (2016).

[237] X. Chen, H. Wang, J. Li, K.-y. Wong, and D. Lei, *Scattering Asymmetry and Circular Dichroism in Coupled PT-Symmetric Chiral Nanoparticles*, Nanophotonics **11**, 2159 (2022).

[238] C. W. Ling, K. H. Choi, T. C. Mok, Z.-Q. Zhang, and K. H. Fung, *Anomalous Light Scattering by Topological PT-Symmetric Particle Arrays*, Sci. Rep. **6**, 38049 (2016).

[239] R. Y. Chiao, *Superluminal (but Causal) Propagation of Wave Packets in Transparent Media with Inverted Atomic Populations*, Phys. Rev. A **48**, R34 (1993).

[240] A. Dogariu, A. Kuzmich, and L. J. Wang, *Transparent Anomalous Dispersion and Superluminal Light-Pulse Propagation at a Negative Group Velocity*, Phys. Rev. A **63**, 053806 (2001).

[241] T. Savels, A. P. Mosk, and A. Lagendijk, *Light Scattering from Three-Level Systems: The T Matrix of a Point Dipole with Gain*, Phys. Rev. A **71**, 043814 (2005).

[242] A. A. Govyadinov, V. A. Podolskiy, and M. A. Noginov, *Active Metamaterials: Sign of Refractive Index and Gain-Assisted Dispersion Management*, Appl. Phys. Lett. **91**, 191103 (2007).

[243] S. Campione, M. Albani, and F. Capolino, *Complex Modes and Near-Zero Permittivity in 3d Arrays of Plasmonic Nanoshells: Loss Compensation Using Gain*, Opt. Mater. Express **1**, 1077 (2011).

[244] S. Schwaiger, M. Klingbeil, J. Kerbst, A. Rottler, R. Costa, A. Koitmäe, M. Bröll, C. Heyn, Y. Stark, D. Heitmann, and S. Mendach, *Gain in Three-Dimensional Metamaterials Utilizing Semiconductor Quantum Structures*, Phys. Rev. B **84**, 155325 (2011).

[245] N. Arnold, K. Piglmayer, A. V. Kildishev, and T. A. Klar, *Spasers with Retardation and Gain Saturation: Electrodynamic Description of Fields and Optical Cross-Sections*, Opt. Mater. Express **5**, 2546 (2015).

[246] V. Caligiuri, L. Pezzi, A. Veltri, and A. De Luca, *Resonant Gain Singularities in 1d and 3d Metal/Dielectric Multilayered Nanostructures*, ACS Nano **11**, 1012 (2017).

[247] G. V. Kristanz, N. Arnold, A. V. Kildishev, and T. A. Klar, *Power Balance and Temperature in Optically Pumped Spasers and Nanolasers*, ACS Photonics **5**, 3695 (2018).

[248] S. Baur, S. Sanders, and A. Manjavacas, *Hybridization of Lattice Resonances*, ACS Nano **12**, 1618 (2018).

[249] P. Yeh, *Optics of Anisotropic Layered Media: A New 4 × 4 Matrix Algebra*, Surf. Sci. **96**, 41 (1980).

[250] A. Kwadrin, C. I. Osorio, and A. F. Koenderink, *Backaction in Metasurface Etalons*, Phys. Rev. B **93**, 104301 (2016).

[251] N. M. Lawandy, *Localized Surface Plasmon Singularities in Amplifying Media*, Appl. Phys. Lett. **85**, 5040 (2004).

[252] A. Veltri, and A. Aradian, *Optical Response of a Metallic Nanoparticle Immersed in a Medium with Optical Gain*, Phys. Rev. B **85**, 115429 (2012).

[253] E. Tiguntseva, K. Koshelev, A. Furasova, P. Tonkaev, V. Mikhailovskii, E. V. Ushakova, D. G. Baranov, T. Shegai, A. A. Zakhidov, Y. Kivshar, and S. V. Makarov, *Room-Temperature Lasing from Mie-Resonant Nonplasmonic Nanoparticles*, ACS Nano **14**, 8149 (2020).

[254] D. G. Baranov, A. Krasnok, and A. Alù, *Coherent Virtual Absorption Based on Complex Zero Excitation for Ideal Light Capturing*, Optica **4**, 1457 (2017).

[255] N. de Gaay Fortman, R. Kolkowski, D. Pal, S. R. K. Rodriguez, P. Schall, and A. F. Koenderink, *Spontaneous Symmetry Breaking in Plasmon Lattice Lasers*, Sci. Adv. **10**, eadn2723 (2024).

[256] P. Hamel, S. Haddadi, F. Raineri, P. Monnier, G. Beaudoin, I. Sagnes, A. Levenson, and A. M. Yacomotti, *Spontaneous Mirror-Symmetry Breaking in Coupled Photonic-Crystal Nanolasers*, Nat. Photonics **9**, 311 (2015).

[257] B. Garbin, A. Giraldo, K. Peters, N. Broderick, A. Spakman, F. Raineri, A. Levenson, S. Rodriguez, B. Krauskopf, and A. Yacomotti, *Spontaneous Symmetry Breaking in a Coherently Driven Nanophotonic Bose-Hubbard Dimer*, Phys. Rev. Lett. **128**, 053901 (2022).

[258] M. M-Tehrani, and L. Mandel, *Mode Competition in a Ring Laser at Line Center*, Opt. Lett. **1**, 196 (1977).

[259] M. Sorel, P. J. R. Laybourn, G. Giuliani, and S. Donati, *Unidirectional Bistability in Semiconductor Waveguide Ring Lasers*, Appl. Phys. Lett. **80**, 3051 (2002).

[260] G. V. d. Sande, L. Gelens, P. Tassin, A. Scirè, and J. Danckaert, *Two-Dimensional Phase-Space Analysis and Bifurcation Study of the Dynamical Behaviour of a Semiconductor Ring Laser*, J. Phys. B: At. Mol. Opt. Phys. **41**, 095402 (2008).

[261] S. V. Zhukovsky, D. N. Chigrin, and J. Kroha, *Bistability and Mode Interaction in Microlasers*, Phys. Rev. A **79**, 033803 (2009).

[262] Q.-T. Cao, H. Wang, C.-H. Dong, H. Jing, R.-S. Liu, X. Chen, L. Ge, Q. Gong, and Y.-F. Xiao, *Experimental Demonstration of Spontaneous Chirality in a Nonlinear Microresonator*, Phys. Rev. Lett. **118**, 033901 (2017).

[263] L. Del Bino, J. M. Silver, S. L. Stebbings, and P. Del'Haye, *Symmetry Breaking of Counter-Propagating Light in a Nonlinear Resonator*, Sci. Rep. **7**, 43142 (2017).

[264] R. C. Keitel, B. le Feber, K. M. Dettlaff, R. Brechbühler, E. De Leo, H. Rojo, and D. J. Norris, *Single-Pulse Measurement of Orbital Angular Momentum Generated by Microring Lasers*, ACS Nano **15**, 19185 (2021).

[265] E. Wertz, L. Ferrier, D. D. Solnyshkov, R. Johne, D. Sanvitto, A. Lemaître, I. Sagnes, R. Grousson, A. V. Kavokin, P. Senellart, G. Malpuech, and J. Bloch, *Spontaneous Formation and Optical Manipulation of Extended Polariton Condensates*, Nat. Phys. **6**, 860 (2010).

[266] H. Ohadi, E. Kammann, T. C. H. Liew, K. G. Lagoudakis, A. V. Kavokin, and P. G. Lagoudakis, *Spontaneous Symmetry Breaking in a Polariton and Photon Laser*, Phys. Rev. Lett. **109**, 016404 (2012).

[267] V. G. Sala, F. Marsault, M. Wouters, E. Galopin, I. Sagnes, A. Lemaître, J. Bloch, and A. Amo, *Stochastic Precession of the Polarization in a Polariton Laser*, Phys. Rev. B **93**, 115313 (2016).

[268] H. Sigurdsson, Y. S. Krivosenko, I. V. Iorsh, I. A. Shelykh, and A. V. Nalitov, *Spontaneous Topological Transitions in a Honeycomb Lattice of Exciton-Polariton Condensates Due to Spin Bifurcations*, Phys. Rev. B **100**, 235444 (2019).

[269] M. Haelterman, *All-Optical Set-Reset Flip-Flop Operation in the Nonlinear Fabry-Pérot Interferometer*, Opt. Commun. **86**, 189 (1991).

[270] B. Maes, M. Soljačić, J. D. Joannopoulos, P. Bienstman, R. Baets, S.-P. Gorza, and M. Haelterman, *Switching through Symmetry Breaking in Coupled Nonlinear Micro-Cavities*, Opt. Express **14**, 10678 (2006).

[271] H. Saito, D. Yoshimoto, Y. Moritake, T. Matsukata, N. Yamamoto, and T. Sannomiya, *Valley-Polarized Plasmonic Edge Mode Visualized in the Near-Infrared Spectral Range*, Nano Lett. **21**, 6556 (2021).

[272] Q. T. Trinh, S. K. Nguyen, D. H. Nguyen, G. K. Tran, V. H. Le, H.-S. Nguyen, and Q. Le-Van, *Coexistence of Surface Lattice Resonances and Bound States in the Continuum in a Plasmonic Lattice*, Opt. Lett. **47**, 1510 (2022).

[273] L. Lu, J. D. Joannopoulos, and M. Soljačić, *Topological Photonics*, Nat. Photonics **8**, 821 (2014).

[274] P. Gartner, *Spontaneous Symmetry Breaking in the Laser Transition*, Phys. Rev. B **99**, 115313 (2019).

[275] T. Ochiai, and K. Sakoda, *Dispersion Relation and Optical Transmittance of a Hexagonal Photonic Crystal Slab*, Phys. Rev. B **63**, 125107 (2001).

[276] J. F. Wheeldon, T. Hall, and H. Schriemer, *Symmetry Constraints and the Existence of Bloch Mode Vortices in Linear Photonic Crystals*, Opt. Express **15**, 3531 (2007).

[277] D. Malterre, B. Kierren, Y. Fagot-Revurat, C. Didiot, F. J. G. d. Abajo, F. Schiller, J. Cordón, and J. E. Ortega, *Symmetry Breaking and Gap Opening in Two-Dimensional Hexagonal Lattices*, New J. Phys. **13**, 013026 (2011).

[278] L. Hill, G.-L. Oppo, and P. Del'Haye, *Multi-Stage Spontaneous Symmetry Breaking*

of Light in Kerr Ring Resonators, Commun. Phys. **6**, 1 (2023).

[279] N. de Gaay Fortman, D. Pal, P. Schall, and A. F. Koenderink, *Accessing Beyond-Light Line Dispersion and High-Q Resonances of Dense Plasmon Lattices by Bandfolding*, ACS Photonics (2025).

[280] R. Kazarinov, and C. Henry, *Second-Order Distributed Feedback Lasers with Mode Selection Provided by First-Order Radiation Losses*, IEEE J. Quantum Electron. **21**, 144 (1985).

[281] K. Sakai, E. Miyai, and S. Noda, *Two-Dimensional Coupled Wave Theory for Square-Lattice Photonic-Crystal Lasers with TM-Polarization*, Opt. Express **15**, 3981 (2007).

[282] J. Mørk, J. Mark, and B. Tromborg, *Route to Chaos and Competition between Relaxation Oscillations for a Semiconductor Laser with Optical Feedback*, Phys. Rev. Lett. **65**, 1999 (1990).

[283] H. Wenzel, U. Bandelow, H.-J. Wunsche, and J. Rehberg, *Mechanisms of Fast Self Pulsations in Two-Section Dfb Lasers*, IEEE J. Quantum Electron. **32**, 69 (1996).

[284] T. Heil, I. Fischer, W. Elsässer, J. Mulet, and C. R. Mirasso, *Chaos Synchronization and Spontaneous Symmetry-Breaking in Symmetrically Delay-Coupled Semiconductor Lasers*, Phys. Rev. Lett. **86**, 795 (2001).

[285] H. Erzgräber, D. Lenstra, B. Krauskopf, E. Wille, M. Peil, I. Fischer, and W. Elsäßer, *Mutually Delay-Coupled Semiconductor Lasers: Mode Bifurcation Scenarios*, Opt. Commun. **255**, 286 (2005).

[286] T. D. Happ, M. Kamp, A. Forchel, J.-L. Gentner, and L. Goldstein, *Two-Dimensional Photonic Crystal Coupled-Defect Laser Diode*, Appl. Phys. Lett. **82**, 4 (2003).

[287] H. Altug, and J. Vučković, *Photonic Crystal Nanocavity Array Laser*, Opt. Express **13**, 8819 (2005).

[288] A. N. Pisarchik, and F. R. Ruiz-Oliveras, in *Nonlinear Dynamics New Directions: Models and Applications*, edited by H. González-Aguilar, and E. Ugalde (Springer International Publishing, Cham, 2015), pp. 129–155, ISBN 978-3-319-09864-7.

[289] J. Ohtsubo, *Semiconductor Lasers: Stability, Instability and Chaos*, vol. 111 of *Springer Series in Optical Sciences* (Springer International Publishing, Cham, Switzerland, 2017).

[290] J. Schmutzler, P. Lewandowski, M. Aßmann, D. Niemietz, S. Schumacher, M. Kamp, C. Schneider, S. Höfling, and M. Bayer, *All-Optical Flow Control of a Polariton Condensate Using Nonresonant Excitation*, Phys. Rev. B **91**, 195308 (2015).

[291] N. Bachelard, S. Gigan, X. Noblin, and P. Sebbah, *Adaptive Pumping for Spectral Control of Random Lasers*, Nat. Phys. **10**, 426 (2014).

[292] P. P. Iyer, N. Karl, S. Addamane, S. D. Gennaro, M. B. Sinclair, and I. Brener, *Sub-Picosecond Steering of Ultrafast Incoherent Emission from Semiconductor Metasurfaces*, Nat. Photonics **17**, 588 (2023).

[293] L. Sirovich, and M. Kirby, *Low-Dimensional Procedure for the Characterization of Human Faces*, J. Opt. Soc. Am. A **4**, 519 (1987).

[294] R. D. Buijs, N. J. Schilder, T. A. W. Wolterink, G. Gerini, E. Verhagen, and A. F. Koenderink, *Super-Resolution without Imaging: Library-Based Approaches Using Near-To-Far-Field Transduction by a Nanophotonic Structure*, ACS Photonics **7**, 3246

(2020).

[295] R. Röhrich, G. Oliveri, S. Kovaios, V. T. Tenner, A. J. den Boef, J. T. B. Overvelde, and A. F. Koenderink, *Uncertainty Estimation and Design Optimization of 2d Diffraction-Based Overlay Metrology Targets*, ACS Photonics **7**, 2765 (2020).

[296] Y. Liang, C. Peng, K. Ishizaki, S. Iwahashi, K. Sakai, Y. Tanaka, K. Kitamura, and S. Noda, *Three-Dimensional Coupled-Wave Analysis for Triangular-Lattice Photonic-Crystal Surface-Emitting Lasers with Transverse-Electric Polarization*, Opt. Express **21**, 565 (2013).

[297] O. Jamadi, E. Rozas, G. Salerno, M. Milićević, T. Ozawa, I. Sagnes, A. Lemaître, L. Le Gratiet, A. Harouri, I. Carusotto, J. Bloch, and A. Amo, *Direct Observation of Photonic Landau Levels and Helical Edge States in Strained Honeycomb Lattices*, Light Sci. Appl. **9**, 144 (2020).

[298] R. Barczyk, L. Kuipers, and E. Verhagen, *Observation of Landau Levels and Chiral Edge States in Photonic Crystals through Pseudomagnetic Fields Induced by Synthetic Strain*, Nat. Photonics **18**, 1 (2024).

[299] W. L. Barnes, T. W. Preist, S. C. Kitson, J. R. Sambles, N. P. K. Cotter, and D. J. Nash, *Photonic Gaps in the Dispersion of Surface Plasmons on Gratings*, Phys. Rev. B **51**, 11164 (1995).

[300] W. L. Barnes, T. W. Preist, S. C. Kitson, and J. R. Sambles, *Physical Origin of Photonic Energy Gaps in the Propagation of Surface Plasmons on Gratings*, Phys. Rev. B **54**, 6227 (1996).

[301] M. Carras, and A. D. Rossi, *Field Concentration by Exciting Surface Defect Modes*, Opt. Lett. **31**, 47 (2006).

[302] C. J. Summers, C. W. Neff, and W. Park, *Active Photonic Crystal Nano-Architectures*, J. Nonlinear Optic. Phys. Mat. **12**, 587 (2003).

[303] C. W. Neff, *Optical Properties of Superlattice Photonic Crystals*, Ph.D. thesis, Georgia Institute of Technology (2005).

[304] C. W. Neff, and C. J. Summers, *A Photonic Crystal Superlattice Based on Triangular Lattice*, Opt. Express **13**, 3166 (2005).

[305] C. W. Neff, T. Yamashita, and C. J. Summers, *Observation of Brillouin Zone Folding in Photonic Crystal Slab Waveguides Possessing a Superlattice Pattern*, Appl. Phys. Lett. **90**, 021102 (2007).

[306] N. Le Thomas, R. Houdré, L. H. Frandsen, J. Fage-Pedersen, A. V. Lavrinenko, and P. I. Borel, *Grating-Assisted Superresolution of Slow Waves in Fourier Space*, Phys. Rev. B **76**, 035103 (2007).

[307] D. P. Gaillot, E. Graugnard, J. Blair, and C. J. Summers, *Dispersion Control in Two-Dimensional Superlattice Photonic Crystal Slab Waveguides by Atomic Layer Deposition*, Appl. Phys. Lett. **91**, 181123 (2007).

[308] N. Le Thomas, R. Houdré, D. M. Beggs, and T. F. Krauss, *Fourier Space Imaging of Light Localization at a Photonic Band-Edge Located below the Light Cone*, Phys. Rev. B **79**, 033305 (2009).

[309] N.-V.-Q. Tran, S. Combrié, and A. De Rossi, *Directive Emission from High-Q Photonic Crystal Cavities through Band Folding*, Phys. Rev. B **79**, 041101 (2009).

[310] C. M. Anderson, and K. P. Giapis, *Larger Two-Dimensional Photonic Band Gaps*,

Phys. Rev. Lett. **77**, 2949 (1996).

[311] A. Cerjan, and S. Fan, *Complete Photonic Band Gaps in Supercell Photonic Crystals*, Phys. Rev. A **96**, 051802 (2017).

[312] A. C. Overvig, S. Shrestha, and N. Yu, *Dimerized High Contrast Gratings*, Nanophotonics **7**, 1157 (2018).

[313] W. Wang, Y. K. Srivastava, T. C. Tan, Z. Wang, and R. Singh, *Brillouin Zone Folding Driven Bound States in the Continuum*, Nat. Commun. **14**, 2811 (2023).

[314] K. Sun, W. Wang, and Z. Han, *High-Q Resonances in Periodic Photonic Structures*, Phys. Rev. B **109**, 085426 (2024).

[315] V. G. Kravets, F. Schedin, and A. N. Grigorenko, *Extremely Narrow Plasmon Resonances Based on Diffraction Coupling of Localized Plasmons in Arrays of Metallic Nanoparticles*, Phys. Rev. Lett. **101**, 087403 (2008).

[316] J. A. Fan, K. Bao, C. Wu, J. Bao, R. Bardhan, N. J. Halas, V. N. Manoharan, G. Shvets, P. Nordlander, and F. Capasso, *Fano-Like Interference in Self-Assembled Plasmonic Quadrumer Clusters*, Nano Lett. **10**, 4680 (2010).

[317] A. D. Humphrey, N. Meinzer, T. A. Starkey, and W. L. Barnes, *Surface Lattice Resonances in Plasmonic Arrays of Asymmetric Disc Dimers*, ACS Photonics **3**, 634 (2016).

[318] A. D. Humphrey, and W. L. Barnes, *Plasmonic Surface Lattice Resonances in Arrays of Metallic Nanoparticle Dimers*, J. Opt. **18**, 035005 (2016).

[319] N. Mahi, G. Lévêque, O. Saison, J. Marae-Djouda, R. Caputo, A. Gontier, T. Maurer, P.-M. Adam, B. Bouhafs, and A. Akjouj, *In Depth Investigation of Lattice Plasmon Modes in Substrate-Supported Gratings of Metal Monomers and Dimers*, J. Phys. Chem. C **121**, 2388 (2017).

[320] N. Wang, M. Zeisberger, U. Huebner, V. Giannini, and M. A. Schmidt, *Symmetry-Breaking Induced Magnetic Fano Resonances in Densely Packed Arrays of Symmetric Nanotrimers*, Sci. Rep. **9**, 2873 (2019).

[321] S.-D. Liu, P. Yue, S. Zhang, M. Wang, H. Dai, Y. Chen, Z.-Q. Nie, Y. Cui, J.-B. Han, and H. Duan, *Metasurfaces Composed of Plasmonic Molecules: Hybridization Between Parallel and Orthogonal Surface Lattice Resonances*, Adv. Opt. Mater. **8**, 1901109 (2020).

[322] S. Murai, D. R. Abujetas, L. Liu, G. W. Castellanos, V. Giannini, J. A. Sánchez-Gil, K. Tanaka, and J. Gómez Rivas, *Engineering Bound States in the Continuum at Telecom Wavelengths with Non-Bravais Lattices*, Laser Photonics Rev. **16**, 2100661 (2022).

[323] G. Salerno, R. Heilmann, K. Arjas, K. Aronen, J.-P. Martikainen, and P. Törmä, *Loss-Driven Topological Transitions in Lasing*, Phys. Rev. Lett. **129**, 173901 (2022).

[324] D. Wang, A. Yang, W. Wang, Y. Hua, R. D. Schaller, G. C. Schatz, and T. W. Odom, *Band-Edge Engineering for Controlled Multi-Modal Nanolasing in Plasmonic Superlattices*, Nat. Nanotechnol. **12**, 889 (2017).

[325] R. Heilmann, K. Arjas, T. K. Hakala, and Päivi Törmä, *Multimode Lasing in Supercell Plasmonic Nanoparticle Arrays*, ACS Photonics **10**, 3955 (2023).

[326] X. M. Bendaña, G. Lozano, G. Pirruccio, J. G. Rivas, and F. J. G. de Abajo, *Excitation of Confined Modes on Particle Arrays*, Opt. Express **21**, 5636 (2013).

[327] K. Guo, G. Lozano, M. A. Verschuuren, and J. Gómez Rivas, *Control of the External Photoluminescent Quantum Yield of Emitters Coupled to Nanoantenna Phased Arrays*, J. Appl. Phys. **118**, 073103 (2015).

[328] P. Bharadwaj, B. Deutsch, and L. Novotny, *Optical Antennas*, Adv. Opt. Photon. **1**, 438 (2009).

[329] R. Carminati, J. J. Sáenz, J.-J. Greffet, and M. Nieto-Vesperinas, *Reciprocity, Unitarity, and Time-Reversal Symmetry of the S Matrix of Fields Containing Evanescent Components*, Phys. Rev. A **62**, 012712 (2000).

[330] O. T. A. Janssen, A. J. H. Wachters, and H. P. Urbach, *Efficient Optimization Method for the Light Extraction from Periodically Modulated LEDs Using Reciprocity*, Opt. Express **18**, 24522 (2010).

[331] E. Bailly, J.-P. Hugonin, J.-R. Coudevylle, C. Dabard, S. Ithurria, B. Vest, and J.-J. Greffet, *2d Silver-Nanoplatelets Metasurface For Bright Directional Photoluminescence, Designed With The Local Kirchhoff's Law*, ACS Nano **18**, 4903 (2024).

[332] M. S. Bin-Alam, O. Reshef, Y. Mamchur, M. Z. Alam, G. Carlow, J. Upham, B. T. Sullivan, J.-M. Ménard, M. J. Huttunen, R. W. Boyd, and K. Dolgaleva, *Ultra-High-Q Resonances in Plasmonic Metasurfaces*, Nat. Commun. **12**, 974 (2021).

[333] Q. Le-Van, E. Zoethout, E.-J. Geluk, M. Ramezani, M. Berghuis, and J. Gómez Rivas, *Enhanced Quality Factors of Surface Lattice Resonances in Plasmonic Arrays of Nanoparticles*, Adv. Opt. Mater. **7**, 1801451 (2019).

[334] Y. Zhou, Z. Guo, X. Zhao, F. Wang, Z. Yu, Y. Chen, Z. Liu, S. Zhang, S. Sun, and X. Wu, *Dual-Quasi Bound States in the Continuum Enabled Plasmonic Metasurfaces*, Adv. Opt. Mater. **10**, 2200965 (2022).

[335] A. Manjavacas, L. Zundel, and S. Sanders, *Analysis of the Limits of the Near-Field Produced by Nanoparticle Arrays*, ACS Nano **13**, 10682 (2019).

[336] A. Fischer, T. Severs Millard, X. Xiao, T. Raziman, J. Dranczewski, R. C. Schofield, H. Schmid, K. Moselund, R. Sapienza, and R. F. Oulton, *Surface Lattice Resonance Lasers with Epitaxial InP Gain Medium*, ACS Photonics **11**, 4316 (2024).

[337] A. Cuartero-González, S. Sanders, L. Zundel, A. I. Fernández-Domínguez, and A. Manjavacas, *Super- and Subradiant Lattice Resonances in Bipartite Nanoparticle Arrays*, ACS Nano **14**, 11876 (2020).

[338] K. M. McPeak, S. V. Jayanti, S. J. P. Kress, S. Meyer, S. Iotti, A. Rossinelli, and D. J. Norris, *Plasmonic Films Can Easily Be Better: Rules and Recipes*, ACS Photonics **2**, 326 (2015).

[339] J. J. Penninkhof, L. A. Sweatlock, A. Moroz, H. A. Atwater, A. van Blaaderen, and A. Polman, *Optical Cavity Modes in Gold Shell Colloids*, J. Appl. Phys. **103**, 123105 (2008).

Epilogue

Summary

Since ages, humanity has been captivated by the physics of light. Progress in our understanding of light paved the way for many applications, pushing the rational design of optical instruments for microscopy, astronomy and spectroscopy to great heights since the mid-19th century. The past hundred years has displayed further magnificent advances in light-based technologies, such as the laser, LED, CCD camera and optical fibers for long range communication - each of these light-technologies forms a backbone of our modern-day society. The next push forward is to assert control over light at very small scales, comparable to and shorter than the wavelength of light. This is the objective of the field called *nanophotonics*. Such miniaturized light control enables, for instance, chip-scale control over the generation, routing, and processing of light, and is pursued to strongly couple light and matter. Currently, within nanophotonics, much attention is given to so-called metasurfaces: Thin patterned surfaces that promise control over incoming light beams through near-arbitrary reshaping of wavefronts by means of scattering. Metasurfaces are composed of subwavelength resonant nanoparticles that are strongly scattering, with scattering cross sections much larger than their physical size. These nanoparticles are generally either metallic, with plasmon resonances due to the free electron see, or they have such high refractive indices that they feature strong Mie resonances. Alongside such *scattering metasurfaces* there are also *light-emitting metasurfaces*. Whereas, scattering metasurfaces perform designed functions on incident wavefronts, light-emitting metasurfaces are structures into which light emitters are embedded to form a radiating light source with engineered brightness, spectrum, polarization and directionality.

This thesis considers metasurfaces with embedded optical gain, i.e., amplification of light by stimulated emission. Amplification is enabled by including emitters into metasurfaces, and then providing sufficiently strong optical pumping to realize net amplification. Amplification is promising both for scattering metasurfaces and for light-emitting metasurfaces. In the context of scattering metasurfaces, active tunability receives much interest to overcome the drawback of passive metasurfaces that function is fixed after fabrication. A motivation for this thesis is that gain can be used to dynamically modulate the response of metasurfaces. For scattering metasurfaces, gain-induced response tuning has received little attention. For light-emitting metasurfaces, optical gain is a common route to obtain metasurface lasing, where distributed feedback is offered by the scatterers. Such systems generally operate by hybridization of diffractive conditions and the localized scattering resonances. While the essential operating mechanisms in such lasers have been explored in several groups in the last decade, there are still many open questions relating to their dynamics – phenomena such as mode competition and spontaneous symmetry breaking – and programmability of laser emission through spatial

and dynamic control of the gain. These questions are also driven by an analogon between amplifying periodic lattices of scatterers and seminal problems in condensed matter physics regarding Parity-Time symmetry and topology in non-Hermitian 2D systems. The motivation of this thesis is to develop techniques to address amplifying scattering metasurfaces and to obtain a better understanding of amplifying scattering as well as lasing metasurfaces at optical frequencies.

In **Chapter 2**, we report on the development of an ultrafast pump-probe microscope to study amplifying metasurfaces, through the combination of Fourier microscopy with femtosecond pump-probe techniques. Operating with visible and near-infrared pump and probe beams, we show the capability to perform synchronized single-shot real-space and Fourier-space imaging on amplifying metasurfaces. An important capability of the setup is that we can spatially program where gain is induced in a metasurface, by means of a digital micromirror device. We highlight the new setup's capabilities for two testbeds: Amplifying plasmonic lattices and amplifying 1D gratings. For the former, we show that metasurface band structures can be recorded using the white-light probe beam. For the latter, we report gain-induced 1D-grating efficiency modulations of 15% on picosecond time scales. We observe that gain can induce both enhancement and suppression of diffraction efficiencies. The new experimental setup is equipped for the study of PT-symmetry breaking scattering metasurfaces, metasurfaces with perfect absorption and amplification singularities, and amplifying wave-based computing metasurfaces.

Chapter 3 is a theoretical study of singular responses in the reflection of light from a scattering metasurface with gain. The proposed family of metasurfaces are inspired by a common and powerful design strategy to create perfect absorption singularities: Scattering anomalies at which all incoming light is absorbed by the metasurface. This problem has been widely studied in the radio-frequency community, where so-called Salisbury and Dallenbach screens achieve perfect absorption by holding modestly absorbing structured sheets at carefully chosen distances from non-absorbing mirrors. We study such geometries with a plasmonic metasurface as structured sheet, but we consider optical gain as opposed to absorption, using a transfer matrix model to calculate reflectivity from the stack. What is more, we present the implications of different frequency-dispersive gain models one can use. Most notably, in the field of PT-symmetry, time-reversal symmetry is often invoked to argue that loss and gain are simply interchangeable in material response functions (mathematically, time-reversal becomes a sign-reversal of decay rate). However, for scatterers with gain, such arguments do not hold, and we review self-consistent models for the polarizability and cross sections of amplifying scatterers. Our main finding is that, when the metasurface contains scatterers with both gain and loss, gain can induce both perfect absorption (reflectivity zeros) and perfect amplification (reflectivity poles). We describe topological constraints on the creation and annihilation of these singularities. The find-

ings of this chapter have implications for the fields of non-Hermitian photonics, parity-time symmetric scattering systems, and metasurface pixels that are dynamically controllable.

In **Chapter 4**, we report on the first observation of spontaneous symmetry breaking (SSB) in plasmonic metasurface lasers. We study diffractive lattices of hexagonal symmetry, where the K-points in momentum space come with two modes, K and K'. These modes are not only degenerate in frequency, but they are also identically distributed in space. We energize the gain medium with femtosecond pulses and we simultaneously capture real- and Fourier-space images of laser emission in a single-shot fashion. By combining the real and Fourier space, we resolve the two order parameters for which symmetry breaking simultaneously occurs: Spatial parity and U(1) (rotational) symmetry breaking. The order parameters belong respectively to a relative amplitude and phase between K and K', and they are randomly 'picked' for every subsequent pulse of laser emission. The methodology reported in this work opens numerous opportunities, for instance in studying SSB in metasurfaces, or in mapping the emergence of spatial coherence during the laser transition of amplifying nonlocal metasurfaces.

Chapter 5 builds on the SSB-study of Chapter 4. We focus on K-point lasing in hexagonal lattices, and we subject the 2D laser to boundary conditions in metasurface gain. We project optical pump fields of programmable geometries by means of the digital micromirror device. In Fourier space, we observe vortex beams of laser emission typical for 2D lasers, and we find that they strongly depend on gain field geometry and size in real space. With single-shot acquisition, we observe spontaneous parity symmetry breaking between lasing in the degenerate KK and K' modes, and we study the relation between real-space laser shape, Fourier-space output, and local spatial intensity distribution in the spontaneous symmetry breaking process. Spatial programming also gives access to creating nearby coupled lasers. We show that two closely spaced metasurface lasers synchronize both in phase and in amplitude, which depends on their coupling strength set by separation distance.

Finally, in **Chapter 6**, we study dense plasmon light-emitting metasurfaces. These systems display both near field as well as diffractive coupling, for which they make highly interesting platforms for the study of plasmon versions of seminal tight-binding Hamiltonians. However, the lattice plasmon dispersions lie beyond the light line, and are therefore not accessible with standard far-field optical experiments. In this work, we make these guided plasmon dispersions visible by band folding, which we induce by applying size perturbations to the scatterers and introducing a supercell periodicity. Both in fluorescence enhancement experiments and in reciprocity-based T-matrix simulations, we observe bandfolding for a systematic variation of perturbation strength. Folding the K-point into the light cone creates a narrow plasmon mode. This mode exhibits among the highest reported quality factors

for plasmon lattice resonances in the visible wavelength range, despite the fact that the antenna array comes in a doubled areal density. Finally, we show K-point lasing and spontaneous symmetry breaking between the bandfolded K- and K'-modes. From the spontaneous symmetry breaking behavior, we conclude that intrinsic symmetry properties of the dense plasmon lattice are maintained and can be observed upon bandfolding.

Samenvatting

De mensheid is al eeuwenlang gefascineerd door de natuurkunde van licht. Vooruitgang in ons begrip van licht heeft de weg vrijgemaakt voor vele toepassingen, en heeft het ontwerp van optische instrumenten voor microscopie, astronomie en spectroscopie sinds het midden van de 19e eeuw tot grote hoogten gebracht. De afgelopen honderd jaar is er een verdere geweldige vooruitgang geweest in technologieën die op licht gebaseerd zijn, zoals de laser, de LED, de CCD-camera en optische glasvezelkabels voor langeafstandscommunicatie - elk van deze lichttechnologieën zijn essentieel in onze moderne samenleving. De volgende stap voorwaarts is om controle te krijgen over licht op zeer kleine lengteschaal, vergelijkbaar met of zelfs korter dan de golflengte van licht. Dit is het doel van het vakgebied nanofotonica. Dergelijke geminiaturiseerde lichtcontrole wordt bijvoorbeeld nagestreefd om licht en materie sterk te koppelen, en maakt het mogelijk om op de schaal van elektronische microchips de generatie van licht, het versturen van lichtsignalen, en de logische verwerking van informatie gecodeerd in licht te bewerkstelligen. Momenteel wordt er binnen de nanofotonica veel aandacht besteed aan zogenaamde meta-oppervlakken: dunne, gestructureerde oppervlakken die controle uitoefening over inkomende lichtbundels door de golffronten van de bundel naar wens vorm te geven door middel van deeltjesverstrooiing. Meta-oppervlakken bestaan uit resonante nanodeeltjes die kleiner zijn dan de golflengte van het licht, en die licht zeer sterk verstrooien: ze hebben verstrooiingsdoorsneden die veel groter zijn dan hun fysieke grootte. Deze nanodeeltjes zijn over het algemeen ofwel gemaakt uit edele metalen, in welk geval plasmonische verstrooiingsresonanties optreden vanwege hun vrije elektronen wolk, of ze hebben zulke hoge brekingsindices dat ze sterke Mie-resonanties vertonen. Naast dergelijke verstrooiende meta-oppervlakken zijn er ook licht-uitstralende meta-oppervlakken. Terwijl verstrooiende meta-oppervlakken functies uitvoeren door invallende golffronten te verstrooiien, zijn licht-uitstralende meta-oppervlakken structuren waarin licht-emitterende deeltjes zijn ingebed om een lichtbron te vormen die straalt met naar wens ontworpen helderheid, spectrum, polarisatie en richting.

Dit proefschrift beschouwt meta-oppervlakken met ingebedde optische versterking, welke behaald wordt door middel van gestimuleerde emissie. Versterking wordt mogelijk gemaakt door licht-emitterende moleculen in meta-oppervlakken op te nemen en vervolgens een voldoende sterke optische pompbundel als energiebron aan te bieden om netto versterking te realiseren. Versterking is veelbelovend voor zowel verstrooiende meta-oppervlakken als voor lichtgevende meta-oppervlakken. Een motivatie voor dit proefschrift is dat versterking kan worden gebruikt om de respons van meta-oppervlakken dynamisch te moduleren. In de context van verstrooiende meta-oppervlakken is er veel onderzoek naar actieve controle over functionaliteit om het probleem

op te lossen dat voor de meeste meta-oppervlakken de functie na fabricage niet meer veranderd kan worden. Versterking als mechanisme voor actieve en dynamische controle over functie heeft echter weinig aandacht gekregen. In het onderzoeksveld van lichtgevende meta-oppervlakken is optische versterking een gebruikelijke route om een meta-oppervlak laser te maken, waarbij terugkoppeling ontstaat door Bragg verstrooiing aan het periodieke rooster van deeltjes. Dergelijke systemen werken over het algemeen door een samenspel van traliediffracties en de lokale verstrooiingsresonanties van de individuele verstrooiers. Hoewel de essentiële werkingsmechanismen in dergelijke lasers in het afgelopen decennium zijn onderzocht door verschillende groepen, zijn er nog steeds veel open vragen met betrekking tot hun gedrag in de tijd. Dit betreft bijvoorbeeld verschijnselen zoals competitie tussen de laser modes en spontane symmetriebreking, en ook de vraag of de laseremissie programmeerbaar is door ruimtelijke en dynamische controle van de versterking. Deze vragen worden ook aangestuurd door een analogon tussen versterkende periodieke roosters van verstrooiers en fundamentele problemen in de fysica van gecondenseerde materie, welke betrekking hebben tot pariteit-tijd symmetrie en topologie in niet-Hermitische 2D-systemen. De motivatie van dit proefschrift is om technieken te ontwikkelen om versterkende verstrooiende meta-oppervlakken te onderzoeken, en om een beter begrip te krijgen van versterkende verstrooiende en laser meta-oppervlakken.

In **Hoofdstuk 2** rapporteren we over de ontwikkeling van een ultrasnelle pomp-sondemicroscoop om versterkende meta-oppervlakken te bestuderen. In deze opstelling wordt Fourier-microscopie met femtoseconde pomp-sondetechnieken gecombineerd. Werkend met zichtbare en nabij-infrarood pomp- en sondestralen, tonen we de mogelijkheid tot het gesynchroniseerd afbeelden in een enkele laserflits van de response van meta-oppervlakken in zowel de reële (plaatsopgeloste) en reciproke (hoekopgeloste) ruimte tegelijkertijd. Een belangrijke mogelijkheid van de opstelling is bovendien dat we ruimtelijk kunnen programmeren waar versterking wordt geïnduceerd in een meta-oppervlak, door middel van een digitaal microspiegelapparaat. We bekijken de mogelijkheden van de nieuwe opstelling door twee systemen te onderzoeken: plasmonische roosters en versterkende van 1-dimensionale (1D) diffractietralies. Voor de eerstgenoemde laten we zien dat bandenstructuren van een meta-oppervlak kunnen worden vastgelegd met behulp van een spectraal breedbandige sondestraal. Voor de laatstgenoemde rapporteren we versterking-geïnduceerde 1D tralie diffractie efficiëntiemodulaties van 15% op picoseconde tijdschalen. We observeren dat versterking tot zowel vergroting als vermindering van diffractie-efficiënties kan leiden. De nieuwe experimentele opstelling is uitgerust voor de studie van verstrooiende meta-oppervlakken met PT-symmetrie, meta-oppervlakken met perfecte absorptie- en versterkingssingulariteiten en versterkende golfgebaseerde meta-oppervlak computers.

Hoofdstuk 3 is een theoretische studie van singuliere responsen in de reflectie van licht van een verstrooiende meta-oppervlak met versterking. De voorgestelde familie van meta-oppervlakken is geïnspireerd door een veelvoorkomende en krachtige ontwerpstrategie om perfecte absorptie singulariteiten te creëren: verstrooiingsanomalieën waarbij al het binnenkomende licht wordt geabsorbeerd door een meta-oppervlak. Dit probleem is uitgebreid bestudeerd in de radiofrequentiegemeenschap, waar zogenaamde Salisbury en Dallenbach schermen perfecte absorptie bewerkstelligen door een op zichzelf maar zwakjes absorberende laag op zorgvuldig gekozen afstanden van een niet-absorberende spiegel te houden. We bestuderen dergelijke geometrieën met een plasmonisch meta-oppervlak, maar we beschouwen optische versterking in tegenstelling tot absorptie, met behulp van een transfer matrix model om de reflectiviteit van het gehele systeem te berekenen. Met name in het onderzoeksgebied van PT-symmetrie wordt tijdsomkeringsymmetrie vaak aangeroepen om te beargumenteren dat verlies en versterking eenvoudigweg uitwisselbaar zijn in materiaalresponsfuncties (wiskundig gezien wordt tijdsomkering een tekenomkering van de vervalsnelheid). Voor verstrooiers met versterking houden dergelijke argumenten echter geen stand, en we bekijken zelfconsistente modellen voor de polariseerbaarheid en verstrooiingsdoorsneden van versterkende verstrooiers. Onze belangrijkste bevinding is dat, wanneer het meta-oppervlak verstrooiers met zowel versterking als verlies bevat, versterking zowel perfecte absorptie (reflectiviteitsnullen) als perfecte versterking (reflectiviteitspolen) kan induceren. We beschrijven topologische beperkingen op de creatie en vernietiging van deze singulariteiten. De bevindingen van dit hoofdstuk hebben implicaties voor de vakgebieden van niet-Hermitische fotonica, pariteit-tijd symmetrische verstrooiingssystemen en meta-oppervlak pixels die dynamisch controleerbaar zijn.

In **Hoofdstuk 4** rapporteren we over de eerste observatie van spontane symmetriebreking (SSB) in plasmonische meta-oppervlak lasers. We bestuderen diffractieve roosters van hexagonale symmetrie, waarbij lasing kan optreden bij de K-punten in de reciproke ruimte. Hoewel er zes K-punten zijn in de Brillouin zone, is er sprake van precies twee eigenmodes, aangeduid als K en K', die elk drie K-punten door roosterdiffractie verbinden. Deze eigenmodes zijn niet alleen exact ontaard in frequentie, maar ze zijn ook precies identiek verdeeld in de ruimte. We pompen het versterkingsmedium met femtoseconde pulsen en voor elke afzonderlijke pompflits leggen we tegelijkertijd reële- en reciproke-ruimtebeelden van laserlicht vast. Door de reële- en reciproke-ruimte te combineren, vinden we de twee ordeparameters waarmee symmetriebreking gelijktijdig optreedt: ruimtelijke pariteit en U(1) (rotatie) symmetriebreking. De ordeparameters behoren respectievelijk tot een relatieve amplitude en fase tussen K en K', en ze worden willekeurig 'gekozen' voor elke volgende puls van uitgezonden laserlicht. De methodologie die in dit werk wordt gerapporteerd opent talloze mogelijkheden, bijvoorbeeld voor

het bestuderen van SSB in meta-oppervlakken, of voor het in kaart brengen van het spontaan ontstaan van ruimtelijke coherentie tijdens de laserovergang in versterkende niet-lokale meta-oppervlakken.

Hoofdstuk 5 bouwt voort op de SSB-studie van Hoofdstuk 4. We richten ons op K-punt lasers in hexagonale roosters, en we onderwerpen de 2D-laser aan randvoorwaarden in versterking in het meta-oppervlak. We projecteren optische pompvelden van programmeerbare geometrieën door middel van het digitale microspiegelapparaat. In de reciproke ruimte observeren we vortexstralen van laseremissie die typisch zijn voor 2D-lasers, en we ontdekken dat ze sterk afhankelijk zijn van de geometrie en grootte van het versterkingsveld in de reële ruimte. Zo kunnen we spontane pariteitssymmetriebreking observeren voor de ontaarde K- en K'-eigenmodes, als functie van de vorm van de laser in de reële ruimte. Ruimtelijke programmering geeft ook toegang tot het creëren van nabijgelegen gekoppelde lasers. We laten zien dat twee dicht bij elkaar gelegen meta-oppervlak-lasers zowel in fase als in amplitude synchroniseren, wat afhankelijk is van hun koppelingssterkte die weer wordt bepaald door de afstand tussen de lasers.

Tot slot bestuderen we in **Hoofdstuk 6** plasmonische licht-uitstralende meta-oppervlakken met hoge deeltjesdichtheid. In deze systemen ervaren deeltjes zowel nabije veld- als diffractieve koppeling, waardoor deze systemen zeer interessante platformen vormen voor de studie van plasmon versies van bekende tight binding Hamiltonianen. De dispersies van de plasmon roosters liggen echter buiten de lichtkegel en zijn daarom niet toegankelijk met standaard verre-veld optische experimenten. In dit werk maken we deze golfgeleide plasmonische dispersies zichtbaar door bandvouwing. Bandvouwing induceren we door kleine verstoringen toe te passen in de grootte van de verstrooiers waardoor een superperiodiciteit tevoorschijn komt, die groter is dan de periodiciteit van het onderliggende rooster. Zowel in fluorescentie experimenten als in op reciprociteit gebaseerde T-matrixsimulaties, observeren we bandvouwing voor een systematische variatie van de verstoringsterkte. Het vouwen van het K-punt naar binnen de lichtkegel creëert een spectraal zeer smalle plasmon resonantie. Deze resonantie vertoont zelfs één van de hoogst gerapporteerde kwaliteitsfactoren voor plasmonische rooster resonanties in het zichtbare golflengtebereik, aanzienlijk hoger dan de kwaliteitsfactor in roosters waar de deeltjes veel verder uit elkaar zitten. Dit is opvallend omdat een plasmonisch rooster met een verdubbelde oppervlaktedichtheid in de meeste gevallen juist veel meer, in plaats van minder, optische absorptie vertoont. Tot slot tonen we aan dat ook deze systemen K-punt lasing en spontane symmetriebreking vertonen, nu tussen de bandgevouwen K- en K'-eigenmodes. Uit het spontane symmetriebrekingsgedrag concluderen we dat intrinsieke symmetrie-eigenschappen van het originele plasmonisch rooster behouden blijven en kunnen worden waargenomen bij het bandenvouwen.

List of publications

Related to this thesis

1. N. de Gaay Fortman, R. Kolkowski, D. Pal, S. R. K. Rodriguez, P. Schall and A. F. Koenderink, *Spontaneous symmetry breaking in plasmon lattice lasers*, Sci. Adv. **10**, eadn2723 (2024). (**Chapter 4**)

2. N. de Gaay Fortman*, D. Pal*, P. Schall and A. F. Koenderink, *Accessing beyond-light line dispersion and high-Q resonances of dense plasmon lattices by bandfolding*, ACS Photonics, DOI: 10.1021/acsphotonics.4c02323. (**Chapter 6**)

3. N. de Gaay Fortman, G.-M. Krause, P. Schall and A. F. Koenderink, *Absorption and amplification singularities in plasmon metasurface etalons with gain*, submitted to Nanopotonics. (**Chapter 3**)

4. N. de Gaay Fortman, R. Kolkowski, N. Feldman, P. Schall and A. F. Koenderink, *Plasmon lattice lasers programmed in size, shape and symmetry*, in preparation. (**Chapter 5**)

Other

5. J. S. van der Burgt, S. A. Rigter, N. de Gaay Fortman and E. C. Garnett, *Self-tracking solar concentrator with absorption of diffuse sunlight*, Adv. Opt. Mater. **11**, 2202013 (2023)

6. H. van der Graaf, A. Bertolini, J. van Heijningen, B. Bouwens, N. de Gaay Fortman, T. van der Reep, L. Otemann, *The ultimate performance of the Rasnik 3-point alignment system*, Nucl. Instrum. Methods Phys. Res. A **1050**, 168160 (2023)

* These authors contributed equally.

Author contributions

Chapter 2 *Nelson de Gaay Fortman* designed and built the set up, with technical support from *Marko Kamp* and the AMOLF technical support departments . He performed 1D-grating sample fabrication, measurements, analysis, interpretation, model implementation, and writing. *Georg Krause* performed pump-probe measurements on gain gratings and proposed the first version of the diffraction model. *Debapriya Pal* fabricated the plasmonic array sample. *Peter Schall* assisted in interpretation and commented on the manuscript. *A. Femius Koenderink* contributed to data analysis, interpretation, model implementation, cowriting the manuscript, and overall supervision.

Chapter 3 *Nelson de Gaay Fortman* performed model implementation, analysis, interpretation, and writing. *Georg Krause* contributed to model implementation, analysis, and interpretation. *Peter Schall* assisted in interpretation and commented on the manuscript. *A. Femius Koenderink* contributed to model implementation, analysis, interpretation, cowriting the manuscript, and overall supervision.

Chapter 4 *Nelson de Gaay Fortman* performed measurements, analysis, interpretation, and writing. *Radoslaw Kolkowski* contributed to the measurements, interpretation, and visualization and developed the theoretical model. *Debapriya Pal* fabricated the sample. *Said R. K. Rodriguez* and *Peter Schall* assisted in interpretation and commented on the manuscript. *A. Femius Koenderink* contributed to data analysis, interpretation, cowriting the manuscript, and overall supervision.

Chapter 5 *Nelson de Gaay Fortman* performed measurements, analysis, interpretation, and writing. *Radoslaw Kolkowski* performed measurements and interpretation. *Nick Feldman* fabricated the sample. *Peter Schall* assisted in interpretation and commented on the manuscript. *A. Femius Koenderink* contributed to data analysis, interpretation, cowriting the manuscript, and overall supervision.

Chapter 6 *Nelson de Gaay Fortman* performed measurements, analysis, interpretation, and writing. *Debapriya Pal* performed treams and COMSOL modelling and fabricated the sample. *Peter Schall* assisted in interpretation and commented on the manuscript. *A. Femius Koenderink* contributed to data analysis, interpretation, treams and COMSOL modelling , cowriting the manuscript, and overall supervision.

Acknowledgements

Femius, I feel honoured to have had you as my mentor during my time at AMOLF. I admire you as a scientist, and I have been inspired by your tendency for deep understanding and thorough methodology. I also value you high as a person. I've grown very fond of your unique character, with your peculiar and sharp humor, but also your caring side. I always had the feeling that you would go to great lengths for me. And with that feeling of support from your side, I reached a level of quality in my work that I could not have dreamed of before starting.

And Peter, I am grateful for your kind and cheerful supervision. From you I learned to comprehend the larger picture of a project, and you also helped me to become a better writer, conveying the main message more clearly and in simpler terms.

I have made two very dear friends at AMOLF. Deba, we started almost at the same time and since then I have grown very attached to your loyal, philosphical, supportive and warm character. I will miss our whiteboard sessions, our scientific collaborations, but mostly our calm and deep conversations about life. Falco, my extravagant spiritual leader! Rarely one sees a level of sheer exuberance as which can be radiated by you. And our NanoBIG rapping adventure is a thrilling highlight of my scientific career. But I have also got to know your quiet and wise side, which I appreciate perhaps even more.

Being situated in the Resonant Nanophotonics group is a privilege. This is a stimulating set of people, regardless of the generations that I happened to interact with. I wish to especially mention Nick, Ilan, Tom, Isabella, Zihao, and Masha as important people for my scientific development and my feeling of joy at the workplace. What is more, I wish to thank both Jake and Georg for the trust they have given me as daily supervisor of their thesis projects. Finally, Radek, I feel greatly indebted to you, for much of my work is based on your ideas. I thank you for helping me with setting up my project, and for our close collaboration on beautiful papers ever since.

Having spent much time with the Soft Matter Physics group and 2D Nanophotonics group over at the UvA, I learned a great deal from Yingying, Marco, Suzanne, Ludovica, Tom, Freek and Jorik.

One key aspect of my PhD work was designing and building from scratch the Coyote setup (see Chapter 2). It is a remarkable example of how much the AMOLF supportive structures enables one to progress to a level of advancement far beyond what could be achieved alone. Marko, your technical skill is exceptional, and I learned my experimental skills mostly from your patient guidance in the lab. Furthermore, I am greatly indebted to various people from the AMOLF support departments - Brahim, Marco, Ivo, Xander, Mels, Bob, Remco - for their crucial help in developing the electronics, hardware and

software that drive the Coyote setup. Finally, I had the honour to collaborate with both Julia and Tom on the setup, and our measurements lead to beautiful works.

Being part of the Nanophotonics department at AMOLF, I learned the arts of critical listening, asking questions, and presenting science. I will mention Said and Ewold as especially valuable to my development in this regard. Being part of AMOLF as a whole was a delight for me. There is something about the spirit of this place, with its cheerful, curious and helpful people. During coffee and lunch, I often had the pleasure to find myself in the enjoyable company of a cheerful bunch of Nanophotonics people: Fons, Menno, Roel, Jesse, Jente, Rene, Kevin, Zhou, Chiel, Roos, Vashist, Nassim, Andrea, Evelijn, Matthias, Alex, and many more.

I move onward by acknowledging the value of my friends and family to the accomplishment of this thesis. First of all, a set of dear friends have been of invaluable support to me during the past four and a halve years. Roel, Daan, Sander, Benjamin, Nick, Thom, Ewout, Yuval, Joris, Felix, Thomas, Joram, Rutger, Pieter. I thank you for listening to me and on rare occasions taking me and my work serious – and often just making fun of me.

Then I wish to express my appreciation and gratitude to Wouter, Yvette, Casper, Quint, and Pien, for your feeling along with the progress of my PhD work. Your love and support have been very invaluable to me.

I am fortunate to be born into two large and caring families. I received much love from my uncles, aunts, nephews and nieces from both my Van Reenen and De Gaay Fortman families. To my grandparents Bas and Ina, you have always taken such an important place in my life, and now I feel proud and grateful that I can share my completed work with you.

My brother Olivier and sister Duveke, I cherish how deeply involved we are in each other's life – the exciting parts and the hard parts – and how much love and appreciation you give me. Carl and Betteke, I view your love, care and support for me as the prime reason I got to this point in my career. I feel immensely fortunate to have such great parents as you.

And finally, Emily. You've been an integral part of my life during my PhD work: How many times did I bombard you with my excitement of the research; How many times I voiced my work-related frustrations and insecurities to you; How often did you whisper some good advice in my ear! The final stage of my PhD work coincided with your pregnancy of Yuna, and although this was hard sometimes, we supported each other and I look back on it as a beautiful time. I am very proud of you and our beautiful daughter Yuna, and I am deeply grateful for having you both by my side.

About the author

Nelson de Gaay Fortman graduated from the Gymnasium school at the Willem de Zwijger College in Bussum, The Netherlands, in 2012. Afterwards he spent a few months living in Rome to study the language and immerse himself in the Italian culture, which he still enjoys today, before going on a long travel to India and Nepal where he explored the beautiful countries and hiked in the high Himalaya mountains. In 2013, Nelson started his bachelor in physics at the University of Amsterdam, from which he graduated in 2018. In the meantime he was an active and joyful member of one of Amsterdam's student associations, while also keeping himself busy doing many kinds of student jobs. He has good memories of his time being Financial Analyst at A-Insight, conducting financial research used by customers for their commercial strategy decisions, and also of his role as Software Analyst at WellDecommissioned, developing a software tool for well closure strategies for major oil and gas companies.

In 2017, Nelson started his Master of Science in Applied Physics at the TU Delft. He greatly enjoyed his MSc thesis research project at Nikhef, where he worked as an experimentalist within the Virgo collaboration and helped improve sensitivity of two motion sensors, both crucial for reducing seismic noise in next generation gravitational wave telescopes. After completing the thesis research project, Nelson did his industrial internship at Siemens Gamesa, where he engineered a software package that calculates costs of the foundations of offshore wind turbines. Although Nelson appreciated engineering problems and industry, at that point he still felt drawn to science - to the gratifying feelings of (slightly) grasping how nature works on a deep level and making contributions to the pool of knowledge. The Resonant Nanophotonics group of Prof. Dr. A. Femius Koenderink fitted greatly to his desires, and in this group Nelson worked with tremendous joy on his PhD research from 2020 until 2025. In his free time Nelson enjoys to read, to care for his balcony garden, and to express himself through writing, painting, dancing or improvisation theater. In 2025, just after completing his PhD thesis, Nelson became a proud father of his daughter Yuna.